ADVANCED MATERIALS
FOR SOLID OXIDE FUEL CELL ANODES
PRODUCED BY MAGNETRON SPUTTERING

K STEIER

PhD 2024

Advanced materials for solid oxide fuel cell anodes produced by magnetron sputtering

Katharina Steier

A thesis submitted in partial fulfilment of the requirements of Manchester Metropolitan University for the degree of Doctor of Philosophy

Department of Engineering

Faculty of Science and Engineering

Manchester Metropolitan University

2024

Declaration

I declare that the thesis submitted is my own work and I have maintained professional integrity during all aspects of my research degree, and I have complied with the Institutional Code of Practice and the Regulations for Postgraduate Research Degrees. It has not been previously submitted, partially or whole, to any other university or institution for any degree, diploma, or other qualification. In accordance with the Department of Engineering, this thesis does not exceed 80,000 words (excluding references).

The electrochemical characterisation in chapter 8 has been carried out by colleagues from Imperial College London, as listed below:

Dr. Inyoung Jang and Dr. Anna Hankin.

Katharina Steier

Haywards Heath, 30/03/2024

Acknowledgements

In addition to the professional support, I would like to give a special shout-out to my dear friend Debora, as you also acknowledged me in your thesis ☺. Thank you for your friendship, encouragement, and willingness to stay after work to give support and motivation. Your presence has made challenging moments in a PhD more bearable and triumphs more joyful. I am looking forward to our new adventures outside the lab too!

Last but not least, I am deeply thankful to my sister Ludmilla. Your unwavering love, encouragement, and support during the last years were the pillars of strength that sustained me during the hardest of times. You provided enormous encouragement and inspiration and acted almost as a third supervisor at times, guiding me through personal and academic challenges with endless dedication. This thesis is for you, big sis!

This thesis would not have been possible without the generous support and contributions of all those mentioned above, and for that, I am truly grateful.

Glossary

AC	Alternating Current
AFL	Anode Functional Layer
ALD	Atomic Layer Deposition
ASR	Area-Specific Resistance
BSE	Backscattered Electrons
BF	Bright Field
CZ	Cerium Zirconate
CCD	Charge-Couple Device
CTE	Coefficients Of Thermal Expansion
CHP	Combined Heat And Power
CE	Counter Electrode
COD	Crystallography Open Database
DF	Dark Field
DFT	Density Function Theory
DC	Direct Current
EIS	Electrochemical Impedance Spectroscopy
EDS	Energy-Dispersive X-Ray Spectroscopy
ECM	Equivalent Circuit Model
FWHM	Full width at half maximum
GDC	Gadolinia-Doped Ceria
GHG	Greenhouse Gas
HAADF	High-Angle Annular Dark-Field
HOR	Hydrogen Oxidation Reaction
ISEE	Ion-Induced Secondary Electron Emission
LSM	Lanthanum Strontium Manganite
LSV	Linear Sweep Voltammetry
LL	Load-Lock
MFC	Mass Flow Controller
NZ	Niobium Zirconate
OAD	Oblique Angle Deposition
OCV	Open Circuit Voltage
PEMFC	Proton Exchange Membrane Fuel Cells
PLD	Pulsed Laser Deposition
PVD	Physical Vapour Deposition
PE-CVD	Plasma-Enhanced Chemical Deposition
RF	Radio Frequency
RE	Reference Electrode
SDC	Samaria-Doped Ceria
ScZ	Scandia Stabilised Zirconia
SEM	Scanning Electron Microscopy
STEM	Scanning Transmission Electron Microscopy

SE	Secondary Electrons
STP	Standard Conditions
SZM	Structure Zone Models
TPBs	Triple Phase Boundaries
WLI	White Light Interferometry
WE	Working Electrode
WS	Working Sense
XRD	X-Ray Diffraction
XPS	X-ray Photoelectron Spectroscopy
YSZ	Yttria-Stabilised Zirconia

Abstract

The present global energy problems stem from environmental pollution caused by the world's ongoing energy generation from fossil fuels. To ensure a clean and sustainable future, it is essential to use energy conversion systems that are both environmentally friendly and efficient, such as Solid Oxide Fuel Cells (SOFCs). SOFCs convert the chemical energy stored in fuels like hydrogen or gaseous hydrocarbons, directly into electrical and thermal energy. The efficiency and performance of SOFCs are inextricably linked to the material properties of the electrodes and the electrolyte. These properties are influenced by the nature of their microstructure, such as the percolated paths of their ionically and electronically conductive phases, the porosity, and most importantly, the grain size. As finer particle sizes in SOFC anodes increase the number of reaction sites, leading to higher performance, magnetron sputtering has been chosen in this work to develop advanced materials for SOFC anodes with enhanced properties in terms of efficiency and cost.

A reactive feedback control system was applied to manage quantities of oxygen introduced during the deposition of yttria-stabilised zirconia (YSZ) as well as NiO-YSZ thin films based on the oxygen partial pressure. This facilitated stable operation conditions and controlled the coating characteristics, *i.e.*, its microstructure and desired composition while varying process parameters, such as the deposition pressure or the substrate temperature during deposition. Both, the deposition at higher temperatures as well as at lower deposition pressures, resulted in densification of the microstructure of the deposited layers and a consequent loss of performance. In contrast, deposition at high total pressures resulted in significantly higher performance comparable to commercial SOFCs. After defining the optimal process parameter to create catalytically active Ni-YSZ films, complex oxides of vanadium and manganese were incorporated as dopants into the Ni-YSZ films in this work. The study found that the high dopant concentrations of vanadium or manganese resulted in significant performance degradation, showing structural and morphological changes in the doped Ni-YSZ films compared to undoped Ni-YSZ.

This work will continue in the future to advance the state of SOFC anodes by lowering dopant concentrations or developing a graded composition in the film. The substitution of YSZ for an alternative electrolyte material, such as gadolinia-doped ceria represents another promising approach regarding the doping of Ni-based anodes.

List of Figures

List of Tables

Table of Contents

I. Introduction and Literature Review

1   Introduction

1.1   Background and context

1.1.1   A net-zero future

As the United Kingdom (UK) moves towards a net-zero future, it is crucial to reflect on it in the context of the Paris Agreement which is an international commitment aimed to tackle climate change. It states that global warming will be limited to only 1.5°C if greenhouse gas (GHG) emissions peak by 2025 at the latest and fall by 43% from 2010 levels by 2030 [1]. With 40% of Britain's energy still generated from fossil fuels in 2022, strategies must be put in place to align our journey with the goals of the agreement [2]. Utilising renewable and low carbon technologies, such as hydropower, active solar technology, solar farms and wind turbines, as well as modernising our existing energy infrastructure is key for meeting Britain's commitments under the Paris Agreement, leading global efforts to combat climate change and creating a net-zero future for generations to come [3].

1.1.2   Hydrogen as an alternative to fossil fuels

To meet the target of a net-zero future, hydrogen has become recognised as a potential long-term alternative to fossil fuels for energy generation and storage solutions in recent years. However, a hydrogen-based energy transition in the UK is not trivial and will rely on government strategies to develop the energy infrastructure for hydrogen [4]. Recent reports have shown that heat and hot water account for ca. 37% of the UK's greenhouse gas emissions, as 85% of residential homes rely on natural gas, highlighting the urgent need to decarbonise end-user households [5], [6].

For that reason, projects across the UK, such as HyNet or HyDeploy at Keele University campus, are looking into mixing up to 20% of hydrogen gas into natural gas lines to allow burning hydrogen with existing gas boilers, showing the ambition to transition into green energy generation systems [6]. However, more development of boiler technologies is carried out to use higher ratios of hydrogen in the gas mixture due to a higher flame speed of hydrogen [8], [9].

Hence, fuel cell technologies have become increasingly important as an alternative for providing heat with green energy [9], [10], decreasing the carbon dioxide emission from private end-user households.

1.1.3   Fuel cell technologies

The basic principle of a fuel cell is the conversion of the chemical energy of hydrogen and oxygen into electricity, water, and heat [11].

A single fuel cell supplies only a low voltage, whereas several cells can be electrically connected in series using interconnectors to form a fuel cell stack. The number of stacked cells determines the total voltage of the stack [12].

When combining the generated power and excess heat from a fuel cell, known as a fuel cell combined heat and power (FC-CHP) system, high efficiencies of up to 90% can be achieved [9]. The two leading fuel cell technologies for domestic applications are proton exchange membrane fuel cells (PEMFCs) and solid oxide fuel cells (SOFCs) [9], [13].

1.1.3.1   PEMFCs

The most developed fuel cell technology is the PEMFC due to its high efficiency, durability, reliability and reduced costs due to mass production [13]. Key advantages are the rapid start-up time and low-temperature operation, which makes them most suitable in mobile applications using the stack technology in fuel cell vehicles [13], [14]. However, operating at low temperatures requires sophisticated water and heat management and more importantly, expensive catalyst materials, such as platinum, to drive the reactions in a fuel cell [14].

1.1.3.2   SOFCs

In contrast to PEMFCs, Solid Oxide Fuel Cells (SOFCs) work at higher temperatures (> 500 ºC) and therefore benefit from the use of inexpensive materials and the ability to operate on a variety of fuels, which enables the use of existing infrastructure (*e.g.,* natural gas lines) and makes SOFCs already suitable as transition technology into a net zero future.

Many commercial companies are investing in the deployment of SOFC CHP units, such as Bosch, who increased its stake in Ceres Power from 4% to ca. 18%, netting Ceres £38 mln through a share subscription. Their demonstrator of a commercial SOFC CHP is the SteelCell, which is a 5kW SOFC from Ceres Power for domestic applications [15], [16]. The fuel cell provides green electricity with an efficiency of about 50-60% but when using additionally the generated heat as a FC-CHP unit, the system is up to 90% efficient and durable [17].

Considering fabrication methods of SOFCs, physical vapour deposition (PVD) processes, such as magnetron sputtering [18], are usually associated with high costs in the literature in terms of equipment and production [19]. However, it is important to note that manufacturing costs must be examined from a different point of view with regard to the performance of the cell. In this context, the US Department of Energy has studied the difference in stack costs for standard processes, such as tape casting and screen-printing techniques, and a full sputtering process [20]. Their report revealed that the stack-only cost per kW could be decreased by 33% [from £72.91 ($91.29/kW) to £49.14 ($61.53/kW)] when using the sputtering process. The decrease in costs was mainly attributed to the 50% increase in cell power density due to the quality of the films, resulting in a decreased number of cells and hence, material and production costs for a 270 kW fuel cell stack [20]. Thus, PVD techniques, such as magnetron sputtering, present a promising technology to achieve desired power densities in SOFC systems and to support the transition into cleaner energy generation.

1.2 Aim and objectives

The aim of this work is to advance the state-of-the-art electrocatalyst in SOFC systems by employing a flexible and scalable production technique, such as magnetron sputtering, for the development of novel materials with enhanced properties for energy applications. Through careful engineering of the coating's microstructure and the incorporation of promising materials, whose beneficial features will be presented in section 2.3.3, the advanced materials are designed to improve the electrocatalytic performance of the SOFC anode.

The first objective features the deposition of pure YSZ films by an extension of the basic sputtering process, reactive pulsed DC magnetron sputtering, in order to understand the material characteristics, its morphology with regard to various deposition parameters which will be detailed later. This outcome will provide the framework for this thesis and lead to the second objective which is to integrate nickel into the YSZ matrix, creating a nanostructured state-of-the-art Ni-YSZ active functional layer by reactive pulsed DC magnetron sputtering. It includes the investigation of various deposition and process parameters to determine their effect on the microstructure and electrochemical performance of the material. The goal is to understand the influence of above parameters and to define optimal conditions for a Ni-YSZ film to be used as reference material in further studies.

The third objective represents the principal goal for this work, *i.e.,* the doping of the nanostructured Ni-YSZ anode architecture by adding different concentrations of selected non-precious elements, *i.e.,* vanadium and manganese. The performance evaluation of the dopant and its concentration on the electrochemical performance will give insights into their future applications or explain why these materials are not efficient in SOFC operations.

In addition to that, part of this work included the development of a functional SOFC button cell test at the Manchester Fuel Cell Innovation Centre which required the engineering and fabrication of gas manifolds for the anode and cathode gas streams and the electrical connections for current collection and voltage measurements.

1.3   Thesis outline

This thesis is composed of four distinct sections: (I) Introduction and literature review, (II) Methodology, (III) Results and (IV) Synopsis. The first section introduces SOFC fundamentals, such as their current-voltage characteristics, followed by a literature review on SOFC materials and different cell designs (Chapter 2). After giving a brief overview of fabrication techniques for SOFCs with a focus on magnetron sputtering (Chapter 3), a gap analysis and summary at the end of the section draws together the key findings of the literature review (Chapter 4). The aim of the second section is to give an overview of the analytical and experimental techniques used in this work, such as material characterisation techniques (Chapter 5), the magnetron sputtering rig and the in-house developed SOFC button cell test setup (Chapter 6). The third section comprises three subchapters which analyse and discuss the main findings after the deposition of pure YSZ films using different deposition parameters (Chapter 7), the deposition of a state-of-the-art SOFC electrocatalyst, investigating various deposition and process parameters (Chapter 8) and the doping of the state-of-the-art SOFC electrocatalyst with either vanadium or manganese. The purpose of the final section is to draw conclusions by reflecting on the presented results and to give recommendations for future studies that could be beneficial to further advance the state-of-the-art SOFC anodes (Chapter 9).

2   Solid Oxide Fuel Cells

This chapter describes the Solid Oxide Fuel Cell (SOFC) operation and its electrochemical principles, in particular, the resulting current-voltage characteristics for performance evaluation and electrochemical impedance spectroscopy (EIS) as a diagnostic technique.

Secondly, materials and requirements of SOFC components will be presented, focusing on a comprehensive literature review of anode materials.

2.1   Working principle

In general, fuel cells are based on the principle that electrochemical reactions take place at two electrodes separated by an electrolyte; the electrolyte transfers ionic species from one electrode to another. Two different semi-reactions take place simultaneously at the interface of the two electrodes with the electrolyte; the electrons involved in the reactions are transferred from the electrodes to an outer circuit if connected to the cell, thus supplying electrical power. To avoid a short circuit of the cell, a dense electrolyte layer is often used, which operates as a pure ionic conductor (*i.e.*, no electrons allowed to pass) as well as a physical gas barrier between the two electrodes (*i.e.*, as a membrane).

At temperatures from 500 to 1000 °C, SOFCs directly convert the chemical energy stored in fuels, such as hydrogen and gaseous hydrocarbons, into electrical energy through single step electrochemical reactions. This involves operating with air/oxygen as the oxidant at the cathode and hydrogen or hydrocarbons as fuel at the anode.

Hydrocarbons (*e.g.,* methane) can react with steam or air by internal reforming or partial oxidation, in order to generate hydrogen and carbon monoxide as sources of fuel. Hence, the key benefits of SOFCs are fuel flexibility with low CO_2 emissions, when running on hydrocarbons, and high efficiencies of up to 50-60% or even 80-90% when used as CHP system, in terms of energy conversion [17].

For the sake of simplicity, the reduction/oxidation (redox) reactions of a SOFC are hereafter presented with hydrogen as the fuel and oxygen as the oxidant gas [21], [22]. Planar SOFCs consist of two porous ceramic electrodes, which are electrically separated but ionically connected by a gas-tight solid electrolyte [23]. The working principle is shown in Figure 2.1.
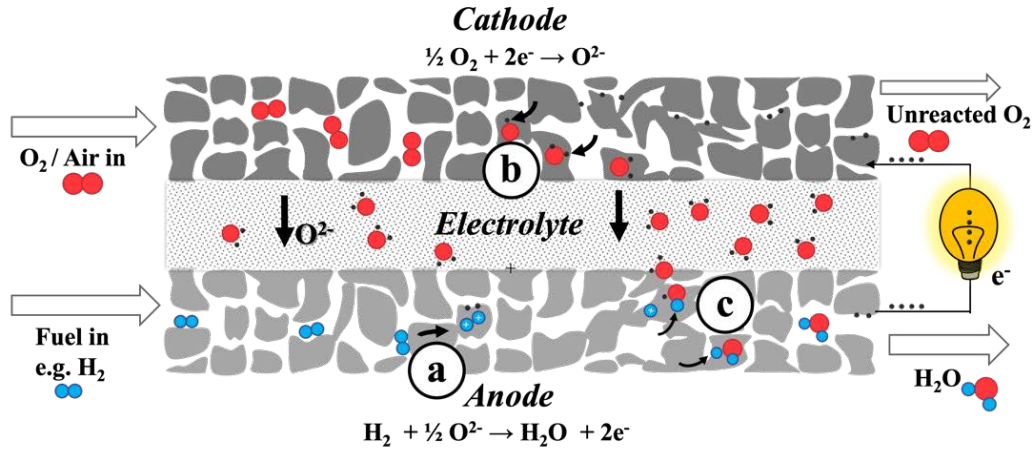
Figure 2.1: Working principle of a Solid Oxide Fuel Cell (SOFC), adapted from [23].

At the anode, hydrogen molecules are adsorbed and dissociated to H^+ ions, releasing electrons, as shown as **a** in Figure 2.1, which are conducted to the connected electrical load:

$$H_2 \rightarrow 2\ H^+ + 2\ e^- \qquad\qquad 2.1$$

Oxygen molecules (O_2) from air or pure oxygen are transported to the cathode and are reduced to ionic species (O^{2-}) by the arriving electrons from the load, according to the reaction (cf. **b** in Figure 2.1):

$$\frac{1}{2}\ O_2 + 2\ e^- \rightarrow O^{2-} \qquad\qquad 2.2$$

Due to the oxygen partial pressure difference between the cathode (1 atm $> p_{O2} > 0.01$ atm) and anode side (10^{-13} atm $> p_{O2} > 10^{-27}$ atm) the oxygen anions migrate through the electrolyte towards the anode by diffusion and annihilation of oxygen vacancies.

At the anode side, these O^{2-} ions react with the hydrogen protons in an exothermic reaction to form water (H_2O), while donating electrons to the system for power generation (cf. **c** in Figure 2.1), [23].

$$2\ H^+ + O^{2-} \rightarrow\ H_2O \qquad\qquad 2.3$$

The overall reaction of a SOFC can be thereby expressed by the following equation:

$$H_2 + \frac{1}{2}\ O_2 \rightarrow\ H_2O \qquad\qquad 2.4$$

Operation with Hydrocarbon Fuels

As mentioned before, a beneficial characteristic of SOFCs is the ability to operate on a wide range of hydrocarbons through internal reforming processes. The reason for the application of hydrocarbon fuels is that they provide a good energy storage density

compared to hydrogen, and the existing infrastructure of natural gas can be utilised as the gas supply for domestic applications.

Since the present work focuses on SOFC operation on hydrogen, the reader can find principles of hydrocarbon operation in Appendix A.

2.2 Electrochemical principles

2.2.1 Ideal cell

If no electrical load is applied to the SOFC (open circuit), the released electrons are kept at the anode side, leading to an electrochemical equilibrium, where a further diffusion of oxygen ions is inhibited. Consequently, the charges of the anode and cathode generate an electric field in the opposite direction to the diffusion of O^{2-} ions. Assuming a thermodynamically reversible system, the potential of this electric field, also called the open circuit voltage (OCV), is described by the electrical work required to transfer the electrons (decrease in Gibbs free energy):

$$\Delta G^0 = - n_{el} \, F \, E^0 \qquad\qquad 2.5$$

where ΔG is the temperature dependent standard free energy (Gibbs free energy), E^0 is the standard cell potential, F is the Faraday constant and n_{el} is the number of transported electrons in the reaction (*i.e., n_{el}=2 for hydrogen*).

The standard cell potential E^0 or OCV for the hydrogen-oxygen redox couple under standard conditions (STP) results in 1.229 V for liquid water and 1.168 V for water in the gaseous phase, using Gibbs energy of formation with *$\Delta G_{H2} = \Delta G_{O2} = 0$, $\Delta G_{H2O,l} = -237.2 \ kJ/mol$ and $\Delta G_{H2O,g} = -225.3 \ kJ/mol$* [11], [14].

Based on the thermodynamics of systems in equilibrium, the change in Gibbs free energy is a function of the temperature and pressure of the reactants and the products in the electrochemical redox reaction and can be written as follows [14]:

$$\Delta G = \Delta G^0 - RT \ln \left(\frac{p_{H_2O}}{p_{H_2} \, p_{O_2}^{1/2}} \right) \qquad\qquad 2.6$$

where ΔG is the temperature dependent standard free energy (Gibbs free energy), R is the universal gas constant, T is the temperature and p_x is the normalised partial pressure of the utilised gas x [23].

When converting Gibbs free energy to a voltage by using equation 2.5, the theoretical Nernst potential E_{Nernst} is derived:

$$E_{Nernst} = E^0 - \frac{RT}{n_{el}F} \, ln \left(\frac{p_{H_2O}}{p_{H_2} \, p_{O_2}^{1/2}} \right) \qquad\qquad 2.7$$

The theoretical Nernst potential characterises the ideal cell performance of the reaction as a function of the standard cell potential E^0 and of the equilibrium potential under specific conditions (*i.e., T, p_x*). As a result, the Nernst potential takes the effect of reactant pressure and concentration into account.

2.2.2 Voltage-current characteristics

When an electric load is connected to the fuel cell (closed circuit), an electric current is drawn leading to a decrease in the equilibrium cell voltage (OCV) due to the internal irreversible losses. These irreversible losses, which are also called polarisation or over-potential losses, have different natures and can be classified into four categories: i) activation losses, ii) ohmic losses, iii) concentration losses and iv) crossover losses [21]. Hereafter, the current-voltage characteristics are discussed with respect to the loss mechanisms.

The performance of a SOFC is assessed by a polarisation curve (*i.e.,* current-voltage curve), in which the actual voltage is plotted against the current density *j*, as depicted in Figure 2.2.
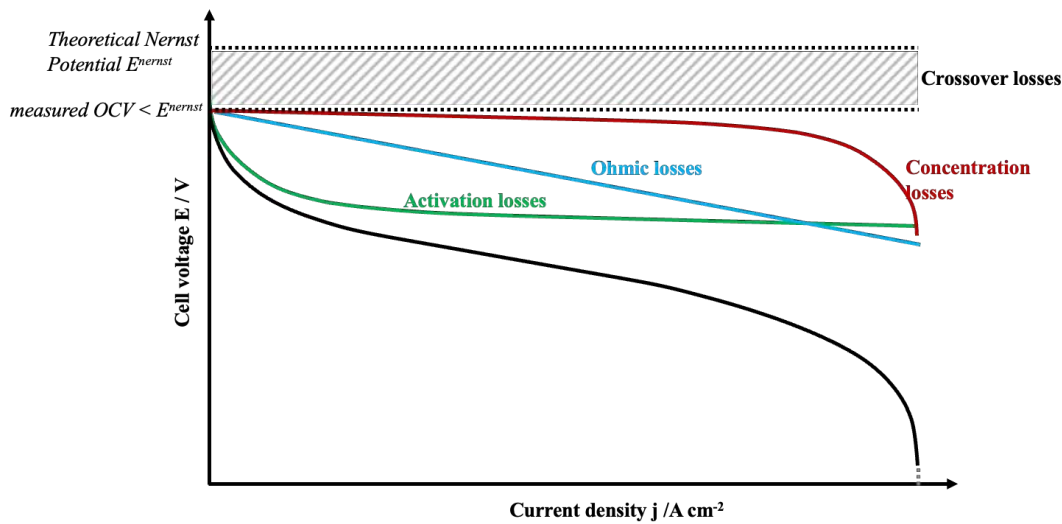
Figure 2.2: Polarisation curve, cell performance by loss type adapted from [14], [21].

2.2.2.1 Activation losses

The activation losses η_{act}, mainly related to the kinetics of catalytic reactions at the electrode sites, are dominant at low current densities because the reactants need activation energy to drive forward the electrochemical reaction at the electrode/electrolyte

interface. High temperature operation, such as in SOFCs, reduces activation losses because reactants are more likely to absorb the required activation energy, as catalytic reactions are promoted at higher temperatures. The Butler-Volmer equation presented in equation 2.8, describes the relation between current and voltage in electrochemical systems. The current that is produced by the reaction increases exponentially with the activation overpotential, resulting in an increased voltage loss when drawing more current from the fuel cell [14], [24].

$$j = j_0 \left[exp\left(\frac{\alpha_a F \eta_{act}}{RT}\right) - exp\left(\frac{-\alpha_c F \eta_{act}}{RT}\right) \right] \qquad 2.8$$

where j_0 is the exchange current density of the electrode, α_x are the anodic and cathodic charge transfer coefficient, respectively and η_{act} is the activation polarisation [14], [22], [25].

The exchange current density of an electrode resembles the rate of exchange between reactants and the reaction product at equilibrium. Hence, the kinetic performance can be improved by increasing the exchange current density j_0, which is defined by the following equation:

$$j_0 = nF c_R^* f \ exp\left(\frac{-\Delta G^{\ddagger}}{RT}\right) \qquad 2.9$$

where c_R^* is the reactant surface concentration, f is the decay rate (likelihood of conversion to the reaction product instead of back to the reactant and $\Delta G^{\ddagger}$ is the activation barrier energy.

It can be seen from above equation that the kinetic performance is dependent on the reactant flow rate, the temperature and the activation barrier for the reaction. Since SOFCs operate at much high temperatures compared to PEMFC, the exchange current density is already drastically increased, leading to a higher kinetic performance, which can be seen in lower activation losses at low current densities in the below figure.
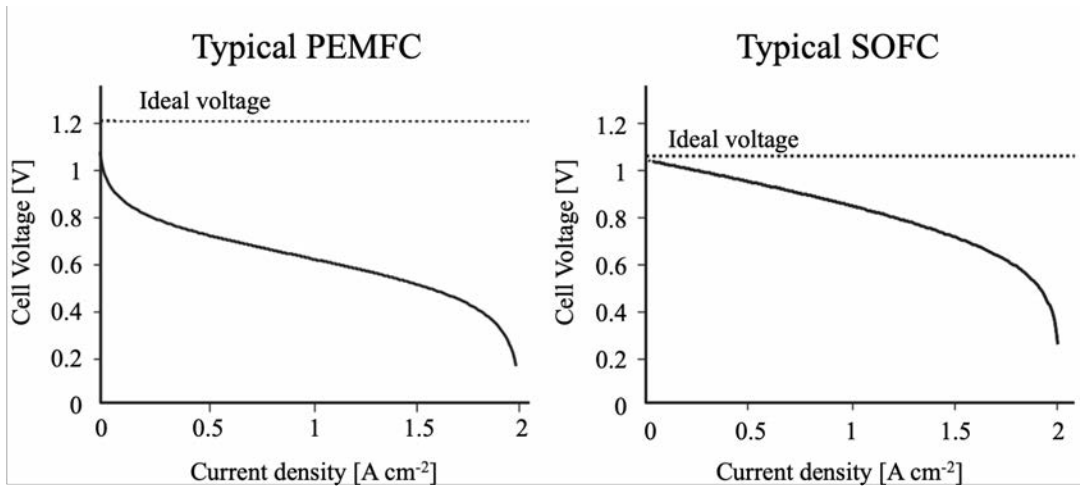
Figure 2.3: Comparison of activation losses between PEMFCs and SOFCs in the polarisation curve, adapted from [24].

Other measures to lower activation losses include the increase in reactant flow, which can be realised by operating the fuel cell at a higher pressure, or the selection of a highly catalytic electrode that substantially decreases the activation barrier.

2.2.2.2 Ohmic losses

As the current density increases, ohmic losses gain in importance by influencing the performance of the system (cf. Figure 2.2). Although the ohmic resistance of a SOFC is characterised by the sum of conduction losses across the electrolyte, electrodes and contacts, the predominant role is attributed to the transport of oxygen anions through the electrolyte due to its high ionic resistivity [14].

The resistance of the electrolyte across a uniform thickness L, and a constant cross-sectional area A and ionic conductivity σ_i can be written as a linear equation (see Figure 2.2) [22], [24]:

$$R_\Omega = \frac{L}{A\,\sigma_i} \qquad\qquad 2.10$$

According to Ohm's law, the ohmic voltage loss across the electrolyte layer can be calculated as:

$$\eta_{ohmic} = R_\Omega\, i \qquad\qquad 2.11$$

Where the current i is expressed by $i = jA$.

In order to compare the ohmic losses between different fuel cells, an area-normalised resistance needs to be calculated, which is also known as the area-specific resistance (ASR) [24].

$$ASR_{ohmic} = R_\Omega A \qquad\qquad 2.12$$

Typical values for ohmic resistance of supported electrolytes are below 0.15 Ω cm^2 (layer thickness $\sim$ 15 µm), while the combined area-specific resistance (ASR) of an entire cell should not exceed 0.5 Ω cm^2 to achieve high power densities [26].

2.2.2.3 Concentration losses

As the current density further increases, concentration losses (also indicated as mass transport losses) can influence the performance of the cell. According to Faraday's law, a minimum diffusion rate $\dot{n}_{consumed}$ of the reactants has to be provided to preserve a requested current flow:

$$\dot{n}_{consumed} = \frac{jA}{nF} < \dot{n}_{transport} \qquad\qquad 2.13$$

where A is the active surface area of the SOFC, F is the Faraday constant and n is the number of transported electrons in the reaction ($n = 2$ for hydrogen, $n = 4$ for oxygen).

For instance, in order to generate a current of 1A, a minimum mass flow rate of 7 sccm is required, as presented below:

$$\dot{n}_{H_2,\,consumed} = \frac{jA}{nF} = \frac{1\ amp}{2\cdot 96485\,\frac{C}{mol}} = \frac{1\,\frac{C}{s}}{2\cdot 96485\,\frac{C}{mol}} = 5.18\cdot 10^{-6}\ \frac{mol}{s}$$

According to the ideal gas law, 1 mol of any gas occupies a volume of 22.71 l at STP.

$$\dot{m}_{H_2,\,consumed} = 5.18\cdot 10^{-6}\ \frac{mol}{s}\cdot 22710\,\frac{ml}{mol} = 0.1176\ \frac{ml}{s} = 7.06\ \frac{ml}{min} \approx 7\ sccm$$

As one oxygen molecule requires two hydrogen molecules, the ratio between hydrogen and oxygen yields 2:1, leading to a minimum oxygen flow rate of 3.5 sccm ($\dot{m}_{H_2} = 2\cdot\dot{m}_{O_2}$).

High current densities are associated with a higher consumption of the fuel and oxidant gases. Since the electrochemical reactions occur at so-called triple phase boundaries (TPBs), the reactants have to be transported through the porous electrode. However, this diffusion process is limited, implying the reactants do not arrive quickly enough at the TPBs [21]. To conclude, the concentration polarisation expresses the mass transport limitation of the utilised gases.

The voltage drop due to the concentration losses is described by the concentration polarisation η_{conc}, as follows:

$$\eta_{conc} = -\frac{RT}{nF} \, ln \left(1 - \frac{j}{j_l} \right) \qquad\qquad 2.14$$

where j_l is the limited current density at which the reactant is consumed at its maximum rate, resulting in a decline of the cell potential to zero [14], [22].

2.2.2.4 Crossover losses

The reason for measuring a reduced open circuit voltage (OCV), instead of the theoretical Nernst potential, as illustrated in Figure 2.2, are crossover losses. These crossover losses stem from two effects: firstly, the material properties of the electrolyte can exhibit a mixed ionic and electrical conductivity, which enables the transport of electrons through the electrolyte, causing internal electrical short circuits in the cell.

Secondly, cracking or gas permeability due to porosity of the electrolyte leads to a crossover of the reactants. Oxygen inserted at the cathode would react with crossover hydrogen rather than being reduced, followed by a decrease in the partial pressure of hydrogen at the anode, and thus, a reduced OCV. Therefore, an essential requirement for SOFC electrolytes is a dense and crack-free microstructure in order to ensure the separation of the reactants [11], [14].

Another reason for a reduced OCV can be the sealing design of the cell, causing reactants to leak out of the system.

2.2.3 Electrochemical Impedance Spectroscopy (EIS)

Whilst direct current (DC) diagnostics, such as the polarisation curve, can directly determine the ohmic polarisation through the electrolyte and its adjacent components, the processes of the charge transfer across a double layer and the concentration polarisation show frequency-dependent behaviour, and thus require the application of alternating current (AC) techniques.

A commonly used technique to study the electrochemical processes involved in the fuel cell is AC impedance spectroscopy (hereinafter referred to as Electrochemical Impedance Spectroscopy or EIS). EIS characterises the dynamic behaviour obtaining detailed information on transport and reaction processes. In particular, EIS is able to distinguish charge-transfer and transport at the electrode/electrolyte interface, mass transport and electrochemical interface reactions [11], [27].

During an EIS measurement, a sinusoidal AC current, I_ω, of defined frequency, f, is drawn, while the response, *i.e.,* the AC voltage, E_ω, across the SOFC, is measured. As a result, a frequency-dependent resistance, so-called impedance, Z, can be calculated

analogous to Ohm's law for resistors. The applied current and voltage are phase-shifted by a phase angle φ:

$$Z_\omega = \frac{E_\omega}{I_\omega} = \frac{E_0 \sin(\omega t + \varphi)}{I_0 \sin(\omega t)} = Z_0 \frac{\sin(\omega t + \varphi)}{\sin(\omega t)} \qquad 2.15$$

where Z_ω is the impedance, I and E represent current and voltage, ω is the radial frequency $(\omega = 2\pi f)$, and Z_0 is the impedance when the current and voltage are in phase $(\varphi = 0)$.

Criteria for the data acquisition during an EIS are a steady state operation of the cell, expecting no changes of the systems, such as temperature changes, coating degradation, as well as a linearity between current and voltage of the electrochemical system. Although electrochemical systems show non-linear response, the consideration of an applied AC current (usually 10 % of the DC current) and a voltage signal on a small scale presents a pseudo-linearity of the system, as shown in Figure 2.4 [11], [28].
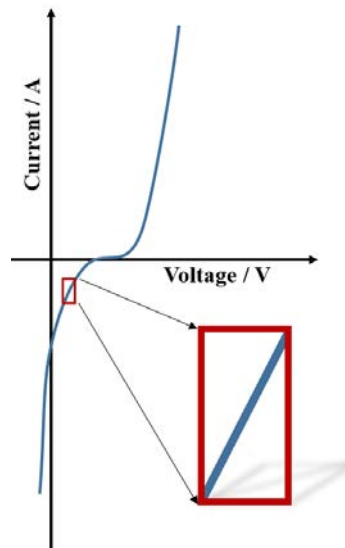
Figure 2.4: Pseudo-Linearity of an electrochemical system, showing current versus voltage.

Representation of EIS

On the other hand, the impedance can be expressed in a complex plane, using Euler's relationship for complex functions as follows:

$$Z_\omega = |Z_\omega| \, e^{-j\varphi} = \frac{E_\omega}{I_\omega} = |Z_\omega| \cos\varphi + j \, |Z_\omega| \sin\varphi = Re(Z) + j \, Im(Z) \qquad 2.16$$

where *ReZ (Z')* is the real part and *ImZ (Z")* is the imaginary part [11], [27].

An impedance spectrum is generated during the acquisition of EIS data when sweeping various frequencies, usually from 0.01 Hz to 1.0 MHz for SOFC applications. These impedance data can be represented in a Nyquist plot, as demonstrated in Figure 2.5.
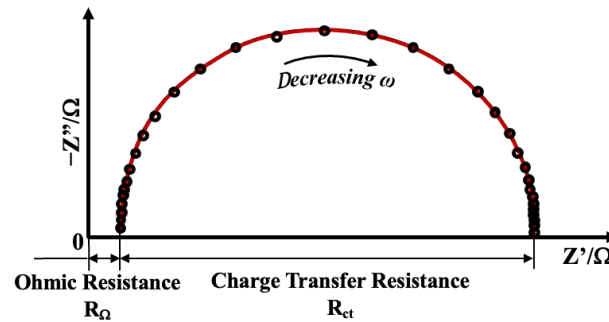
Figure 2.5: EIS data representation using a Nyquist plot, adapted from [11], [29].

In a Nyquist plot, the imaginary part Z'' is plotted over the real impedance Z', resulting in the impedance arc (semi-circle). The ohmic resistance, R_Ω, can be obtained from the intercept with the x-axis at high frequencies, which is identical with the slope of the cell performance in the I-V characteristics (cf. Figure 2.2). Furthermore, the difference between the intercept at low frequencies and high frequencies yields the charge-transfer resistance, R_{ct}, at the electrode/electrolyte interface, which represents an accumulation of the loss mechanisms explained in the previous chapter [11], [27]. Although, a Nyquist plot does not indicate the corresponding frequency for each individual EIS data point [27], it can still provide information about the process resistance. The specific processes occurring in an electrochemical system can be modelled as equivalent circuit elements from electrical engineering, such as resistors, capacitors, or inductors, and then integrated into an equivalent circuit model (ECM) [29].

The simplest equivalent circuit element is the so-called Voigt element, which consists of a parallel circuit of a resistance R and a capacitance C. The capacitance is often replaced by a constant-phase-element Q because the electrochemical reactions do not show perfect RC behaviour due to the complex microstructure of the electrode compared to an ideal capacitor plate [29]. In a Nyquist plot, the capacitance is expressed by the y-axis [11].

The impedance arc in the Nyquist plot shown above can be modelled as a simplified Randle circuit [27], which places an electrolyte resistance R_Ω in series with a Voigt element, including a double-layer capacitance C_{dl} (ideal capacitor) parallel to the charge-transfer resistance R_{ct} [29], as illustrated in Figure 2.6a.
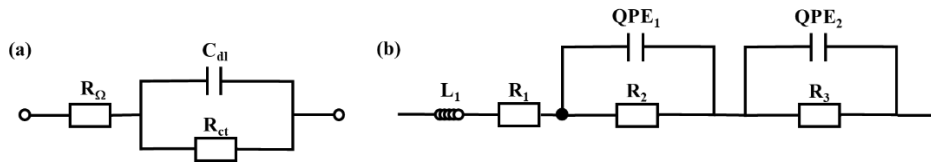
Figure 2.6: Electrical circuit modelling. (a) simplified Randle circuit (b) ECM for a SOFC by Sarruf *et. al*, adapted from [30], [31].

When using appropriate software, such as *Zplot*, equivalent circuits can be applied to the impedance spectrum of a SOFC to model the processes taking place in this electrochemical system and extrapolate the measured impedance into electrode (cf. Figure 2.6b), diffusion, or fuel conversion-related processes [28], [32].

When considering the SOFC assembly, comprising anode, electrolyte, and cathode, various ECMs can be used to characterise the specific processes, resulting in an identical fit to that of the impedance spectroscopy. However, the simplest structure with a minimum number of circuit elements is preferred for EIS analysis [27].

2.3 Materials and requirements

In order to ensure the SOFC operation presented in section 2.1, each component of a SOFC has to meet specific requirements. The aim of this chapter is to introduce these requirements and important properties for electrolytes, cathodes and anodes. After a brief overview of commonly used materials for electrolytes and cathodes, the section will focus on providing a detailed literature review of researched anode materials to derive the objectives of this project.

2.3.1 SOFC Electrolyte

A SOFC electrolyte needs to possess high ionic conductivity to enable the transport of oxygen ions through vacancies from the cathode towards the anode, negligible electrical conductivity and chemical stability at high temperatures. Additionally, it has to be chemically stable in reducing and oxidising environments. Thin electrolyte layers benefit from reduced ohmic losses in the cell and features, such as gas-tightness and mechanical stability to withstand thermal cycles and prevent internal short circuits [22]. Electrolyte materials, such as ceramic oxides with a fluorite structure, expressed as AO_2, are favourable, since a large number of materials with this crystal structure have presented high oxygen ion conductivity and comply with most of the SOFC electrolyte

requirements [17]. The mechanism of ionic conductivity is based on oxygen ions moving through point defects or oxygen vacancies in the crystal lattice, enabling the diffusion of the oxygen ions from the cathode to the anode in an SOFC.

A commonly used material for electrolyte applications is yttria-stabilised zirconia (YSZ), which requires temperatures above 800 ºC to benefit from its high ionic conductivity (circa 0.14 S cm^{-1} at 1000 °C). Zirconia is known for its three polymorphs: i) monoclinic at room temperature, ii) tetragonal above 1170 ºC and iii) cubic above 2370 ºC. To achieve the fully stabilised cubic fluorite phase of ZrO_2 and create high amounts of oxygen vacancies, 8–10.5 mol% Y_2O_3 is used as a doping agent [22]. When adding Y_2O_3 into the zirconia lattice, charge compensation results in the creation of oxygen vacancies due to the substitution of Zr^{4+} by Y^{3+}. Thus, every two Y^{3+} atoms create one oxygen vacancy, as shown in the following figure: [24], [33]
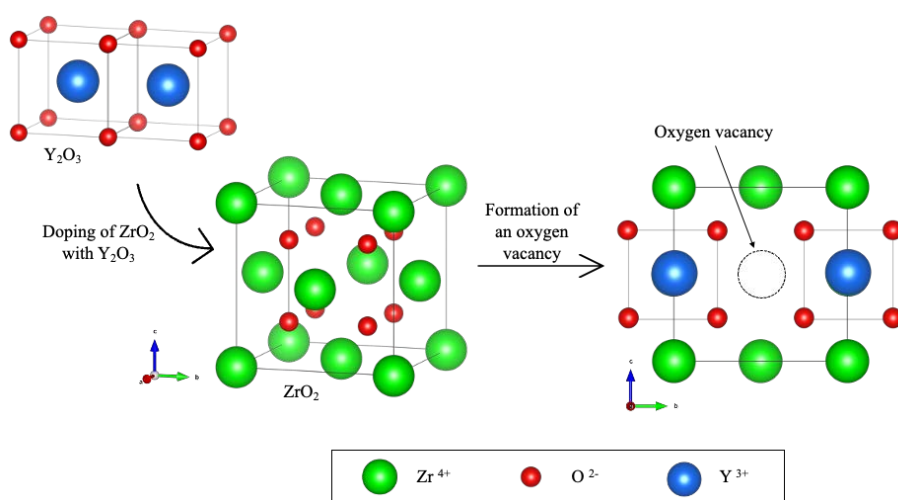
Figure 2.7: Formation of cubic yttria-stabilised zirconia (YSZ) by doping ZrO_2 with Y_2O_3 and creating one oxygen vacancy for the substitution of two Zr^{4+} with two Y^{3+}[33].

However, the high temperature operation creates problems associated with the difference in the coefficients of thermal expansion (CTE) between the electrolyte and its adjacent components. The thermo-mechanical mismatch results in thermal stresses, which can lead to the cell failure [34], [35], [36]. For that reason, recent studies suggest reducing the operation temperature of SOFCs to an intermediate range of 500 to 750 ºC [34].

The literature [37] has identified three alternative materials as promising candidates for SOFC electrolytes and these are: gadolinia-doped ceria $Ce_{0.9}Gd_{0.1}O_{2-\delta}$ (GDC) [38],

strontium, magnesium-doped lanthanum gallate $La_{0.9}Sr_{0.1}Ga_{0.8}Mg_{0.2}O_{3-\delta}$ (LSGM) [39], [40] and scandia stabilised zirconia (ScZ) [19].

Figure 2.8 presents the ionic conductivity of these alternative materials operating at low temperatures compared to YSZ. Based on an ionic conductivity of 0.01 S cm^{-1}, electrolytes with thicknesses of 15 μm require an operation temperature of 700 ºC for YSZ and circa 500 ºC for GDC [26].
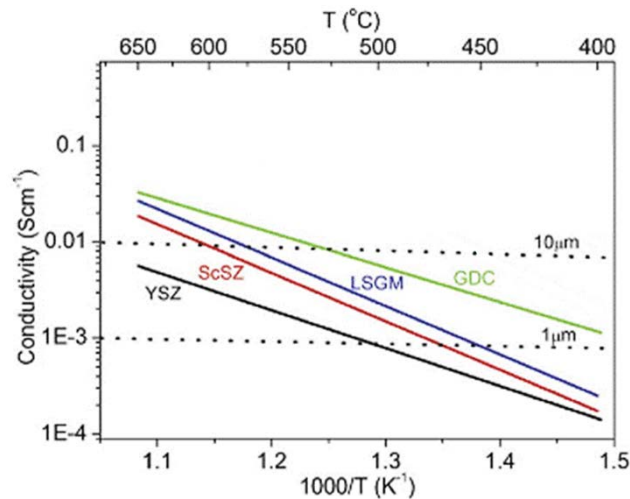
Figure 2.8: Ionic conductivity of SOFC electrolyte materials for low temperatures, adapted from [41].

GDC is a mixed ionic and electronic conductor. It shows a high ionic conductivity at low temperatures and it is reported to possess an additional electrical conductivity at low oxygen partial pressures. At these low partial pressures, GDC becomes partially reduced from Ce^{4+} to Ce^{3+} at the anode side, leading to the conduction of electrons through the electrolyte at around 550 ºC [22], [37].

A strategy to suppress this electrical conductivity, presented in the literature, is to add an additional barrier layer of pure ion-conducting material, such as YSZ [42], [43], [44], between an anode and the electrolyte to create a bi-layer electrolyte. An interlayer of GDC has already been introduced into the SOFCs electrocatalyst stack to prevent the reaction between zirconia and cobalt-containing cathodes [45], [46]. Shri Prakash *et al.* even suggested combining these two approaches in order to create a triple-layer electrolyte [41]. However, further studies of the minimum layer thickness were required. Meanwhile, Ceres Power Holding plc introduced a commercialised SOFC, the so-called SteelCell, on the market in 2015, comprising a triple layered GDC-YSZ-GDC electrolyte [15].

2.3.2 SOFC Cathode

The cathode is responsible for the reduction of oxygen molecules to oxygen ions through electron transport to the cathode/electrolyte interface. Therefore, the cathode materials require a high catalytic activity in oxygen reduction and a high electrical conductivity. A mixed ionic-electrical conductivity is favourable to enhance the reactive sites in the porous electrode. Furthermore, it has to be chemically and mechanically stable and compatible with the adjacent components of the cell. Perovskite-type oxides are used as SOFC cathodes due to their mixed ionic-electronic conductivities that facilitate an expansion of the TPBs region, which are active electrochemical reaction sites at the predetermined thickness of the cathode layer [17].

At early stages, perovskite-type oxides containing cobalt were introduced as cathodes but showed poor chemical and mechanical stability on YSZ electrolytes due to the formation of a lanthanum zirconate layer. For that reason, further research presented improved chemical stability using lanthanum manganite-based cathodes such as lanthanum strontium manganite (La,Sr)MnO$_3$ (LSM), which possesses high catalytic activity at temperatures above 800 ºC. However, the drive to lower cell operation temperatures resulted in insufficient SOFC performance when using LSM as cathode material. Hence, further studies lead to a performance improvement by adding iron to the pure cobaltite perovskites, forming (La,Sr)(Co,Fe)O$_3$ (LSCF). LSCF still requires an additional barrier layer of ceria-based oxides because of the reaction with YSZ, as mentioned in the section above, but exhibits good performance without degradation at intermediate-temperatures (IT-SOFC) [22].

2.3.3 SOFC Anode

A SOFC anode is responsible for directing fuel and ensuring its oxidation, as well as transporting free electrons to the load, as presented in section 2.1. This means that the anode material must provide a high electrocatalytic activity for fuel oxidation and should exhibit electronic and ionic conduction with predominant electrical conductivity to facilitate the electron transport. Furthermore, a continuous porous microstructure is required to transport fuel and reaction by-products rapidly. The anode material and the adjacent components should possess similar coefficients of thermal expansion (CTEs) and be mechanically and chemically compatible to prevent failure of the cell caused by excessive thermal stresses in their structures [21], [47].

2.3.3.1   State-of-the-art anodes

Lee *et al.* quoted three factors that anodes need to provide in order to achieve the best cell performance. These are: (i) enough electrochemical activity (related to chemical reactions at the anode), (ii) proper microstructural condition (related to diffusion of the reaction products), and (iii) high electrical conductivity, which will be explained in more detail below [48].

I.   Catalyst activity

As the right catalyst needs to be selected for the reactions that take place at the anode, the Sabatier principle will be introduced within the following. A catalyst is required to possess the optimal binding energy to chemically adsorb the reacting species (*i.e.,* hydrogen). If its binding energy is too strong, the catalytic active sites are blocked by the reactant, reducing the reaction rate and thus, lowering the activity. Conversely, if the binding energy is too weak, little or no species will be chemically adsorbed on the catalyst surface which limits the activity drastically. Catalytic activity is also expressed as reaction rate per catalytically active site, called turnover frequency [24]. It was shown in recent computational studies that the adsorption strength for different materials can be explained by the density function theory (DFT). DFT calculations represent the electron density of the molecules, *e.g.*, when the orbitals of hydrogen and the catalyst interact [24]. The hydrogen oxidation reaction follows the Horiuti-Polanyi mechanism, which consists of two major steps, as illustrated in Figure 2.9: (i) approaching hydrogen in **a** dissociates on the catalyst surface through physisorption and chemisorption, as shown by the dashed lines in **b**, resulting in the formation of atomic hydrogen; (ii) during the hydrogenation, the atomic hydrogen undergoes a reaction with the catalyst, forming a chemical bond in **c** [49], [50].
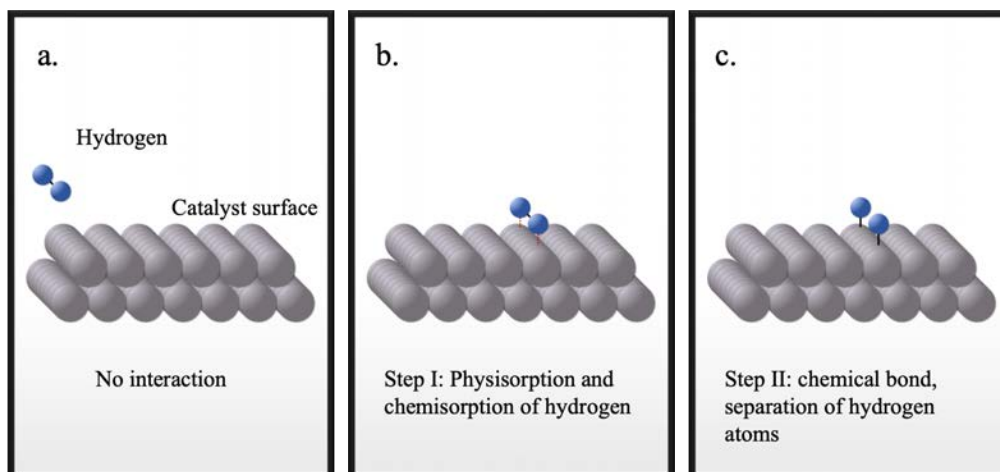
Figure 2.9: Interactions between hydrogen and catalyst following the Horiuti-Polanyi mechanism [49].

Furthermore, the literature debates about two different mechanisms for the reaction occurring at the anode [51], [52]: (i) the so-called "hydrogen spillover mechanism" describes the transfer of hydrogen atoms to the electrolyte through a surface spillover, where the oxygen ions further react with these hydrogen protons, forming water; (ii) on the contrary, the "oxygen spillover mechanism" suggests that oxygen ions are transferred from the electrolyte to the catalyst surface.

In general, the activity of the catalyst can be expressed by a so-called volcano curve, where the activity, which is based on the exchange current density j_o (cf. section 2.2.2.1), is plotted over the material's adsorption energy for the reactant species, *e.g.*, hydrogen, as presented in Trassati's volcano plot in Figure 2.10.
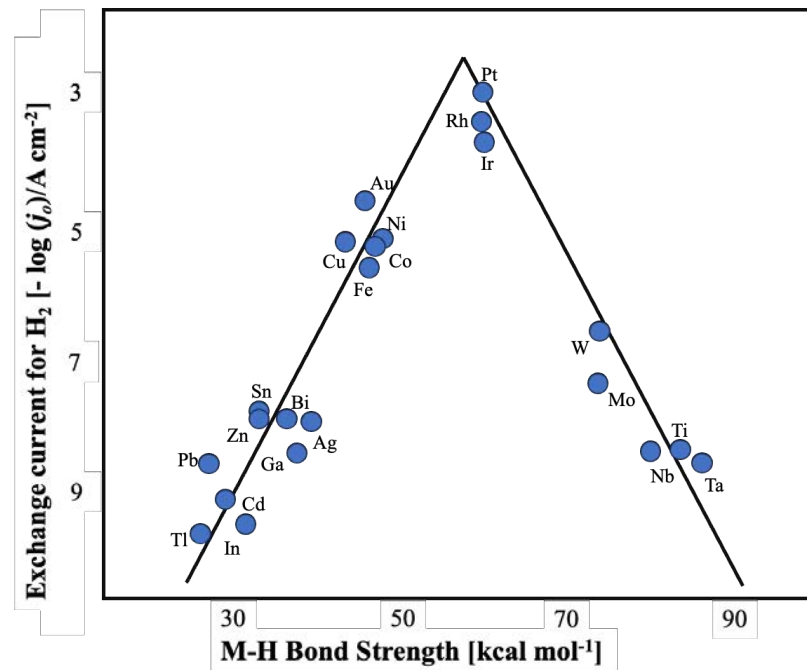
Figure 2.10: Trassati's volcano plot for metal-hydrogen bonding, showing elements with the highest activity (based on exchange current density j_o, cf. section 2.2.2.1) and associated binding energy of hydrogen, adapted from [53]. Note: Ni comprises two unpaired electrons in the 3d orbital.

Rossmeisl and Bessler investigated the correlation between the anodic polarisation conductivity from [54] and their calculated adsorption energies for oxygen and hydrogen on pure metal surfaces by DFT [51]. The anodic polarisation conductivity is a measure of activity based on the activation losses η_{act}. Figure 2.11a and b illustrate the plotted data for oxygen and hydrogen, respectively. The adsorption energy of hydrogen presented no correlation with activity, suggesting that ΔE_H is not an appropriate representation for the anode reaction. However, the activity plotted over the oxygen adsorption energy presents a volcano-type plot, indicating a good representation for the anode reactions, which will be later used to compare activities in bimetallic materials in section 2.3.3.3
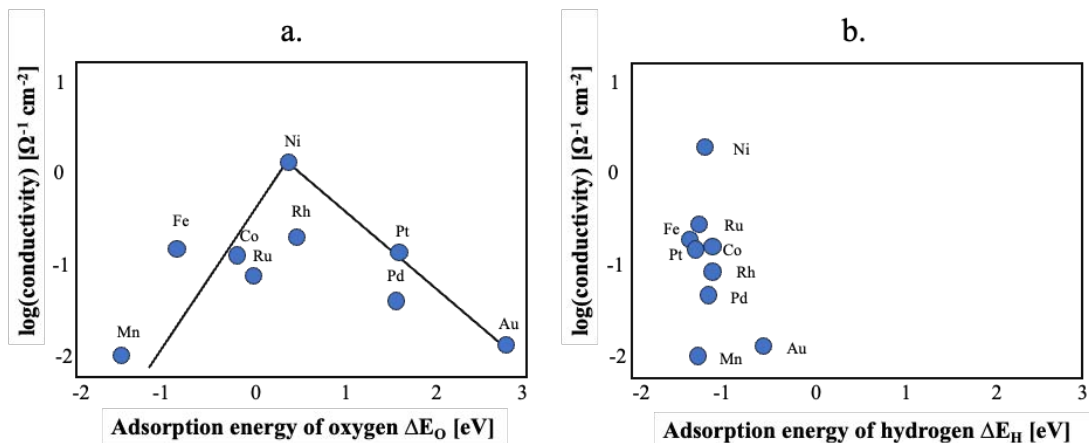
Figure 2.11: Conductivity measured over adsorption energies for oxygen (a) and hydrogen (b), adapted from [51], [54].

From the above figures, it can be seen that nickel along with cobalt and iron, presents a good catalytic activity for the anode reactions if one excludes the precious metals shown. For that reason, early attempts in SOFC development focused on single-phase electrocatalysts made of pure nickel. Although nickel was confirmed to be catalytically active and electrically conductive, its relatively low melting temperature and Ni agglomeration due to particle growth at high temperatures resulting in a decrease in active reaction sites, made it impractical in SOFC operation [55]. Besides, a significant mismatch of the coefficient of thermal expansion (CTE) between Ni and the electrolyte (YSZ) causes high thermal stresses and leads to degradation in SOFC performance [56].

II. Microstructural design

Consequently, composite anode materials of ceramic and metal (cermet), such as nickel-zirconia (Ni/YSZ), that combine electrical and ionic conductive properties have been heavily studied in the last decades. When combining ionic and electronic conductive phases as an anode material, the surface area of the reactive sites, where the gas phase, ion conductive phase and electron conductive phase meet, is not confined to a planar 2D interface between an anode and an electrolyte. Instead, these triple-phase boundaries (TPB) are enlarged to a 'volumetric' active zone, which enhances the potential reaction locations within the structure [22], [57].

Figure 2.12 illustrates these electrochemically active TPBs that require a percolated path (*i.e.*, dashed lines), in order to conduct oxygen ions to the TPBs as well as transfer the released electrons towards the current collectors (interconnectors). The prohibition

signs localise the inactive TPBs to indicate that no further ion or electron transport is attainable.
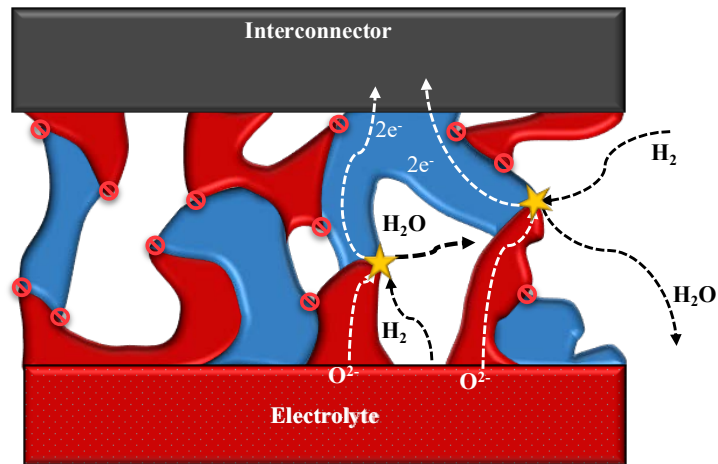
Figure 2.12: 2D-schematic of active (yellow stars) and inactive (prohibition signs) triple phase boundaries, red: ionically conductive phase; blue: electronically conductive phase; dashed arrows show percolated paths, adapted from [21], [58].

This volumetric active zone is especially important when operating a SOFC at reduced temperatures due to a higher internal resistance at low temperatures (lower thermal activation) [59]. Since the design of the anode structure has a strong effect on the cell performance, Atkinson *et al.* suggested graded anode structures to divide its functions as an electrochemical reaction catalyst and current collector. This results in a finer-structured, electrocatalytically active anode functional layer (AFL) combined with a highly porous anode substrate [22], [60].

III.   Electrical conductivity

Ni-YSZ anodes represent the state-of-the-art material for high temperature operation (~ 800 ºC). As mentioned before, nickel supplies the catalytic activity for the hydrogen oxidation reaction (HOR) as well as the high electrical conductivity, whereas YSZ gives ionic character of the bulk conductivity and thus, increases the amount of TPBs. Both phases are chemically stable in reducing atmospheres at high temperatures and do not react with each other over a wide range of temperatures [56].

A high Ni content leads to high electrical conductivity but also causes instability of the microstructure due to a large Ni coarsening [48]. On the other hand, a high YSZ ratio avoids significant changes in the bulk dimensions due to a closer CTE to that of the electrolyte and inhibits Ni agglomeration. Apart from the microstructure, the com-

position of the cermet has a great impact on the electrical, electrochemical and mechanical properties. Thus, an appropriate ratio between ion conducting and electron conducting phases must be chosen to achieve the best possible compromise for the requirements [56].

The electrical conductivity of Ni/YSZ depends on the Ni content, as shown in Figure 2.13 [61], [62]. At Ni volume fraction of ~ 32 %, the electrical conductivity at 1000 ºC increases significantly, as shown by the "S-shaped" curve (percolation of nickel), indicating a sudden change in the electrical conductivity mechanism of Ni/YSZ cermets. Based on the findings of Kawashima and Hishinuma, the strong increase in electrical conduction is caused by a formation of conduction clusters in the Ni phase. At this point, 20 % of the total nickel forms the conduction clusters, but the remaining 80 % of Ni is not electrically connected to operate as an anode. However, when the Ni ratios are above 44 %, more than 90 % of Ni is able to form conduction clusters.
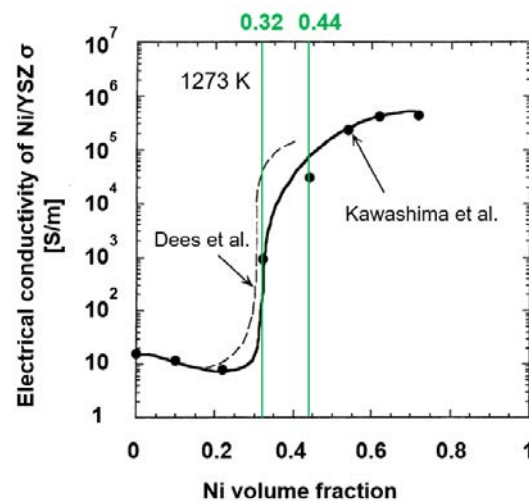
Figure 2.13: Electrical conductivity σ of Ni/YSZ versus Ni volume fraction, adapted from the literature [62].

A porous anode structure requires an electrical conductivity of 100 S cm^{-1}, in order to achieve a total resistance of the cell below 0.15 Ω cm^2. However, this can be lowered to 1 S cm^{-1}, when using an appropriate structurally engineered design of the current collection paths. From the figure above, it can be seen that using a nickel content of above 30% can yield the required electrical conductivity of an anode.

2.3.3.2 Doped Ni-based anodes

Ni-based anodes comprise metals or metal oxides incorporated into the microstructure to adjust the surface of Ni particles and suppress nickel coarsening or carbon deposition when running on hydrocarbon fuels. In order to operate SOFCs at lower temperatures, alternative electrolyte materials, as introduced in section 2.3.1, were used in the studies presented below to replace the conventional YSZ-based anodes by variations of scandia-doped zirconia (ScZ), gadolinia-doped ceria (GDC) or samaria-doped ceria (SDC). Similar to the doping of zirconia with yttria or scandia (cf. Figure 2.7), ceria's initial concentration of oxygen vacancies at low oxygen partial pressures can be increased through dopants of certain transition elements, such as Gd, Sm or Nb [63].

He and Wang reported the addition of 0-6 wt.% Al_2O_3 to Ni-YSZ anodes in [64]. It was found that the addition of more than 2 wt.% alumina resulted in the formation of $NiAl_2O_4$ as a spherical phase on the Ni surface after annealing. $NiAl_2O_4$ was still present after the reduction in hydrogen and substantially decreased the electrical conductivity of the anode material with higher concentrations of alumina. The authors also found another nanosized secondary phase on the boundaries of YSZ, which they suggested to be Al_2O_3. This study implies that alumina might not be a suitable dopant for cell operation, as it might contribute to the increased ohmic resistance in the anode.

Another study examined the structural characteristics of chromium-doped Ni-YSZ anodes [65]. The addition of 1 mol.% Cr resulted in the oxidation of chromium to Cr_2O_3 after annealing. Interestingly, the authors found Cr_2O_3 precipitations between the anode and the electrolyte, although not the entire interface was covered with it. It was suggested that the saturation of the Ni-YSZ layer with Cr_2O_3 caused the remaining chromium to precipitate at the Ni-YSZ/YSZ interface. It is important to note that higher concentrations of Cr in Ni-YSZ might be unfavourable, as it could result in a full coverage of the interface with Cr_2O_3, leading to an increase in the ohmic resistance due to the low electrical conductivity of Cr_2O_3 at SOFC operation temperatures [66].

The authors in [67] presented the effect of doping 1 wt.% Fe into a Ni-GDC electrocatalyst. This concentration of iron was found in Ni-rich regions after reduction at 800 ºC without affecting the particle size of nickel. No electrochemical data were reported in this study. A higher concentration of Fe in Ni-GDC led to alloying between nickel and iron, which will be discussed in the subsequent section of this chapter.

Tiwari and Basu investigated the addition of titania in Ni-YSZ anodes [68]. They compared the electrochemical performance of NiO-YSZ (40/60 % v/v) with NiO-TiO$_2$-YSZ (30/10/60 % v/v/v) anodes at 800 ºC. Although the maximum peak power density of the titania-doped anode decreased from 111 to 85 mW cm^{-2}, it presented marginally improved redox stability (after 130 h, NiO-YSZ: 84 mW cm^{-2}, NiO-TiO$_2$-YSZ: 85 mW cm^{-2}). After annealing in air, a secondary phase of zirconium titanate (ZrTiO$_4$) was formed due to the interaction between YSZ and TiO$_2$. The authors suggested that the improved redox stability is caused by the formation of this secondary phase which suppresses nickel agglomeration during cell operation. Besides, they attributed the lower Ni concentration (30 vol.%) in the titania-doped anode to the reduced power density.

In addition to titania-doping, Tawari and Basu also analysed the effect of modifying a Ni-YSZ anode-support with 10 vol.% ceria [69]. Like titania, doping of ceria reportedly led to the formation of a solid solution of cerium zirconate (CZ), which was still present after cell operation in hydrogen. The maximum power density improved from 275 to 332 mW cm^{-2} at 800 ºC. It was found that CZ was well interconnected with Ni particles that might have prevented Ni coarsening according to the authors.

Within the same study, they explored the addition of 10 vol.% Nb$_2$O$_5$ into Ni-YSZ, which led to an increase in power density from 275 to 301 mW cm^{-2} at 800 ºC [69]. After annealing at high temperature, Nb$_2$O$_5$ reacted with YSZ and formed niobium zirconate (NZ) which further reduced to NbO$_2$ during calcination in hydrogen. The authors stated that NbO$_2$ improved the performance of the cell due to the higher electrical conductivity compared to Nb$_2$O$_5$.

Another study by Yao *et al.* focused on the impregnation of various mole ratios between niobium and nickel of 0.01, 0.03 and 0.05 into a Ni-SDC (samaria-doped ceria) anode [70]. The electrode polarisation declined with increasing Nb content, resulting in an improved performance in contrast to un-doped Ni-SDC anodes. The increase in the peak power density from 530 mW cm^{-2} to 687 mW cm^{-2} at 700 ºC was achieved by forming the 5NbO$_x$-Ni-SDC phase.

The surface enrichment of Ni-YSZ cermets by the infiltration of either 1 wt.% tin or 1 wt.% copper prior to calcination has been studied [71]. The electrochemical performance was tested at 750 ºC using H$_2$/N$_2$ as fuel. A maximum power density for the undoped Ni-YSZ was 263 mW cm^{-2}. In both cases, doping with either 1 wt.% Sn or 1

wt.% Cu increased the power density by 17 and 23 mW cm^{-2}, respectively. The ohmic resistance also declined from 0.11 (undoped) to 0.08 Ω cm^2 (for Sn- and Cu-doped), which is likely caused by improved electrical conductivity due to addition of tin and copper.

Authors in [72] have investigated the doping of molybdenum in Ni-ceria-zirconia. They studied Mo fractions of 0 wt.%, 3 wt.% and 5 wt.% (within the NiO-MoO$_x$ matrix) used in a modified Ni-Ce-Zr anode, tested in dry hydrogen and in an isooctane/air mixture at 800 ºC. The authors stated an increase in the peak power density from 260 to 420 mW cm^{-2} in hydrogen and from 70 to 212 mW cm^{-2} in isooctane/air mode, when doping Ni-ceria-zirconia with 5 wt.% Mo. Electrochemical impedance spectra showed that the addition of Mo resulted in a decrease in anodic losses (from 6.98 to 3.81Ω cm^2). The authors interpreted the increase in performance by DFT (density function theory) calculations in which the addition of Mo to form NiMo increased the hydrogen binding energy on Ni, leading to improved hydrogen adsorption and dissociation.

The effect of the addition of manganese oxide (MnO) in Ni-YSZ has been reported [73], [74]. Hua *et al.* fabricated a dual-layer anode design of two layers Ni-YSZ and Ni-MnO on a YSZ electrolyte. A spinel ceramic powder of NiMn$_2$O$_4$ was sintered in air and deposited on NiO-YSZ. After calcination in hydrogen, NiMn$_2$O$_4$ transformed to Ni-MnO and formed the resulting Ni-MnO/Ni-YSZ dual layer. The authors reported a decline in polarisation resistance at temperatures between 650 and 800 ºC by 50% (from 0.55 to 0.26 Ω cm^2 at 800 ºC) in hydrogen when using the Ni-MnO layer.

Based on those results, Chung *et al.* fabricated MnO-doped Ni-YSZ anode catalysts with initial MnO concentrations of 2, 5 and 10 wt.% [74]. After annealing at 1400 ºC for 3 h, the authors reported the formation of a spinel-like secondary phase of NiMn$_2$O$_4$ which was caused by the solid-state reaction between NiO and MnO. After reduction in hydrogen, NiMn$_2$O$_4$ decomposed to metallic nickel and MnO. No solid solution was formed between MnO and YSZ, as the lattice parameter for YSZ remained the same within doped and undoped Ni-YSZ. The final dopant concentration in the reduced state was found to be 1.1, 2.75 and 5.5 wt.% MnO. All three concentrations resulted in an increase in maximum peak power density. While the highest increase in peak power density at 800 ºC from 481 to 556 mW cm^{-2} was achieved by adding 1.1 wt.% MnO, higher concentrations did not further improve the performance. The authors reported

that the electrical conductivity of Ni-MnO/YSZ anodes increases up to 5.5 wt.% MnO, however, higher concentrations of MnO lead to a significant decline in electrical conductivity, as MnO is a non-conductive material and might have interrupted the percolation path within the anode.

Other attempts to improve the performance of SOFCs included alloying of nickel with other metals to create bimetallic alloys (solid solutions of Ni and another metal) which are reviewed in the next section.

2.3.3.3 Ni-based alloy anodes

Promising candidates to be alloyed with nickel were studied in [75]. The authors used DFT calculations to obtain catalytic activity for the binding energy of oxygen to study the impact of $Ni_{(1-x)}M_x$ surface alloys on the anode reactions (cf. section 2.3.3.1). They found that mole fractions between 0.25 and 0.5 for copper, cobalt and 0.25 for iron possess superior theoretical catalytic activity for the oxygen binding energy, and thus for the anode oxidation (cf. Figure 2.10 and Figure 2.11a).

Alloying of nickel and copper is not brought into focus, because Ni-Cu-based alloys were further explored for SOFCs operating in methane where nickel suffers from catalyst poisoning due to the formation of carbon on its surface, resulting in a fast decline in cell performance. As copper is catalytically inert for carbon formation and yet presents electrical conductivity [55], the literature suggested deploying Ni-Cu-based alloys when running on hydrocarbon fuels. Further reading can be found in [76], [77], [78]. In the following, experimental results for the alloying between nickel and cobalt and nickel and iron are presented.

Experimental studies had been conducted [79], [80] that investigated the addition of cobalt to Ni-YSZ anodes to achieve bimetallic alloying between Ni and Co. Grgicak *et al.* reported exchange current densities of 48, 15 and 28 mA cm^{-2} for $Ni_{(1-x)}Co_x$-YSZ anodes with x=0.08, 0.16 and 0.31, respectively, compared to 14 mA cm^{-2} for Ni-YSZ. The results indicated significant improvements in the activity of hydrogen when deploying $Ni_{0.92}Co_{0.08}$-YSZ as an anode. They accounted the increase in surface area by the substitution of Co^{2+} into the NiO lattice for the performance increase, causing smaller metal particles and thus, an increase in TPBs. In addition to that, O'Brien and Giorgi ran alloyed nickel and cobalt in a $Ni_{0.7}Co_{0.3}$-YSZ cermet on various ratios of CO/H_2 fuel mixtures at 800 ºC [79]. Their findings revealed the synergetic effects of Co and Ni. Although Ni exhibits a faster reaction for hydrogen oxidation, Co sites

were beneficial for the oxidation of CO, yielding for the first time an even higher performance in hydrocarbon mixtures (CO/H_2 (20/80 and 30/70)) compared to pure hydrogen.

Previous work has focused on bi-metal alloys of nickel and iron [39], [81], [82], [83], [84], [85], [86], [87], which will be discussed in the following. The most recent work was carried out by Wang *et al.* which compared a dual-layered anode consisting of Ni-YSZ and Ni-Fe with a state-of-the-art Ni-YSZ anode [88]. The sintering of the dual-layer comprising the initial mixture of NiO and Fe_2O_3 resulted in the formation of $NiFe_2O_4$, which was then further reduced in hydrogen to a NiFe alloy. The maximum power density increased from 627 to 690 mW cm^{-2} using the dual-layered anode. Additionally, after eight redox cycles, the Ni-Fe dual-layered anode still delivered a power density of 636 mW cm^{-2}, whereas the single layer of Ni-YSZ declined to 2 mW cm^{-2} after only 1 redox cycle.

As discussed earlier, the authors in [67] presented the effect of adding Fe into a Ni-GDC electrocatalyst for intermediate-temperature SOFCs. While it was found that low concentrations of iron (1 wt.%) did not affect the particle size of nickel, the use of substantially higher concentrations of iron compared to nickel, such as 40 wt.%Fe-5 wt.%Ni/GDC resulted in the formation of $CeFeO_3$ and $GdFeO_3$ due to the diffusion of Fe cations into GDC during reduction in hydrogen. The authors suggested that the conversion of GDC to $CeFeO_3$, which is a semiconducting phase, might impede the ionic conductivity, and in turn, decrease the activity of the anode.

On the other hand, Fu *et al.* investigated a $Ni_{0.75}Fe_{0.25}$-GDC whose chosen mole fractions of nickel and iron were consistent with the theoretical results from DFT [75]. After reduction, solid solutions of $FeNi_3$ and FeNi were found. The authors reported a maximum peak power density of 835 mW cm^{-2} at 600 °C compared with 625 mW cm^{-2} for a Ni-GDC anode in their previous study [89], which concluded that iron can substantially enhance the catalytic activity of the SOFC anode.

2.3.3.4 Copper-based anodes

As mentioned in the last section, other research has focused on SOFC operation on hydrocarbon fuels to combat carbon formation on the Ni catalyst by completely replacing nickel with copper. These oxidation catalysts consist of Cu-CeO_2-YSZ, where ceria acts as oxidation catalyst and copper takes the role as electronic conductor. The

reader is herein referred to further literature for copper-based anodes using hydrocarbon fuels [90], [91], [92].

Yet, the authors in [93] took the approach to compare Ni-free catalysts, such as Cu-CeO$_2$-YSZ (30 wt.% Cu and 15 wt.% CeO$_2$) and Cu-Co-CeO$_2$-YSZ (30 wt.% Cu-Co and 15 wt.% CeO$_2$) catalysts to conventional Ni-YSZ in hydrogen atmospheres. The maximum peak power densities were 305 mW cm^{-2} and 136 mW cm^{-2} for Cu-CeO$_2$-YSZ and Ni-YSZ, respectively. The addition of cobalt led to a bimetallic Cu-Co phase, which further increased the activity, achieving a power density of 310 mW cm^{-2}.

2.3.3.5   Oxide-based anodes

Another approach of replacing Ni in SOFC anodes has been addressed by using electronically conductive oxide-based anodes, which have shown potentially higher redox stability than Ni [17].

Since vanadium oxide became of interest in batteries and redox-flow cells, thin film SOFC anodes (~30 nm) of vanadium oxide with various stoichiometry have been explored for SOFC applications [94]. When running in hydrogen atmospheres, the authors identified maximum peak power densities of 25 mW cm^{-2} at 410 °C for V$_2$O$_3$ and V$_2$O$_5$, compared to porous Pt of 100 mW cm^{-2}. Nevertheless, further investigations regarding operating temperatures and possible application as a dopant are still required.

Ceria is known for enhanced performance due to higher catalytic activity for fuel oxidation of hydrogen, while providing essential ionic conductivity [55]. Considering the required electrical conductivity of a SOFC anode, the literature states that either doped or undoped ceria still require the addition of an electronically conductive material [95]. For that reason, Tu *et al.* have analysed the performance of Ce$_{0.8}$M$_{0.2}$O$_{2-\delta}$ anodes (M refers to the following metals: Mn, Fe and Cu) [96]. Ceria in combination with either manganese or copper presented enhanced performance in hydrogen compared to nickel and iron. The authors concluded that the addition of a high electronically conductive oxide into the Ce$_{0.8}$M$_{0.2}$O$_{2-\delta}$ matrix could improve the performance of the anode.

Combining the results of Tu *et al.* with the performance improvement reported in [74] by adding MnO to Ni-YSZ anodes, it is expected that manganese oxide is a promising candidate for addition to the anode base material to improve its performance.

2.4 Cell designs

The previous section mainly focused on the requirements of SOFC anodes and anode materials already explored in the literature. Before moving forward to SOFC fabrication methods in the next chapter, this section briefly presents commonly used cell geometries and SOFCs concepts, in order to understand the cells that were tested in this work.

2.4.1 Cell geometry

The geometry of SOFCs can vary between tubular or planar designs, as shown in Figure 2.14a and b, respectively.
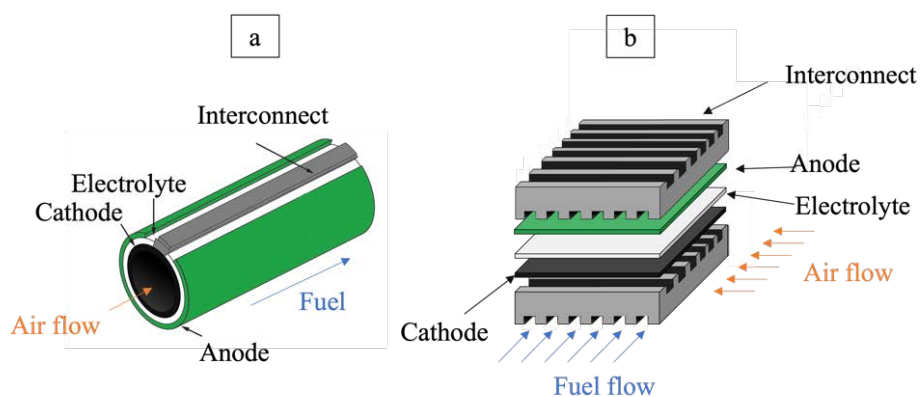
Figure 2.14: Schematic of commonly used SOFC geometries: tubular (a) and planar (b), adapted from [21], [22], [97].The interconnect in both designs acts as a current collector and allows to pass the gas streams to fuel and air electrodes. To increase the voltage (series stack) or current (parallel stack) of a single SOFC, multiple cells are connected through the interconnect into a stack [21].

Although tubular SOFCs offer the advantages of good thermal shock resistance, high mechanical strength and easy sealing, planar SOFC designs are more attractive for lower manufacturing costs and lower volumetric power density [21], [97], [98].

2.4.2 Cell configurations

An important aspect in the design of SOFCs is the consideration of the brittleness of the oxide materials used. To achieve high mechanical strength within the SOFC assembly, different design approaches have been made using a substantially thicker layer as one of the cell components, *e.g.*, cathode, anode or electrolyte, which serves as a supporting structure for the remaining layers to be deposited. Figure 2.15 illustrates the concepts of electrolyte-supported (a), anode-supported (b) and cathode-supported SOFCs (c).

a) Electrolyte-supported SOFC   b) Anode-supported SOFC   c) Cathode-supported SOFC
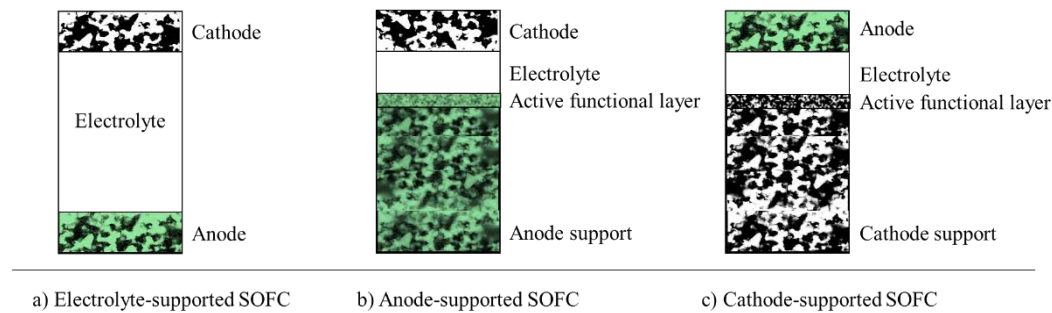
Figure 2.15: Schematic of cell configurations in SOFCs, electrolyte-supported (a), anode-supported (b) and cathode-supported SOFC (c), adapted from [21], [22], [24].

The electrolyte-supported cell comprises a thick electrolyte layer of > 100 μm, which is fired at high temperatures to provide mechanical strength [24]. The anode and cathode layers are deposited on the respective sites via suitable fabrication techniques (cf. chapter 3). While good mechanical stability and resistance to delamination and thermal shock are the advantages of this concept, the thick electrolyte layer causes high ohmic resistance and thus, requires higher operating temperatures (800-1000°C) than other concepts [22], [97].

Cathode-supported SOFCs use a cathode layer thickness of > 1mm. The porous cathode support is created by combining the cathode powder (*e.g.*, LSM) and pore formers. Before applying further layers of electrolyte and anode, a thin composite active cathode layer of a mixture of LSM and YSZ is deposited onto the support to create more TPBs, increasing the catalytic activity of the cathode (cf. section 2.3.3) [24]. Although the thick cathode structure increases oxygen concentration losses (mass transportation limitations), a thinner electrolyte reduces significantly the ohmic losses. Hence, they can run at lower operating temperatures (600-800°C) [97], providing better performance compared to electrolyte-supported cells [24].

The assembly of anode-supported SOFCs is similar to the cathode-supported cells. An anode support with a thickness of >1mm is made of a powder mixture of NiO and YSZ and a thin catalytically active functional layer (AFL) of reduced porosity is then deposited onto the support, followed by thin layers of electrolyte and cathode [24]. While ohmic losses are reduced in this cell configuration, allowing lower operation temperatures (600-800°C) [97], fuel concentration losses increase drastically compared to other cell designs. However, the fuel concentration losses are much lower compared to the high oxygen mass transport limitations in cathode-supported SOFCs, as the anode is fed with 100% pure fuel rather than diluted oxygen in air (21%) at the cathode

side. When operating on hydrocarbons, the fuel resides much longer in anode-supported cells before it diffuses to the AFL, resulting in an overall better performance of the three concepts due to a higher percentage of fuel conversion. For that reason, anode-supported SOFCs are widely studied and commercialised by industry [24].

Since lowering the operation temperature in SOFC systems to prolong their lifetime represents a future goal in research and industry, another interesting cell design has been developed using external support from a porous metallic substrate, as depicted in the figure below. Here, the metal support takes the role of the current collector [97], [99].
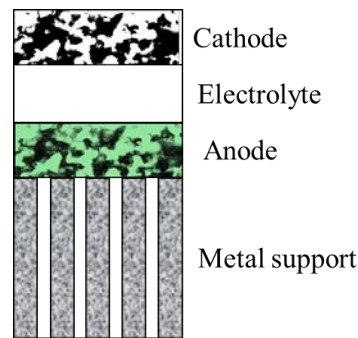
Figure 2.16: Schematic of metal-supported SOFC, adapted from [21].

This section has given an overview of different approaches in the cell design for SOFCs, showing support structures that allow a significant reduction in the thickness of the remaining cell components. The next step is now to understand how these components can be fabricated, in particular thin SOFC anodes or anode active functional layers. Hence, the following chapter will briefly introduce commonly used fabrication techniques and present the fundamentals and advantages of magnetron sputtering, as a promising fabrication route for SOFC anodes.

3 Thin film deposition

Apart from the material combination and chemical composition of SOFC components, their microstructural design has a significant effect on the performance.

Nanostructured materials exhibit a higher degree of triple-phase boundaries through finer particle sizes, resulting in enhanced fuel cell performance, which is crucial towards reduced operation temperatures. For that reason, a suitable thin film deposition technique has to be chosen to create catalytically active materials with fine particle sizes. Fabrication methods for SOFC components range from colloidal processes, such as screen-printing and tape casting to physical and chemical vapour deposition.

In the following, examples of thin film deposition techniques are introduced and classified into three categories: (i) Chemical Solution Deposition (CSD), (ii) Chemical Vapour Deposition and (iii) Physical Vapour Deposition (PVD). Since this work focuses on magnetron sputtering as a deposition technique, a more comprehensive overview is given in section 3.1.3.3.

3.1 Thin film deposition techniques

3.1.1 Chemical solution deposition

Chemical Solution Deposition (CSD) techniques, such as screen printing and tape casting involve the use of a chemical solution (*e.g.,* ink) of a precursor that is suspended or dissolved in a solvent and subsequently deposited onto a substrate.

3.1.1.1 Screen Printing and Tape casting

In terms of cost-effective and economical manufacturing, screen printing and tape casting are presented in the literature as simple and controllable methods for scale-up production [19], [22].

The principles of screen-printing and tape casting (*i.e.,* doctor blading) are illustrated in Figure 3.1 (a) and (b), respectively. During screen-printing, a homogenous ink mixture is applied onto a screen mesh and is pushed through the holes in this mesh using a rubber squeegee or metal blade to print the ink onto the substrate. When fabricating thin films via the tape casting method, also known as the doctor blading technique, a slurry suspension made of ceramics and dispersing agents is spread from a reservoir by a doctor blade onto a moving carrier [19], [57].
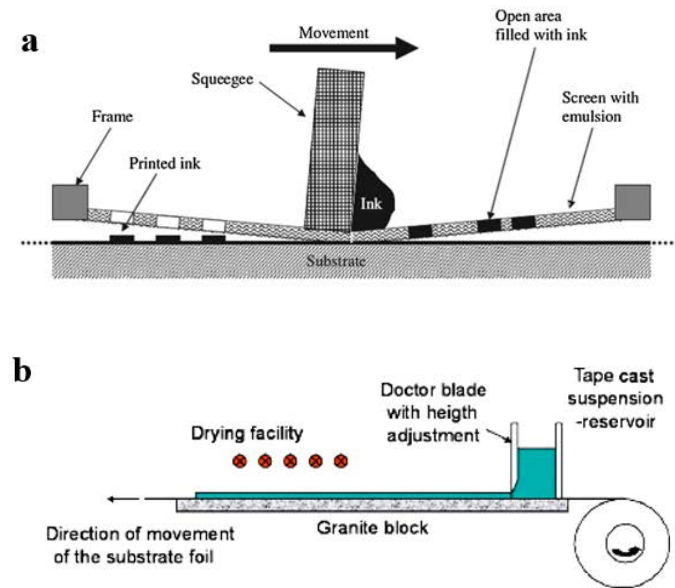
Figure 3.1 Schematic of screen-printing (a) and tape casting (b) adapted from [57], [100]

The created films require a subsequent firing process of the SOFC layers at high temperatures (sintering) to form an interconnected and stable microstructure with sufficient mechanical strength. The sintering of SOFC components at temperatures of ~1400 ºC, in particular Ni-YSZ cermets, causes particle coarsening due to the grain-growth process, which results in the elimination of triple-phase boundaries in SOFC anodes and cathodes. For that reason, different approaches have been presented, involving the reduction of the sintering temperature or the refinement of the particle size of the starting powder, leading to decreased particle coarsening [22], [57]. Nanostructured films can be created by a wealth of manufacturing techniques, such as magnetron sputtering. The reason why this work identified magnetron sputtering as an attractive manufacturing technique is presented in the section below, introducing the fundamentals of magnetron sputtering and then outlining the advantages of this technique.

3.1.1.2 Wet impregnation (Wet infiltration)

Wet impregnation (also known as wet infiltration) is an extension of the chemical solution deposition, as it enables the surface modification of electrode materials by depositing catalytically active nanoparticles into a porous microstructure, so-called support [101].

The first step is to prepare a solid support with a network of pores into which the nanoparticles can be impregnated. The support is then submersed into a chemical solution of the precursor based on the desired catalyst. The capillary force causes the

precursor to infiltrate the pore network of the support. After removing the support from the solution, the impregnated material is subsequently dried and calcined to remove the solvent and convert the precursor into the catalytically active catalyst. Considering SOFC anodes, authors in [102], [103] concluded that wet impregnation can be a promising method to create nanostructured SOFC anodes with improved performance and stability due to inhibited Ni grain growth and agglomeration. Other studies applied wet impregnation to infiltrate precious metal nanoparticles such as platinum or palladium into Ni-based anodes, which resulted in a lower electrode polarisation due to decreased impedance from adsorption and diffusion processes [104], [105].

Overall, wet impregnation is a simple and effective method of improving the electronic or ionic behaviour of the electrode or enhancing its catalytic activity.

3.1.2 Chemical vapour deposition

Chemical Vapour Deposition (CVD) describes the process where a gaseous precursor is transported to a heated surface by an inert carrier gas, such as argon, inside a process chamber [106]. Under controlled conditions of temperature and pressure, these precursors decompose to reactive species and further react chemically on the substrate, forming a thin film [107].

3.1.2.1 Plasma-enhanced CVD

To deposit a thin film at lower temperatures and yet drive the reactions to convert the precursor to the desired film material, additional energy is needed during the process. For this reason, plasma-enhanced CVD has been introduced. While introducing the gaseous precursor, a plasma is created by applying microwave or radio frequency power. The plasma containing ions, electrons, and radicals, energises the precursor molecules, leading to their decomposition to reactive species which are then adsorbed at the substrate[106].

3.1.2.2 Atomic layer deposition

Another widely used thin film deposition method is Atomic Layer Deposition (ALD). Unlike conventional CVD, ALD uses two precursor gases as reactants. The precursor gases are introduced into the process chamber alternately in pulsed cycles, so that the substrate is only exposed to one precursor at a time. In addition to that, the gaseous precursor can only react at the bonding sites of atoms on the surface, which self-limits

film growth. However, the sequential deposition of atomic layers allows precise control of film thickness [108]. Authors in [109] demonstrated the deployment of ALD to create a nanoscale YSZ electrolyte using two precursors for zirconium and yttrium.

3.1.3 Physical vapour deposition

Physical vapour deposition (PVD) techniques involve the generation of vapour species under vacuum due to either thermal evaporation or ion bombardment of a solid source, followed by their condensation onto a substrate [107], [110]. Operating pressures for PVD processes range from high ($0.1 - 10^{-5}$ Pa) to ultra-high vacuum ($< 10^{-5}$ Pa), in order to prevent significant collisions between vapour species and gas phase molecules. Although the required high vacuum operation is related to high investment costs for the equipment, the deposited films are free of atmospheric contamination. In the following, PVD techniques such as thermal evaporation, laser ablation and sputtering are introduced.

3.1.3.1 Thermal evaporation

A target material, typically a metal, is heated to its evaporation point in a high vacuum. The generated vapour particles are transported through the vacuum until they condense onto the substrate's surface into a thin film [106].

3.1.3.2 Pulsed laser deposition

Pulsed Laser Deposition (PLD) uses a high-energy pulsed laser to create the vapour particles from a target material inside a vacuum chamber, which then condenses to form a thin film [106]. When focusing the laser beam onto the target material, the surface rapidly overheats due to the high energy of the laser pulse, causing the formation of a plasma plume containing the ejected atoms, ions and clusters. Thin film formation takes place when the plasma plume expands towards the surface of the substrate so that the vapourised particles condense with the stoichiometry of the target material [111]. PLD allows for precise control of film thickness, composition, and structural properties PLD by controlling parameters such as laser energy, pulse frequency, substrate temperature, and ambient pressure.

The reader is herein referred to the literature [19] for detailed information about other fabrication methods for SOFCs and their features.

3.1.3.3 Sputtering

The general principle of sputtering is based on the bombardment of a target surface by the ionised atoms of an inert gas, such as argon. A target plate of the material to be

sputtered is attached to the magnetron, acting as the cathode in a vacuum chamber at reduced pressure. This target plate can be made of a compound material, a so-called compound target, featuring the desired composition between two or more elements to be deposited. A negative voltage is then applied to the cathode, causing the acceleration of Ar gas ions towards the target, resulting in energetic collisions on its surface. In consequence, target atoms are ejected, or 'sputtered' from the target surface, allowing for thin film deposition on a substrate surface on the atomic scale [110]. During ion bombardment, secondary electrons are emitted from the target surface.

I. Magnetron sputtering

In magnetron sputtering, a perpendicular magnetic field is superposed with the electric field applied to the back of the cathode resulting in a cycloidal electron movement along the magnetic field lines influenced by the Lorentz force. As illustrated in Figure 3.2, the magnetic field lines are responsible for trapping the electrons near the target, leading to a higher degree of ionisation of the argon atoms and hence, higher sputtering rates at the target and higher deposition rates at the substrate [110].
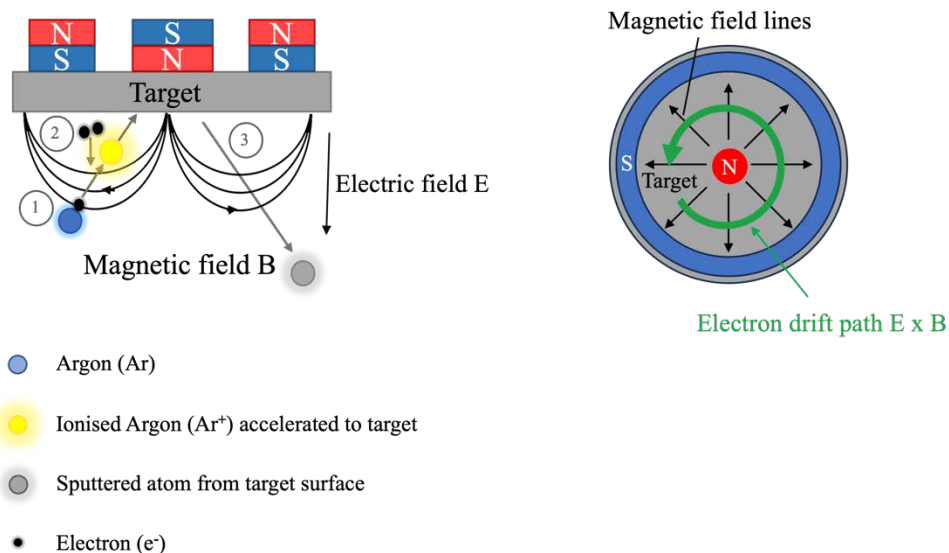
Figure 3.2: Schematic of magnet design in magnetron sputtering [110], [112].

The configuration of magnetrons can be classified into balanced and unbalanced formation. As shown in Figure 3.3 a), a balanced magnetron comprises the same magnetic field strength on the inner and outer magnets. In this case, the plasma is strongly confined in front of the target so that few electrons can escape from the primary magnetic

fields, leading to fewer ionising collisions and therefore, low ion currents transported to the growing film. Ion bombardment of the growing film is an important consideration in magnetron sputtering, as it can strongly modify the structure and properties of the resulting coating. In order to increase the substrate ion current through an extension of the magnetic field towards the substrate, the unbalanced magnetron configuration was developed. Unbalanced magnetrons present different magnetic field strengths of inner and outer magnets, implying an unbalanced magnetic circuit. As illustrated in Figure 3.3 b), type I unbalanced magnetrons have a stronger central magnet so that the magnetic field lines point toward the chamber walls, resulting in low plasma density in the substrate region. The most commonly used design is type II unbalanced magnetrons containing stronger magnets on the outside ring (cf. Figure 3.3c). Here, the magnetic field lines indicate an expansion of the plasma away from the target surface and toward the substrate, yielding increased ion current density and consequently, higher ion bombardment of the growing film, which is beneficial for the formation of dense coating structures [113], [114].

(a) **(b)** **(c)**

Balanced magnetron **Unbalanced magnetron Type I** **Unbalanced magnetron Type II**
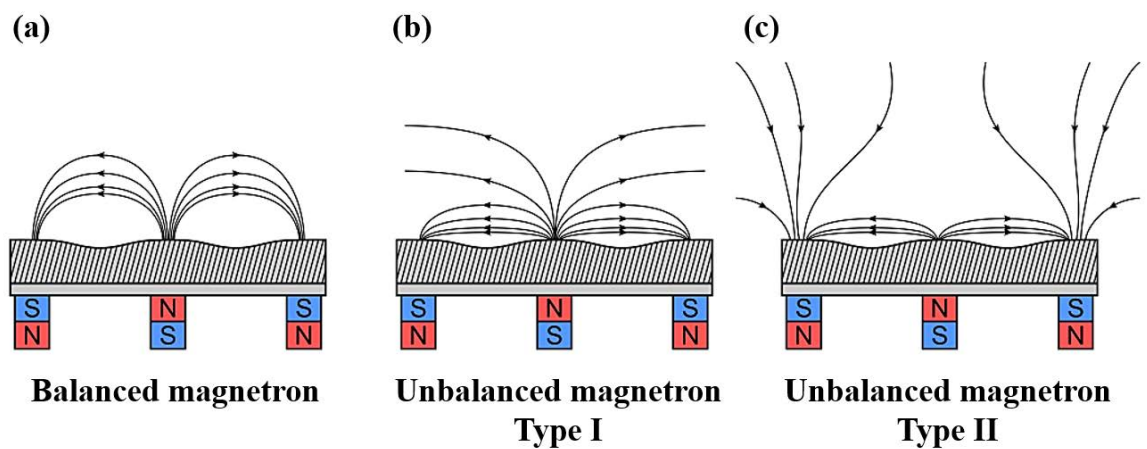
Figure 3.3: Magnetic configuration of (a) balanced magnetron, (b) unbalanced type I magnetron and (c) unbalanced type II magnetron, adapted from [113].

Considering multiple magnetron systems using unbalanced type II magnetrons, the magnetrons can be arranged in closed-field configurations with opposite magnetic polarities or in mirrored configurations with identical magnetic polarities, as shown in Figure 3.4, respectively.
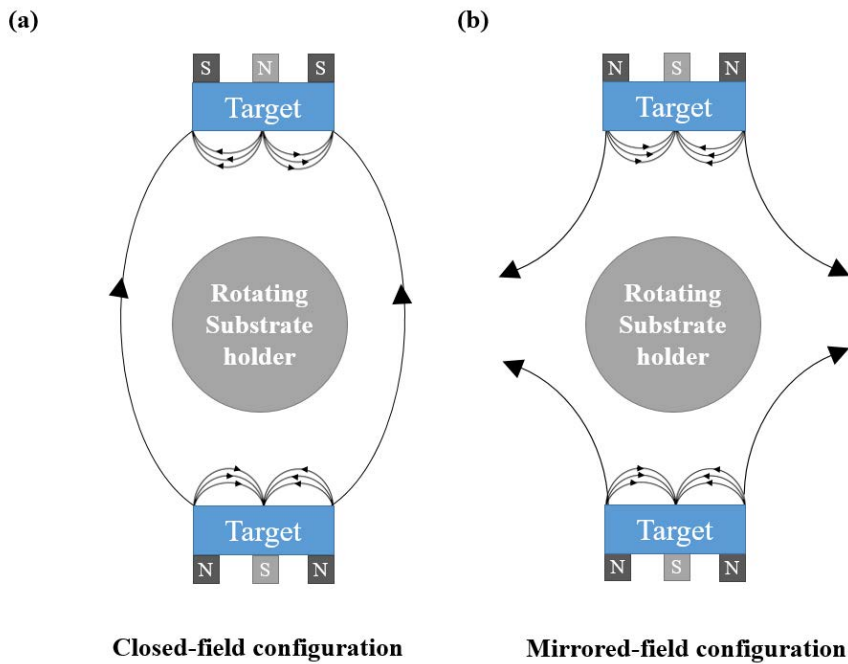
Figure 3.4: Multiple magnetron systems in closed-field configuration (a) and mirrored-field configuration (b), adapted from [115].

In the mirrored configuration, secondary electrons, which are responsible to maintain the plasma, get lost to the ground because they are guided along the magnetic field lines towards the chamber walls. Due to the disappearance of these secondary electrons, the plasma density is reduced in the substrate area. On the contrary, in the preferable closed-field configuration, the magnetic field lines are connected between the magnetrons caused by the opposite polarities of the outside rings, resulting in an excess of secondary electrons and thus, a high density plasma with high substrate ion currents [115].

II.   Power delivery modes

Materials can be deposited using magnetron sputtering in a combination of various power delivery modes, such as direct current (DC), pulsed DC or radio frequency (RF). DC sputtering is a simple and cost-effective technique to deposit coatings from electrically conductive target materials. When using a DC power supply, a negative DC voltage is applied to a metallic target material, representing the cathode. The glow discharge is then sustained between the cathode and the chamber walls or the anode plate in front of the target [114].

Thinking of the deposition from a dielectric target material, DC sputtering would require excessive voltages in the order of 10^{12} V because of the high electrical resistivity

of dielectrics. For the deposition of insulating materials, an RF power supply can be used as RF voltages can be applied through any type of impedance. The frequency used in an RF sputtering system is 13.56 MHz.

On the other hand, dielectric films can be created by sputtering from a metallic target and introducing a reactive gas, such as oxygen, a process also known as reactive sputtering (see section III). However, during this process, the target is covered with an insulating layer of its compound materials, also known as target poisoning. The target charges up until an electrical breakdown occurs, leading to an unstable operation, so-called arcing, where micro-particles are ejected and incorporated in the coating. This could lead to non-uniform deposition, defects in the thin films or damage of the power supply in more extreme cases [116], [117].

Pulsed DC magnetron sputtering has been introduced to overcome the problem of arcing. During the 'pulse-on' phase, a negative voltage is applied to the target and the target is sputtered in the conventional way. In the 'pulse-off' phase, the target voltage is reversed to a low positive voltage (typically 10-20 % of the magnitude of the pulse-on voltage). An electron current is drawn to the target during the off phase, which will discharge the positive build-up on the surface and prevent arc events from occurring. Pulse frequencies are in the range 100 to 350 kHz. [118]. In addition to important process parameters such as power, deposition pressure, pulse frequency and target-substrate distance in pulsed DC sputtering, the literature has identified that the duty cycle plays an important role to maintain process stability. The duty cycle is expressed by the negative pulse active time (pulse-on period) divided by the total duration of the pulsing cycle, as presented in the following equation [116]:

$$D = \frac{t_{on}}{T_{total}} = t_{on} \cdot f \qquad 3.1$$

where D is the duty, t_{on} is the negative pulse active time (s), T_{total} is the total duration of the pulsing cycle (pulse-on + pulse-off periods) and f is the pulse frequency (kHz).

Arcing can still occur if inaccurate process parameters are used. However, duty cycles below 70 % have been reported to prevent arcing [119].

III.   Reactive magnetron sputtering

As mentioned before, another technique to create compound materials is the deposition from metal targets in a reactive gas atmosphere, such as oxygen/argon gas mixtures

for oxides. When producing thin films by reactive sputtering, the behaviour of the cathode voltage with increasing reactive gas flow shows hysteresis behaviour. Considering oxygen as a reactive gas, two stable states can be identified as the metallic mode and oxide mode in the hysteresis curve, which are illustrated in Figure 3.5.
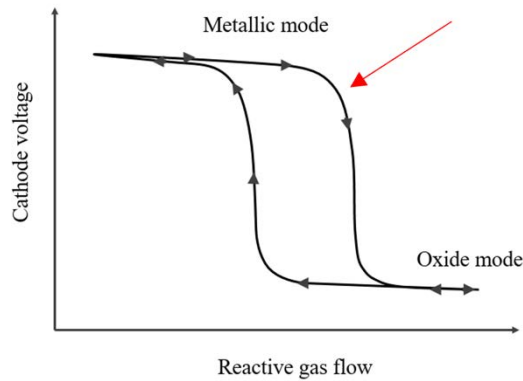
Figure 3.5: Hysteresis curve of cathode voltage as a function of reactive gas flow rate, adapted from [110].

The transition from metallic to oxide mode indicates a rapid change in the discharge voltage, caused by the formation of a compound layer on the target surface. The discharge voltage can either drastically increase or decrease depending on the material's secondary electron emission coefficients for metal and oxide (cf. Chapter 7, [120]). A characteristic of the oxide mode is significantly lower deposition rates. Hence, the optimal conditions for stoichiometric oxides deposited at high sputtering rates are achieved, when sputtering at the knee of the curve.

Reactive sputtering is often applied using a pulsed DC power supply and a feedback control system for the reactive gas which will be further explained in the methodology chapter. (cf. section 5.1).

3.2 Thin film growth

In order to understand how the SOFC anode films are formed on the YSZ electrolyte, this chapter introduces the processes of thin film formation and growth, occurring during magnetron sputtering on the substrate surface. Film formation and growth consist of three stages: (i) nucleus formation, (ii) nucleation growth and (iii) microstructure evolution [106], [110], [114].

3.2.1 Nucleation and growth

An ejected vapour atom or molecule from the target surface impacts on a substrate as an 'adatom' and diffuses over the surface of the substrate, using up its remaining kinetic energy depending on the temperature of the substrate, until it is finally adsorbed on the film's surface, usually trapped at low-energy lattice sites. When meeting another vapour atom, they form a so-called *nucleus*, undergoing a phase transformation from vapour to condensation phase [106].

During the nucleation growth stage, three occurring growth modes had been observed in the literature [110], as listed below:

a) Volmer-Weber growth (Island-like type, 3D):

When deposited atoms bond more strongly to each other than to the substrate, small stable dispersed clusters grow in three different dimensions on the substrate surface, forming islands, as illustrated in Figure 3.6a. This growth type is characteristic for metallic films on insulating substrates.

b) Frank-van der Merwe growth (Layer-by-layer type, 2D):

The layer-by-layer growth mode is the opposite of the island growth, since the smallest stable nucleus expands in two dimensions, forming planar sheets (see Figure 3.6b). The reason for that is that the atoms bond more strongly to the substrate rather than bonding to each other. An example of this mechanism is the single-crystal epitaxial growth of semiconductor coatings.

c) Stranski-Krastanov growth (Mixed type, layer + island)

This growth mode combines the mechanisms of the Volmer-Weber growth and Frank-van der Merwe growth. The nucleation growth begins with a layer-by-layer growth, forming a single or multiple layers. However, further layer growth becomes energetically unfavourable, causing a transition from 2D to 3D island growth (see Figure 3.6c). A hypothesis is that lattice mismatches between the deposited film and the substrate cause the accumulation of strain energy within the film. A subsequential release of that energy might induce a transition in the growing mode at the interlayer interface [110].
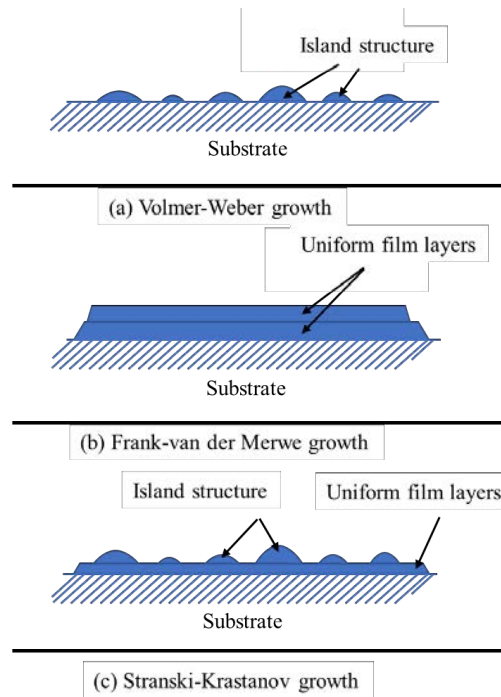
Figure 3.6: Growth modes of thin films: (a) Volmer-Weber growth, (b)   Frank-van der Merwe growth and (c) Stranski-Krastanov growth, adapted from [110], [114].

The deposited film's microstructure and properties can be controlled through a variety of parameters during the process, as listed below:

- Power delivery mode (cf. section II)

- Substrate temperature

- Deposition pressure (mean free path of gas particles in the vacuum)

  o Mean free path represents the distance of a gas particle between two subsequent collisions. A high deposition pressure leads to a higher gas particle density, resulting in a lower mean free path and vice-versa.

- Substrate bias

- Deposition set-up and geometry

  o Deposition angle and target-substrate distance (cf. section 5.1, chapter, 7)

In order to understand the impact of each deposition parameter on the growing film's microstructure and its properties, structure zone models will be introduced in the next section

3.2.2 Microstructure evolution and structure zone models

Structure zone models (SZM) are a tool for researchers to predict the resulting microstructure depending on the used deposition parameters. Although empirical studies, which are related to extensive experimental work, are still needed, classical structure zone models can give indications of the type of microstructure to be expected [121].

3.2.2.1 Substrate temperature

The microstructure evolution is subjected to four processes: (i) shadowing, (ii) surface diffusion, (iii) bulk diffusion and (iv) recrystallisation [110]. Shadowing results from the geometrical constraint during the interaction of the condensed atoms and the substrate morphology (roughness) at low substrate temperatures. Surface diffusion occurs at medium substrate temperatures and describes the diffusion of adatoms across the surface of the film. At high substrate temperatures, atoms move through bulk diffusion to low-energy lattice sites to attain their equilibrium position, causing recrystallisation and grain growth.

In addition to the substrate temperature that has a major influence on the resulting microstructure, the melting point of the condensed atoms must also be considered. For that reason, the first SZM established by Movchan and Demchishin, also known as the MD model, proposed three zones based on their microstructural investigations of thick nickel, titanium, tungsten, alumina and zirconia films deposited by evaporation, as illustrated in Figure 3.7 [122]. The three zones 1, 2 and 3 were defined as a function of the ratio between the substrate temperature T_S and the melting temperature of the material T_M, both expressed in degrees Kelvin. The resulting ratio T_S/T_M is also known as the homologous temperature [106], [110].
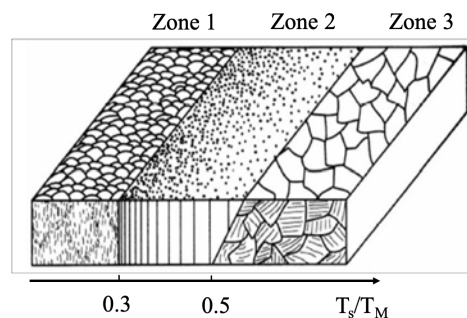
Figure 3.7: First structure zone model for evaporated films proposed by Movchan and Demchishin [122].

Zone 1 is defined for $T_S/T_M < 0.3$, where the adatoms have low mobility, meaning little to no diffusion occurs. The microstructure presents tapered crystals and voided boundaries, resulting in a porous film with fine grains due to the continued nucleation of grains. Zone 2 presents columnar grains with dense grain boundaries at $0.3 < T_S/T_M < 0.5$, as surface diffusion takes place due to the increase in adatoms mobility. Dense films with larger grains are characteristic for zone 3 at $T_S/T_M > 0.5$ as bulk diffusion through the lattice results in recrystallised grains.

3.2.2.2   Deposition pressure

Thornton extended the original SZM from Movchan and Demchishin by introducing a second axis to account for the effect of the deposition pressure, *i.e.*, argon gas pressure, on metallic films when using cathodic sputtering [123]. Herein, zone 1 characteristics persist in increasing deposition pressures, as illustrated in Figure 3.8.
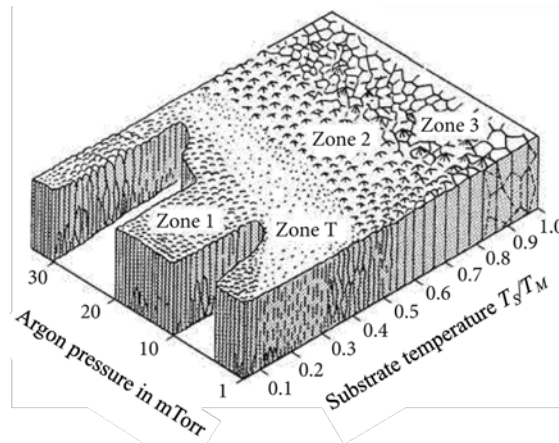
Figure 3.8: Structure zone model proposed by Thornton, considering the deposition pressure and homologous temperature [106], [123].

The reason for this phenomenon is that the mean free path between the atoms decreases at higher pressures due to a higher degree of atomic scattering, which leads to a lower kinetic energy for the adatoms and thus, to an increased shadowing effect.

Furthermore, Thornton reported an additional transition zone T between zone 1 and 2, where the higher energy of adatoms reduces the shadowing effect and creates a more closely packed fibrous microstructure with a smooth surface. However, the literature in [124] suggested that this transition zone should be considered as an extended zone 1 at low pressures rather than a separate zone because the distinction between zone 1 and zone T was not defined.

3.2.2.3 Substrate bias

Ion-assisted PVD processes, such as bias sputtering, use a negative voltage applied to the substrate during deposition, which enables continuous ion bombardment of the growing film which leads to its densification [106], [125]. For that reason, Messier proposed another SZM which replaced the pressure axis with a substrate bias voltage axis that represented the energy of the ion impinging on the surface, as shown in Figure 3.9 [126].
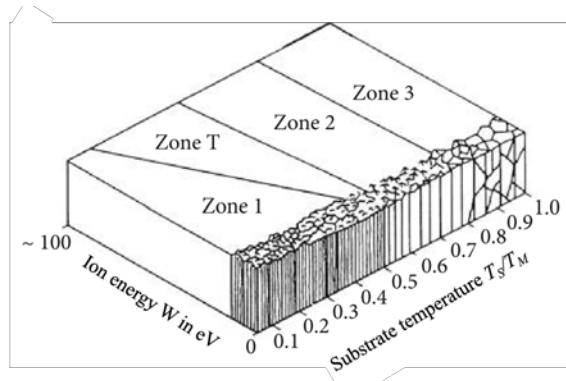
Figure 3.9: Structure zone model by Messier, considering substrate bias and homologous temperature [126].

Further readings on novel structure zone models for ion-assisted PVD processes using close-field magnetron sputtering can be found in [124].

4 Summary

4.1 Comparison of deposition techniques

Various deposition techniques to deposit nanoparticle films have been presented in the previous chapter. The table below illustrates major advantages and disadvantages of each deposition technique.

Table 4.1: Advantages and disadvantages of previously introduced deposition techniques [102], [103], [106], [108], [110], [127], [128], [129].

Deposition method	Advantages	Disadvantages
Screen printing/ Tape casting	Simple, cost-effective, and scalable for large areas. Suitable for thick film applications. Suitable for porous structures in SOFC anode supports.	Limited control over microstructure and uniformity. Difficulty achieving precise fine feature control.
Wet impregnation	Simple and low-cost setup. Tailored microstructures by adding nanoparticles of catalytic phases. Versatile for porous substrates.	Limited penetration depth for high-density materials. Requires multiple impregnation cycles for high catalyst loading.
PE-CVD	Deposition of dense or porous films depending on conditions. Works at lower temperatures, preserving substrates. Uniform and large area coating.	High equipment and operational costs. **Difficulty to control film growth** Production rate is limited by the chemical reaction rate.
.ALD	Exceptional control of thin film thickness and composition. Ideal for coating porous substrates uniformly.	**Very slow deposition rate** - not suited for thick layers High cost and limited availability of precursors.
Evaporation	Simple process with high purity films Suitable for metals and simple compounds. High deposition rates.	Limited capability for porous layer formation. Limited step coverage for complex geometries. Requires high vacuum equipment. High material wastage.
PLD	High-quality functional films. Excellent for stoichiometric transfer of multi-component materials.	**Non-uniform coating thickness.** Very high equipment costs. Limited scalability for large substrates
Magnetron Sputtering	Dense or porous film deposition. Versatile for depositing conductive and catalytic coatings. High uniformity and adhesion. Scalable for large areas. Repeatability.	High equipment cost. Lower deposition rates compared to evaporation. Argon incorporation in films can occur.

From above table, it can be clearly seen that chemical solution processes such as screen printing and wet impregnation present low-cost fabrication routes when scaling up manufacturing, while providing the option to tailor the electrode microstructure through wet impregnation.

On the other hand, PVD techniques require a significant initial investment due to high equipment costs but offer control over the microstructural film growth in return by adjusting deposition parameters (ALD, PLD and magnetron sputtering).

Given the low deposition rate of ALD and the difficulties encountered by PLD in achieving uniformity over large areas, the fabrication of SOFC anode functional layers was carried out using magnetron sputtering in this work. The control of the microstructural film growth by altering the deposition parameters, such as the substrate temperature or deposition pressure, as introduced in section 3.2.2, presented a significant area of interest.

4.2 Novel contribution of the thesis

4.2.1 Deposition process

Recent studies have already deployed magnetron sputtering as a means of producing SOFC anodes.

The authors in [130] fabricated anode-supported SOFCs with and without nanostructured anode functional layers (AFL) of Ni-GDC and Ni-YSZ using magnetron sputtering. Ni-YSZ anodes were tested at 600-800 ºC and Ni-GDC anodes at 400-600 ºC, respectively. When comparing the peak power densities of these anodes with and without a functional layer, an increase of 50-60 % for Ni-GDC at 600 ºC and 30% at 800 ºC, and 68 % at 600 ºC for Ni-YSZ has been reported, respectively. During deposition, a power of 700 W and 1500 W was applied to nickel and zirconium-yttrium sputter targets, respectively, both with a diameter of 75 mm, yielding 34 mol.% nickel within the Ni-YSZ coating. They achieved a deposition rate of 2 μm/h.

However, no information was given regarding the use of a feedback control system to avoid target poisoning due to excess oxygen, as only constant flows of argon and oxygen were introduced into the deposition chamber. The reason for the significantly high applied power density used on the sputter targets may have been target poisoning during the deposition, which is related to quality issues of the film due to non-uniform deposition and defects.

This work demonstrated that comparable deposition rates can be obtained at substantially lower power densities applied to the sputter targets (Ni: 200 W and Zr-Y: 250 W) through the implementation of a reactive feedback control strategy which regulated the partial pressure of the reactant (*i.e.*, oxygen) during deposition, thereby facilitating a noticeably more stable and controlled process.

Another innovative and seminal work has been presented in [131] using magnetron sputtering in oblique angle deposition (deposition angle of 80º to the normal) from two compound targets: Ni-YSZ and Ni-GDC. The study investigated the effect of alternating thin layers of Ni-GDC and Ni-YSZ compared to a hybrid Ni-YSZ-GDC anode (*i.e.,* GDC-doped Ni-YSZ) via co-deposition. Such prepared cells were then tested at 850 ºC operating with hydrogen. The thicknesses of the alternating layers of Ni/YSZ and Ni-GDC varied between 200 nm and 1000 nm. As depicted in Figure 4.1, alternating 200 nm layers revealed better performance than the single component anodes, whereas anodes with 1000 nm alternating layers demonstrated relatively poor performance, which was attributed to the formation of a metallic Ni barrier layer at the Ni-GDC and Ni-YSZ interfaces.
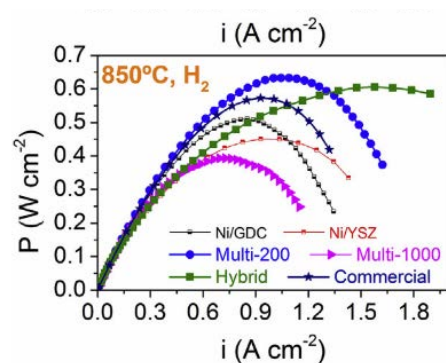
Figure 4.1: I-V curves of anodes with alternating layers of Ni-YSZ and Ni-GDC and a hybrid Ni-YSZ-GDC operating at 850 ºC with hydrogen fuel adapted from [131].

On the contrary, the Ni-GDC-YSZ anode ('hybrid anode') yielded unusual and beneficial high power densities at high current densities. The authors attributed the high degree of dispersion and intermixing of the elements to this improved performance. The above work used a 50 mm diameter sputter target of a Ni/Zr/Y alloy (68.8/26.6/4.6 wt%) to achieve 50 vol. % Ni in the GDC-doped Ni-YSZ film.

Obtaining the desired film composition using magnetron sputtering is more straightforward with compound targets, as the composition has been already pre-defined in

the target material. However, this approach is more costly and does not allow for flexibility in modifying the composition of the film across the entire layer in the case of graded composition designs.

The present work allowed the decoupling of the sputter targets of nickel and zirconium-yttrium, which provided more flexibility to vary the nickel composition in the film when considering the addition of promising dopants into the Ni-YSZ microstructure. It also sets the groundwork for a graded nickel composition across the films in potential future works.

In combination with the process control features mentioned above, such as the partial pressure control of the amount of oxygen present during the deposition, it has been shown that stable deposition process conditions can be established during the co-deposition of up to four magnetrons.

4.2.2   Choice of dopants

Dopants can be used to improve the electrochemical performance of the SOFC anode due to either enhancing its catalytic activity or increasing the ionic or electronic conductivity of the SOFC anode material. Other performance increases can be due to the mitigation of nickel agglomeration in the Ni-YSZ matrix.

Table 4.2 summarises the effect of the presented dopants on the catalyst performance in the literature review in section 2.3.3, focusing on the catalyst's fabrication route.

Table 4.2: Overview of transition metal-doped Ni-based anode catalyst operating on hydrogen in the literature.

Anode material	Dopant	Temperature [ºC]	Fabrication route	Effect on performance[1]	Reference
Ni-YSZ	Cr/ Cr_2O_3	-	PVD (evaporation)	↓	[65]
Ni-GDC	Fe	800	Wet chemistry	↓	[67]
Ni-YSZ	TiO_2	800	Solid-state reaction	↓	[68]
Ni-YSZ	Nb_2O_5 /NbO_2	800	Solid-state reaction	↑	[69]
Ni-SDC	Nb_2O_5	700	Wet chemistry	↑	[70]
Ni-YSZ	Cu	750	Wet chemistry	↑	[71]
Ni-YSZ	MoO_x/ NiMo	800	Wet chemistry	↑	[72]
Ni-YSZ/ Ni-MnO	Dual layer	650-800	Wet chemistry	↑	[73]
Ni-YSZ	MnO	800	Wet chemistry	↑	[74]

---

[1] Increased performance = ↑; declined performance = ↓.

From above table, it can be seen that niobium, molybdenum and manganese presented improved performance in SOFC anodes in the literature. While molybdena is considered to increase the catalytic activity (for hydrogen adsorption and dissociation) through the NiMo bond [72], the addition of niobium oxide and manganese oxide resulted in the formation of discrete phases.[69], [74].

4.2.2.1 Manganese

Considering the SOFC fabrication route of post-annealing in air and subsequent reduction in hydrogen, manganese oxide (II) is considered the most stable manganese oxide form. The literature has shown that adding 1.1, 2.75 or 5.5 wt.% MnO into Ni-YSZ increased the catalytic activity as well as the electronic conductivity for the hydrogen oxidation and improved the electrical conductivity [74]. Manganese oxide underwent a solid-state reaction with nickel during calcination, forming $NiMn_2O_4$, however, it decomposed to MnO after reduction in hydrogen. The authors analysed the lattice parameters of YSZ before and after reduction and found no changes in either state or compared to YSZ in undoped Ni-YSZ anodes. They concluded that Mn and YSZ do not form a solid solution.

Since manganese proved to be the most cost-effective material when comparing the price per kilogram on the market [132] of the three elements mentioned above, the approach taken in this work was to add MnO into the Ni-YSZ anode by magnetron sputtering to allow for the uniform incorporation of manganese oxide at the nanoscale, thus ensuring a consistent dopant distribution in form of a discrete phase within the Ni-YSZ matrix (cf. HAADF-TEM micrograph in [131]).

4.2.2.2 Vanadium

Vanadium can form a variety of complex oxides due to its multiple oxidation states, which can undergo redox reactions and hence, might improve the catalytic activity at the anode. The literature investigated different oxidation states of pure vanadium oxide thin films for SOFC applications [94] and found electrocatalytic activity at 410 ºC for V_2O_3 and V_2O_5. While vanadium oxide (V) is not stable under calcination nor SOFC operation, vanadium (III) oxide represented a promising candidate for the doping of the Ni-YSZ anode. V_2O_3 was successfully used as a second phase in combination with YSZ as anode catalyst against hydrogen sulphide-containing hydrogen [133]. No solid state reactions between YSZ and V_2O_3 were observed. Potential reactions and resulting

phase transformations of V_2O_3 with Ni under calcination and SOFC operation temperatures needed to be determined and whether V_2O_3 can be incorporated as dopant at the nanoscale, resulting in a uniform dopant distribution across the film.

To the best of the author's knowledge, no studies have reported the fabrication of doped SOFC anode materials using co-deposition of more than two sputtering targets. The combination of incorporating a new oxide-based dopant, such as manganese oxide or vanadium oxide into the Ni-YSZ microstructure and applying feedback control for the magnetron sputtering process outlines the novel approach in research and provides the framework for this project, namely the creation of nanostructured advanced anodes produced by magnetron sputtering.

II. Methodology

5 Experimental techniques

The first part of this chapter presents the methodology of the deposition process that is used to deposit the SOFC anode functional layers at stable conditions. The second part focuses on the instrumentation to test the electrochemical performance of the newly created films.

5.1 Deposition system

Nanostructured state-of-the-art Ni-YSZ films and doped Ni-YSZ films have been deposited by using reactive pulsed DC magnetron co-sputtering of metallic targets, *i.e.*, zirconium-yttrium (Zr−Y, 85−15 at.%, 99.5% purity), nickel (Ni, 99.95% purity), vanadium (V, 99.9% purity), and manganese (Mn, 99.9% purity). An analysis of the impurities in the Zr-Y target is presented in Appendix B, which details concentrations for impurities higher than 100 ppm for Fe, Hf and Al. It is not believed that these impurities have had an influence on the final structure.

To deliberately generate columnar nanostructures, the sputtering process was performed in oblique angle deposition mode (*i.e.*, 60° angle of incidence for Ni and Zr-Y and 30° for the dopant materials), in mixed argon/oxygen atmospheres to allow sputtering in a reactive mode. Figure 5.1 illustrates the co-sputtering process of metallic targets of zirconium-yttrium, nickel, and the respective dopant chosen in this work, which is tilted at an angle α to the substrate surface direction.
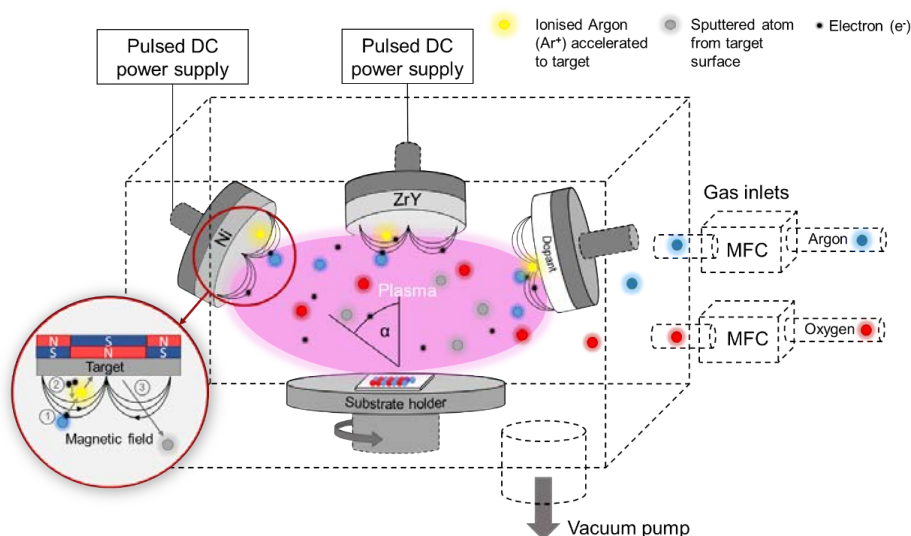
Figure 5.1: Co-sputtering of nickel, zirconium-yttrium, and a dopant.

The Minilab 060 vacuum coating system from *Moorfield Nanotechnology Ltd*. consists of two vacuum chambers: i) process chamber and ii) load-lock (LL) chamber, which are connected through a gate valve. This gives the advantage of loading samples into the process chamber via the LL chamber transfer arm mechanism while maintaining the base pressure in the process chamber. Approximate pressure readings during pumping and venting routines are displayed through wide-range gauges installed on both chambers. First, the process chamber must be pumped down by the system of a rotary air pump that allows a suitable base pressure to be achieved to activate the turbo-molecular pump, which brings the chamber down to the high vacuum range of 10^{-6}–10^{-7} mbar (10^{-4}–10^{-5} Pa). Once a pressure below 5×10^{-5} mbar (5×10^{-3} Pa) is achieved in the process chamber, the LL is ready to be pumped down by a second system of rotary and turbo-molecular pumps to achieve its base pressures.

The process chamber comprises four unbalanced magnetrons, each with a target diameter of 76.2 mm. The magnetrons are arranged in a mirrored configuration, *i.e.*, all magnetrons are configured with the same magnetic polarity.

The power is applied by a dual-channel *Advanced Energy Pinnacle Plus* pulsed DC power supply and by two *Seren R301* RF power units. The second RF power unit supplies a negative bias voltage to the substrate, allowing for sputter cleaning of the substrate prior to sputter deposition and/or applying bias during the deposition and increasing the energy of ion bombardment on the sample surface to create denser coatings. In addition to that, the substrate holder can be heated up to a temperature of circa 500 °C by an IR bulb heater.

During the deposition process, an implemented capacitance manometer (baratron) from *Inficon Ltd.* facilitates accurate pressure control. The working pressure depends on the introduced working gas (argon, purity N4.8, 99.998%), which was regulated by a 0-20 sccm mass flow controller (MFC) from *MKS Ltd.* Typical working pressures range from 0.1 to 1 Pa (10^{-3} to 10^{-2} mbar). The reactive gas (*i.e.*, oxygen, purity N2.6, 99.6%) was regulated by a 0-10 sccm MFC from the same supplier.

In reactive mode, the argon flow rate was kept constant, while the oxygen partial pressure was adjusted by a pressure control system, using a PID controller from the *Moorfield IntelliNet* software.

5.2 Cell testing

5.2.1 SOFC test rig

In order to test the performance of the deposited SOFC anodes, an 855 SOFC test system was acquired from *Scribner Associates Inc.* equipped with an 885 fuel cell potentiostat (max. current 2 A, combined with frequency response analyser for galvanostatic EIS in the range of 1 mHz and 10 kHz) and a box furnace from *Mellen Company Inc.* (max. operation temperature of 1200 ºC). The included software *FuelCell*® allowed to control the temperatures of the furnace and cell as well as the gas flows of the reactants through the cell.

The setup is presented in the following figure.

Figure 5.2: SOFC test rig, featuring the 855 SOFC test station with potentiostat 885 (left) and furnace (right).

A detailed schematic of the above assembly of the SOFC test station is illustrated in Figure 5.3a. The fuel cell is located in the furnace between two gas manifolds (see Figure 5.3b) for the reactant gases which serve as a gas delivery system for the gas inlet and outlet. The load terminals were connected to the cathode (red, positive) and the anode (black, negative) of the fuel cell in the furnace. The voltage was measured in a 4-probe configuration, where the current is collected by tube clamps (Figure 5.3c), which are attached to two manifold tubes of the reactant gases, and the voltage senses (*i.e.*, platinum wires) were positioned at the interface of current collector and electrode.

The furnace temperature and cell temperature are controlled through two thermocouples (Figure 5.3a). An additional 855 furnace control unit includes a third thermocouple to actively monitor the furnace temperature. If the temperature limit is exceeded due to malfunctions, the control unit will turn the power to the furnace heaters off.
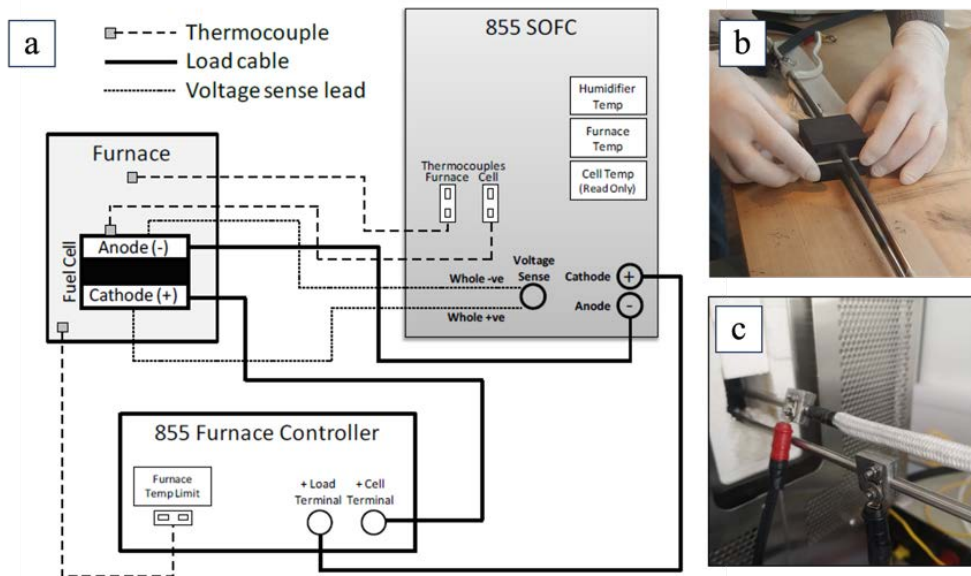
Figure 5.3: Schematic of 855 SOFC test system (a), adapted from [134]; gas manifolds for gas delivery from *fuelcellmaterials* for SOFCs with an area of 5x5 cm^2 (b); in-house made tube clamps attached to gas manifolds for SOFC button cell testing (c).

In order to provide a well-sealed fuel cell atmosphere, the test station uses an integrated compression system. As shown in Figure 5.4, this compression system contains a defined weight on a threaded bolt as a lever arm, which applies the compression onto the cell assembly depending on the size of the cell.
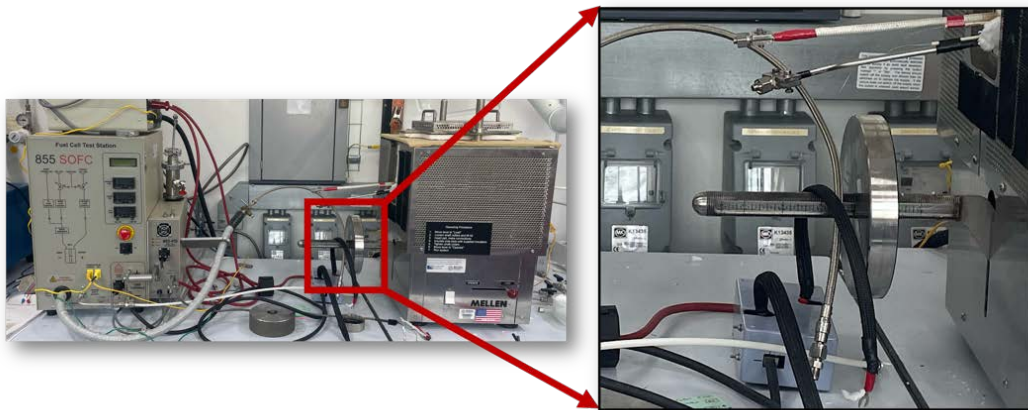
Figure 5.4: Compression system of the 855 SOFC test station.

The manufacturer suggests a compression of 5 PSI (34.5 kPa), resulting in 19.4 lbs (86.3 N) for the manifolds' surface area of 25 cm^2 (5x5 cm^2) and 10 lbs (44.5 N) for the button cell manifolds' surface area of 12.57 cm^2 (40 mm diameter).

Figure 5.5 shows the gas delivery system for a cell area of 5x5 cm^2 in (a) and for SOFC button cells in (b). In the framework of this project, gas manifolds for SOFC button cells had been developed to allow performance testing of the deposited AFLs, which will be described in more detail at the end of this chapter.
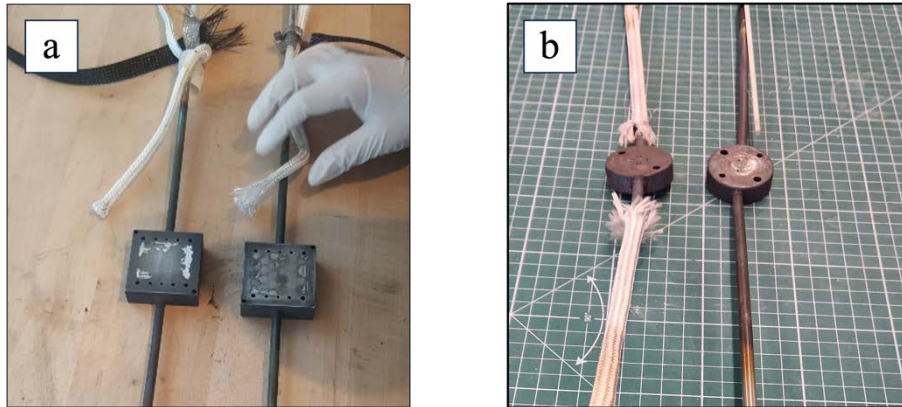
Figure 5.5: Gas delivery systems: manifold for cell area of 5x5 cm^2 (a) and in-house made manifolds for SOFC button cell testing.

5.2.2   Cell assembly

5.2.2.1   *NextCell – 5 x 5 cm^2 SOFC assembly*

In order to carry out cell performance tests using the supplied manifolds and the SOFC test fixture, the fuel cell has to be prepared to ensure good contact with the current collectors and proper sealing of the cell.

Figure 5.6 depicts each step (1-12) of the procedure to assemble a 5 x 5 cm^2 SOFC, hereinafter referred to as NextCell, according to the manufacturer's guidelines.
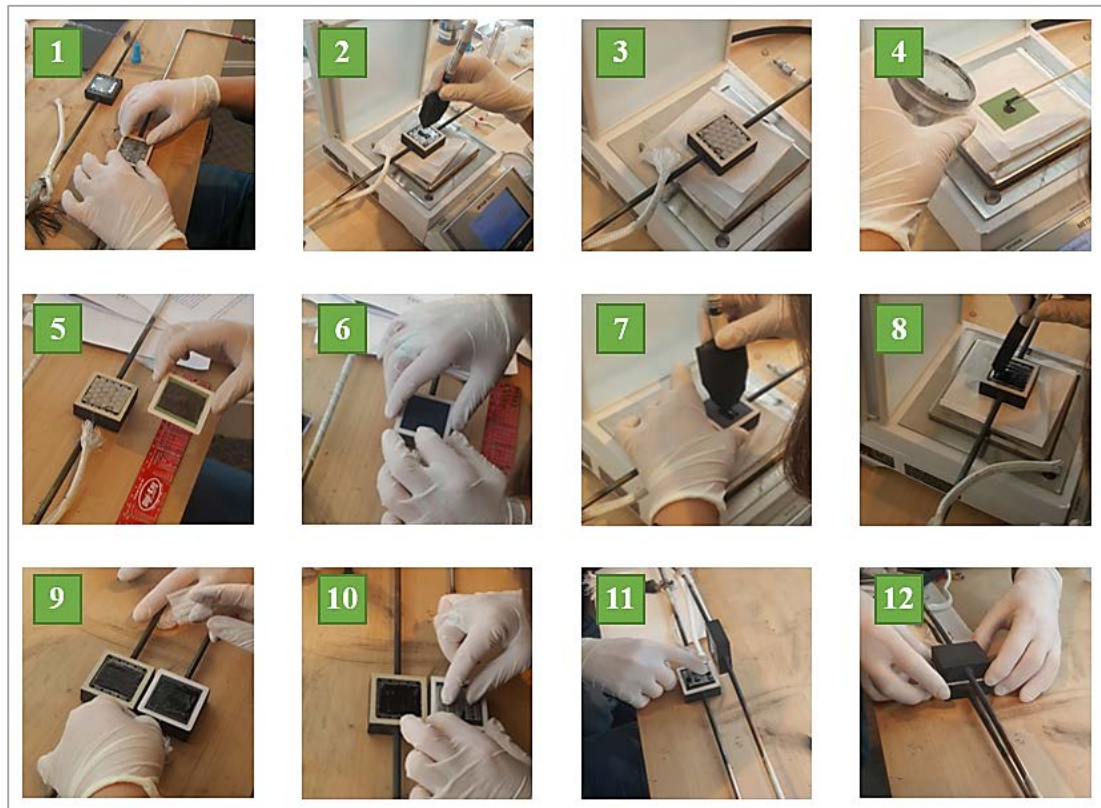
Figure 5.6: The procedure for assembling a cell with an area of 5x5 cm^2 (NextCell) when using the 855-test fixture.

Firstly, a seal is placed on the cathode and anode manifolds by applying little drops of super glue (cyanoacrylate) in each corner (1). Secondly, 0.5 grams of Ni ink is spread homogenously over the surface of the anode manifold (3), while the gas flow ports remain free from the ink (2). A nickel mesh is then placed on the active area (3) so that the raised patterns of the Ni mesh are facing upwards. In the next step, another 0.5 grams of Ni ink is applied onto the anode active area of the fuel cell (4-5). While placing the platinum wire (voltage sense –) onto the Ni mesh on the anode manifold, the anode side of the cell is aligned against the wire and the Ni mesh (5-6). After that, 0.75 grams of lanthanum strontium manganite (LSM) ink is applied onto the up-facing cathode active area (7). Another 0.5 grams of LSM ink is used to coat the cathode manifold area (8). The second platinum wire (voltage sense +) is placed onto the cath-ode active side of the cell and then, a silver mesh is applied on top so that its channels are parallel to the manifold tubes (9-10). Finally, the cathode manifold (coated with LSM ink) is aligned with the anode manifold (11-12) [135].

5.2.2.2   Button cell assembly

The button cell assembly follows the above-described procedure for the NextCell. Major differences include the geometry of the gasket, of the current collector meshes and of the gas ports for the active area of the button cell. Figure 5.7 illustrates each individual step to assemble a SOFC button cell.
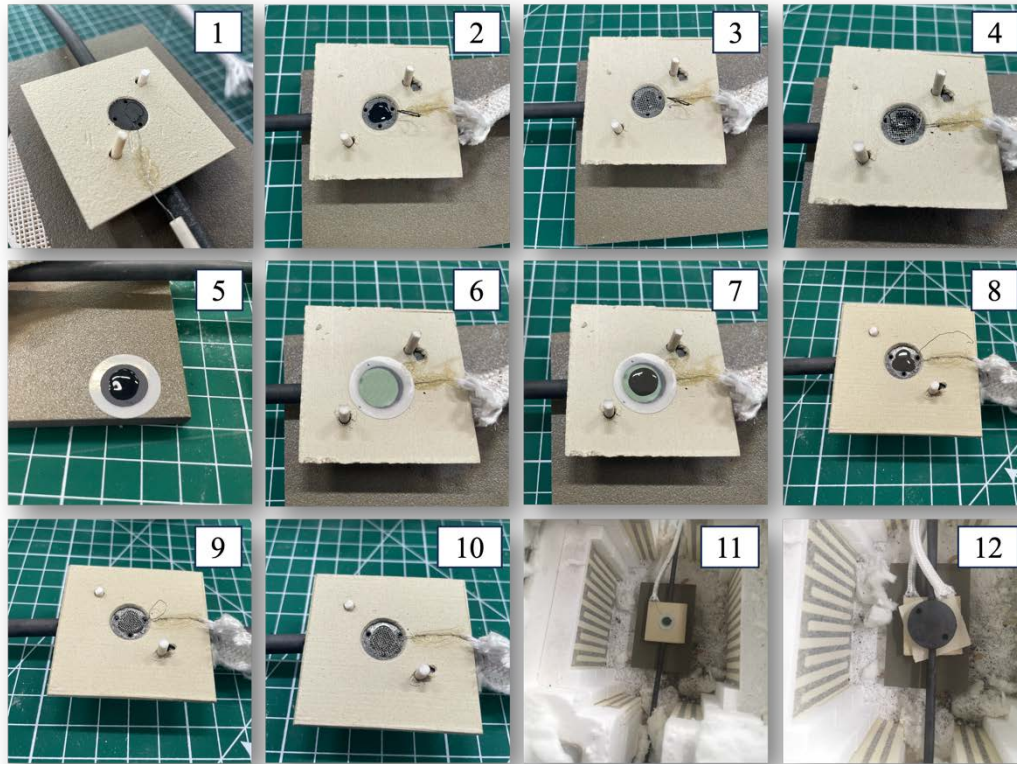
Figure 5.7: The procedure of the button cell assembly when using the 855-test fixture.

Firstly, two gaskets were prepared by cutting out an area of 5 x 5 cm^2 of a *Thermiculite* sheet supplied by *Flexitallic UK Ltd*. A hole was cut out of each gasket for the catalyst active area of the anode and cathode using a hole puncher with a 12 mm diameter. The gaskets were fixed onto the cathode and anode manifolds by applying little drops of super glue (cyanoacrylate) (1). Secondly, a small amount of LSM ink was deposited homogeneously over the surface of the cathode manifold using a glass rod, while the gas flow ports remained free from the ink (2). A silver mesh was then positioned on top of the ink layer (3), followed by placing the platinum wire (voltage sense +) onto the Ag mesh (4). The Pt wire was held in place by applying additional super glue on the gasket material; the remaining glue had been burned out during the consecutive heating cycle. In the next step, additional LSM ink was applied onto the cathode active

area of the fuel cell (5), which was then carefully turned and pressed against the wire and the Ag mesh (6) so that the anode was facing up. After that, small amounts of Ni ink were deposited onto the anode active area of the cell (7) and on the anode manifold area (8). A Ni mesh and the second platinum wire (voltage sense –) were positioned on the anode manifold. The voltage senses were parallel to the manifold tubes, avoiding contact with each other. After placing the cathode manifold (coated with LSM ink) into the furnace (11), the anode manifold (gas channels facing downwards) was aligned with it (12). The last steps included putting the furnace gasket in place to avoid heat losses and securing the furnace lid on top of the furnace by tightening the collar screws so that the compression system to the cell assembly could be applied.

5.2.3 Cell conditioning

5.2.3.1 NextCell conditioning

In order to achieve the test system to the required temperature, the test fixture was heated to 850 ºC at a ramp rate of 1 ºC/min, while purging a flowrate of 150 sccm nitrogen (N_2 purity N4.8, 99.998%) on the anode to avoid further oxidation. The cathode was supplied with 150 sccm oxygen (O_2 purity N2.6, 99.6%) during heat-up.

Prior to the performance testing, the cell requires conditioning by reducing NiO to catalytically active nickel. For that reason, an anode-forming process was conducted, where the hydrogen flow rate was successively increased, while the nitrogen flow decreased, according to Table 5.1. As a result, the final feed streams for the anode and the cathode of the NextCell were 225 sccm hydrogen (H_2 purity N5, 99.999%) and 750 sccm oxygen (O_2 purity N2.6, 99.6%), respectively.

Table 5.1: Anode forming process for Next Cell with surface area of 5 x 5 cm^2 (cell reduction).

Step	Duration [min]	Anode flow rate		Cathode flow rate
		Nitrogen [sccm]	Hydrogen [sccm]	Air [sccm]
1	25	150	50	250
2	10	150	75	250
3	10	100	125	420
4	10	50	175	580
5	30	0	225	750

5.2.3.2 Button cell conditioning

The cell conditioning of the SOFC button cell requires substantially lower flow rates in the range of 25 sccm for 25 % H_2 in N_2, when considering a target flow rate of 100 sccm hydrogen. Since the existing mass flow controllers in the 855 SOFC test station operate at a range of 1000 sccm, the minimum flow rate yielded 50 sccm. For that reason, the anode reduction process steps were reduced to two steps, increasing the hydrogen flow in nitrogen from 50 % to 100 %, while allowing the system to stabilise over 60 minutes, as shown in the table below.

Table 5.2: Anode forming process (cell reduction).

| Step | Duration [min] | Anode flow rate | | Cathode flow rate |
		Nitrogen [sccm]	Hydrogen [sccm]	Oxygen [sccm]
1	60	50	50	100
2	60	0	100	100

5.2.4 Cell testing

5.2.4.1 NextCell testing

While the 855 test system controlled both the reactant gas streams and the furnace temperature, a potentiostat (*855, Scribner, USA*) was used to perform galvanostatic linear sweep voltammetry (LSV) at a scan rate of 0.2 mA/s, acquiring characteristic performance data of the commercial SOFC. Electrochemical impedance spectra were obtained at a frequency between 10 kHz and 0.1 Hz, under conditions similar to those of the polarisation curves at 3 and 5 psi (20.7 and 34.5 kPa).

The NextCell was used in these experiments to determine optimal operation conditions for future SOFC testing regarding compression, flow design (*i.e.*, counter flow or co-flow between inlet and outlet of both reactants), temperature and flow rates. Firstly, the influence of the compression of the cell assembly on the results has been analysed by recording the polarisation curve at a compression load of 12 and 20 lbs, respectively, resulting in 3 and 5 psi (20.7 and 34.5 kPa) for a cell area of 25 cm^2. Secondly, the impact of the gas delivery system on the cell performance was measured. The arrangement of the gas inlets was changed from co-flow to counter-flow by swapping the air inlet and outlet fittings. After that, polarisation curves were recorded at 750 ºC and 850 ºC to determine the effect of the operation temperature on the performance of

the NextCell. Finally, the performance was studied at various flow rates of 300, 600 and 900 sccm for both, hydrogen (H_2 purity N5, 99.999%) and air.

In this work, fitting of the impedance spectra was performed in *Zplot*, applying an ECM for SOFC button cells from [31], which applied two Voigt elements for the electrochemical charge-transfer at the anode/electrolyte and at the cathode/electrolyte interface as well as an ohmic ion transport resistance (R_I) for the electrolyte . An inductor (L_I) was added to the circuit to describe the impedance loops under the x-axis at very high frequencies, which results from the wire connections in the set-up [31].

Detailed results of these experiments are presented and discussed in Appendix B.

5.2.4.2 *In-house button cell testing*

While using the in-house button cell manifolds in the 855 test system, the reactant gas streams were set to 100 sccm hydrogen (H_2 purity N5, 99.999%) and 100 sccm oxygen (O_2 purity 2.6, 99.6%) for the anode and cathode, respectively. Polarisation curves were obtained by galvanostatic linear sweep voltammetry (LSV) at a scan rate of 0.2 mAs^{-1} using the potentiostat (*885, Scribner, USA*) to determine the peak power density of the deposited AFLs.

5.2.4.3 *Outsourced button cell testing*

While the in-house button cell testing was developed, the performance testing of deposited Ni-YSZ AFLs in chapter 8 was outsourced using the facility at Imperial College London according to the methodology from [136]. The gas lines for inlet and exhaust were attached to anode and cathode. Pt wires with 0.4 mm diameter for voltage senses were connected following a two-electrode configuration, where the working electrode (WE) and working sense were connected to the Pt wire of the anode (–), and counter electrode (CE) and reference electrode (RE) connected to the cathode wire (+), as shown in Figure 5.8.
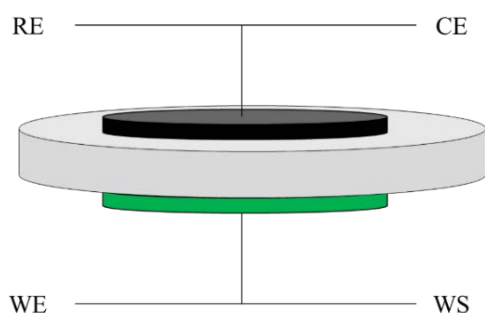
Figure 5.8: Two-electrode configuration for SOFC testing, showing working electrode (WE), working sense (WS), counter electrode (CE), and reference electrode (RE).

Contact paste of nickel and silver was applied to the anode and cathode, respectively, using silver meshes as current collectors. The cell was sealed on one end (*i.e.,* the anode) onto a 25 mm outer diameter alumina tube using a ceramic adhesive (*Adhesive 668, Aremco, USA*). Cell conditioning was performed in 10% H_2/Ar atmosphere for 18h at 700 ºC.

Polarisation curves were acquired at 850 ºC using a potentiostat (*PGSTAT302N, Eco-chemie, Metrohm, The Netherlands*) with a scan rate of 20 mVs^{-1} and constant flow rates for 3%-humidified hydrogen (H_2 purity N5, 99.999%) and air of 100 and 200 sccm, respectively.

5.2.4.4 Development of a gas delivery system for button cell testing

As mentioned before (cf. section 1.2), the development of an in-house SOFC testing rig for button cells was part of this work, resulting in designing a new concept for the gas manifold. This design must ensure that the button cell is properly sealed and still allows pathways for the gas streams and current collection (Pt wires and current collectors).

Figure 5.9 illustrates the dimensions of the commercial gas manifolds for SOFCs with a total surface area of 25 cm^2 and catalyst surface area of 16 cm^2. When calculating the cross-sectional surface area of the gas ports for the reactant using the presented diameters, the ratio between the gas inlet/outlet and the catalyst surface area is 0.03.

Catalyst surface area CSA for NextCell: 1600 mm^2
Cross-sectional area for reactant gas stream XA: 50 mm^2

Ratio between CSA and XA: <u>0.03</u>
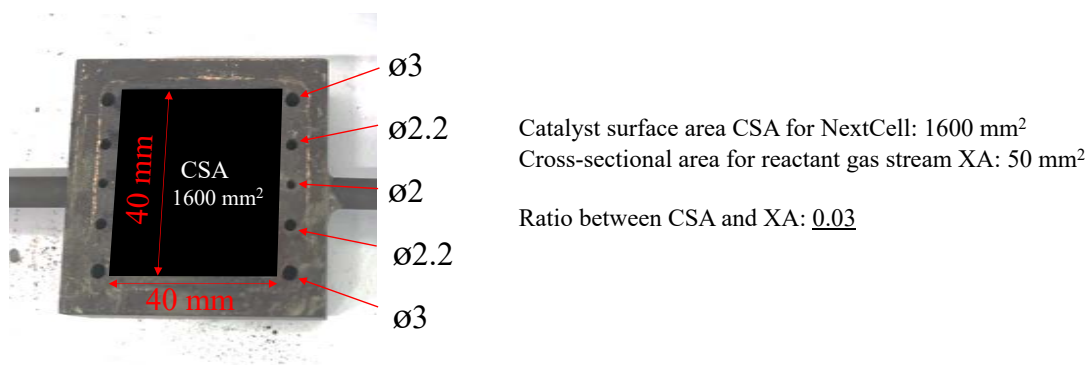
Figure 5.9: Geometrical manifold design of commercial gas manifolds from *fuelcell-materials, USA*, showing gas port dimensions and catalyst surface area.

Reducing the catalyst surface area from the NextCell to the SOFC button cell with 12 mm diameter yields a cross-sectional area of 3.5 mm^2 for the reactant gas streams, resulting in three gas ports with 1.3 mm diameter (minimum available drill bit) to achieve a cross-sectional area of 4 mm^2.

In order to facilitate sufficient stability to utilise the compression system for anode and cathode in the 855 test station, an outer dimension of 40 mm was chosen for the size of the manifolds. The concept for the manifold design with three gas ports is presented in the technical drawing in Figure 5.10.

Further details and dimensions can be found in the complete technical drawing in Appendix D.
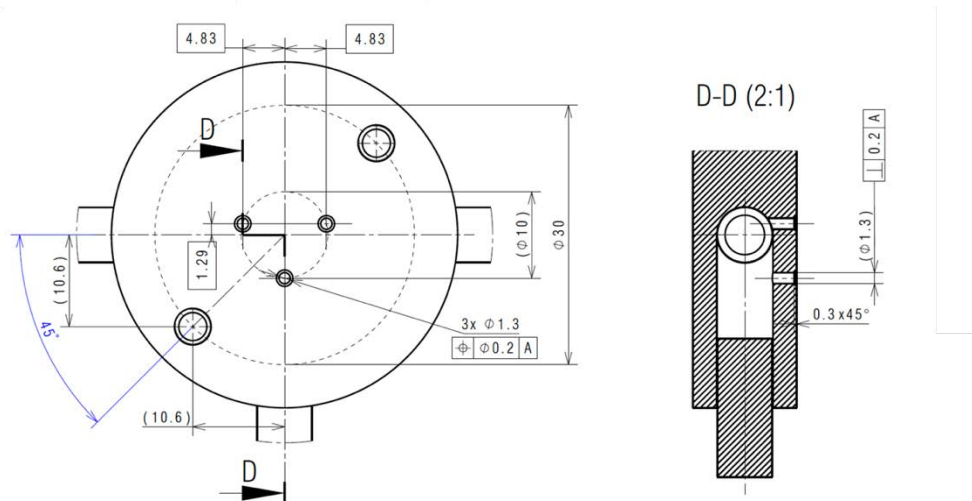
Figure 5.10: Technical drawing of gas manifolds with three gas ports for SOFC button cells.

Figure 5.11 shows the fabricated gas manifolds derived from the technical drawing above.

Figure 5.11: In-house designed gas manifolds for SOFC button cell. CAD design (a) and in-house fabricated manifold (b).

Commercial SOFC button cells (*fuelcellmaterials, USA*) had been used during the commissioning of these gas manifolds, in order to ensure optimal condition for cell testing and to generate reference data for future experiments. The results can be found in Appendix E.

6 Analytical techniques

This chapter describes the principles of the material characterisation techniques, such as scanning electron microscopy (SEM), energy-dispersive X-ray spectroscopy (EDS), and X-ray diffraction (XRD), which were used to analyse deposited coatings concerning their microstructure, composition, oxidation state, degree of elemental dispersion and crystallinity.

6.1 Scanning electron microscopy

The use of scanning electron microscopy (SEM) leads to a generation of highly magnified images of a material's surface and its cross-section. This results in acquiring information of the material's microstructure in terms of density, topography, and defects. The working principle is presented in Figure 6.1.

Primary electrons are accelerated towards a sample from an electron gun, which raster scans a small rectangular area of the sample. These incident electrons interact with the sample surface, resulting in the emission of secondary electrons, backscattered electrons, and characteristic X-rays. Scattered electrons with energies below 50 eV are assigned to secondary electrons (SE), whereas high-energy electrons above 50 eV are considered backscattered electrons (BSE). While BSEs are backscattered through elastic interactions between the electron beam and the sample itself, SEs are based on inelastic interactions. The scattered electrons can further be classified into i) SE1, ii) SE2, and iii) SE3. Electrons of group SE1 are directly emitted at a high angle from the incident electron beam. Backscattered electrons leaving the sample belong to group SE2 electrons, which undergo deeper interactions with the sample material. SE3 are generated when backscattered electrons contact the chamber's interior surfaces after leaving the sample.

The scattered electrons are collected by an appropriate detector, which transforms the signal into an image with different contrast caused by differences in the analysed elements [137, pp. 70–75]. In BSE images, material phases of heavier atoms appear brighter, as heavier elements scatter the electrons significantly stronger, leading to a stronger signal [138]. For instance, while imaging a cross-section of a Ni-YSZ film, the YSZ phase will appear brighter than nickel, since zirconium and yttrium are stronger scatterers.
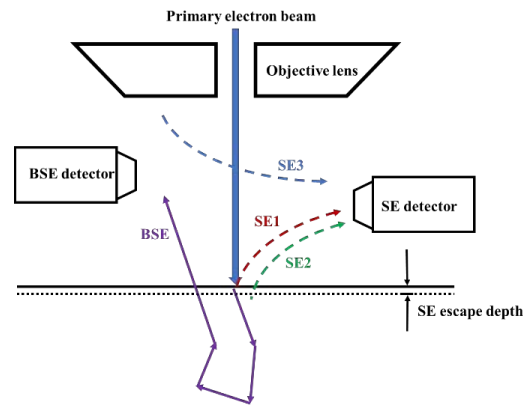
Figure 6.1: Principle of SEM, adapted from [139].

To analyse microstructural features in this work, SE images of thin film's top surfaces and cross sections were generated with a 2 kV electron beam, while BSE images were created by applying 20 and 10 kV. Both SE and BSE images were obtained from a Supra 40 VP-FEG-SEM *(Carl Zeiss Ltd.)* and a FIB-SEM Crossbeam 350 *(Carl Zeiss Ltd.)*.

6.2   Energy-dispersive X-ray spectroscopy

The analysis of the composition and elemental distribution of elements in a material is carried out using energy-dispersive X-ray spectroscopy (EDS) with silicon drift detectors. The principle behind EDS is illustrated in Figure 6.2.
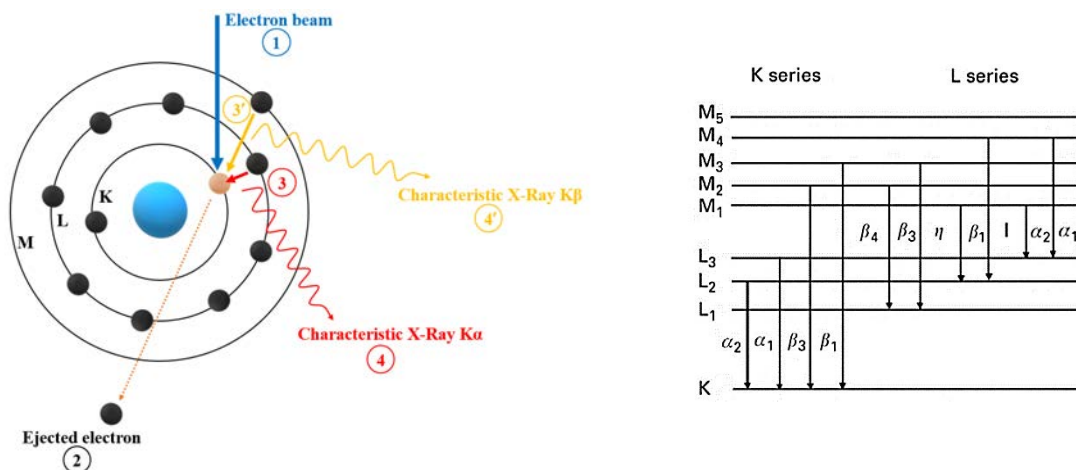
Figure 6.2: Schematic of the working principle of EDS adapted from the literature [140].

As mentioned before, the primary electrons from the electron beam in the SEM (1) are used as an energy source to interact with the sample. When an inner shell electron of the sample material is ejected during the electron bombardment (2), consequently, an outer shell electron from the L_3 (3) or M_3 (3') shell replaces the hole at the lower

energy level by emitting a characteristic X-ray photon (4 or 4'). Considering an ionisation of the K_1 shell, an electron from the L_3 shell will replace the removed electron, emitting a characteristic $K\alpha_1$ X-ray. A characteristic X-ray $K\beta_1$ occurs when this vacant inner shell is filled by an electron from the M_3 shell [137, p. 122].

An X-ray detector collects the X-rays and converts the signal into an energy spectrum, as depicted in Figure 6.3.
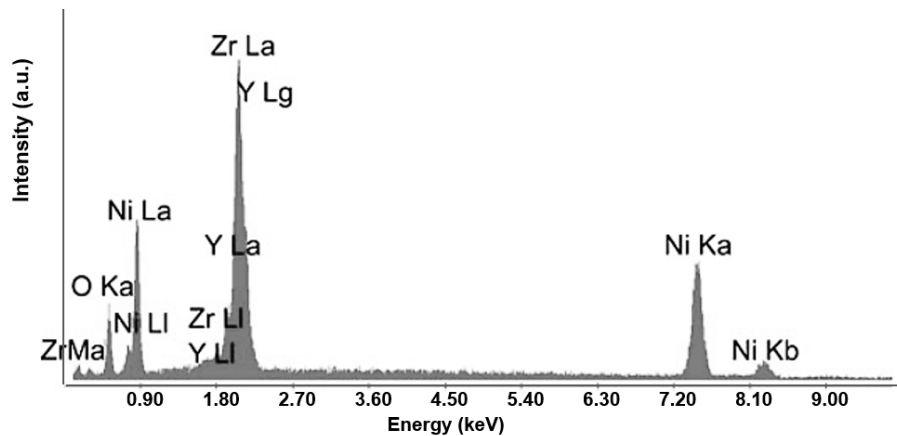
Figure 6.3: Typical EDS spectra from a reduced Ni/YSZ anode from the literature [140].

The series of characteristic peaks are assigned to the elements by their peak IDs (*i.e.,* the energy of characteristic X-rays) and the elemental weight and/or atomic percentages are calculated from the intensity of each peak. For instance, the Kα and Lα peaks of zirconium yield energies of 15.744 and 2.042 keV, respectively. Hence, the peak at around 2 keV in the above chart results from zirconium (Lα X-ray).

Furthermore, elemental mapping images that show the distribution of the elements can be produced by EDS analysis over a selected region of interest. In the framework of this project, the use of element mapping will facilitate the analysis of the created SOFC nanostructures, for example in terms of elemental distribution.

The composition of deposited films used in this work was quantified on an imaged area of approximately 100 μm^2 under an acceleration voltage of 20 kV using a Quantax 75 from *Bruker Corporation* with a self-calibrating P/B-ZAF correction (*i.e.,* no system calibration measurement required). Elemental maps were generated under an acceleration voltage of 20 kV using an Ultim Max 170 from *Oxford Instruments plc*.

6.3 X-ray diffraction

To identify crystalline phases, the crystallite orientation, and crystallite size, X-ray diffraction (XRD) was conducted.

The fundamentals of XRD are based on Bragg's law, which is presented in Figure 6.4. During XRD analysis, two in-phase X-ray beams 1 and 2 with a typical wavelength of 0.05−0.2 nm are emitted towards a sample with an incident angle θ. The crystalline material comprises lattice planes with spacing d_{hkl}, where the X-rays are being scattered. When the resulting phase-shift of beam 2, represented by the path length $\overline{ADC}$, is proportional to the wavelength (*i.e.,* $\overline{ADC} = n\lambda$), the diffracted beam forms a diffraction angle of 2θ with the incident beam, resulting in constructive interference [141, p. 90].

Bragg's law is derived using trigonometric formulas on the triangle ABD with the angle θ.
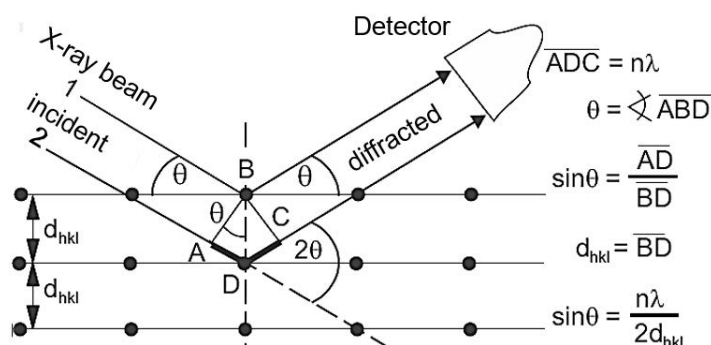
Figure 6.4: XRD principle according to Bragg's law, adapted from [141, p. 90].

The constructive interference is detected by the X-ray detector and yields a diffraction peak of high intensity. The intensity of these diffraction peaks is plotted against the diffraction angle 2θ in an XRD spectrum. The position of the diffraction peak depends on the material and the orientation of the crystal in the sample. When calculating the spacing of the lattice planes (d_{hlk}), the material phases are identified using the Crystallography Open Database. The orientation of these lattice planes is defined by the Miller indices (*hkl*), which represent the reciprocal intercepts of the plane with the three axes a, b, and c of a unit cell (*i.e.*, a=b=c for a cubic crystal unit cell) [137, pp. 200–202].

Figure 6.5 shows the XRD pattern before and after the annealing of a deposited NiO-YSZ anode produced by magnetron sputtering [142]. The as-deposited films did not

exhibit well-crystallised structures. However, sharp characteristic peaks were obtained after post-deposition heat treatment.
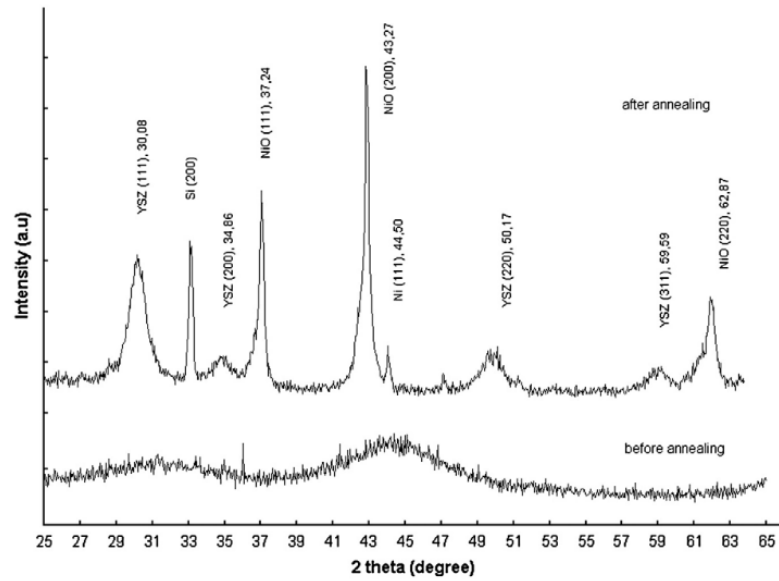
Figure 6.5: XRD pattern of NiO-YSZ film before and after annealing at 900 ºC [142].

Furthermore, XRD patterns can determine the actual strain in materials, leading to the analysis of the stress condition, *e.g.*, residual stresses in deposited films. Due to these mechanical stresses, the d-spacing of a crystal changes from $d_{hkl,0}$ to d_{hkl}, as shown in Figure 6.6. Typical changes in Bragg's angle range from 0.01° to 0.5°.
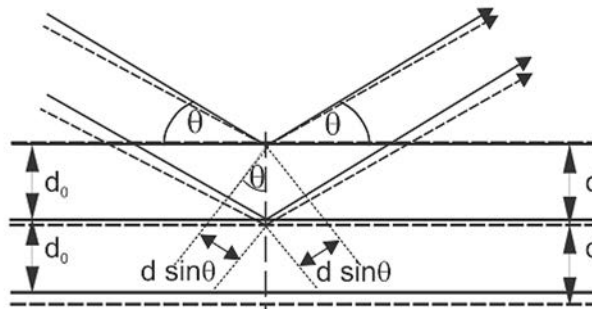
Figure 6.6: XRD with unstrained d-spacing $d_{hkl,0}$ (solid lines) and strained d-spacing d_{hkl} (dashed lines) [141, p. 333].

The strain can be calculated using equation 6.1 as follows [141, p. 333]:

$$\Delta\theta = -\varepsilon \, tan \, \theta \, \frac{180°}{\pi} \qquad\qquad 6.1$$

where θ is Bragg's angle, $\Delta\theta$ represents the change in Bragg's angle caused by the mechanical stresses and ε is the strain perpendicular to the lattice plane derived from $(d_{hlk} - d_{hlk,0})/d_{hlk,0}$.

The shape of the diffraction peaks can give further insights into imperfections or inhomogeneous strains. The latter can cause a broadening of the diffraction peaks, which accumulates with increasing *sin θ* [137, p. 207].

If the XRD pattern presents sharp high-intensity peaks, the crystal grain size D can be calculated from the diffraction peaks using the Scherrer formula in equation 6.2:

$$D = \frac{K\lambda}{FWHM \cdot cos\theta} \qquad\qquad 6.2$$

where *K* is the Scherrer constant, ranging from 0.62-2.08 (typical *K* = 0.89, for cubic Ni *K* = 0.94), *λ* is the wavelength of the X-ray, *FWHM* is the full width at half maximum of the diffraction peak and *θ* is the diffraction angle.

In this work, the deposited films were characterised by X-ray diffraction. Measurements in chapter 7 and 8 were obtained from a PANalytical X'pert powder X-ray diffractometer with Cu Kα radiation (*λ* = 0.1540598 nm) at 40 kV/30 mA. The diffraction patterns were recorded in grazing incidence mode at 1° with *2θ* in the range of 10−90° in steps of 0.05° 2θ at 3.52 s per step. XRD results presented in chapter 9 were acquired using Cu Kα radiation (λ= 1.540596Å) at 40 kV/40 mA on a Bruker D8 Advance in grazing-incidence diffraction mode. The samples were mounted on a compact cradle and the sample height optimisation and rocking curve scans were carried out before analysis. Data was collected in the range 10−100° 2θ with a step size of 0.04° 2θ at a step time of 0.2 s per step.

Phase identification was performed using the background subtraction and the search-match function in the HighScore Plus software against the Crystallography Open Database.

6.4 X-ray photoelectron spectroscopy

X-ray photon electron spectroscopy (XPS) was used as an analytical technique to determine the material's surface chemistry of deposited films. The principle is based on bombarding a sample material with soft monoenergetic (fixed wavelength) X-rays, causing the emission of core-level electrons, so-called photoelectrons, from the atoms in the sample. By measuring the kinetic energy of the detected photoelectrons, their binding energy can be determined according to Einstein's photoelectric law:

$$KE = h\nu - BE \qquad\qquad 6.3$$

where *KE* is the measured kinetic energy of the photoelectron, *BE* is the binding energy of the material's electron from its atomic orbital and *hv* is the known photon's energy. After calculating the core-level binding energy ($hv - KE$), the material's atoms and chemical state can be analysed and identified using databases from [143], [144], [145], [146], [147].

An electron spectrometer is used to detect the electrons ejected from the sample, allowing only electrons within a fixed energy window, *i.e.*, the pass energy, to enter the energy analyser (hemispherical electron energy analyser), as shown in Figure 6.7. This is achieved by applying an electrostatic field before the energy analyser, leading to a constant energy resolution for the data acquisition.
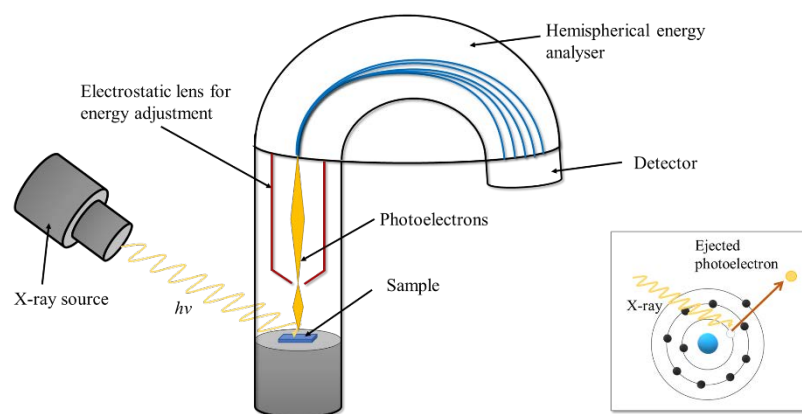
Figure 6.7: Principle of XPS.

The oxidation state of the deposited films in this work was determined using an X-ray photoelectron spectrometer from the *Kratos Axis Supra system*, equipped with a monochromated Al Kα_1 X-ray excitation source (*hv* = 1486.6 eV). Survey scans were obtained using a slot collimator with an analysis area of 300 x 700 microns with a pass energy of 160 eV and region scans at passing energy of 20 eV and 40 eV. For reference, the FWHM of the Ag 3d$_{5/2}$ peak using a pass energy of 40 eV was 0.71 eV. XPS analysis on as-deposited samples was repeated after sputter cleaning with an ion gun at 5 keV Ar+ for 30 s.

Peak model fitting was carried out in the software *CasaXPS*. All peaks were charge corrected to the acquired C 1s region scan, in which a linear background was used, and the adventitious carbon peak (C-C) position was adjusted to A = 284.5 eV, using position constraints of A+1.2, A+3, and A+4 for the remaining peaks of C-O-C, C=O, and O-C=O, respectively, to enable appropriate fitting parameters. Since Ni spectra are complex, their analysis was carried out according to comprehensive studies of

Biesinger *et al.* on mixed Ni metal and oxide systems, using a Shirley background with an offset of 2 and an average width of 5. Symmetric line shapes were applied to oxides using a Gaussian-Lorentzian function with a respective ratio of 70:30 and asymmetric line shapes for metals (metallic nickel) (LA(1.53,243)) [147].

6.5 Scanning transmission electron microscopy

Scanning transmission electron microscopy (STEM) was used to analyse the particle size and elemental distribution of the coatings. Since the technique offers high spectral resolution and accurate elemental detection it was employed in this study to investigate the incorporation of dopants within the deposited doped Ni-YSZ films.

In conventional transmission electron microscopy (TEM), a thin sample (usually less than 500 nm) of approx. 3 mm diameter is penetrated by a very high monoenergetic electron beam with energies from 100 to 400 keV [148]. Compared to SEM, which detects scattered electrons, TEM collects the transmitted electrons that pass through the sample thickness, acquiring structural information about the sample. Multiple electromagnetic lenses are used to accelerate the electrons to high potentials and focus on the sample's region of interest, allowing for spatial magnifications of up to 1,000,000 and resolution better than 0.2 nm [137]. Two operation modes can be used: (i) diffraction and (ii) imaging mode. In diffraction mode, electrons are diffracted on crystalline regions, creating a diffraction pattern that gives information about the sample's crystal structure, *i.e.*, crystalline phase, orientation, and lattice parameters [148]. In imaging mode, two types of images can be formed by the collected electrons: bright field images (BF) are obtained from transmitted electrons with little or no change in their angle (undeviating), and dark field images (DF) result from scattered and diffracted electrons by the sample material [106].

STEM is a particular form of TEM and can be performed by three different types of instruments: (i) a modified TEM instrument that can operate in STEM mode, (ii) an SEM instrument that achieves high resolutions modified for STEM or (iii) STEM instruments [137]. In STEM, the electron beam is focused on a smaller spot size (minimum 3 Å). Figure 6.8a illustrates the interaction between the electron beam and a sample, resulting in the emission of various signals, such as scattered and diffracted electrons for DF and undeviating electrons for BF imaging and characteristic X-rays for EDS analysis (cf. section 6.2), that can be collected by appropriate detectors (Figure 6.8b). Some STEMs are equipped with an annular dark-field detector that only collects

electrons that scatter in high angles, greater than 80 milliradians, allowing imaging of individual atoms as well as compositional information. For instance, Garcia-Garcia *et al.* presented cross-section images of a GDC-doped Ni-YSZ reduced film using high-angle annular dark-field STEM (HAADF-STEM), showing the particle size and elemental distribution of nickel, cerium, gadolinium, zirconium, and yttrium [149].
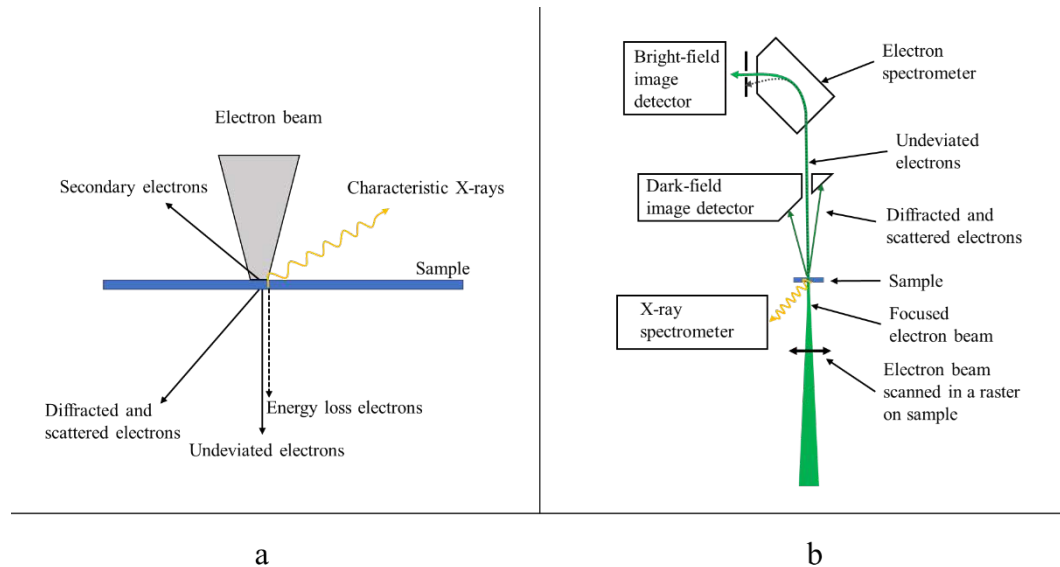
Figure 6.8: STEM: Interaction between a sample and the electron beam (a), Schematic of STEM instrument with various detectors for emitted signals (b), adapted from [137].

In this work, the TEM analysis of the cross-sections of vanadium-doped Ni-YSZ films that underwent annealing and subsequent reduction in hydrogen atmosphere was outsourced at the University of Manchester. The samples were prepared via FIB-SEM FIB (FEI Helios Nanolab 660 focussed ion beam with a Ga ion accelerating voltage of 30 kV) for lamella extraction (100 nm) according to the methodology described by Langford and Long [150]. Subsequently, the lamellae were analysed via HAADF-STEM (High-angle annular dark-field scanning transmission electron microscopy) at 300 kV (FEI, Tecnai G2 TF30). Elemental maps were collected using EDX spectroscopy on an Oxford Instruments X-Max T 80.

6.6   Optical profilometry

Before coating deposition, a strip of Kapton tape was affixed to the sample surface, such that when removed it would leave an uncoated area for thickness measurements of the deposited films using the so-called step height method.

The deposition rates are directly calculated when dividing a measured thickness of the coating by the deposition time. Thickness measurements were performed using Profilm3D optical profilometer from *Filmetrics*. The Profilm3D is based on white light interferometry (WLI) to analyse surface profiles in the range of 50 nm up to 10 mm and is equipped with 10x and 50x Nikon objective lenses.

The principle of WLI is shown in Figure 6.9.
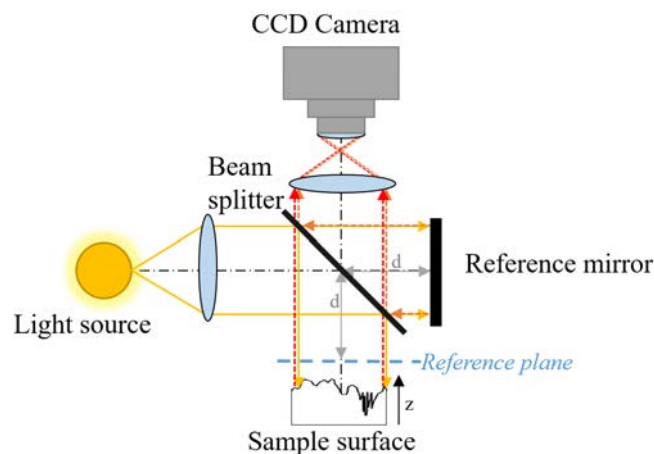
Figure 6.9: Principle of WLI for thickness measurements, adapted from the literature [151].

The light emitted from a light source is divided into a reference and a measuring beam (yellow arrows) by a beam splitter. While the reference beam is reflected by the reference mirror (orange arrows), the measuring beam is reflected at the surface of the measured sample (red arrows). The travelling reflected beams pass to a charge-couple device (CCD) camera, which detects the incoming beams. The beams are superimposed and depending on whether they are in-phase ($2n\pi$) or out-of-phase ($(2n+1)\lambda$), constructive or deconstructive interference occurs, respectively. The sample is moved vertically to cross a reference plane (Figure 6.9, dashed horizontal line), resulting in interference signals with different intensities for each pixel of the CCD camera. Since the distance between the reference mirror and the beam splitter is identical to the distance between the reference plane and the beam splitter, the interference signal reaches its maximum. Correlating the z-position of the sample with this maximum interference signal of each pixel yields a height profile of the measured sample [151], [152].

In this work, the sample thickness was measured at six positions with the 10x Nikon objective lens, *i.e.*, three successive measurements on the right and left sides of the uncoated area were averaged, as illustrated in Figure 6.10.
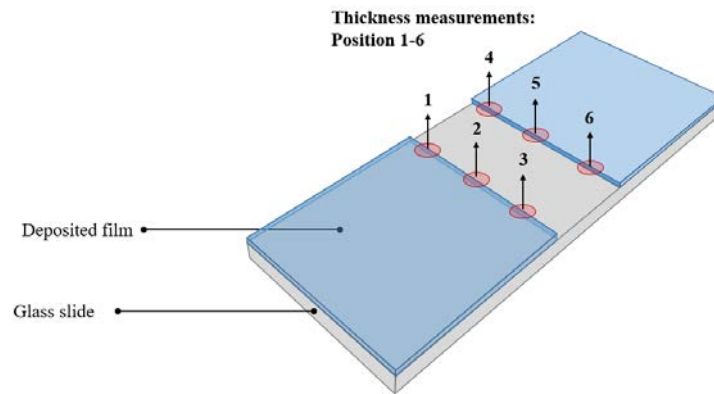
Figure 6.10: Position of thickness measurement of deposited films.

The Profilm3D software provides options to remove outlines of the surface profile and to level out any differences between the plane of the uncoated area and the sample holder. An example of the measured step height between coated and uncoated area is presented in the following figure.
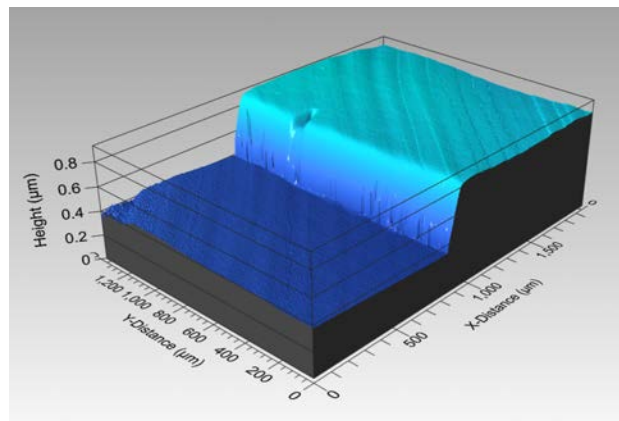
Figure 6.11: Representative thickness measurement of a YSZ coating using Profilm3D.

The mean and associated standard deviation were calculated from the thickness values of each sample to determine the resulting deposition rate of the produced coatings.

III. Results

7 The influence of process parameters on the YSZ microstructure

7.1 Introduction

As mentioned in the literature review in Chapter 2 the cermet anode, consisting of nickel and YSZ, takes on the roles of electron transport through the nickel network and oxygen ion transport through the YSZ phase. Therein, the YSZ microstructure serves as a ceramic matrix with nickel incorporated in it. For that reason, the deposition of a state-of-the-art Ni-YSZ thin film anode from metallic targets requires a fundamental understanding of the deposition of YSZ using reactive magnetron sputtering and of the related effects of deposition parameters on its microstructure. This chapter introduces the process control used to maintain a stable deposition process and presents a detailed study of the process parameters, such as deposition pressure and deposition angle, on the microstructure of deposited YSZ.

7.2 Experimental

The appropriate amount of oxygen must be determined to create films containing stoichiometric yttria-stabilised zirconia (YSZ). For that reason, hysteresis curves were conducted to study the transition between metallic and oxide modes at varying oxygen flow rates. In a hysteresis curve, either the discharge voltage, the current or the system total pressure can be plotted as a function of the reactive gas flow, i.e., oxygen.

During the hysteresis studies of zirconium-yttrium in this work, the target was tilted at 30˚ to the normal to the plane of the substrate at a target-substrate distance of 14 cm in the process chamber, as illustrated in Figure 7.1.
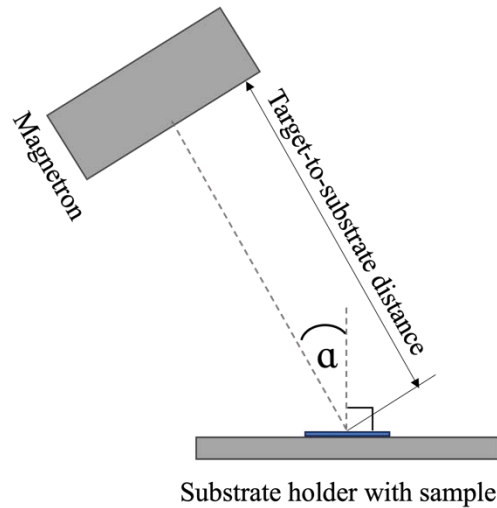
Figure 7.1: Magnetron sputtering configuration during hysteresis analysis, showing deposition angle a and target-to-substrate distance from the centre of the magnetron to the centre of the sample.

A maximum power of 250 W, at a working pressure of 0.65 Pa, was applied using a pulsed DC frequency of 75 kHz with a pulse-off time of 4 µs (70% duty) [153].

After defining an appropriate oxygen partial pressure, a parameter study was conducted investigating the effect of the deposition angle and deposition pressure on the microstructure of the YSZ films. While keeping the power, frequency and target-substrate distance constant (250 W, 75 kHz, 14 cm), the deposition angle was varied between 30°, 45° and 60° at a total pressure of 0.5 Pa, 0.7 Pa and 1 Pa, respectively. A list of the experiments with their sample IDs is given in the following table.

Table 7.1: Sample IDs for parameter study varying deposition pressure and angle.

Sample ID	Deposition pressure/ Pa	Deposition angle/ °
0.5 Pa, 30°	0.5	30
0.5 Pa, 45°	0.5	45
0.5 Pa, 60°	0.5	60
0.7 Pa, 30°	0.7	30
0.7 Pa, 45°	0.7	45
0.7 Pa, 60°	0.7	60
1 Pa, 30°	1	30
1 Pa, 45°	1	45
1 Pa, 60°	1	60

7.3 Hysteresis of YSZ

Figure 7.2 presents the variation in discharge voltage of the Zr-Y target and the system pressure with an increased oxygen flow rate.
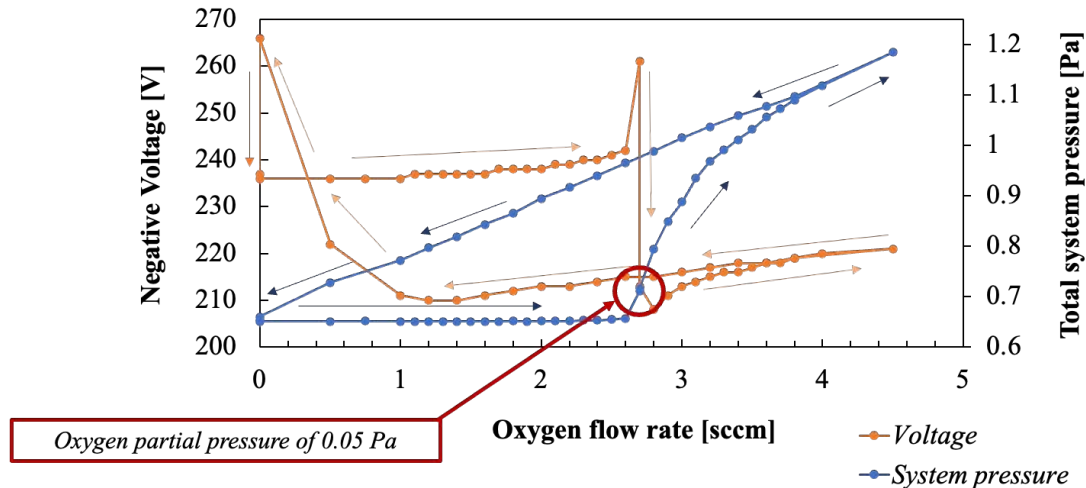
Figure 7.2: Hysteresis behaviour of Zr-Y at an applied power of 250W and a working pressure of 0.65 Pa under oxygen flow control.

The target voltage hysteresis curve shows characteristics of a purely metallic film of Zr-Y at a negative voltage of 236 V in a pure argon atmosphere. The slight increase in the discharge voltage magnitude with increasing oxygen flow is caused by a thicker insulation layer formed on the Zr-Y target surface than is seen in other materials, as shown in the literature [44], [154]. The voltage rose to a high point and peaked temporarily at -261 V, at 2.7 sccm of added oxygen, leading to an oxygen partial pressure of 0.05 Pa, before it dropped again to -208 V. That substantial voltage drop indicates the characteristic transition of the target from metallic mode to a compound mode. However, to the author's knowledge, the temporary voltage peak for the material studied has not been reported in the literature previously.

It is well known that the hysteresis behaviour of a discharge voltage in the reactive magnetron sputtering process strongly depends on the formation of an oxide layer on the target surface. In order to understand this behaviour in detail, Depla *et al.* have investigated the ion-induced secondary electron emission (ISEE) coefficient of metals and their oxides [120]. They classified the materials into two categories: (i) materials, in which the ISEE coefficient of the target increases after oxidation, resulting in a voltage drop, such as Al, Ce, Li, Mg and Y, and (ii) materials, which show a decrease in ISEE coefficient with increasing oxygen flow, leading to a voltage rise, such as Cr,

Ti and Ta. Zirconium was described by the authors as a more complex material due to the relatively insignificant difference in voltages between metallic and oxide modes, found to be only 9 V in their system. Based on their mathematical modelling, it was determined that the ISEE coefficient decreases when Zr oxidises, however, the experimental data have demonstrated an increasing ISEE coefficient for ZrO_2, which places Zr in the former class of materials [120]. Based on these findings, the sharp peak observed from the hysteresis study of Zr-Y could be attributed to either the complex characteristics of the oxidation of zirconium or the impact of yttrium alloying into the zirconium and modifying the characteristics of the target material.

As shown in Figure 7.3, transparent coatings of YSZ were created by using the direct partial pressure oxygen gas monitoring function at an oxygen partial pressure of 0.05 Pa. Thus, the sputtering was conducted at process conditions near the sharp peak in Figure 7.2 at a working pressure of 0.65 Pa, resulting in a total pressure of 0.7 Pa.
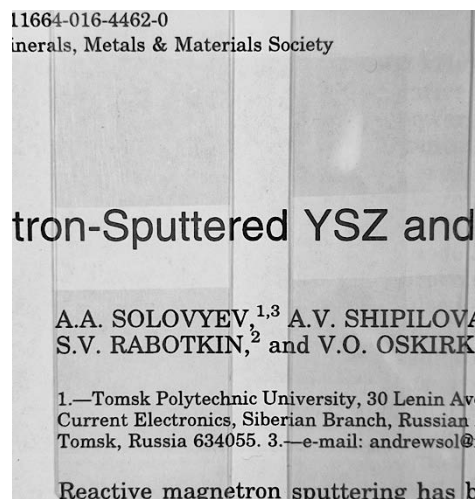
Figure 7.3: Transparent coatings of YSZ on glass slides with a thickness of ca. 275 nm after 30 min deposition at 250W, 75 kHz, 4 μs pulse-off time, 0.7 Pa total pressure and 0.05 Pa oxygen partial pressure.

7.4 Structural properties of YSZ films as a function of deposition angle and deposition pressure

7.4.1 Coating microstructure

Figure 7.4 reveals the resulting deposition rates of each experiment shown in Table 7.1.
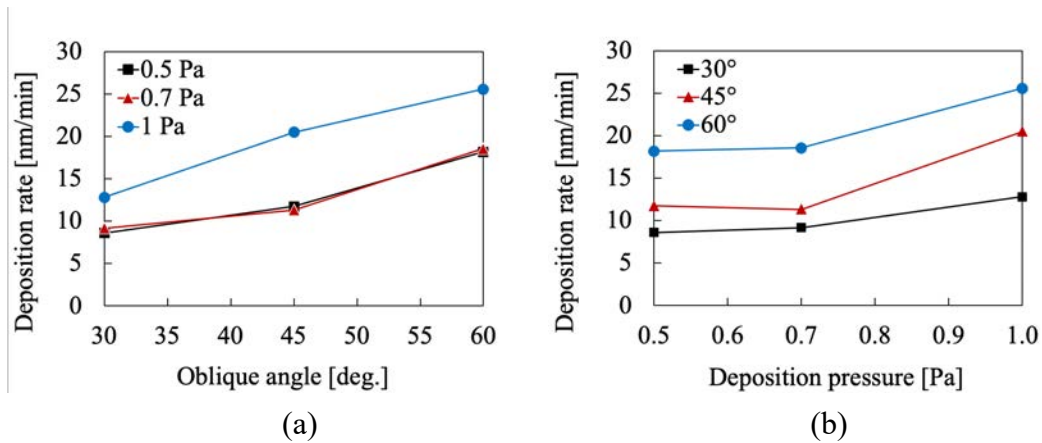
Figure 7.4: Influence of the deposition angle (normal to the substrate plane) (a) and pressure (b) on the deposition rate of the YSZ film.

From Figure 7.4a, it can be clearly seen that the increase in deposition angle from 30° to 60° leads to an increase in the deposition rate at all three pressure ranges. However, the difference in the deposition rate is not substantially affected by the deposition pressure until a relatively high pressure of 1 Pa is set in the process chamber. Figure 7.4b shows more comprehensive information about the influence of the deposition angle on the deposition rate. At an angle of 60°, the deposition rate nearly doubles, when compared with the results at 30°. In order to identify the effect of these two parameters on the structural properties, SEM images were collected from the top surface of the deposited films, as shown in Figure 7.5.
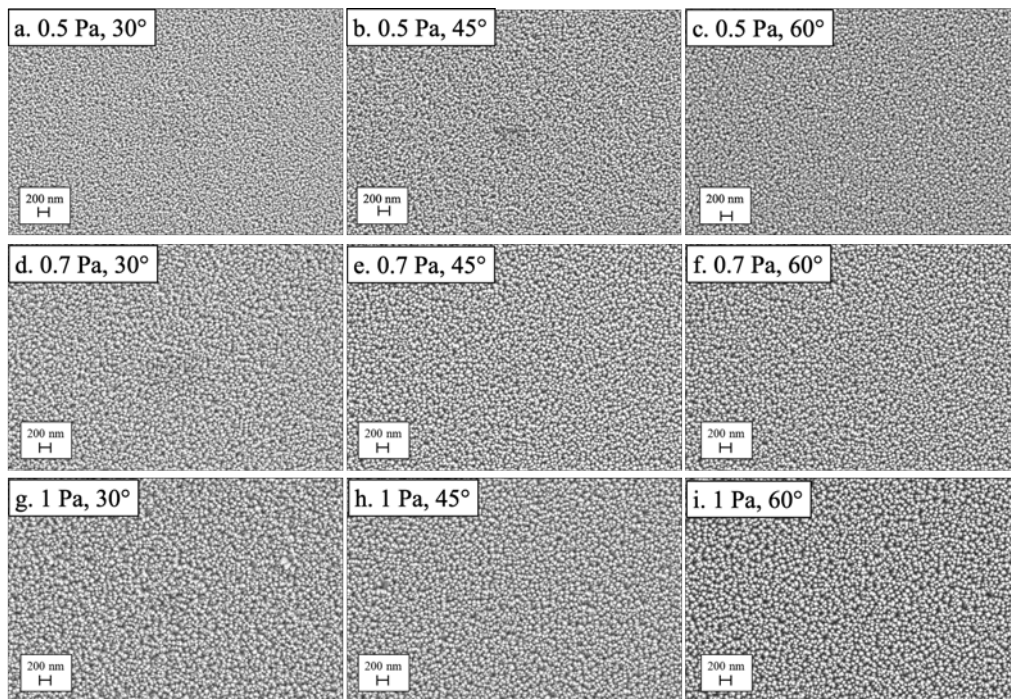
Figure 7.5: SEM images of the top surfaces of YSZ coatings at 30°, 45° and 60° deposition angles and deposition pressures of 0.5, 0.7 and 1 Pa.

First of all, the top surfaces of the deposited films exhibit a characteristic columnar architecture of YSZ, which is also confirmed by the example of the SEM cross section of the YSZ film deposited at 1 Pa and 60º in Figure 7.6.
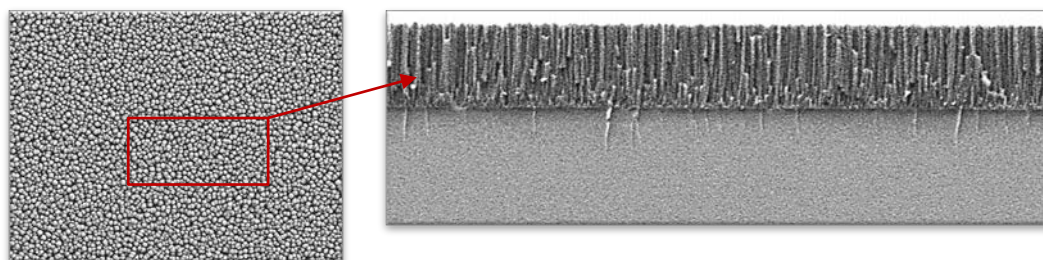
Figure 7.6: SEM images of the top and the cross section of YSZ film deposited at 1 Pa and 60º angle, showing characteristic columnar structure.

The voids between these columns vary with the deposition parameters, i.e., angle and pressure. At the lowest pressure and lower angles, no significant differences in microstructural features can be observed (Figure 7.5 a, b). However, the films' top surfaces present more distinct columns of YSZ with significantly enlarged voids at higher angles and the highest pressure (1 Pa), indicating a higher degree of porosity, (Figure 7.5 f, h, i).

To determine the difference in porosity within the YSZ films and thus, the effect of the pressure and angle on the YSZ microstructure, image processing was performed using *ImageJ* software. Since the above cross section presents vertically oriented columns, the next steps are to estimate a theoretical porosity based on the top surface images, assuming ideal straight columnar growth from the substrate to the top surface. A histogram of grey shades was generated for each SEM image (Figure 7.5 a-i), showing the number of counted pixels in the image on the vertical axis over the greyscale value (grey shade) ranging from zero (black) to 255 (white).

All pixels darker than a given grey shade were counted and summed up, resulting in a cumulated pixel count for this greyscale value. The cumulated pixel count was normalised resulting in the cumulated fraction of all pixels darker than a given grey shade in the SEM image. Figure 7.7 presents the cumulated fraction of pixel counts over the given greyscale values.
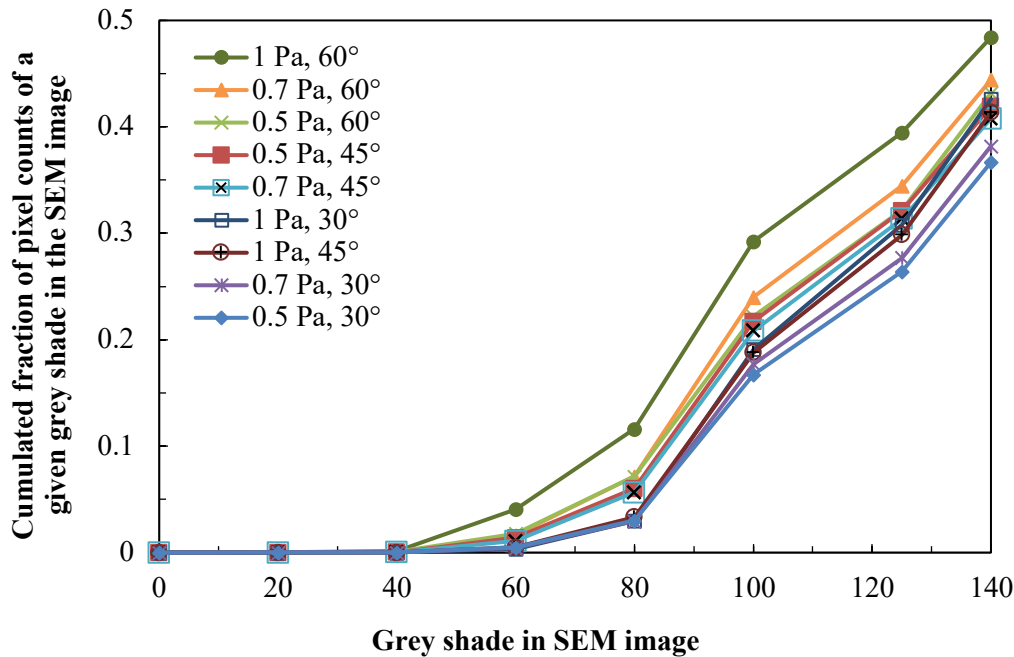
Figure 7.7: Cumulated fraction of pixel counts representing the porosity within the YSZ films over the greyscale values in the SEM image.

The segmentation of YSZ and pores is carried out by defining a threshold value that distinguishes darker pixels for pores and brighter pixels for YSZ, however, small errors can occur due to the overlapping of pore and YSZ grey scales [155]. The fraction of the pixel count on the vertical axis in the above figure is a representation of the porosity from the SEM images in Figure 7.5, as it calculates the ratio between pixels that are darker than a chosen grey scale on the horizontal axis to all pixels within the image. In order to estimate and compare the porosity of the presented samples, a plausible threshold value to separate YSZ from the pores needs to be defined considering the overlap of pores and YSZ. Figure 7.8 demonstrates a procedure used in ImageJ to adjust the threshold to capture a minimum and maximum area of pores from the original SEM image in (a). A minimum coverage of the pore phase can be visualised in (b) by setting the threshold value for the grey shade to 125, which intentionally underestimates the pore area, whereas the maximum area is taken at a threshold of 140 in (c), i.e., significant overestimation of pores.

(a)   (b)   (c)
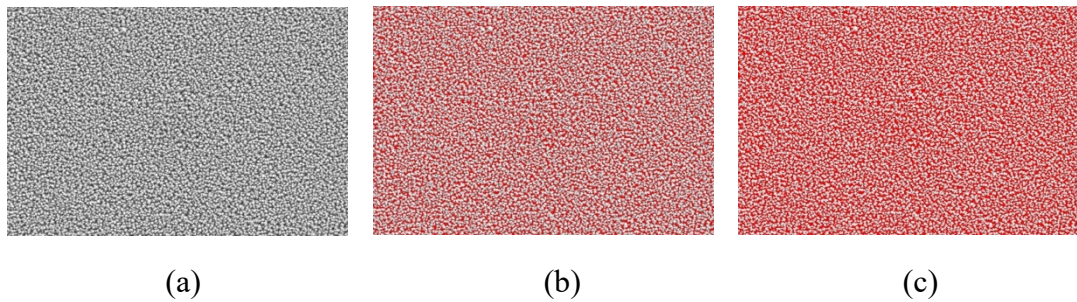
Figure 7.8: Estimation of threshold values for porosity analysis using ImageJ: original SEM image of the top surface (a), minimum threshold value of porous area: greyscale of 125 (b), maximum threshold value of porous area: greyscale of 140 (c).

Applying the values of minimum and maximum thresholds of 125 and 140, respectively, into Figure 7.7, resulted in estimating a minimum and maximum for the theoretical porosity for each sample, as illustrated in

Figure 7.9.
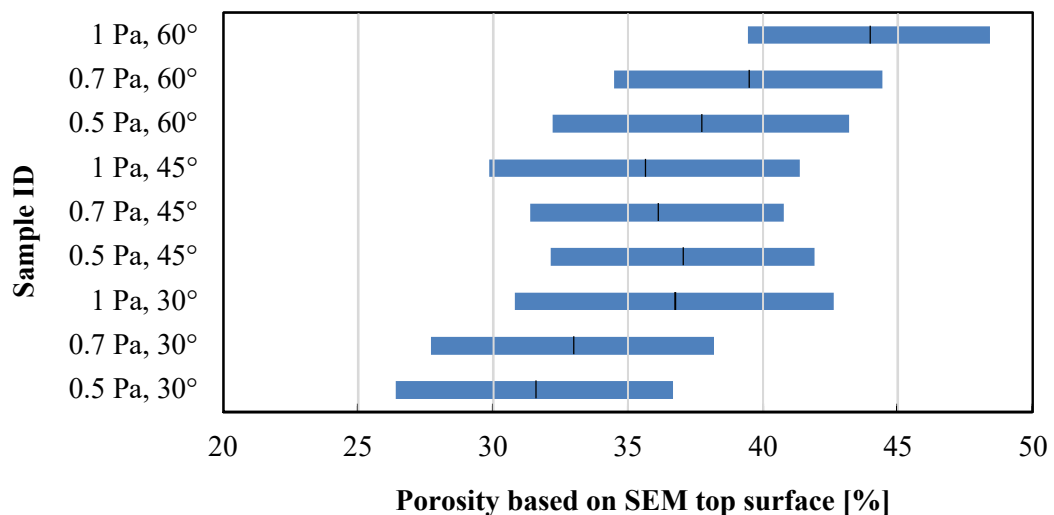
Figure 7.9: Estimation of the porosity of deposited YSZ films using ImageJ, indicating average porosity (middle lines).

The results show that the deposition at a high angle of 60° has a significant effect on the porosity. The highest porosity can be seen in the samples deposited at 0.7 Pa and 1 Pa at an angle of 60°, with an average of 39 % and 44%, respectively, indicating a slight overestimation of the porosity, as literature reported the highest porosity values of ca. 40 % for magnetron-sputtered coatings [131], [156]. At lower deposition angles, the average porosity is estimated between 32 and 37 %.

7.4.2   XRD results

Another important aspect of the film characterisation is the degree of crystallinity of the YSZ. In order to facilitate the diffusion of oxygen ions O^{2-} through oxygen vacancies, crystalline cubic structures of YSZ are essential to enhance their ionic conductivity. The XRD patterns after deposition are shown in Figure 7.10.
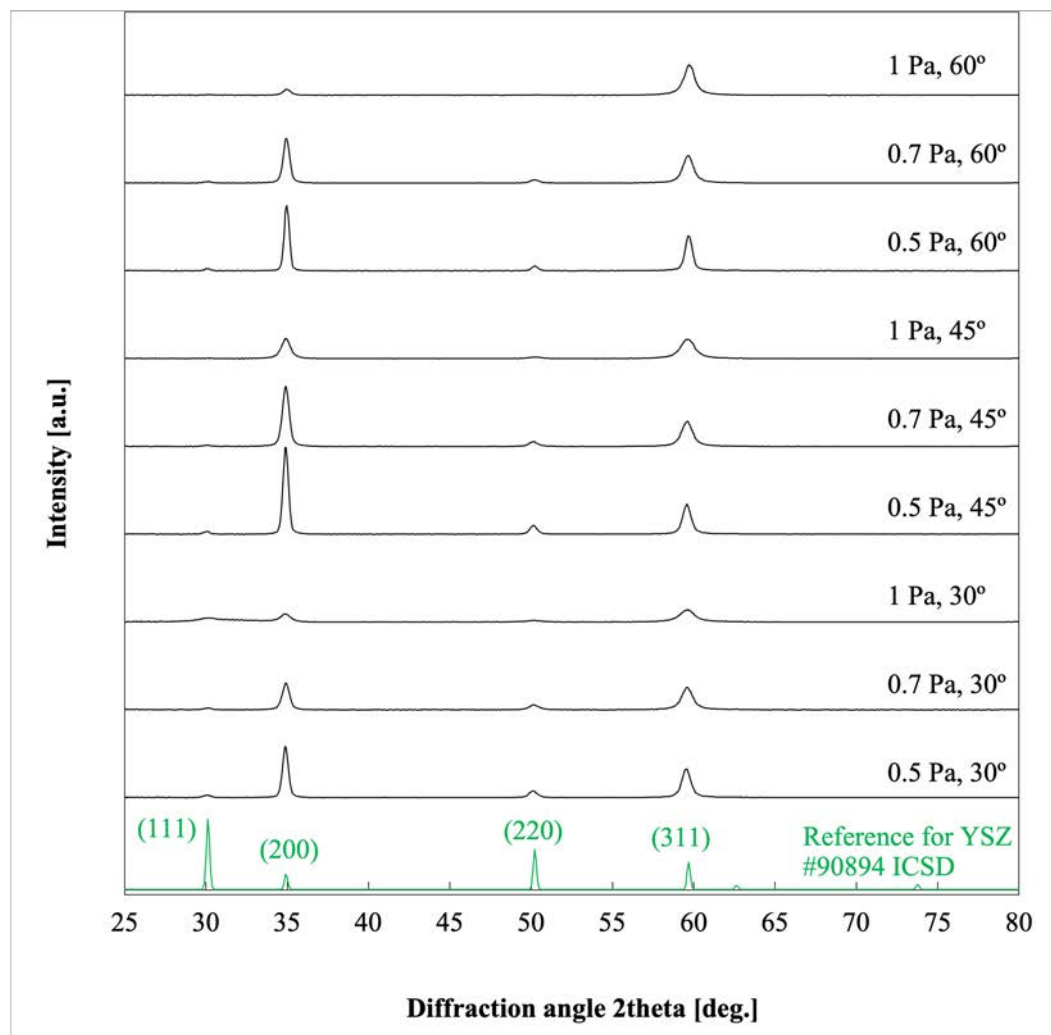
Figure 7.10: XRD patterns of as-deposited YSZ films developed under variable deposition angle and pressure.

The XRD patterns were assigned to 12 mol.% yttria stabilised zirconia $((ZrO2)_{0.88}$ $(Y2O3)_{0.12})_{0.893}$ using the Crystallography Open Database (COD) with the COD ID 1521478 in HighScorePlus [148], [149]. Reference patterns are plotted from the ICSD database with reference ICSD-90894 [150]. It can be observed that at each deposition angle, the YSZ films present a slightly higher degree of crystallinity as the deposition pressure decreases. The maximum intensity was recorded for the orientation (200) at an angle of 45° and 0.5 Pa operating pressure. Yet, these XRD patterns tend to have a

broadened peak shape rather than sharper high-intensity peaks usually seen in crystal-line materials. For that reason, in-situ hot-stage XRD experiments were performed to determine a suitable post-annealing temperature to facilitate crystalline growth in the as-deposited YSZ.

Figure 7.11 presents the XRD patterns of a YSZ film (deposited at 0.5 Pa and 60º angle) with increasing temperature from 25 ºC to 1200 ºC with a measurement taken every 12 min.
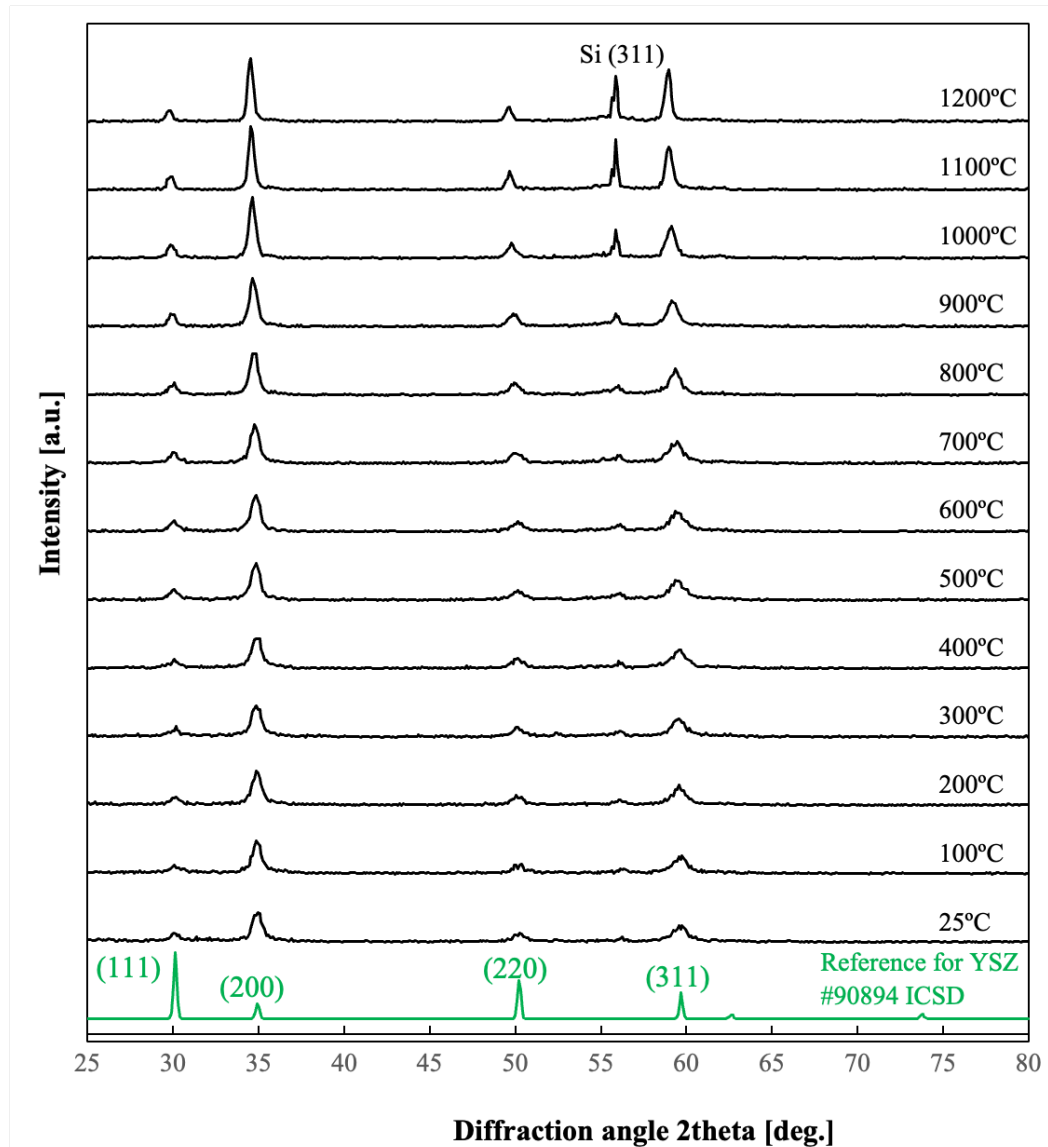
Figure 7.11: In-situ hot-stage XRD patterns of a YSZ film deposited at 0.5 Pa and 60º collected after each increment in the temperature.

From the above figure, it can be seen that the peak patterns gain in intensity with increasing temperature and become less broad at temperatures above 1000 °C. The highest intensities for YSZ occurred with the orientations (200) and (311) at temperatures

of 1100 and 1200 °C. The change in the peak ratio between the orientations (200) and (311) is plotted over the temperatures investigated in the below figure to determine any change in texture within the film.
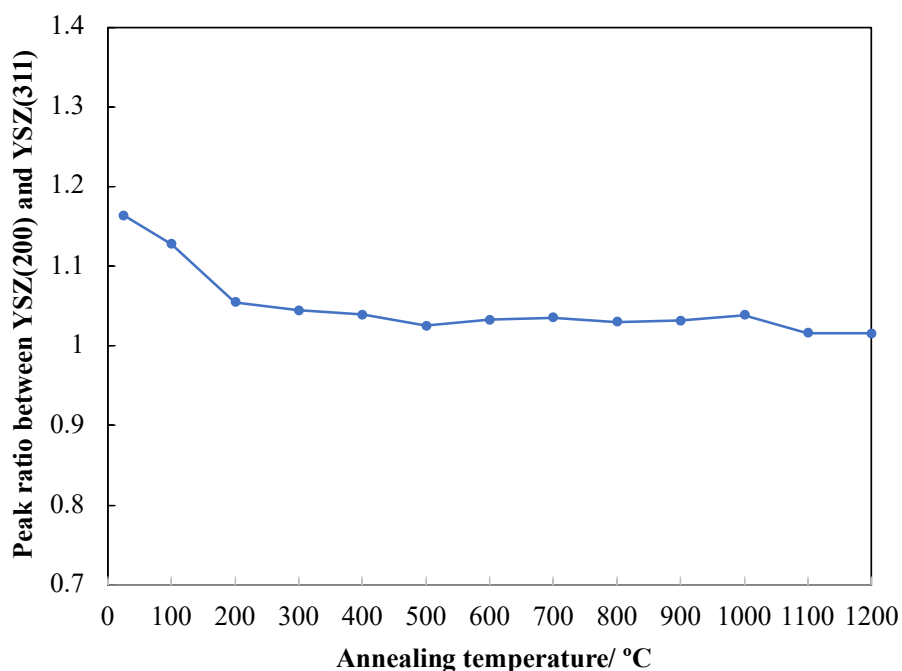
Figure 7.12: Peak ratio between YSZ(200) and YSZ(311) over post-annealing temperature.

The peak ratio changes noticeably from room temperature to 200 ºC, followed by a further slight decline to 500 ºC indicating slight changes in the film's texture. While it remains stable between 500 and 900 ºC, another decline can be observed between 1000 and 1200 ºC, indicating the intensification of YSZ(311).

In addition to the diffraction patterns of YSZ, a peak at 55.85º was recorded which most likely originated from the silicon wafer (100) used as the substrate material for the deposition.

7.5 Discussion

As mentioned in section 3.2.2, it is well established that film microstructure can be controlled through deposition parameters that control the energy of the incident ions on the growing film. The results in Figure 7.4 and Figure 7.5 reveal that the microstructure of the deposited YSZ strongly depends on the deposition pressure and deposition angle. The reason for this dependence is the change in energy that is delivered to the growing film during deposition which can be explained by the introduced structure zone models (SZM) [122], [123], [124], [157].

Higher apparent deposition rates, based on film thicknesses, were observed with increasing deposition pressure (Figure 7.4b). Since the sputtering rate of the material mainly relates to the applied power and the duty cycle in pulsed DC mode, which in this study remained unchanged during the deposition, the reported increase in deposition rate is due to the microstructural changes in the coating. From a subjective observation of the SEM micrographs in Figure 7.5, most open structures were produced at higher deposition pressures of 0.7 and 1 Pa when comparing the micrographs in a-d-g, b-e-h and c-f-i. This can be explained by the decreased mean free path between the atoms in the deposition chamber at higher deposition pressure, leading to a higher degree of atomic scattering which reduces the energy during film growth [123]. The XRD results presented increased intensity for low-pressure YSZ films deposited at 0.5 Pa compared to 0.7 and 1 Pa. Koski *et al.* reported weaker peaks for deposited zirconia films when increasing the deposition pressure from 0.3 to 0.5 and 1 Pa [158]. This phenomenon can be explained by the kinetic energy of the sputtered atoms arriving at the substrate. At low deposition pressures, sputtered atoms have a greater mean free path, leading to higher kinetic energies. This allows further migration for the adatoms to find the most stable site and form a denser, crystalline structure [159].

Similarly, as the deposition angle was increased, higher deposition rates were reported (Figure 7.4a). The SEM micrographs presented a slight increase in cavities between the columns, which is also indicated in the cumulated fraction of pixel counts in Figure 7.7 when comparing samples deposited at identical deposition pressures.

In oblique angle deposition (OAD), the incident vapour flux and the substrate normal are not parallel but instead form the deposition angle α [160]. When considering the nucleation and growth of thin films (cf. section 3.2.3) during oblique angle deposition, as illustrated in Figure 7.13, no further vapour atoms can be deposited behind an already formed nucleus due to self-shadowing, which leads to a more strongly pronounced columnar structure. Hawkeye *et al.* stated that the most important growth mode for OAD is island growth according to Volmer-Weber [160]. As the islands continue to grow, the nuclei will intercept more and more vapour, resulting in a ballistic shadowing effect at OAD.
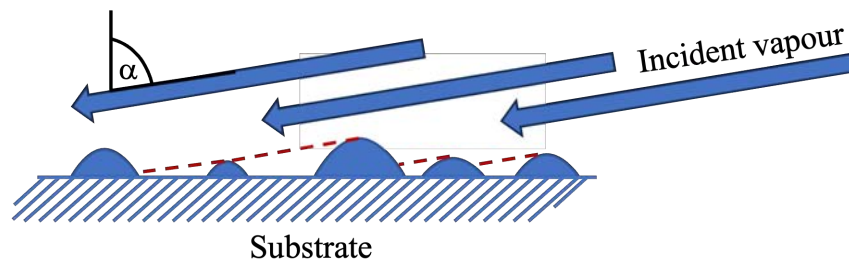
Figure 7.13: Island growth in oblique angle deposition resulting in ballistic shadowing effects in the surrounding region.

Kelly *et al.* deposited pyrophoric coatings by magnetron sputtering at deposition angles of 0º, 40º and 80º [156]. They found that the most porous films were produced at the highest deposition angle of 80º due to self-shadowing, which corresponds well with the outcome in this chapter when increasing the deposition angle from 30º to 60º.

7.6 Conclusion

The structural properties of YSZ films can be seen as a function of deposition angle and deposition pressure. The most porous columnar structures (Zone 1-type) were produced at high deposition pressures of 0.7-1 Pa and the highest deposition angle of 60º.

Regarding the crystallinity of the deposited YSZ films, these conditions were found to result in broader and less intense peaks in the XRD patterns and indicated the need for additional post-annealing within this work to optimise structure.

In the following chapter, nickel has been integrated into the YSZ scaffold to produce Ni-YSZ active functional layers for SOFCs. Based on the results presented in this chapter, further analysis of the deposition parameters is still of great interest in this work. Since the deposition system does not allow for deposition angles greater than 60º, the focus of the next study will be on the effect of the deposition pressures of 0.5, 0.7 and 1 Pa, and the enhancement of crystallinity by post-annealing.

8 Influence of process parameters on the microstructure and performance of state-of-the-art Ni-YSZ AFLs

8.1 Introduction

While the effect of different deposition parameters was studied in the previous chapter in terms of microstructural changes in YSZ films, this chapter presents the integration of nickel as a second phase into the porous YSZ microstructure to produce the state-of-the-art anode material for SOFCs.

The hysteresis behaviour of the co-sputtering of nickel and Zr-Y was analysed in section 8.2 to determine a suitable oxygen partial pressure for the oxidation of Zr-Y without affecting the deposition rate of Ni-YSZ coatings when using higher oxygen partial pressures.

Further studies investigated the effect of deposition parameters, such as elevated temperature during the deposition in section 8.3, and varied deposition pressures in section 8.4, on the SOFC performance of the created Ni-YSZ films through microstructural and electrochemical characterisations. Both studies included the analysis of different post-annealing temperatures of the NiO-YSZ films.

To conclude the results of this chapter, the electrochemical performance of the best-performing Ni-YSZ AFL was compared with the commercial SOFC button cell (NextCell, *fuelcellmaterials*, USA).

8.2 Deposition of Ni(O)-YSZ at different oxygen partial pressures

8.2.1 Experimental

The deposition process during the co-sputtering of the two materials was analysed through the hysteresis behaviour. Hysteresis curves of the discharge voltage and total system pressure were acquired at 200 W and 75 kHz (70% duty) on Ni, 250 W and 75 kHz (70% duty) on Zr-Y, 0.65 Pa working pressure, 12 cm target-substrate distance and a deposition angle of 60° for both nickel and Zr-Y, to achieve a nickel content between 35-40 vol.%.

As listed in Table 7.1, three samples OPP025, OPP050 and OPP075 have been sputtered from nickel and Zr-Y targets onto silicon substrates under the abovementioned parameters, but under different oxygen partial pressures of 0.025, 0.05 and 0.075 Pa along the hysteresis curve, to investigate its impact on the material structure and oxidation state.

Table 8.1: Sample IDs of specimens deposited at variable oxygen partial pressure ranges.

Sample ID	Oxygen partial pressure/ Pa	Total pressure/ Pa
OPP025	0.025	0.675
OPP050	0.050	0.700
OPP075	0.075	0.725

8.2.2 Hysteresis of Ni(O)-YSZ

Figure 8.1 illustrates the discharge voltage of nickel and zirconium-yttrium during the co-sputtering over the increasing oxygen flow rate.
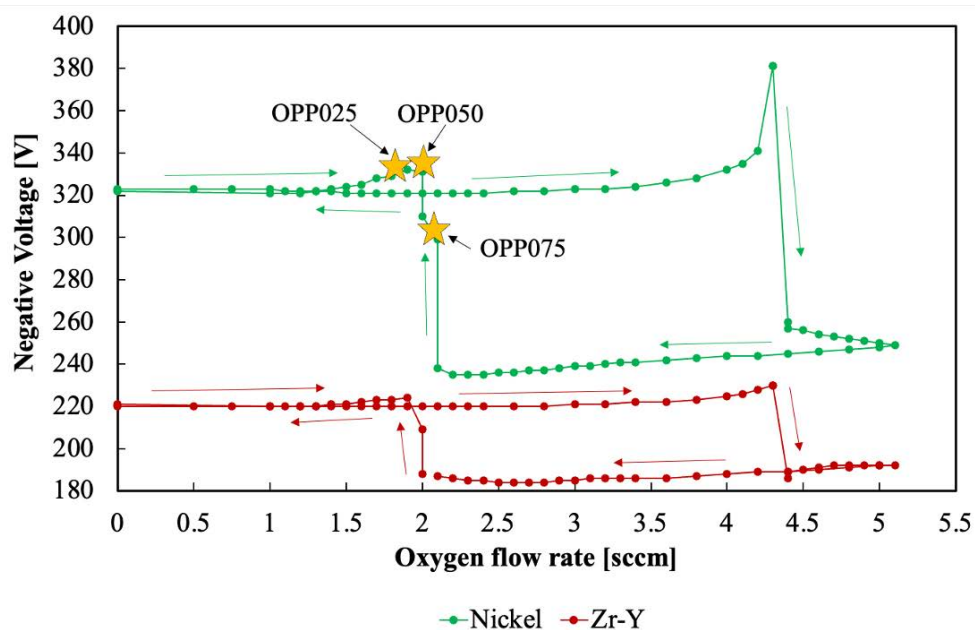
Figure 8.1: Hysteresis behaviour of the co-deposition of nickel and zirconium-yttrium, showing the discharge voltage over the set oxygen flow rate.

The sharp rise in the magnitude of the discharge voltage to -381 V at 4.3 sccm oxygen, which was previously seen in the hysteresis behaviour of Zr-Y in the previous chapter, is now present in the discharge voltage of the nickel target. It can be assumed that the zirconium or yttrium species might have an impact on the nickel target. A possible explanation could be that the two targets, which are tilted by 60º and thus, face each other, suffer from cross-contamination, resulting in the oxidation of zirconium and yttrium at the nickel surface area, leading to this high point in the nickel discharge voltage.

8.2.3 Material characterisation

The figure below demonstrates the process set points that were chosen for the three samples OPP025, OPP050 and OPP075.
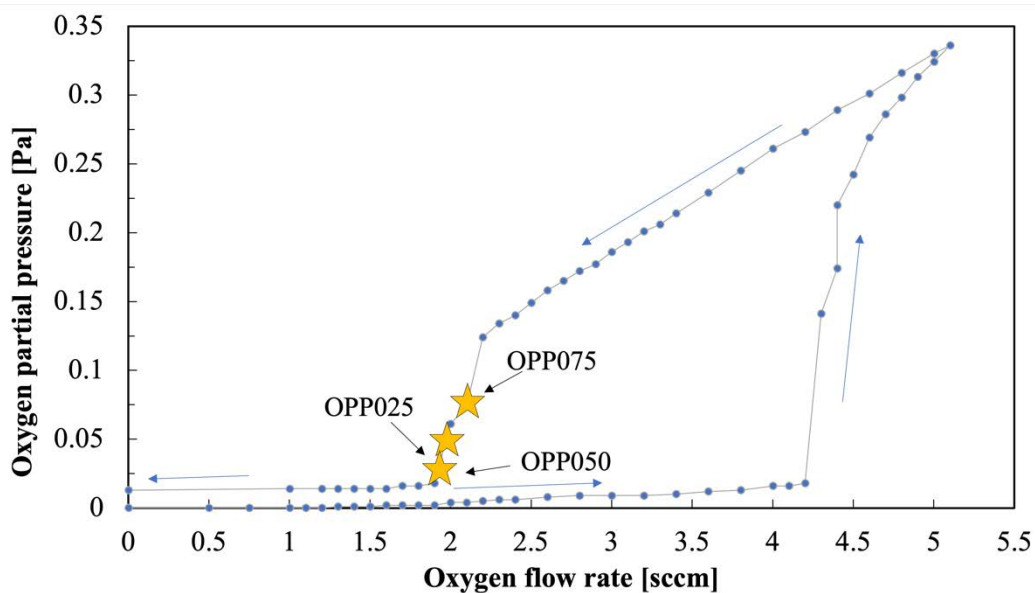
Figure 8.2: Hysteresis behaviour of the co-deposition of nickel and zirconium-yttrium, showing oxygen partial pressure over the set oxygen flow rate and process position of samples OPP025, OPP050 and OPP075 at oxygen partial pressures of 0.025, 0.05 and 0.075 Pa, respectively.

The application of the partial pressure control during the co-deposition of the three samples caused the oxygen flow rate to ramp up to its maximum and then slowly reduce the amount of oxygen until the set point is reached. Hence, the samples were deposited on the reverse of the hysteresis around the second peak at 2 sccm oxygen in Figure 8.1. Sample OPP025 was deposited before the high peak in the discharge voltage of nickel, sample OPP050 was deposited directly on the peak position and sample OPP075 after the peak (cf. Figure 8.1). However, slight voltage drifts have been observed directly at the peak position (OPP050). The deposition time was set to 60 min.

8.2.3.1 Coatings microstructure

The obtained SEM images of the fracture sections of samples OPP025, OPP050 and OPP075 are depicted in Figure 8.3.

OPP025	OPP050	OPP075
1078 nm	1125 nm	852.5 nm
(a)	(b)	(c)
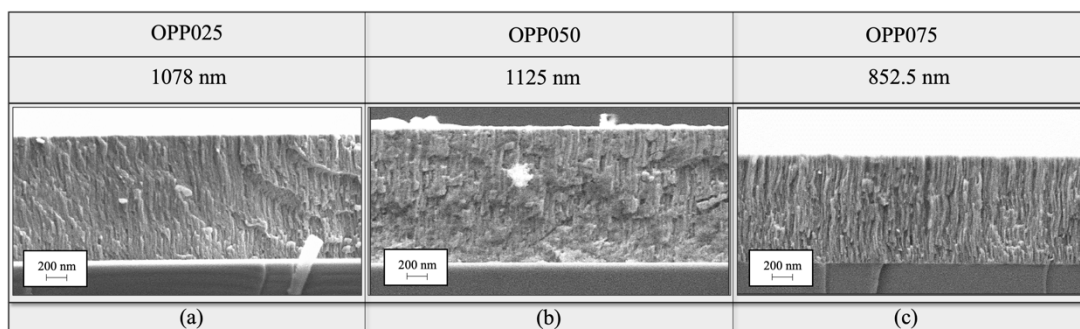
Figure 8.3: SEM images of fracture sections as-deposited samples OPP025 (a), OPP050 (b) and OPP075 (c) at respective oxygen partial pressures of 0.025, 0.05 and 0.075 Pa and assigned thicknesses.

While the above figures present a similar characteristic columnar microstructure, all three samples exhibit denser microstructures, when comparing it with previous results of YSZ films deposited without Ni (cf. Chapter 7). After a deposition time of 60 min, the thickness of samples OPP025, OPP050 and OPP075 yielded 1078, 1125 and 852.5 nm respectively, revealing that the deposition rate increased as the oxygen partial pressure increased from 0.025 to 0.05 Pa, but diminished at an oxygen partial pressure of 0.075 Pa.

8.2.3.2 Film composition

The acquired composition data of the samples OPP025, OPP050 and OPP075 is displayed in Table 8.2. As anticipated, the results confirm the presence of nickel, zirconium, yttrium and oxygen within the film.

Table 8.2: Composition of as-deposited films after EDS analysis of OPP025, OPP050 and OPP075 at different oxygen partial pressures of 0.025, 0.05 and 0.075 Pa, respectively, in mol.%.

Elemental	OPP025	OPP050	OPP075
Ni/ mol.%	43.2	43.7	45.1
Zr/ mol.%	8.1	8.2	5.2
Y/ mol.%	1.9	2.0	1.3
O/ mol.%	46.8	46.1	48.4
Ni/(Zr+Y)	4.3	4.3	6.9

Oxygen partial pressures of 0.025 Pa and 0.05 Pa yielded identical ratios of nickel, zirconium, yttrium and oxygen. When the partial pressure was increased to 0.075 Pa, the oxygen concentration increased by approximately 2 mol.% to 48.4 mol.% and the amount of zirconium-yttrium in the film reduced to 6.5 mol.%, which is indicated by the greater ratio of nickel to Zr-Y of 6.9, instead of 4.3 obtained for samples OPP025

and OPP050. This result suggests that the deposition rate of zirconium-yttrium is more affected than that of nickel at higher oxygen partial pressure.

The compositional data obtained by EDS were compared with XPS analysis, which has greater resolution and surface sensitivity than EDS. The results are illustrated in Table 8.14.

Table 8.3: Comparison of composition data of samples OPP025, OPP050 and OP075 obtained using EDS and XPS. The results are presented in mol.%.

Element	Analysis technique	Sample OPP025	Sample OPP050	Sample OPP075
O/ mol.%	EDS	46.8	46.1	48.4
	XPS	45.1	44.4	42.0
Y/ mol.%	EDS	1.9	2.0	1.3
	XPS	0.0	1.6	1.1
Zr/ mol.%	EDS	8.1	8.2	5.2
	XPS	7.3	7.4	5.1
Ni/ mol.%	EDS	43.2	43.7	45.1
	XPS	47.6	46.6	51.8

Compositional analysis using XPS and EDS techniques showed no significant difference ($\Delta < 1\%$) in the concentrations of yttrium and zirconium, with the exception of sample OPP025 where no yttrium was detected by the XPS. However, the nickel content obtained by XPS and EDS showed substantial discrepancies of approximately 7 mol% in sample OPP075.

8.2.3.3   XRD results

The crystallinity of the deposited films under different oxygen partial pressures was analysed using GI XRD, and the results are depicted in Figure 8.4.
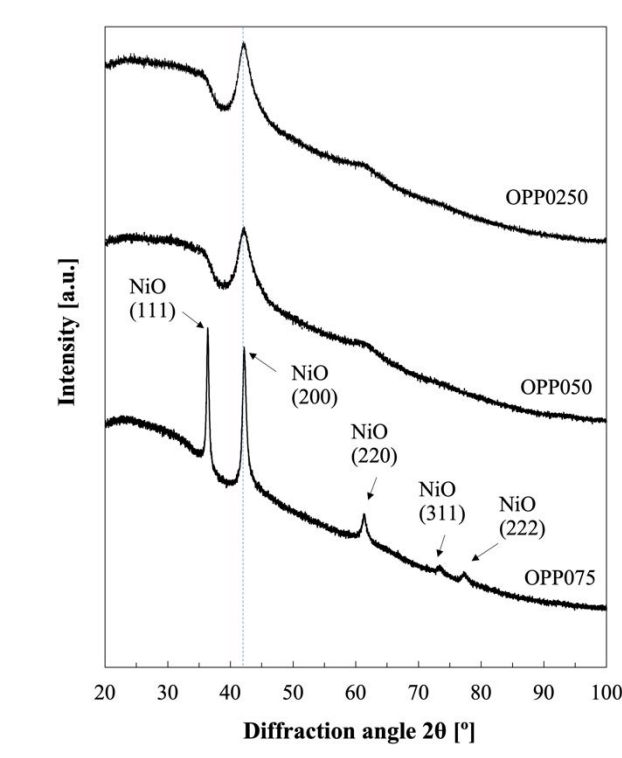
Figure 8.4: XRD patterns of as-deposited samples OPP025, OPP050 and OPP075 at respective oxygen partial pressures of 0.025, 0.05 and 0.075 Pa.

The above data demonstrate that the film structure changed, as no high-intensity peaks of YSZ can be observed after integrating Ni(O) into YSZ films, regardless of the oxygen partial pressure. Yet, low-intensity peaks of NiO oriented in the (200) plane occurred in all samples, identified by COD ID 1010095 from the Crystallography Open Database in *HighScorePlus* [161]. At an oxygen partial pressure of 0.075 Pa, additional NiO peaks at (111), (220), (311) and (222) orientations were observed. The absence of YSZ diffraction patterns is most likely due to the higher amount of nickel than that of Zr-Y within the coatings (cf. Table 8.2). Moreover, these results suggest that sputtered nickel atoms have been oxidised to NiO during the reactive co-sputtering of nickel and Zr-Y.

Furthermore, to evaluate if the crystalline structure evolves after high temperature heat treatment, sample OPP050 was subjected to the in-situ high temperature XRD analysis. The sample was placed onto a hot stage and annealed from 100 °C to 1200 °C in 100 °C intervals and held at temperature for 12 minutes. Between each interval, a diffractogram was collected, which is now presented in Figure 8.5.
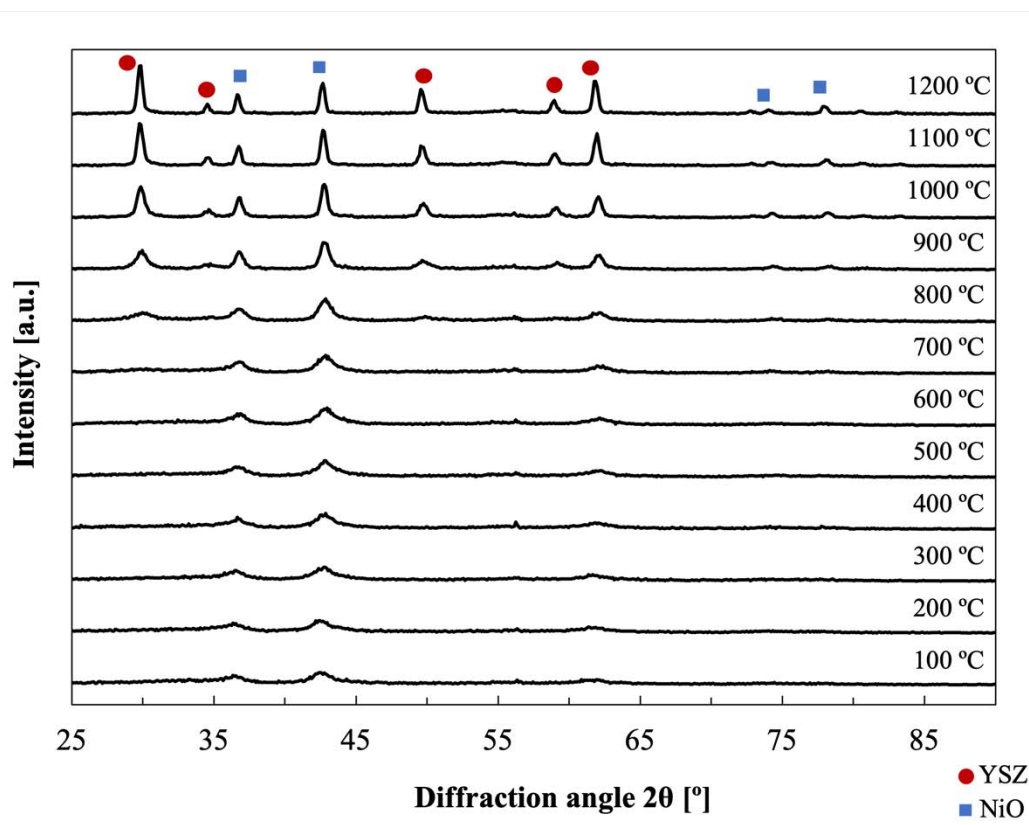
Figure 8.5: In-situ hot-stage XRD analysis of NiO-YSZ film deposited at 0.05 Pa oxygen partial pressure collected after each increment in the temperature.

Similar to the hot stage experiment performed on pure YSZ samples in the previous chapter, the peak patterns gain in intensity with increasing temperature and become less broad at temperatures above 1000 °C. The acquired XRD patterns can be assigned to 12 mol.% $((ZrO_2)_{0.88} (Y_2O_3)_{0.12})_{0.893}$ and NiO using the respective COD IDs 1521478 and 1010095 from previous analyses in this work using *HighScorePlus software* [161], [162], [163].

8.2.3.4 Oxidation states of Ni(O)-YSZ films

The influence of the oxygen partial pressure on the oxygen binding energy in the as-deposited Ni(O)-YSZ coatings is also of interest. The O 1s XPS spectra of samples OPP025, OPP050 and OPP075 are illustrated in Figure 8.6.
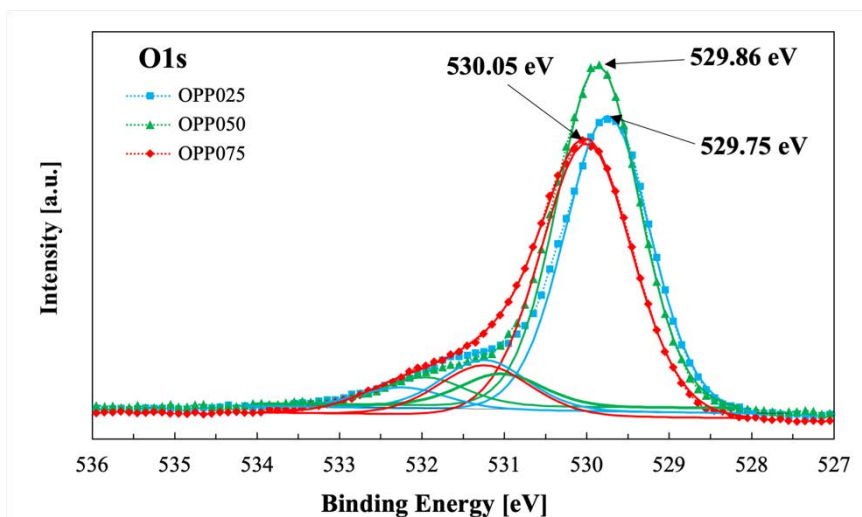
Figure 8.6: O 1s XPS spectra of as-deposited samples OPP025, OPP050 and OPP075 at different oxygen partial pressures of 0.025, 0.05 and 0.075 Pa, respectively.

O 1s spectra present components for the metal oxide as well as various components caused by contamination from water or organic compound types, which are difficult to peak fit due to overlapping [164]. Peak fitting of the above O 1s spectra was carried out by fitting one peak for lattice oxide and two smaller peaks for hydroxide/lattice defects as well as adsorbed water/ organic species. When focusing on the peak fitting of the metal oxide, oxygen binding energies of 529.75 eV, 529.86 eV and 530.05 eV for the samples OPP025, OPP050 and OPP075, respectively. These results are in good agreement with typical binding energies for metal oxides varying between 528.2 eV and 531 eV [146].

Furthermore, Y 3d and Zr 3d region scans for yttrium and zirconium in the deposited Ni(O)-YSZ coatings are presented in Figure 8.7 a and b, respectively. For Y_2O_3, the literature stated binding energies are between 156.4 eV and 157.0 eV [146]. The binding energies of all three samples indicate that the contained yttria had been fully oxidised during deposition. The Zr $3d_{5/2}$ peaks occur at binding energies of 181.7-181.8 eV, which are slightly lower than the reported values for ZrO_2 of 182.0 eV and 182.5 eV [146].
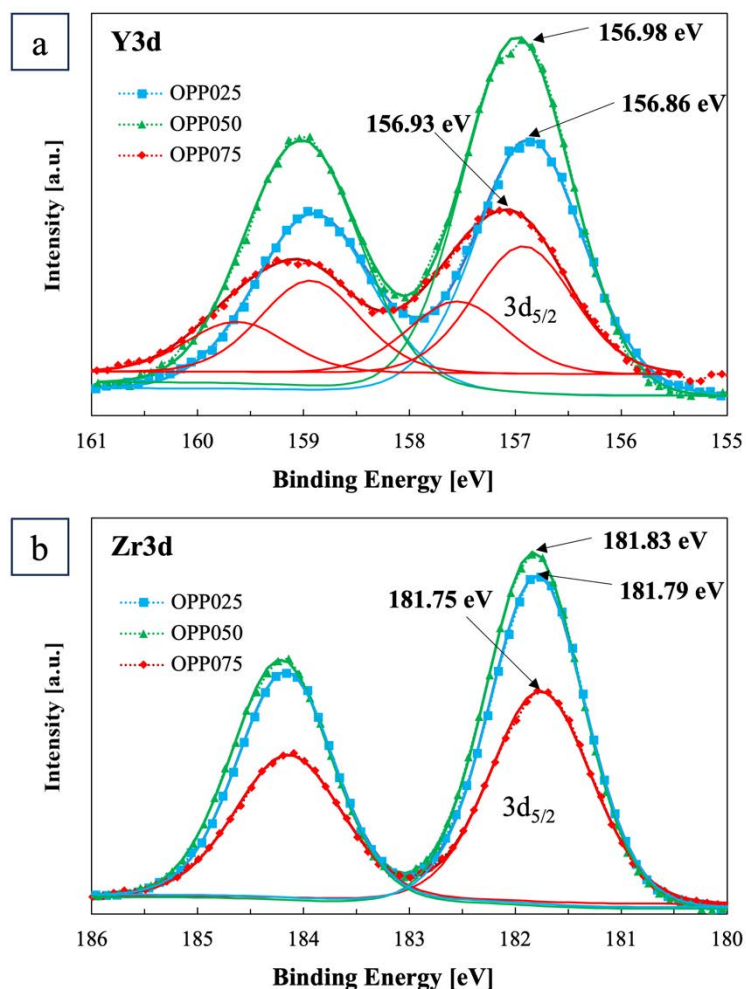
Figure 8.7: Y 3d (a) and Zr 3d (b) XPS spectra of as-deposited samples OPP025, OPP050 and OPP075 at different oxygen partial pressures of 0.025, 0.05 and 0.075 Pa, respectively.

8.2.4 Discussion

The SEM micrographs revealed denser microstructures of Ni(O)-YSZ films compared to the results of the deposited YSZ films in Chapter 7. This is most likely caused by the oxidation of Ni species into nickel oxide during the reactive co-sputtering process of nickel and zirconium-yttrium, which is supported by the XRD results in Figure 8.4 showing evidence of the presence of NiO after the deposition. It should, however, be noted that further deposited Ni(O)-YSZ films underwent a subsequent reduction in hydrogen to increase the porosity of the film, which will be demonstrated later on in sections 8.3 and 8.4.

Moreover, the SEM cross section images demonstrated a decrease in the deposition rate of sample OPP075 when using an oxygen partial pressure of 0.075 Pa. Due to a higher amount of oxygen present in the deposition chamber, a thin insulation layer

could have potentially been created on the target surface, resulting in slight target poisoning of nickel or zirconium-yttrium and thus, a lower deposition rate.

The composition data remained unchanged at oxygen partial pressures of 0.025 Pa and 0.05 Pa, resulting in an identical ratio between nickel and Zr-Y. However, with higher oxygen partial pressure a significantly greater ratio of Ni/(Zr+Y) was observed, implying that more nickel than zirconium-yttrium had been deposited. The combination of a reduced zirconium-yttrium concentration in the film and an overall lowered deposition rate at high oxygen partial pressures gives reason to believe that the Zr-Y target was slightly poisoned during the deposition of OPP075. As can be seen from the hysteresis curve in Figure 8.1, at an oxygen flow rate of ca. 2.1 sccm, Zr-Y appeared to remain in the poisoned mode until the oxygen flow rate was further reduced to 1.9-2 sccm, at which it went into the transition mode. Conversely, nickel was already in the transition mode at 2.1 sccm oxygen, which could explain the higher deposition rate of Ni in sample OPPO75 (cf. Table 8.2).

The XRD patterns of the three coatings at different oxygen partial pressures confirmed the presence of crystalline nickel oxide. An important aspect of the XRD results is that no crystalline YSZ was detected in the deposited films, regardless of the oxygen partial pressure. This finding is very well in line with the literature, as Garcia-Garcia *et al.* had also reported no evidence for the existence of crystalline YSZ after the deposition of Ni(O)-YSZ films, but rather the presence of crystalline Ni in the form of an oxide [165]. Therefore, it is speculated that the crystal orientation of NiO predominates over that of YSZ during thin film growth of Ni(O)-YSZ.

From the O 1s XPS spectra in Figure 8.6, it is apparent that with increasing oxygen partial pressure the oxygen binding energy within the Ni-YSZ film increased. However, caution must be applied as the findings may indicate a false correlation between the binding energy and the varied oxygen partial pressure due to differences in the composition between nickel and YSZ. Sample OPP075 contained considerably more nickel and less Zr-Y (cf. Table 8.2), which could have affected the shift in oxygen binding energy. The literature reported oxygen binding energies of 529.6 eV for NiO and 530.2 eV for ZrO_2 in O 1s [146]. To account for the difference in composition in the O 1s spectra, one could argue that a higher nickel concentration (OPP075) could potentially result in a shift towards lower binding energies (529.6 eV) and higher zirconium concentrations (OPP025 and OPP050), on the other hand, could give higher

oxygen binding energies (530.2 eV). Yet, the reported binding energies in this study showed contradictive behaviour, as sample OPP075 which contained more nickel presented a slightly greater binding energy than samples OPP025 and OPP050. It is possible to hypothesise that the reduced zirconium-yttrium concentration and therefore increased amount of NiO in OPP075 caused fewer oxygen vacancies to be present in the coating compared to the other samples, and thus may have increased the oxygen binding energy.

The Zr 3d spectra depicted in Figure 8.7b exhibited lower binding energies compared to the literature. This could suggest that not enough oxygen was present during the reactive co-sputtering of Zr-Y and Ni, resulting in sub-stoichiometric zirconia. On the other hand, it could be speculated that due to the doping of zirconia with yttria, high levels of oxygen vacancies are present in the film, causing a shift towards lower binding energies.

8.2.5 Conclusion

Overall, the findings in this study presented no significant changes in the microstructure of Ni(O)-YSZ at different oxygen partial pressures but revealed a decreased deposition rate at 0.075 Pa, indicating potential poisoning of the zirconium-yttrium target. As a result, future depositions were carried out at an oxygen partial pressure of 0.05 Pa, sputtering close to the described peak position to deposit Ni(O)-YSZ films without sacrificing higher deposition rates.

8.3 Deposition of Ni(O)-YSZ under elevated substrate temperature

The results of investigating the effect of elevated substrate temperature on Ni(O)-YSZ films using a substrate heater during the deposition are presented below. This section is divided into two parts. The first part presents results of the material characterisation of as-deposited, annealed and reduced Ni(O)-YSZ films in terms of their microstructure, crystallinity and oxidation state, and the second part contains the results of the electrochemical testing of these films regarding their SOFC performance as active functional layers (AFLs).

8.3.1 Experimental

8.3.1.1 Deposition of Ni(O)-YSZ under elevated substrate temperature
In order to study the effect of the substrate temperature during the deposition, two samples were deposited onto 20 mm diameter YSZ substrates (from *fuelcellmaterials, USA* for electrochemical testing, 150 µm thick*, and from the *University of Sheffield,*

UK for material characterisation, ca. 800 µm thick) and silicon wafer (p-type (100) orientation, *PI-KEM, UK*). The deposition was carried out at 200 W and 75 kHz (70% duty) on Ni, 250 W and 75 kHz (70% duty) on Zr-Y, 0.45 Pa working pressure, 0.05 Pa oxygen partial pressure, 14 cm target-substrate distance and a deposition angle of 60° for nickel and Zr-Y. The deposition time varied to achieve a film thickness of 3 µm. While no heater was applied during the deposition of sample Ni-YSZ-NH, the heater was ramped up to 400 ºC and remained at this temperature during the deposition of sample Ni-YSZ-H, as listed in Table 8.4.

Table 8.4: Sample IDs of specimens deposited with and without substrate heating during the sputtering.

Sample ID	Heater temperature/ ºC
Ni-YSZ-NH	No heater
Ni-YSZ-H	400

8.3.1.2 Material characterisation of as-deposited, annealed and reduced Ni(O)-YSZ under elevated substrate temperature

In addition to studying the impact of the substrate temperature during coating deposition, the effect of the post-deposition annealing temperature on the microstructure of samples Ni-YSZ-NH and Ni-YSZ-H was analysed. Each sample which contained YSZ as the substrate was separated into three sections to undergo individual post-deposition heat treatment at 1100 ºC, 1200 ºC and 1250 ºC in air for 1 h, followed by a subsequent reduction in 10% H_2/N_2 atmospheres at 850 ºC for 10 h. The resulting sample IDs can be found in Table 8.5.

SEM of the top surface and cross-section, EDS, XRD and XPS analyses were conducted after each individual state, *i.e.*, as-deposited, annealed and reduced. EDS was performed on as-deposited samples with YSZ and Si substrates to rule out penetration of the underlying YSZ substrate in the annealed and reduced samples.

Table 8.5: Sample IDs of specimens deposited under variable substrate temperature after annealing at 1100, 1200 and 1250 °C, respectively, and hydrogen reduction.

Sample ID	Heater / ºC	Annealing / ºC	Reduction in H_2/ ºC
Ni-YSZ-NH-A1100	-	1100	-
Ni-YSZ-NH-A1200	-	1200	-
Ni-YSZ-NH-A1250	-	1250	-
Ni-YSZ-H-A1100	400	1100	-
Ni-YSZ-H-A1200	400	1200	-
Ni-YSZ-H-A1250	400	1250	-
Ni-YSZ-NH-A1100-R	-	1100	850

Sample ID	Heater / ºC	Annealing / ºC	Reduction in H$_2$/ ºC
Ni-YSZ-NH-A1200-R	-	1200	850
Ni-YSZ-NH-A1250-R	-	1250	850
Ni-YSZ-H-A1100-R	400	1100	850
Ni-YSZ-H-A1200-R	400	1200	850
Ni-YSZ-H-A1250-R	400	1250	850

8.3.1.3 *Electrochemical characterisation of Ni(O)-YSZ films under elevated substrate temperature*

YSZ substrates coated with NiO-YSZ AFLs and annealed in air for 1 h were coated with a 20 µm-thick layer of LSM-YSZ (50:50 wt.%) ink (*fuelcellmaterials*, USA), which acted as the cathode during the performance testing of Ni-YSZ AFLs. The cathode layer was applied by doctor blading and dried on a heating plate at 100 ºC for 1 h. The dried LSM-YSZ-NiO/YSZ electrodes were then sintered in air at 1100 ºC for 1 h and reduced in hydrogen before electrochemical cell tests were carried out. The influence of the different thicknesses of the cathode layer on the SOFC performance was analysed and can be found in Appendix F.

The electrochemical tests of the AFLs were carried out under 100 sccm 3%-humidified hydrogen (H$_2$ purity N5, 99.999%) and 200 sccm air at 850 ºC by Imperial College London.

8.3.2 Material characterisation

8.3.2.1 *Coatings microstructure*

The SEM top surface micrographs of sample Ni-YSZ-NH (no heater applied during the deposition) for as-deposited, annealed and reduced states and different post-deposition annealing temperatures of 1100 ºC, 1200 ºC and 1250 ºC and reduced in hydrogen are depicted in Figure 8.8.
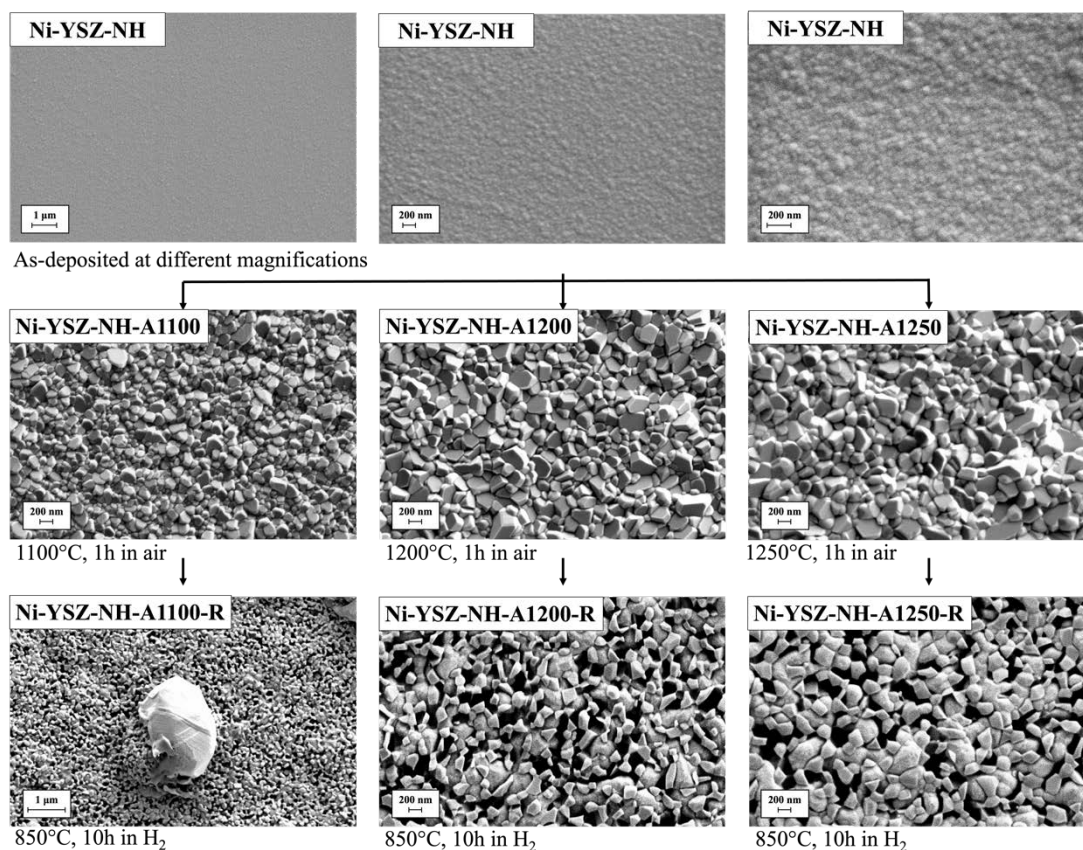
Figure 8.8: SEM images of the top surface of sample Ni-YSZ-NH, no substrate heater applied. (Ni-YSZ-NH) as-deposited state, showing increasing magnification from left to right, (Ni-YSZ-NH-A1100): after annealing at 1100 ºC in air for 1 h, (Ni-YSZ-NH-A1200): after annealing at 1200 ºC in air for 1 h, (Ni-YSZ-NH-A1250): after annealing at 1250 ºC in air for 1 h, (Ni-YSZ-NH-A1100-R): Ni-YSZ-NH-A1100 followed by a reduction in 10% H_2/N_2 for 10 h, (Ni-YSZ-NH-A1200-R): Ni-YSZ-NH-A1200, followed by a reduction in 10% H_2/N_2 at 850 ºC for 10 h and (Ni-YSZ-NH-A1250-R): Ni-YSZ-NH-A1250, followed by a reduction in 10% H_2/N_2 at 850 ºC for 10 h.

The top surface SEM images of as-deposited Ni(O)-YSZ films at different magnifications show a characteristically dense microstructure with no significant features. After sintering in air at high temperatures, the top surfaces of Ni-YSZ-NH-A1100, Ni-YSZ-NH-A1200 and Ni-YSZ-NH-A1250 are presented with crystalline particles. It can be observed that their particle size increases with increasing annealing temperature. The further reduction of these samples in hydrogen/nitrogen atmosphere resulted in a finely porous top surface, where particle size showed a similar dependency on the previously used annealing temperature. Sample Ni-YSZ-NH-A1100-R exhibited particle agglomerates on the surface varied in size between 2 and 3.2 µm.

In contrast, no surface agglomerations were observed in samples Ni-YSZ-A1200-R and Ni-YSZ-A1250-R.

Figure 8.9 illustrates the SEM images of the top surfaces of as-deposited sample Ni-YSZ-H and after annealing at 1100ºC, 1200 ºC and 1250 ºC (Ni-YSZ-H-A1100, Ni-YSZ-H-A1200 and Ni-YSZ-H-A1250), and after subsequent reduction in hydrogen/nitrogen at 850 ºC (Ni-YSZ-H-A1100-R, Ni-YSZ-H-A1200-R and Ni-YSZ-H-A1250-R).
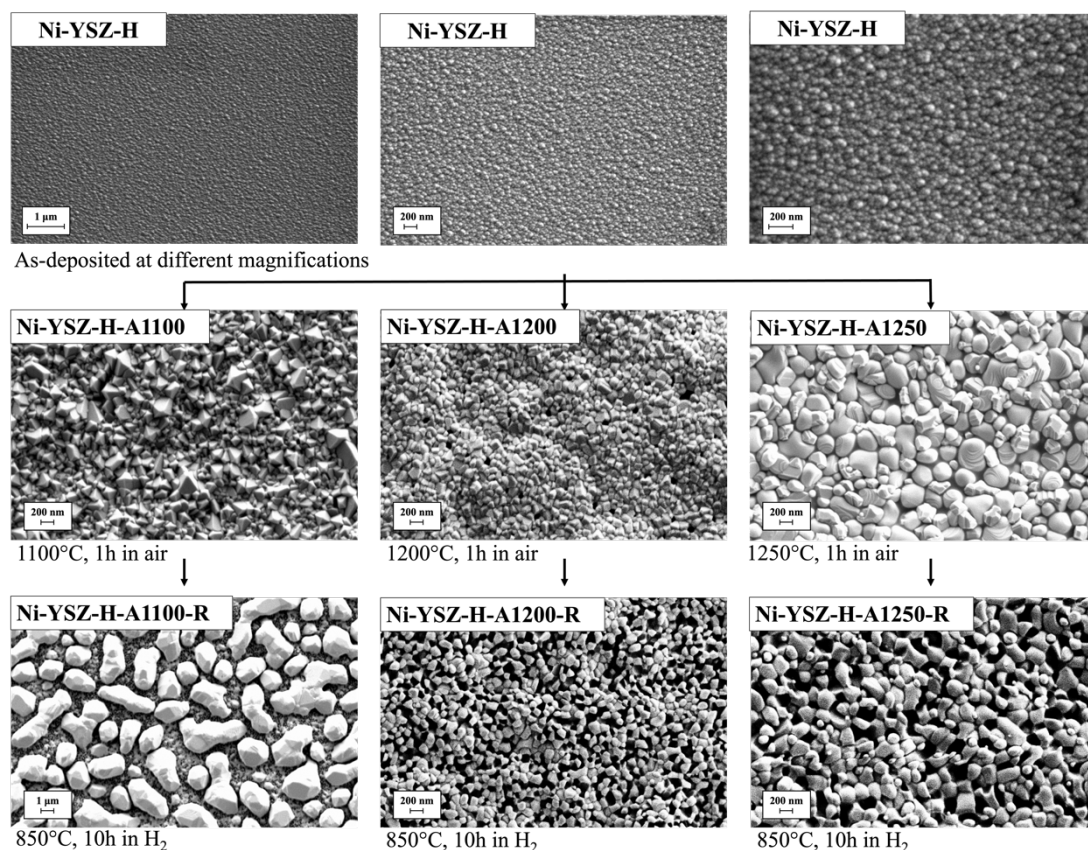
Figure 8.9: SEM images of the top surface of sample Ni-YSZ-H (substrate heater at 400 ºC applied during the deposition). (Ni-YSZ-H) as-deposited state, showing increasing magnification from left to right, (Ni-YSZ-H-A1100): after annealing at 1100 ºC in air for 1 h, (Ni-YSZ-H-A1200): after annealing at 1200 ºC in air for 1 h, (Ni-YSZ-H-A1250): after annealing at 1250 ºC in air for 1 h, (Ni-YSZ-H-A1100-R): Ni-YSZ-H-A1100 followed by a reduction in 10% H_2/N_2 for 10 h, (Ni-YSZ-H-A1200-R): Ni-YSZ-H-A1200, followed by a reduction in 10% H_2/N_2 at 850 ºC for 10 h and (Ni-YSZ-H-A1250-R): Ni-YSZ-H-A1250, followed by a reduction in 10% H_2/N_2 at 850 ºC for 10 h.

The top surface images at various magnifications of sample Ni-YSZ-H also present a characteristically dense columnar structure like sample Ni-YSZ-NH (no heater during deposition). After sintering at high temperatures, significant grain growth (> 200 nm) was observed in sample Ni-YSZ-H-A1250, while Ni-YSZ-H-A1100 exhibited smaller

crystalline particles with an estimated size of 200-300 nm and sharper edges. Sample Ni-YSZ-H-A1200 yielded a substantially finer microstructure with particle sizes of around 150 nm. After the reduction in a hydrogen/nitrogen atmosphere, the differences in particle sizes remained in samples Ni-YSZ-H-A1200-R and Ni-YSZ-H-A1250-R, whereas a severe increase in surface aggregations occurred in sample Ni-YSZ-H-A1100-R compared to Ni-YSZ-NH-A1100-R. During EDS analysis, these agglomerates were identified as nickel, as illustrated in the below figure.

Element	Wt.%	At.%
OK	01.17	04.17
YL	00.00	00.00
ZrL	00.95	00.60
NiK	97.88	**95.24**
Matrix	Correction ZAF	
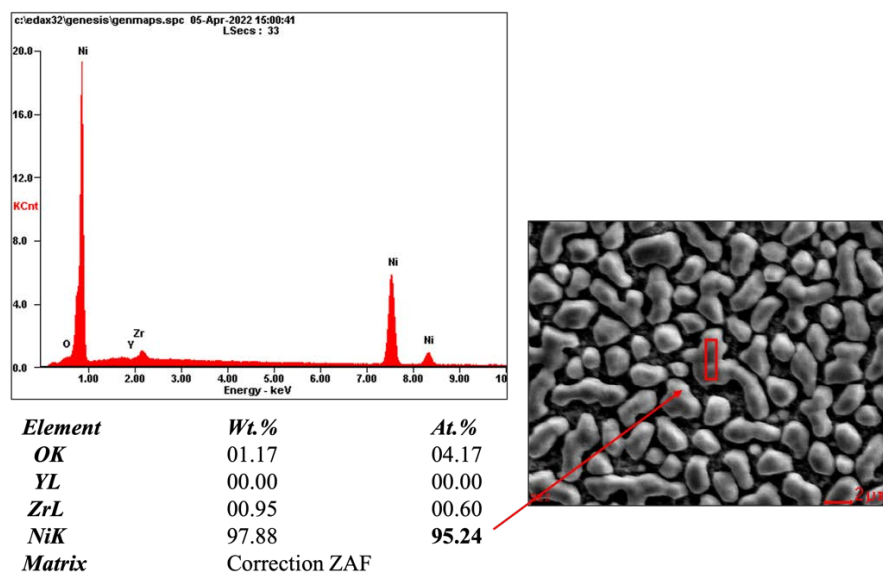
Figure 8.10: EDS analysis of the surface agglomerates of sample Ni-YSZ-A1100-R.

The SEM and BSE cross section images of as-deposited samples Ni-YSZ-NH (no substrate heating during deposition) and Ni-YSZ-NH (400ºC applied to the substrate during deposition), after annealing in air at 1100 ºC, 1200 ºC and 1250 ºC and hydrogen reduction are demonstrated in Figure 8.11 and Figure 8.12, respectively.
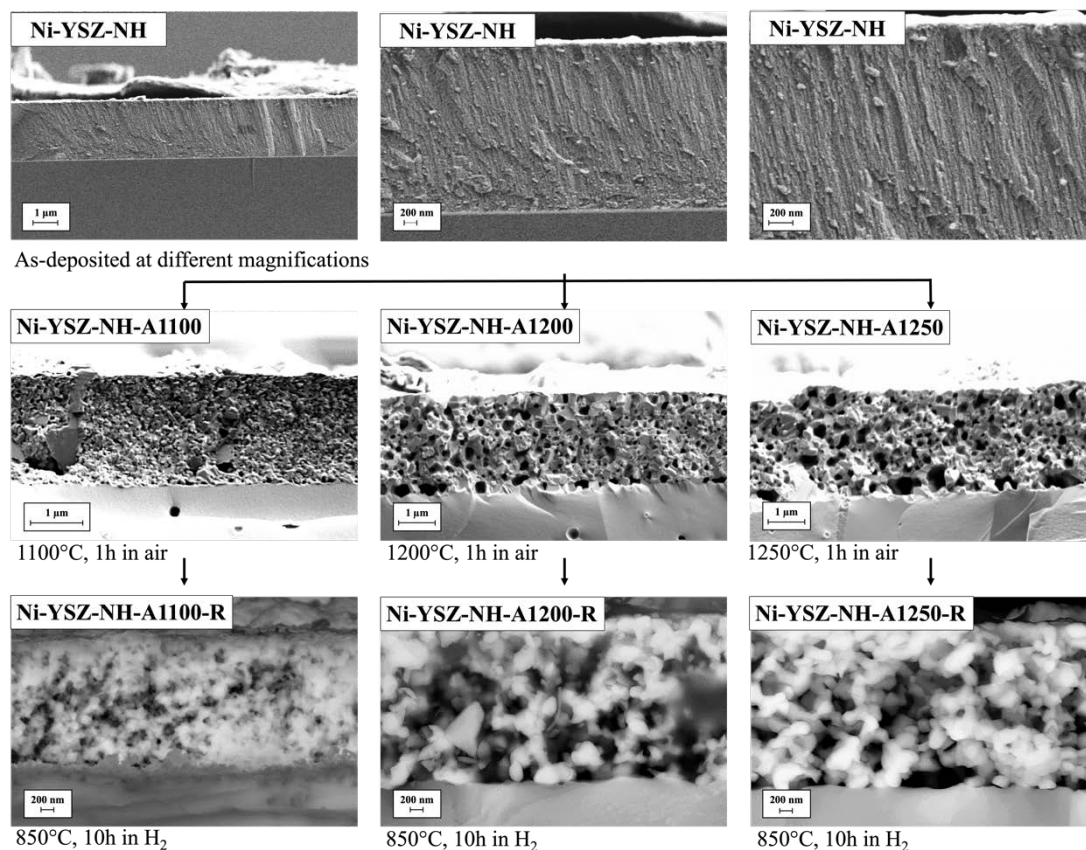
Figure 8.11: SEM and BSE images of the cross section of sample Ni-YSZ-NH, no substrate heater applied. (Ni-YSZ-NH): as-deposited state, showing increasing magnification from left to right, (Ni-YSZ-NH-A1100): after annealing at 1100 ºC in air for 1 h, (Ni-YSZ-NH-A1200): after annealing at 1200 ºC in air for 1 h, (Ni-YSZ-NH-A1250): after annealing at 1250 ºC in air for 1 h, (Ni-YSZ-NH-A1100-R): Ni-YSZ-NH-A1100 followed by a reduction in 10% H_2/N_2 for 10 h, (Ni-YSZ-NH-A1200-R): Ni-YSZ-NH-A1200, followed by a reduction in 10% H_2/N_2 at 850 ºC for 10 h and (Ni-YSZ-NH-A1250-R): Ni-YSZ-NH-A1250, followed by a reduction in 10% H_2/N_2 at 850 ºC for 10 h.

Figure 8.12: SEM and BSE images of the cross section of sample Ni-YSZ-H, substrate heater applied at 400 ºC. (Ni-YSZ-H) as-deposited state, showing increasing magnification from left to right, (Ni-YSZ-H-A1100): after annealing at 1100 ºC in air for 1 h, (Ni-YSZ-H-A1200): after annealing at 1200 ºC in air for 1 h, (Ni-YSZ-H-A1250): after annealing at 1250 ºC in air for 1 h, (Ni-YSZ-H-A1100-R): Ni-YSZ-H-A1100 followed by a reduction in 10% H_2/N_2 for 10 h, (Ni-YSZ-H-A1200-R): Ni-YSZ-H-A1200, followed by a reduction in 10% H_2/N_2 at 850 ºC for 10 h and (Ni-YSZ-H-A1250-R): Ni-YSZ-H-A1250, followed by a reduction in 10% H_2/N_2 at 850 ºC for 10 h.

Comparing the two samples in the as-deposited state, the cross-sectional SEM images indicate characteristic columnar structures. However, the sample deposited at an elevated temperature shows small fine grains stacked into columns compared to the unheated sample Ni-YSZ-NH. After annealing, the cross section of these samples differs significantly. Samples deposited with the heater at 400 ºC during the deposition display a dense microstructure with more predominant grain growth at higher annealing temperatures (Ni-YSZ-H-A1250), whereas samples deposited without the heater contained voids that increased in size with increasing post-deposition annealing temperature from 1100 ºC to 1250 ºC (*i.e.*, Ni-YSZ-NH-A1100 shows smaller grains compared to Ni-YSZ-NH-A1200 and Ni-YSZ-NH-A1250). What stands out in the above

figures is that the initial coating target thickness of 3 μm in as-deposited samples decreased after annealing in all samples, in particular, a substantial reduction in thickness was seen in the samples with no heater applied during the deposition. The BSE images revealed the final microstructure of the Ni-YSZ AFLs in the reduced state, demonstrating the pathways for hydrogen transport (*i.e.,* porosity) during electrochemical testing. Here, samples annealed at 1100 ºC (Ni-YSZ-NH-1100-R and Ni-YSZ-NH-1100-R) with nickel aggregates present on the surface resulted in fine porous cross-sectional microstructures. No significant differences in the microstructure were observed in the reduced samples which were annealed at 1200 ºC and 1250 ºC (Ni-YSZ-NH-1200-R and Ni-YSZ-NH-1200-R) without the use of the substrate heater during the deposition. In contrast, applying the substrate heater resulted in different microstructures after hydrogen reduction when annealing at 1200 ºC and 1250 ºC (Ni-YSZ-H-1200-R and Ni-YSZ-H-1250-R). While Ni-YSZ-H-1200-R features fine pore channels and a fine network of Ni and YSZ, significantly larger grains and pore channels are observed in Ni-YSZ-H-1250-R.

8.3.2.2 Film composition

The composition of Ni(O)-YSZ films with no heater applied during the deposition, after annealing at 1100 ºC, 1200 ºC and 1250 ºC and the final reduction in hydrogen is illustrated in Table 8.6.

Table 8.6: Composition in mol.% of the as-deposited Ni(O)-YSZ films with no heater applied during the deposition, annealed at 1100 ºC, 1200 ºC and 1250 ºC and reduced in hydrogen.

Sample ID	O/ mol.%	Y/ mol.%	Zr/ mol.%	Ni/ mol.%
Ni-YSZ-NH	45.7	1.2	4.3	48.8
Ni-YSZ-NH-A1100	41.6	1.2	6.1	51.1
Ni-YSZ-NH-A1200	48.5	1.4	5.3	44.8
Ni-YSZ-NH-A1250	53.5	1.6	6.2	38.7
Ni-YSZ-NH-A1100-R	18.9	2.5	9.8	68.8
Ni-YSZ-NH-A1200-R	19.0	2.5	9.5	69.0
Ni-YSZ-NH-A1250-R	21.8	2.6	10.0	65.6

When comparing the nickel concentration within the film after each sample preparation state, it can be clearly seen that with higher annealing temperatures the amount of nickel reduced from 51.1 mol.% at 1100 ºC to 44.8 mol% at 1200 ºC and 38.7 mol.% at 1250 ºC, while the oxygen concentration increased from 41.6 mol% at 1100 ºC to

48.5 mol.% at 1200 ºC and 53.5 mol.% at 1250 ºC. After hydrogen reduction, a considerable decrease in oxygen was observed to 18.9 mol.%, 19 mol.% and 21.8 mol.% at the respective annealing temperatures, resulting in a significant increase in nickel to 68.8 mol.%, 69.0 mol.% and 65.6 mol.% (cf. Ni-YSZ-NH-A1100-R, Ni-YSZ-NH-A1200-R and Ni-YSZ-NH-A1250-R).

The composition of Ni(O)-YSZ films with the substrate heater applied at 400 ºC is displayed after the deposition, annealing at 1100 ºC, 1200 ºC and 1250 ºC and final reduction in hydrogen in Table 8.7.

Table 8.7: Composition expressed in mol.% of as-deposited Ni(O)-YSZ films with applied substrate heater at 400 ºC during the deposition, after annealing at 1100 ºC, 1200 ºC and 1250 ºC and reduction in hydrogen.

Sample ID	O/ mol.%	Y/ mol.%	Zr/ mol.%	Ni/ mol.%
Ni-YSZ-H	44.7	1.2	4.3	49.8
Ni-YSZ-H-A1100	40.2	1.1	4.1	54.6
Ni-YSZ-H-A1200	44.4	1.2	4.8	49.6
Ni-YSZ-H-A1250	48.9	1.2	4.6	45.3
Ni-YSZ-H-A1100-R	8.3	1.1	2.2	88.4
Ni-YSZ-H-A1200-R	17.6	2.0	7.8	72.6
Ni-YSZ-H-A1250-R	20.9	2.3	8.8	68.0

The composition of the two as-deposited samples Ni-YSZ-NH and Ni-YSZ-H is equivalent. In addition, a similar trend can be observed in terms of decreasing nickel concentration after annealing at different temperatures compared to the annealed samples deposited without the use of substrate heating. Yet, there is a drastic increase in nickel concentration to 88.4 mol.% in sample Ni-YSZ-H-A1100-R, which showed excessive surface aggregation of nickel in Figure 1.9.

The final volume fractions of nickel and YSZ within the reduced Ni-YSZ films were calculated by using the density values for nickel and YSZ of 21.55 cm^3/mol and 6.59 cm^3/mol, respectively [166].

Table 8.8: Calculated volume percentages of nickel and YSZ after hydrogen reduction of Ni(O)-YSZ films with and without heater applied during the deposition.

Sample ID	Ni / vol.%	YSZ / vol.%
Ni-YSZ-NH-A1100-R	40.3	59.7
Ni-YSZ-NH-A1200-R	40.5	59.5
Ni-YSZ-NH-A1250-R	36.8	63.2
Ni-YSZ-H-A1100-R	70.0	30.0
Ni-YSZ-H-A1200-R	44.7	55.3
Ni-YSZ-H-A1250-R	39.3	60.7

The calculated volume fractions of Ni and YSZ of the annealed samples after the reduction yield nickel concentration between 37 and 45 vol.%, except for sample Ni-YSZ-H-A1100-R, which showed excessive surface agglomerates of nickel in Figure 1.9, giving 70 vol.% Ni instead.

8.3.2.3 XRD results

Figure 8.13 reveals the XRD results of the as-deposited samples with and without a heater, after annealing at 1200 ºC and subsequent reduction in hydrogen. The comparison of XRD data for samples that were annealed at 1250 ºC can be found in Appendix G.
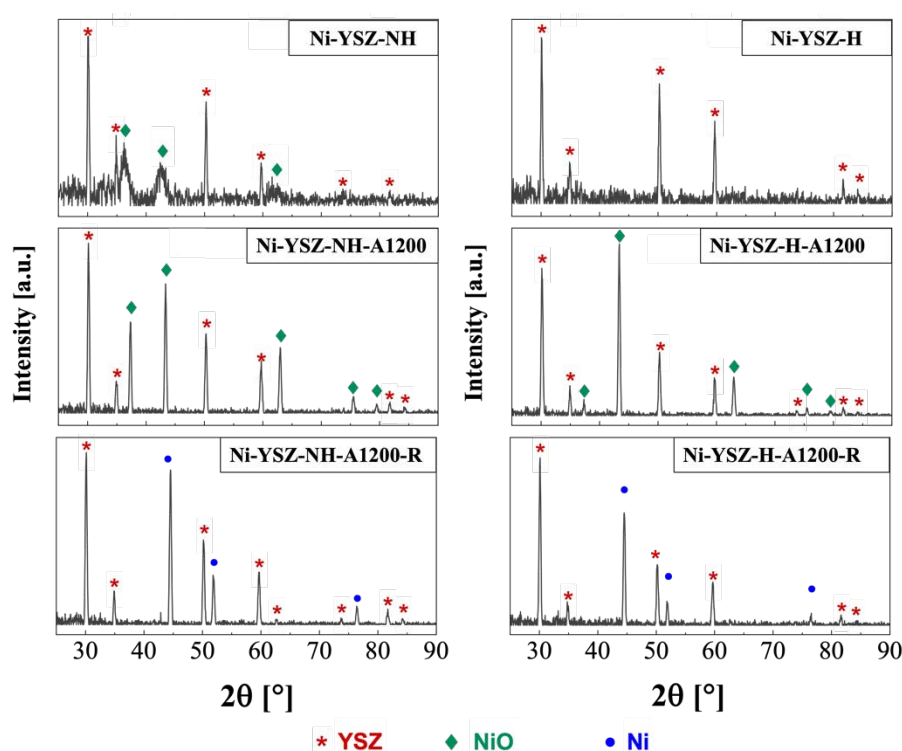
Figure 8.13: XRD patterns of the as-deposited Ni(O)-YSZ films without using a heater (Ni-YSZ-NH) and with a substrate heater (Ni-YSZ-H), after annealing at 1200 ºC in air for 1 h (Ni-YSZ-NH-A1200 and Ni-YSZ-H-A1200) and after subsequent reduction at 850 ºC in 10% H_2/N_2 for 10 h (Ni-YSZ-NH-A1200-R and Ni-YSZ-H-A1200-R).

After the deposition, the XRD patterns were identified as 12 mol.% $((ZrO_2)_{0.88} (Y_2O_3)_{0.12})_{0.893}$ and NiO using the respective COD IDs 1521478 and 1010095 from previous analyses in this work using *HighScorePlus software* [161], [162], [163]. Both samples, Ni-YSZ-NH and Ni-YSZ-H, show strong high-intensity peaks of YSZ (red stars), whereas broad peaks of NiO (green diamonds) were only present in the unheated sample. The YSZ peaks are believed to be due to the use of a YSZ substrate, instead of a silicon wafer in Chapter 7, as it can be seen in the figure below.
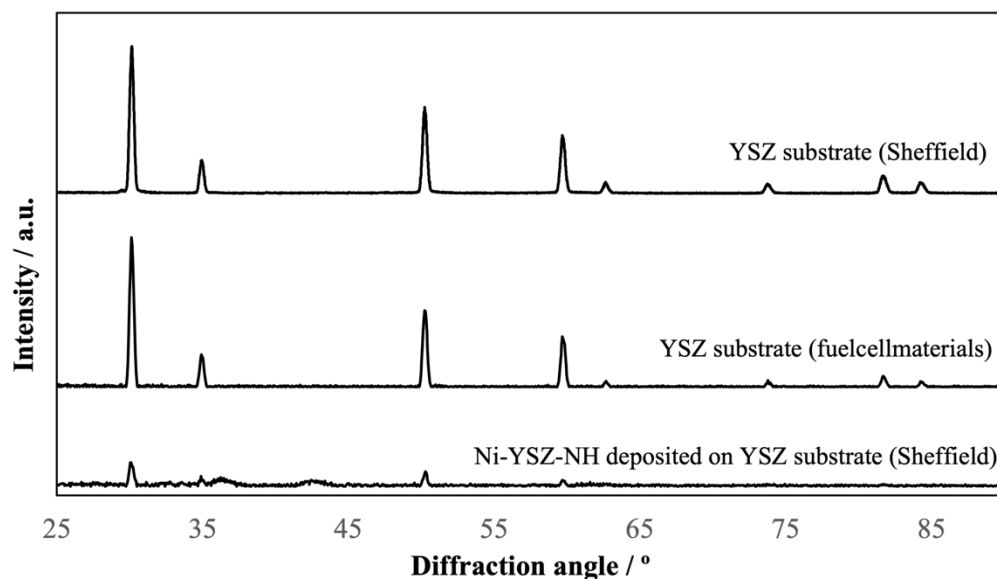
Figure 8.14: Comparison of XRD patterns of used YSZ substrates from the University of Sheffield and *fuelcellmaterials*, USA with as-deposited Ni-YSZ-NH.

Annealing at 1200 ºC resulted in sharp high-intensity peaks of YSZ and NiO. It can also be seen that with the use of the heater during the deposition, the intensity of NiO(200) gained significantly, while the intensity of NiO(111) declined. Table 8.9 illustrates the diffraction angle for NiO(111) and Ni(200) in the annealed samples at 1200 ºC with their resulting d-spacing and crystallite size *D*.

Table 8.9: Calculated crystallite size *D* and d-spacing of NiO in the annealed samples (1200 ºC) with and without applying a substrate heater during deposition in nm.

Sample ID	2θ/ º	FWHM/ º	d-spacing/ nm	D/ nm
Ni-YSZ-NH-A1200: NiO(111)	37.3579	0.3444	0.240719	24.4
Ni-YSZ-NH-A1200: NiO(200)	43.3239	0.3444	0.208853	24.9
Ni-YSZ-H-A1200: NiO(111)	37.2787	0.3444	0.241212	24.4
Ni-YSZ-H-A1200: NiO(200)	43.3336	0.3444	0.208808	24.9

The diffraction angles for NiO in the sample deposited without substrate heating indicate a small shift towards higher diffraction angles, resulting in a slightly smaller d-spacing for NiO(111) in the sample (Ni-YSZ-NH-A1200). The smaller d-spacing in this sample causes the lattice to compress which is likely caused by a higher residual stresses state in the film deposited without an applied heater.

After subsequently reducing the annealed samples in hydrogen/nitrogen atmospheres, metallic nickel was identified by the matching COD ID 9013026 from the Crystallography Open Database in *HighScorePlus* [167]. No NiO was seen in the peak patterns

of the reduced samples, instead peaks characteristic of the Ni metal were detected, which confirms the successful reduction from NiO to catalytically active nickel.

The crystallite sizes were calculated according to the Scherrer equation, as presented in section 6.3. As the calculated crystallite size of YSZ(111) yielded 23.9 nm for all samples in the reduced state, the crystallite sizes of Ni(111) and their d-spacings are presented in the table below.

Table 8.10: Calculated crystallite size D and d-spacing of Ni(111) in the reduced samples with and without applying a substrate heater during deposition in nm.

Sample ID	2θ/ °	FWHM/ °	d-spacing/ nm	D/ nm
Ni-YSZ-NH-A1200-R	44.5643	0.3444	0.203324	25.0
Ni-YSZ-NH-A1250-R	44.5283	0.3936	0.203479	21.8
Ni-YSZ-H-A1200-R	44.5773	0.3936	0.203267	21.8
Ni-YSZ-H-A1250-R	44.5197	0.3412	0.203517	25.2

Using the substrate heater and post-annealing at 1200 ºC resulted in the same crystallite size of 21.8 nm as without the heater and post-annealing at 1250 ºC. The unheated sample (Ni-YSZ-NH-A1200-R) annealed at a lower temperature of 1200 ºC had a slightly larger crystallite size of 25 nm while annealing the heated samples at 1250 ºC produced the largest nickel crystallites with a calculated size of 25.2 nm. Considering conventional electrode manufacturing methods, which result in grain growth (coarsening) after the prolonged sintering process, and thus, micron-sized features, even when using nano-sized powders, magnetron sputtering presents the control of the nanostructure of the AFL [168], [169].

Sample Ni-YSZ-H-A1250-R presented the largest shift in the diffraction angle to 44.5197º, resulting in a higher d-spacing of 0.203517 nm compared to the other samples, indicating a greater lattice expansion.

8.3.2.4 XPS results

This section presents the oxidation state of nickel in the Ni2p 3/2 region after deposition, annealing at 1200 ºC and reduction in hydrogen/nitrogen atmospheres for the unheated and heated samples during coating deposition, as displayed in Figure 8.15.
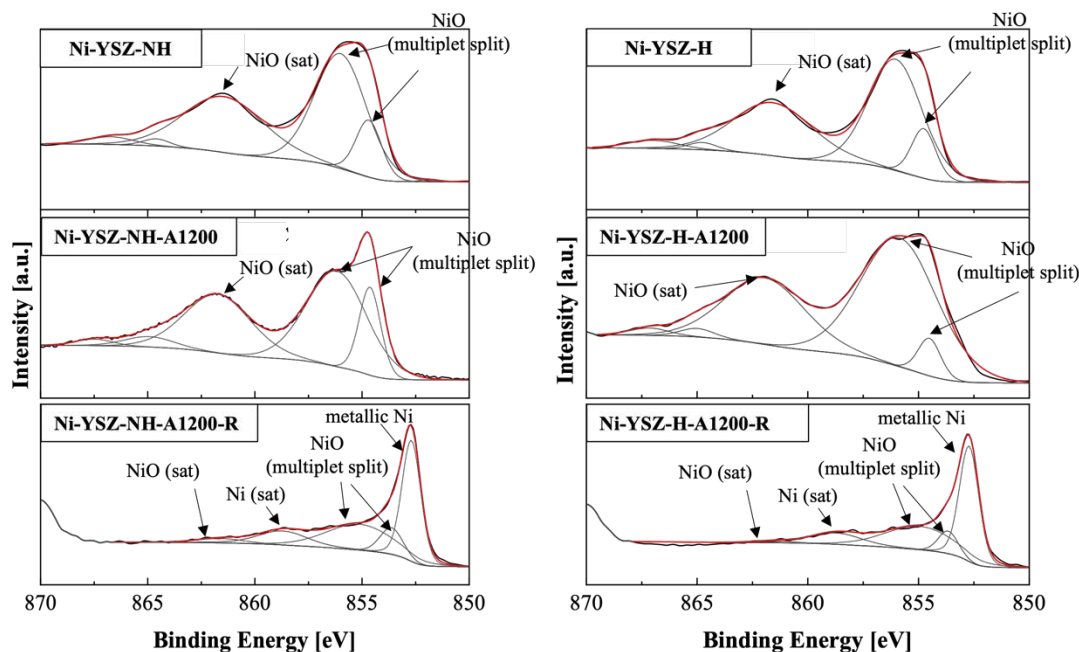
Figure 8.15: Ni 2p$_{3/2}$ XPS spectra of Ni-YSZ-NH (no heater) and Ni-YSZ-H (applied heater at 400 ºC) in as-deposited, annealed (1200 ºC) and reduced state. Peak fitting was performed based on Biesinger *et al.* [147], [170].

The acquired XPS data were fitted based on the work of Biesinger *et al.* regarding their analysis of nickel and nickel oxide in [147], [170]. The results reveal that nickel within the deposited film was present as nickel oxide after reactive sputtering of zirconium-yttrium and nickel. No significant differences in binding energies for the NiO multiplet after deposition were observed between the samples sputtered without the substrate heater and with applying a substrate temperature of 400 ºC, as illustrated in Table 8.11.

Table 8.11: Binding energies in eV of Ni 2p$_{3/2}$ region for nickel oxide and metallic nickel after deposition, annealing at 1200 ºC and hydrogen reduction.

Sample ID	BE for NiO multiplet/ eV	BE for Ni/ eV
Ni-YSZ-NH	854.68| 856.00	-
Ni-YSZ-NH-A1200	854.63| 856.18	-
Ni-YSZ-NH-A1200-R	852.72| 855.22	852.72
Ni-YSZ-H	854.76 856.03	-
Ni-YSZ-H-A1200	854.51| 855.82	-
Ni-YSZ-H-A1200-R	852.72| 855.12	852.72

After annealing at 1200 ºC, the spectrum matched the previous NiO peak fitting, however, the multiplet split of NiO shifted towards a higher binding energy from 855.82 eV to 856.18 eV in the unheated sample during the deposition (cf. Ni-YSZ-NH-A1200 and Ni-YSZ-H-A1200). The shift in binding energy in the annealed sample

without the applied heater is more likely to be stress-related which was already seen in the lower d-spacing in Ni-YSZ-NH-A1200 in the XRD results in Table 8.9.

After hydrogen reduction, both samples show a significant decline in the intensity of the NiO, while a strong peak at a binding energy of 852.72 eV was observed, indicating the reduction of NiO to a metallic nickel which was seen in the XRD results.

8.3.3 Electrochemical characterisation

Figure 8.16 reveals the electrochemical performance of samples deposited with and without substrate heating after annealing at 1200 °C and 1250 °C tested in hydrogen and air fed towards the anode and cathode, respectively.
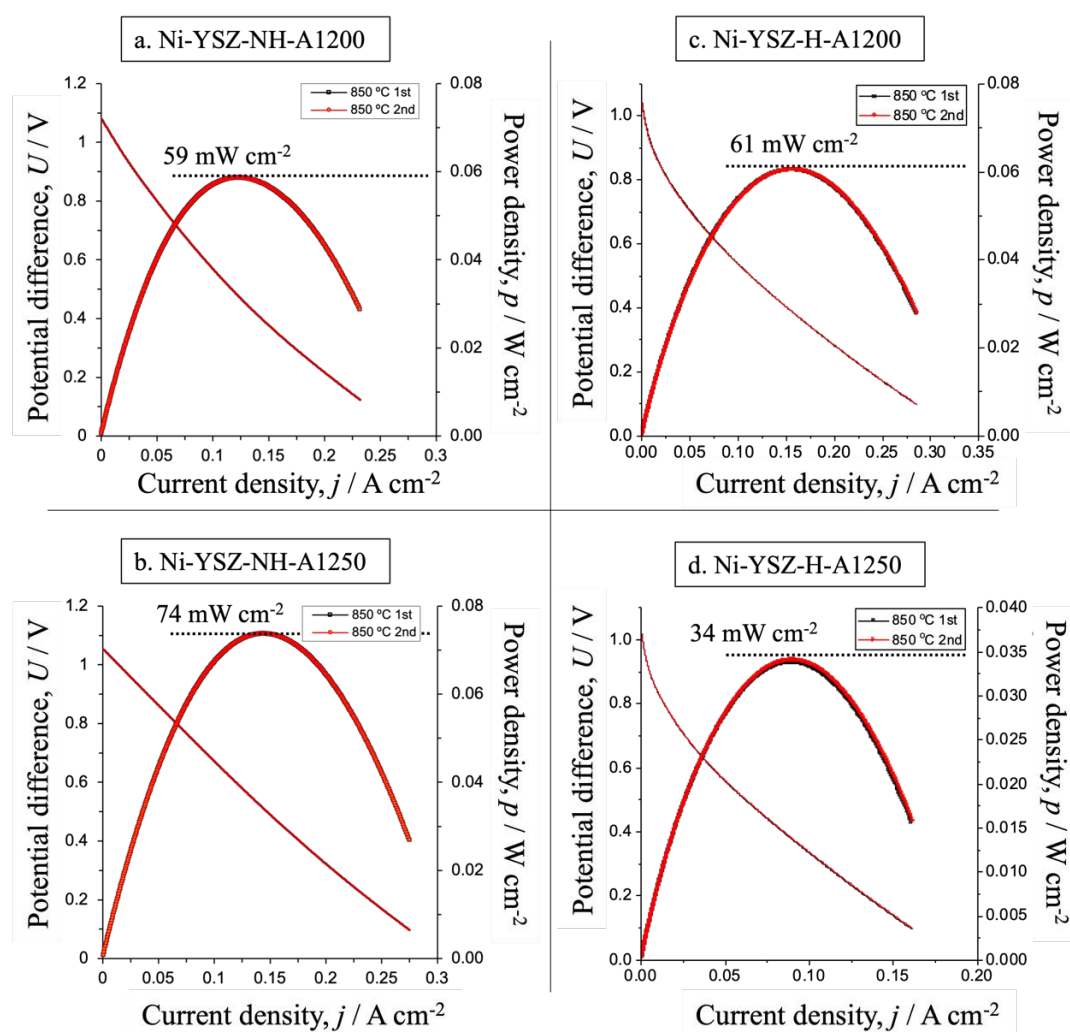
Figure 8.16: Electrochemical performance of Ni(O)-YSZ AFLs at 850 °C tested in 100 sccm 3%-humidified hydrogen and 200 sccm air for anode and cathode, respectively. SOFC button cells with Ni(O)-YSZ AFLs of 3 μm thickness, 150 μm-thick YSZ electrolyte support and 20 μm-thick LSM-YSZ cathode. (a) Ni-YSZ-NH-1200, no heater, annealed at 1200 °C in air for 1 h; (b) Ni-YSZ-NH-1250, no heater, annealed at 1250 °C in air for 1 h; (c) Ni-YSZ-H-1200, heater applied at 400 °C, annealed at 1200 °C in air for 1 h; (d) Ni-YSZ-H-1250, heater applied at 400 °C, annealed at 1250 °C in air for 1 h. *Testing was carried out at Imperial College London.*

The above polarisation curves present an OCV of 1.08 V, 1.05 V, 1.02 V and 1.01 V for Ni-YSZ-NH-A1200, Ni-YSZ-NH-A1250, Ni-YSZ-H-A1200, Ni-YSZ-H-A1250, respectively. The samples which were annealed at 1200 ºC yielded similar power densities of 59 mW cm^{-2} and 61 mW cm^{-2} for Ni-YSZ-NH-A1200 and Ni-YSZ-H-A1200. The sample deposited at a substrate temperature of 400 ºC and post-annealed at 1250 ºC exhibited the lowest performance (cf. Ni-YSZ-H-A1250, 34 mW cm^{-2}), whereas the highest peak power density of 74 mW cm^{-2} was achieved without applying the heating during sample deposition and after postdeposition annealing at 1250 ºC (Ni-YSZ-NH-A1250). Interestingly, samples deposited under a substrate heater presented a slight dip in the polarisation curve at low current densities, which differed from the linear trend observed in samples deposited without substrate heating.

8.3.4 Discussion

When comparing the cross-sectional images of the samples with and without a heater (cf. Figure 8.11 and Figure 8.12), the application of a substrate heater at 400 ºC resulted in denser Ni-YSZ AFLs, which was also noticed by the author through a longer deposition time to achieve a target thickness of 3 μm (7 h compared to 4 h without applied heater at 0.5 bar). Considering the substrate temperature of 400 ºC during deposition and melting temperatures above 2000 ºC or nickel oxide and YSZ, the structure-zone model in section 3.2.2 [122] for sputtering relates to temperature only and does not take into account the simultaneous ion bombardment during magnetron sputtering. However, as both coatings were deposited under the same conditions, except for the substrate temperature, it is unlikely that the energy change associated with the heat generated by the ion bombardment is the dominant cause of the microstructural difference. In contrast, the higher substrate temperature in this work could have facilitated significantly more energy during the deposition, causing diffusion in these samples, and hence, a denser columnar structure in Ni-YSZ-H compared to Ni-YSZ-NH.

Overall, the Ni-YSZ AFLs contained 37-45 vol.% nickel after reduction which is in line with the percolation theory of a minimum of 32 vol.% nickel to facilitate sufficient electrical conductivity through the film, *e.g.*, 90 % of nickel is electrically connected at 44 vol.% nickel [61], [62]. Yet, a loss of 4-5 vol% nickel in both reduced samples was observed when increasing the pre-annealing temperature from 1200 ºC to 1250 ºC (cf. Table 8.8), indicating that nickel is more volatile at higher temperatures. Irrespective of the use of a substrate heater, both samples sintered in air at 1100 ºC presented

Ni agglomerates on the coating surface after hydrogen reduction which were even more predominant when using a substrate heater (cf. Figure 8.8 and Figure 8.9). This corresponds well with the results of the EDS analysis of the reduced sample Ni-YSZ-H-A1100-R which revealed a significantly high nickel content of 70 vol.% (cf. Table 8.8) due to the nickel agglomerates on the coating surface. The growth of nickel agglomerates in Ni-containing thin films for SOFC applications is well studied in [130], [166], [171], [172]. Previous studies by Ionov *et al.* and Solovyey *et al.* investigated magnetron-sputtered NiO-YSZ films unannealed and annealed at 1200 ºC which then underwent hydrogen reduction at 800 ºC [130], [166]. Both studies found massive nickel agglomerates on the coating surface in the unannealed samples. They attributed this phenomenon to the minimisation of the free surface energy and nickel coarsening due to Oswald ripening (transport of volatile nickel via evaporation and condensation). On the other hand, Noh *et al.* annealed NiO-YSZ films deposited via pulsed-laser deposition at three post-annealing temperatures of 1000 ºC, 1100 ºC and 1200 ºC [171]. After a severe reduction in hydrogen for 10 h, samples annealed at 1000 ºC and 1100 ºC still presented nickel agglomerates on the sample's surface. Since Ni agglomerates were found pushed out of cracks in the films annealed at 1000 ºC, they concluded that the mechanism was not simply due to the evaporation and condensation of nickel but was dependent on the strength of the surrounding YSZ matrix [172]. Although no study could explain the exact predominant mechanism, the findings revealed that post-annealing temperatures higher than 1200 ºC are effective in suppressing Ni agglomeration in Ni(O)-YSZ films and thus, preventing a decreased Ni catalyst loading in the remaining AFL. Ni(O)-YSZ films deposited in the present work confirm the successful suppression of nickel aggregation when pre-annealing at 1200 ºC and 1250 ºC compared to 1100 ºC. Therefore, electrochemical testing was conducted on samples pre-annealed at 1200 ºC and 1250 ºC.

The results of the 1200 ºC pre-annealed films indicate that the electrochemical performance of samples with and without the application of the substrate heater is very similar (Ni-YSZ-H-A1200-R and Ni-YSZ-NH-A1200-R). Compared to sample Ni-YSZ-NH-A1200-R, which had a slightly higher crystallite size of 25 nm and lower Ni content of 40.5 vol.%, Ni-YSZ-H-A1200-R showed smaller grains, a smaller crystallite size of 21.8 nm and a slightly higher nickel content of 45 vol.%. Yet, both samples yielded similar electrochemical performance, suggesting that a smaller crystallite size and higher nickel content do not necessarily give better performance. Instead, it is

more likely that microstructural features play a more significant role in performance, as the sample deposited with substrate heater presented a denser microstructure compared to the open microstructure of Ni-YSZ-NH-A1200-R (cf. Figure 8.11 and Figure 8.12).

When using a pre-annealing temperature of 1250 ºC, the sample deposited without a heater gave the highest electrochemical performance (74 mW cm^{-2}), whereas samples deposited at 400 ºC showed the poorest performance (34 mW cm^{-2}) of Ni-YSZ AFLs in this study (cf. Figure 8.16). The difference in performance is most likely caused by the difference in microstructure, as Ni-YSZ-H-A1250-R had a much coarser and denser microstructure with large grains, possibly leading to a reduced connection within the YSZ network in the AFL, and thus an increased ohmic resistance.

When considering a similar open microstructure that was seen in the cross-sectional micrographs of samples deposited without substrate heating (Ni-YSZ-NH-A1200-R and Ni-YSZ-NH-A1250-R, cf. Figure 8.11), the samples annealed at 1250 ºC resulted in a better performance. Here, the crystallite size in the annealed samples at 1250 ºC was smaller than in the samples annealed at 1200 ºC, which possibly led to the improved performance despite the difference in nickel content (cf. Table 8.8), which was higher in the sample pre-annealed at 1200 ºC.

Furthermore, samples deposited with substrate heating displayed a small dip in the polarisation curve at low current densities, indicating issues of the YSZ network in the AFLs, which could be related to the microstructural design of the two phases in the film. Lu *et al.* investigated the densification of Ni-YSZ films via a particle network model of randomly packed spherical particles derived from 3D reconstructed Ni-YSZ anodes [173]. When analysing the impact of different degrees of densification of Ni-YSZ films containing a minimum of 35 vol. % Ni (percolation threshold), it was found that the density of TPBs is inversely proportional to the densification of the film. They stated that over-densification removes active TPBs due to the smoothing of the surface of Ni particles to achieve thermodynamically favourable conditions. They further claimed that better control of the densification process caused by over-sintering of the microstructure could lead to an increase in TPB density by 70 % with only a 7% change in porosity. The samples deposited at 400 ºC in this work indicated densification due to the increased surface energy during deposition, as mentioned earlier, and a further post-annealing could have resulted in an over-densification of these Ni-YSZ

AFLs, leading to a decline in TPBs and thus, a decreased activity, which was observed in the electrochemical characterisation.

8.3.5 Conclusion

The use of post-annealing temperatures above 1200 ºC for Ni(O)-YSZ films resulted in the successful suppression of nickel agglomerates on the film surface. This work supports the literature that future post-annealing should be carried out at 1200 ºC and 1250 ºC. The utilisation of the substrate heater during deposition produced densified coatings which were over-sintered at 1250 ºC causing large grains and issues within the YSZ network, causing an increased ohmic resistance and therefore, yielded poor electrochemical performance. Open microstructures obtained from the samples without substrate heating yielded good electrochemical performance, as no significant densification of the deposited film was observed after deposition.

All Ni-YSZ anode functional layers (AFLs) in this section were deposited at a pressure of 0.5 Pa. The following study aims to investigate whether a further increase in deposition pressure could result in even more open microstructures and performance improvements.

8.4 Deposition of Ni(O)-YSZ under varied deposition pressures

The results presented in this section show the effect of various deposition pressures on Ni(O)-YSZ film microstructures and electrochemical performance. The microstructure and crystallinity of as-deposited, annealed and reduced Ni(O)-YSZ films are discussed and the impact of the deposition pressure on the SOFC performance of the active functional layers (AFLs) is evaluated.

8.4.1 Experimental

8.4.1.1 Deposition of Ni(O)-YSZ under different deposition pressures

The effect of the deposition pressure on the microstructure and electrochemical performance of Ni-YSZ films was studied by depositing three samples, TP5, TP7 and TP10, which are displayed in Table 8.12, at total deposition pressures of 0.5, 0.7 and 1 Pa, respectively. Ni-YSZ films of 4-micron thickness were deposited onto substrates of YSZ with a diameter of 20 mm (from *fuelcellmaterials, USA* for electrochemical testing, 150 μm thick*,* and from the *University of Sheffield*, *UK* for material characterisation, ca. 800 μm thick) and silicon wafer (p-type (100) orientation, *PI-KEM, UK*), while applying 200 W and 75 kHz (70% duty) onto Ni, 250 W and 75 kHz (70% duty)

onto Zr-Y, respectively, at 0.05 Pa oxygen partial pressure, 12 cm target-substrate distance and a deposition angle of 60° (for both targets).

Table 8.12: Sample IDs of specimens deposited at variable pressures during sputtering.

Sample ID	Total pressure/ Pa
TP5	0.5
TP7	0.7
TP10	1.0

8.4.1.2 Material characterisation of as-deposited, annealed and reduced Ni(O)-YSZ films under varied deposition pressures

Similarly, samples TP5, TP7 and TP10 underwent post-deposition heat treatment at 1200 ºC and 1250 ºC in air for 1 h, followed by subsequent reduction in 10% H_2/N_2 atmosphere at 850 ºC for 10 h. The sample IDs are listed in Table 8.13.

The SEM of the top surface and the cross section, as well as EDS and XRD analyses, were conducted after each individual state, *i.e.*, as-deposited, annealed and reduced. The EDS was performed on as-deposited Ni(O)-YSZ samples sputtered onto YSZ and Si substrates to rule out picking up the signal from the underlying YSZ substrate in the annealed and reduced samples.

Table 8.13: Sample IDs of specimens deposited at variable pressures after annealing and reduction in hydrogen.

Sample ID	Total pressure/ Pa	Annealing / ºC	Reduction in H_2/ ºC
TP5-A1200	0.5	1200	-
TP5-A1250	0.5	1250	-
TP7-A1200	0.7	1200	-
TP7-A1250	0.7	1250	-
TP10-A1200	1.0	1200	-
TP10-A1250	1.0	1250	-
TP5-A1200-R	0.5	1200	850
TP5-A1250-R	0.5	1250	850
TP7-A1200-R	0.7	1200	850
TP7-A1250-R	0.7	1250	850
TP10-A1200-R	1.0	1200	850
TP10-A1250-R	1.0	1250	850

8.4.1.3 Electrochemical characterisation of Ni(O)-YSZ films under varied deposition pressures

Electrochemical testing was carried out similarly to the previous parameter study in section 8.3, where YSZ substrates with NiO-YSZ AFLs were annealed in air for 1 h and coated with a 20 μm-thick layer of LSM-YSZ (50:50 wt.%) ink (*fuelcellmaterials*, USA). The cathode layer was applied by doctor blading and dried on a heating plate

at 100 ºC for 1 h. The dried LSM-YSZ-NiO/YSZ electrodes were then sintered in air at 1100 ºC for 1 h prior to electrochemical cell testing.

The electrochemical tests of the AFLs were carried out under 100 sccm 3%-humidified hydrogen (H$_2$ purity N5, 99.999%) and 200 sccm air at an operating temperature of 850 ºC at Imperial College London.

The best-performing the Ni(O)-YSZ film was then deposited on a commercial SOFC half-cell (NextCell-cathode only, *fuelcellmaterials*, USA) and annealed in air at 1250 ºC for 1 h. Its performance was evaluated against that of a commercial SOFC button cell (NextCell, *fuelcellmaterials*, USA) tested under 100 sccm dry hydrogen (H$_2$ purity N5, 99.999%), and 100 sccm oxygen (O$_2$ purity N2.6, 99.6%) at an operating temperature of 850 ºC. This test was performed in-house by using the developed gas manifolds in this work.

8.4.2 Material characterisation

8.4.2.1 Coatings microstructure

Figure 8.17 and Figure 8.18 show the SEM top surface micrographs of the deposited samples TP5, TP7 and TP10 for as-deposited, pre-annealed at 1200 ºC (Figure 8.17) and 1250 ºC (Figure 8.18) and subsequent reduced states.
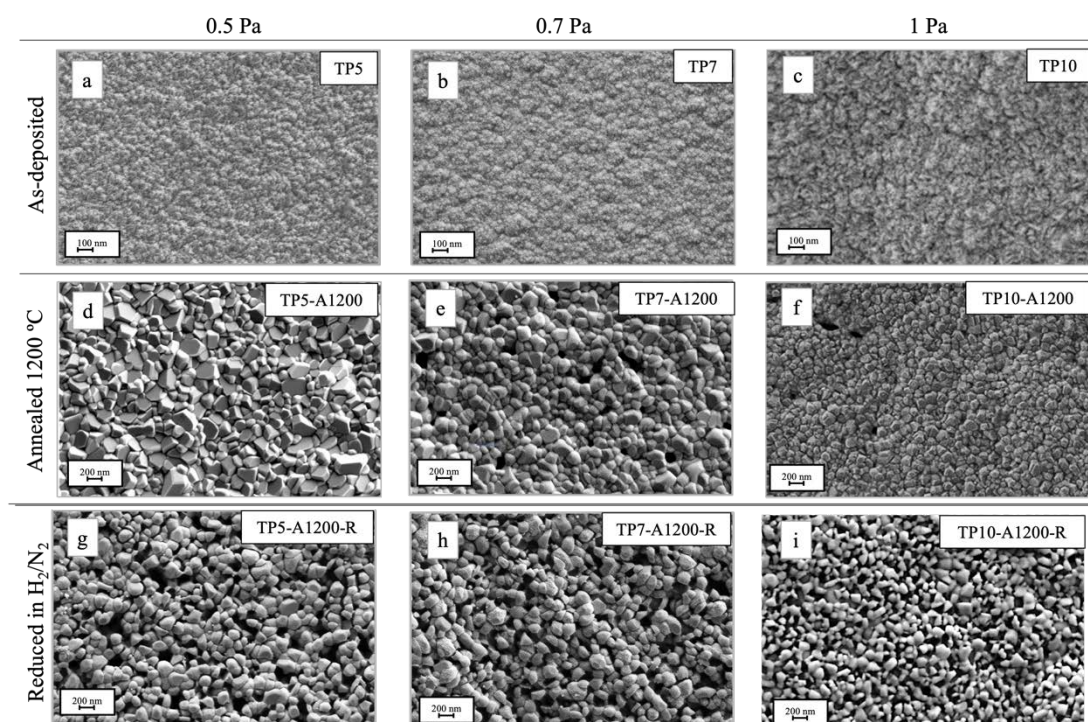
Figure 8.17: SEM images of top surfaces of Ni(O)-YSZ at different deposition pressures of 0.5 Pa (a, d, g), 0.7 Pa (b, e, h) and 1 Pa (c, f, i); as-deposited (a-c), annealed at 1200 ºC in air for 1 h (d-f) and subsequently reduced at 850 ºC in 10% H_2/N_2 for 10 h (g-i).
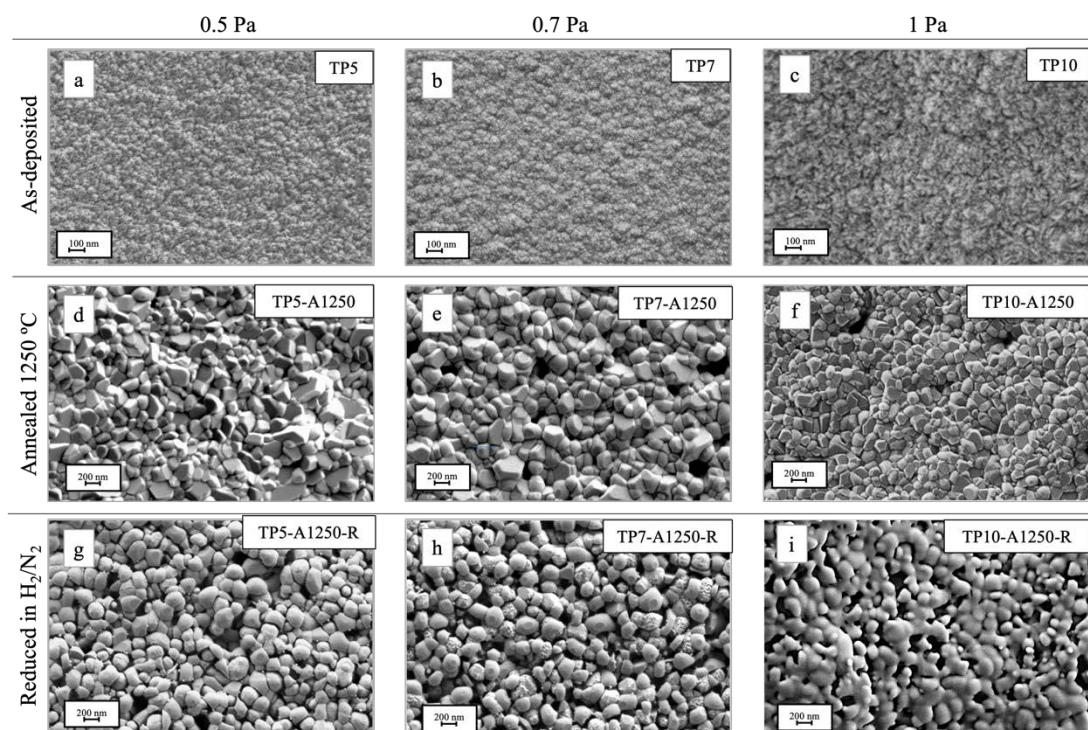
Figure 8.18: SEM images of top surfaces of Ni(O)-YSZ at different deposition pressures of 0.5 Pa (a, d, g), 0.7 Pa (b, e, h) and 1 Pa (c, f, i); as-deposited (a-c), annealed at 1250 ºC in air for 1 h (d-f) and subsequently reduced at 850 ºC in 10% H_2/N_2 for 10 h (g-i).

The top surface exhibits small columnar grains at a deposition pressure of 0.5 Pa, whereas the grain size of these columns increases at higher pressures of 0.7 Pa and 1 Pa in TP7 and TP10, respectively. Increasing the sintering temperature from 1200 ºC to 1250 ºC, resulted in grain growth which was observed in all annealed samples (Figure 8.17 and Figure 8.18). In addition to that, samples deposited at 0.5 Pa and 0.7 Pa presented a similar top surface after annealing at 1200 ºC and 1250 ºC (TP5-A1200 and TP7-A1200; TP5-A1250 and TP7-1250), whereas the sample deposited at 1 Pa produced a top surface with slightly finer grains. After subsequent reduction in H_2/N_2 atmospheres, the top surface images show an open porosity and indicate the same trend which was seen in the annealed samples with regard to the grain size at different deposition pressures.

The cross-sectional SEM and BSE micrographs of the deposited samples TP5, TP7 and TP10 are displayed in Figure 8.19 and Figure 8.20 for as-deposited, pre-annealed at 1200 ºC (Figure 8.19) and 1250 ºC (Figure 8.20) and subsequent reduced states.
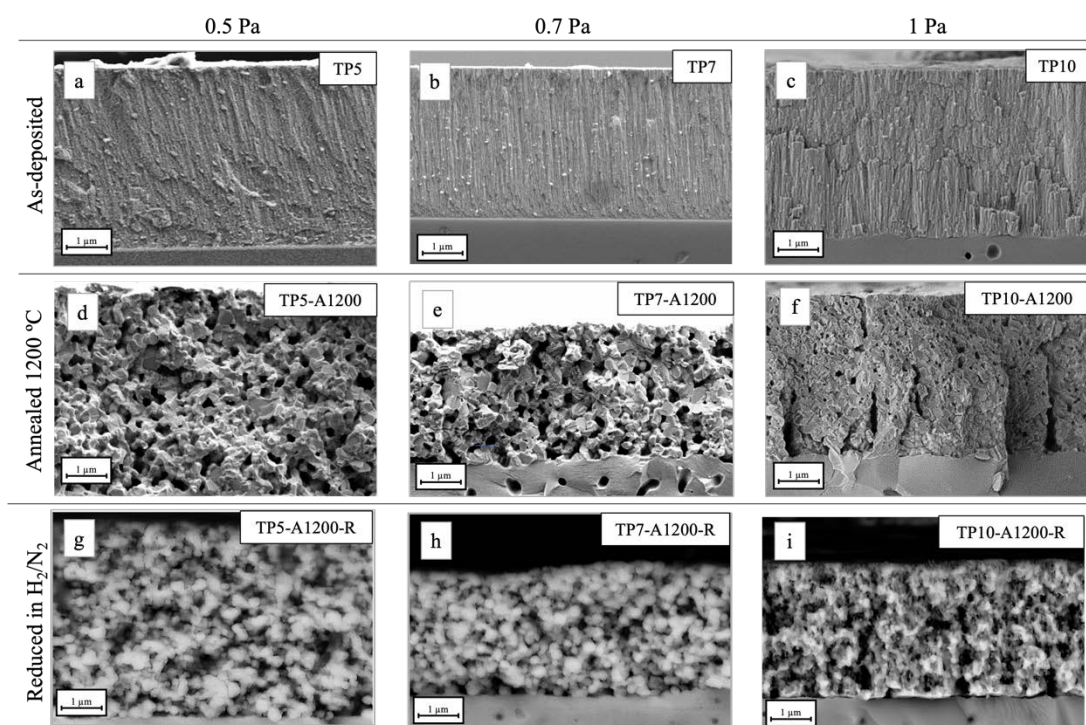
Figure 8.19: SEM images of cross sections of Ni(O)-YSZ at different deposition pressures of 0.5 Pa (a, d, g), 0.7 Pa (b, e, h) and 1 Pa (c, f, i); as-deposited (a-c), annealed at 1200 ºC in air for 1 h (d-f) and subsequently reduced at 850 ºC in 10% H_2/N_2 for 10 h (g-i).

The micrographs after deposition present a columnar microstructure for the samples TP5, TP7 and TP10 which do not indicate any significant differences. Annealing in air

at 1200 ºC resulted in a coarse microstructure with spherical distributed voids seen in the samples TP5-A1200 and TP7-A1200, with TP7-A1200 indicating a slight collapsed film due to the decrease in thickness compared to the as-deposited state. A noticeably finer microstructure with significantly smaller grains was observed in sample TP10-A1200. The subsequent reduction in hydrogen of the samples deposited at 0.5 Pa and 0.7 Pa led to a similar open microstructure of the Ni-YSZ AFLs. However, the cross section of sample TP10-A1200-R displays substantially larger voids within the Ni-YSZ network compared to the other samples.
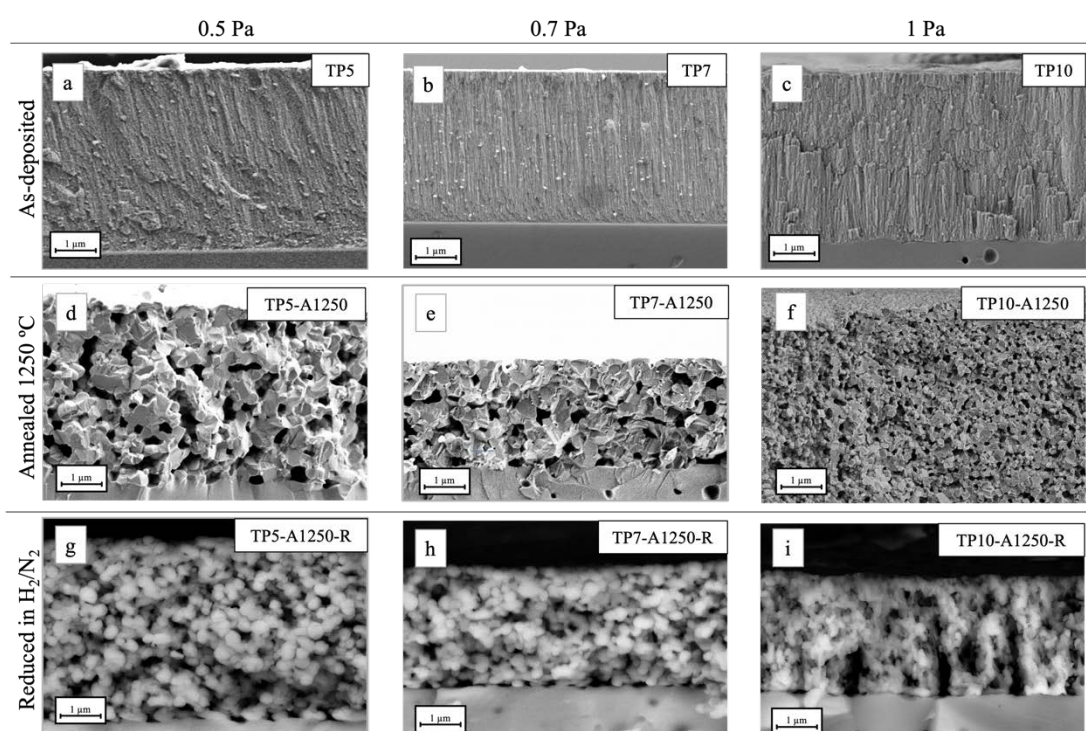
Figure 8.20: SEM images of cross sections of Ni(O)-YSZ at different deposition pressures of 0.5 Pa (a, d, g), 0.7 Pa (b, e, h) and 1 Pa (c, f, i); as-deposited (a-c), annealed at 1200 ºC in air for 1 h (d-f) and subsequently reduced at 850 ºC in 10% H_2/N_2 for 10 h (g-i).

When increasing the annealing temperature to 1250 ºC, the annealed samples TP5-A1250 and TP7-A1250 depict a similar microstructure but larger grain sizes to samples annealed at 1200 ºC. TP7-A1250 exhibits an even more pronounced collapsed coating after post-annealing at 1250 ºC than seen in the cross-section annealed at 1200 º C. TP10-A1250 also presents a significantly finer microstructure compared to the other two samples. The cross sections after hydrogen reduction show similar open microstructures for samples deposited at 0.5 Pa and 0.7 Pa. However, the reduction of

TP10-A1250-R led to even larger voids in the Ni-YSZ microstructure, indicating a higher porosity for gas transport through the thin film.

8.4.2.2 Film composition

The composition data from the EDS analysis of the samples TP5, TP7 and TP10 after the final reduction in hydrogen is listed in Table 8.14.

Table 8.14: Composition of reduced Ni(O)-YSZ films at various deposition pressures of 0.5 Pa, 0.7 Pa and 1 Pa in mol.%.

Sample ID	O/ mol.%	Y/ mol.%	Zr/ mol.%	Ni/ mol.%
TP5-A1200-R	22.4	3.1	11.9	62.6
TP7-A1200-R	21.0	3.7	13.8	61.5
TP10-A1200-R	23.9	2.1	10.7	63.3
TP5-A1250-R	23.5	3.3	12.5	60.7
TP7-A1250-R	22.4	3.5	13.5	60.6
TP10-A1250-R	26.4	2.2	10.3	61.1

All coatings present a similar nickel content in the coating of ca 61-64 mol.%. As seen in previous results in section 8.3.2, after reduction in hydrogen NiO was reduced to metallic nickel, suggesting that the remaining elements of zirconium, yttrium and oxygen indicate the fraction of YSZ within the coating. These results suggest that the change in deposition pressure has no major impact on the composition of the produced Ni-YSZ AFLs.

The volume percentages of nickel and YSZ in these reduced Ni-YSZ AFLs which were deposited at 0.5 Pa, 0.7 Pa and 1 Pa and annealed at either 1200 ºC or 1250 ºC were calculated by using the density values for nickel and YSZ of 21.55 cm^3/mol and 6.59 cm^3/mol, respectively [166], as illustrated in Table 8.15.

Table 8.15: Calculated volume percentages of nickel and YSZ after hydrogen reduction in Ni(O)-YSZ films deposited at various deposition pressures of 0.5 Pa, 0.7 Pa and 1 Pa in vol.%.

Sample ID	Ni / vol.%	YSZ / vol.%
TP5-A1200-R	33.8	66.2
TP7-A1200-R	32.8	67.2
TP10-A1200-R	32.4	67.6
TP5-A1250-R	32.1	67.9
TP7-A1250-R	32.9	67.1
TP10-A1250-R	34.5	65.5

The volume percentages amount to ca. 32-34 vol.% Ni and ca. 66-68 vol.% YSZ in the Ni-YSZ films, which corresponds well with the minimum nickel volume percentage according to the percolation theory in [61], [62]. Previous studies by Garcia-Garcia *et al.* used a nickel content of 50 vol.% to achieve higher electrical conductivity [131], [165]. However, as mentioned in section 2.3.3.1, a high Ni content can cause instability of the microstructure due to a large Ni coarsening [48], whereas a high YSZ ratio avoids significant changes in the bulk dimensions due to a closer CTE to that of the electrolyte and inhibits Ni agglomeration. For that reason, this study was carried out at the minimum percolation threshold for nickel.

8.4.2.3 XRD results

The obtained XRD patterns of the deposited samples TP5, TP7 and TP10 after deposition, annealing at 1250 ºC and subsequent reduction in hydrogen/nitrogen atmospheres is demonstrated in the figure below.
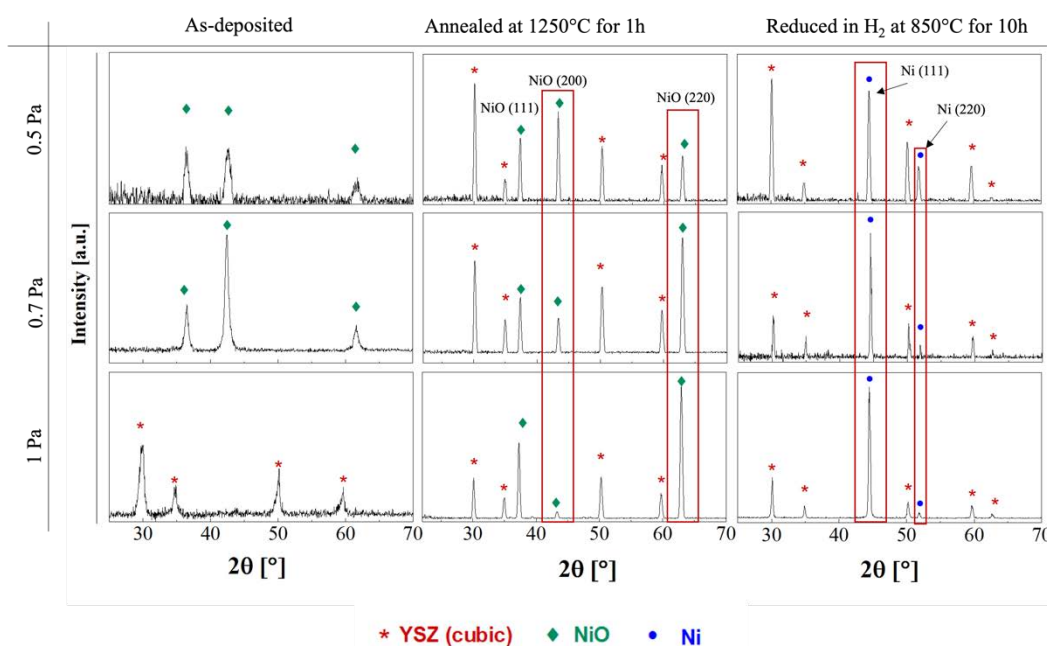
Figure 8.21: XRD patterns of Ni(O)-YSZ films at different deposition pressures of 0.5 Pa, 0.7 Pa and 1 Pa, after annealing at 1250 ºC in air for 1 h and after subsequent reduction at 850 ºC in 10% H_2/N_2 for 10 h.

In the as-deposited state, peak patterns of NiO were observed for samples TP5 and TP7, while TP10 presented peaks for YSZ with no presence of NiO attributed to the increase in deposition pressure. After sintering in air at 1250 ºC for 1 h, sharp high-intensity peaks occurred for NiO and YSZ in all samples. What stands out in the above figure is the decrease in the intensity of NiO(200) and an increase in the intensity of

NiO(220) as the deposition pressure was increased during deposition (annealed, highlighted in red). On reduction of the NiO-YSZ films in hydrogen, the NiO was transformed into catalytically active metallic nickel, as observed in the above figure and the XRD/XPS results of the previous investigation of the substrate temperature in Chapter 8.3. With increasing deposition pressure, the peak intensity of metallic Ni(111) increased, while that of Ni(220) declined significantly. This suggests that nickel was present almost exclusively as a single crystal with the (111) orientation in sample TP10 after undergoing annealing and hydrogen reduction.

In order to investigate the influence of the deposition pressure and the annealing temperature on the structural properties, the d-spacing and crystallite size D of the annealed NiO-YSZ films were determined for the crystal orientations NiO(111) and NiO(200). Table 8.16 illustrates the results of the samples annealed at 1200 ºC, while those of the samples annealed at 1250 ºC are shown in Table 8.17.

Table 8.16: Calculated crystallite size D and d-spacing of NiO in the annealed samples (1200 ºC) deposited at 0.5 Pa, 0.7 Pa and 1 Pa in nm.

Sample ID	$2\theta/$ º	FWHM/ º	d-spacing/ nm	$D/$ nm
TP5-A1200: NiO(111)	37.3579	0.3444	0.240719	24.4
TP5-A1200: NiO(200)	43.3239	0.3444	0.208853	24.9
TP7-A1200: NiO(111)	37.3224	0.3444	0.240939	24.4
TP7-A1200: NiO(200)	43.3358	0.3444	0.208798	24.9
TP10-A1200: NiO(111)	37.2914	0.3444	0.241132	24.4
TP10-A1200: NiO(200)	43.2601	0.3444	0.209146	24.8

Table 8.17: Calculated crystallite size D and d-spacing of NiO in the annealed samples (1250 ºC) deposited at 0.5 Pa, 0.7 Pa and 1 Pa in nm.

Sample ID	$2\theta/$ º	FWHM/ º	d-spacing/ nm	$D/$ nm
TP5-A1250: NiO(111)	37.3447	0.3444	0.240800	24.4
TP5-A1250: NiO(200)	43.3356	0.3936	0.208799	21.7
TP7-A1250: NiO(111)	37.3438	0.3444	0.240806	24.4
TP7-A1250: NiO(200)	43.3404	0.3936	0.208777	21.7
TP10-A1250: NiO(111)	37.2914	0.3444	0.241132	24.4
TP10-A1250: NiO(200)	43.2601	0.3936	0.209146	21.7

The crystallite size of NiO(111) was calculated to be 24.4 nm for all samples, irrespective of the annealing or deposition pressure, whereas crystallites of NiO(200) were present at a size of 24.8-24.9 nm when annealed at 1200 ºC and 21.7 nm at 1250 ºC, regardless of the deposition pressure. This gives evidence that the change in deposition pressure does not affect the crystallite size but influences their orientation, as seen in Figure 8.21.

8.4.3 Electrochemical characterisation

In the following, the electrochemical performance of the Ni-YSZ AFLs deposited at 0.5 Pa, 0.7 Pa and 1 Pa was evaluated under hydrogen and air streams at 850 ºC operation temperature for pre-annealing temperatures of 1200 ºC and 1250 ºC.

8.4.3.1 Electrochemical characterisation after annealing at 1200 ºC

Figure 8.22 presents the polarisation and power density curves for 1250 ºC-pre-annealed Ni-YSZ AFLs.
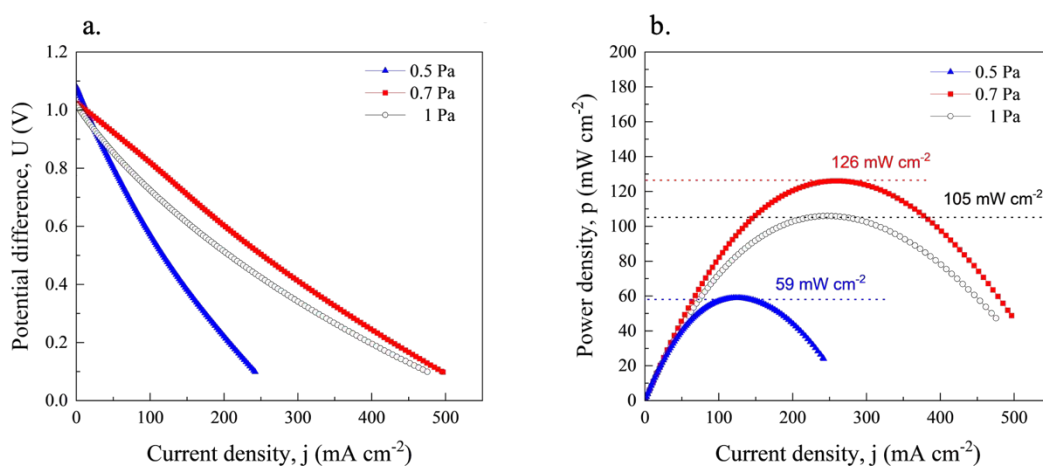
Figure 8.22: Electrochemical performance of Ni(O)-YSZ AFLs deposited at different deposition pressures of 0.5 Pa, 0.7 Pa and 1 Pa, followed by annealing at 1200 ºC in air for 1 h. Tested at 850 ºC in 100 sccm 3%-humidified hydrogen and 200 sccm air for anode and cathode, respectively. Polarisation curves (a) and power density curves (b) for different deposition pressures. *Testing was carried out at Imperial College London.*

The OCV of the samples deposited at 0.5 Pa, 0.7 Pa and 1 Pa yielded 1.08 V, 1.02 V and 1.02 V, respectively, suggesting a sufficient separation of the reactant gases. While the polarisation curve at 0.5 Pa exhibits a steep decline, the curves at 0.7 Pa and 1 Pa present a similar course between cell voltage and current density. Yet, the trend of the sample deposited at 1 Pa indicates a slight dip at low current densities (0-200 mA cm^{-2}), an indication of potential activation losses.

As a result, when increasing the deposition pressure from 0.5 Pa to 0.7 Pa, the maximum power density increased drastically from 59 mW cm^{-2} to 126 mW cm^{-2}. However, a slight reduction in power density to 105 mW cm^{-2} was observed when the Ni-YSZ AFL was deposited at 1 Pa.

8.4.3.2 Electrochemical characterisation after annealing at 1250 ℃.

The electrochemical performance for the samples annealed at 1250 ℃ is presented through the polarisation curves and power density curves shown in Figure 8.23.
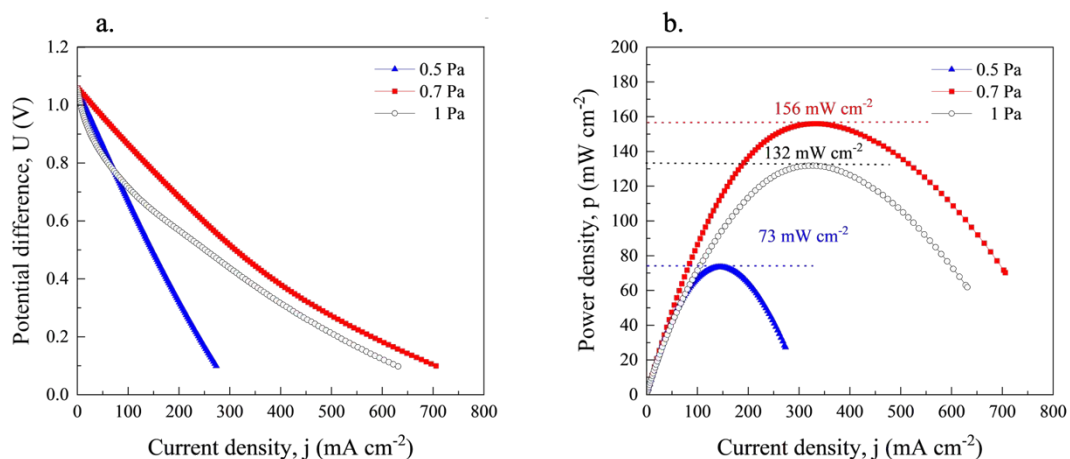
Figure 8.23: Electrochemical performance of Ni(O)-YSZ AFLs deposited at different deposition pressures of 0.5 Pa, 0.7 Pa and 1 Pa, followed by annealing at 1250 ℃ in air for 1 h. Tested at 850 ℃ in 100 sccm 3%-humidified hydrogen and 200 sccm air for anode and cathode, respectively. Polarisation curves (a) and power density curves (b) for different deposition pressures. *Testing was carried out at Imperial College London.*

All samples presented OCVs greater than 1 V (1.06 V, 1.05V and 1.05 V for 0.5 Pa, 0.7 Pa and 1 Pa, respectively). No significant changes in the behaviour of the sample deposited at 0.5 Pa were noted, as the power density increased marginally by 14 mW cm^{-2}. The maximum power density for 0.7 Pa deposited films was improved to 156 mW cm^{-2} by using a higher pre-annealing temperature of 1250 ℃ (increase of 30 mW cm^{-2}). A similar increase in peak power density can be seen in the sample deposited at 1 Pa (from 105 mW cm^{-2} to 132 mW cm^{-2}), suggesting that a higher annealing temperature results in more connected interfaces within the Ni/YSZ network due to higher sintering effect.

However, the dip at low current densities which was also seen in Figure 8.22 when using a pre-annealing temperature of 1200 ℃, is even more pronounced in the 1250 ℃ annealed sample. It should be noted that this sample presented a much higher porosity in the cross-sectional BSE images (cf. Figure 8.20).

8.4.3.3 Comparison of the electrochemical characterisation between commercial SOFC NextCell and Ni(O)-YSZ AFL.

As it is difficult to compare the current electrochemical performance with the literature due to differences in materials (*e.g.,* nickel content), cell design (*e.g.,* electrolyte- or anode-supported SOFCs), cell geometry (*e.g.,* variations in layer thickness) and test setup, the author proposed to evaluate the best-performing Ni-YSZ AFL in this work against a commercial SOFC anode. In this approach, identical electrolyte and cathode characteristics are used and any performance differences can be exclusively attributed to the Ni-YSZ AFL.

Figure 8.24 presents the polarisation curves (a) and power density curves (b) of the Ni-YSZ AFL (deposited at 0.7 Pa and annealed at 1250 ºC) and the commercial NextCell.
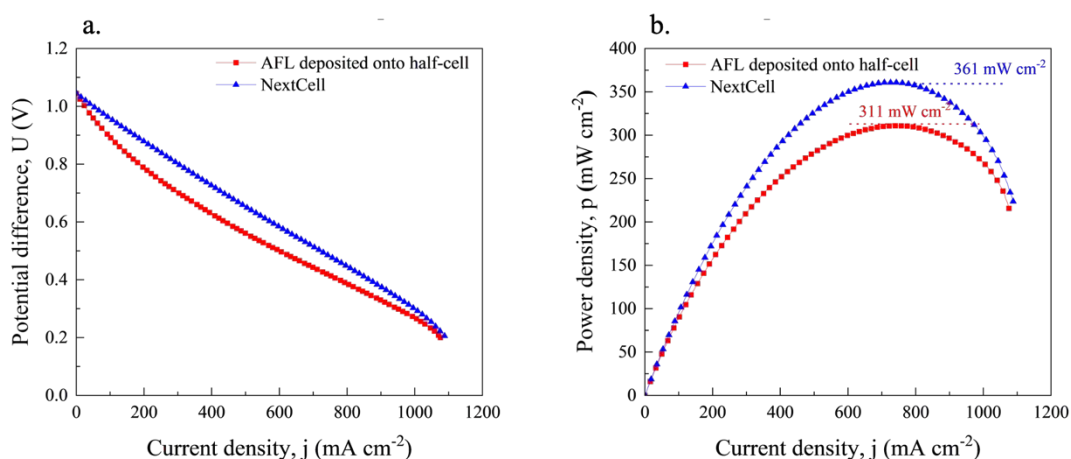
Figure 8.24: Comparison of electrochemical performance between commercial SOFC NextCell and Ni(O)-YSZ AFL deposited at 0.7 Pa onto commercial half-cell (NextCell with cathode only from *fuelcellmaterials, USA)*, annealed at 1250 ºC in air for 1 h prior to testing. Tested at 850 ºC in 100 sccm dry hydrogen and 100 sccm oxygen for anode and cathode, respectively. Polarisation curves (a) and power density curves (b) for different deposition pressures. *Testing was carried out in-house.*

Both polarisation curves show an OCV of 1.05 V and achieve a high current density of ca. 1090 mA cm^{-2} at a minimum cell voltage of 0.2 V, indicating that previous results reporting significantly lower current densities at the minimum cell voltage were influenced by the in-house doctor-bladed cathode layer. The NextCell presents a straight linear curve at low and medium current densities, whereas the AFL shows a slight dip at lower current densities.

The NextCell with a 50 µm-thick anode layer achieved a peak power density of 361 mW cm^{-2} and the created Ni-YSZ AFL with an initial thickness of 4 µm reached

311 mW cm^{-2}. The decrease in performance of the AFL is most likely caused by the dip that can be observed in the polarisation curves at lower current densities, which was reported in the previous results with an in-house-made cathode layer in Figure 8.23.

8.4.4 Discussion

The results of the electrochemical characterisation revealed that the increase in the deposition pressure to 0.7 Pa improved the maximum peak power density drastically. However, a further increase to 1 Pa led to a performance loss. Since the composition data from the analysis showed no significant differences and neither a change in crystallite size was observed, the differences in performance can be attributed to the microstructural features of the coatings at different deposition pressures seen in Figure 8.19 and Figure 8.20. Both polarisation curves of the samples deposited at 1 Pa, in Figure 8.22 and Figure 8.23 demonstrated a slight dip at low current densities which could be caused by potential activation problems. The related SEM micrographs of the cross section in Figure 8.19 and Figure 8.20 showed large voids in the layer, indicating a higher porosity in these samples. As mentioned before, Lu *et al.* used a particle network model to analyse the relationship between microstructural changes of Ni-YSZ anodes regarding porosity and densification [173]. The previous study investigated the effect of using a substrate heater and deposited samples at 0.5 Pa. It was shown that the Ni-YSZ AFLs are underperforming due to the densification of the film which is seen in the samples deposited at 0.5 Pa in this study as well. In addition to the effects of film densification, Lu *et al.* reported that the number of triple-phase-boundaries (TPBs) also slightly decreases due to the shrinkage and detachment of the interfaces between Ni and YSZ. The reduction in TPB density due to a higher porosity could explain the loss in performance that was seen in the samples deposited at 1 Pa.

Comparing the results with the literature, Solovyev *et al.* studied electrolyte-supported SOFC with a 5-μm thick magnetron-sputtered Ni-YSZ AFL, a pasted Ni-YSZ anode and a pasted pure nickel layer, yielding power densities of 210, 90 and 40 mW cm^{-2}, respectively, [166]. They attributed the increase in power density to the nanosized Ni particle of the nanocomposite anode layer, resulting in high catalytic activity. However, they enclosed that the AFL was additionally coated with a 100 μm-thick layer of pure metallic nickel, as the nano-porosity in the initial 5-μm thick Ni-YSZ would not give sufficient electric conductivity due to the narrow paths for the transport of the

reactant gasses. The achieved peak power density of 156 mW cm^{-2} closely matches the reported 210 mW cm^{-2} in the literature. At this point, it cannot be ruled out whether the additional nickel layer caused a slight improvement in the power density or whether the in-house-made cathode caused a performance drop. For that reason, the best-performing AFL deposited at 0.7 Pa and annealed at 1250 ºC has been compared with a commercial SOFC anode by using identical electrolyte and cathode characteristics (NextCell). The 4-µm thick Ni-YSZ AFLs achieved a satisfactory peak power density, 50 mW cm^{-2} less than the 50-µm thick commercial anode, showing that material cost could be significantly reduced by deploying magnetron sputtering as a manufacturing technique.

8.4.5 Conclusion

The best-performing Ni-YSZ AFL was produced by using a deposition pressure of 0.7 Pa to avoid high porosities which would decrease Ni/YSZ interfaces, leading to the decline of triple-phase boundaries and a post-annealing temperature of 1250 ºC to improve the connection of the Ni/YSZ interfaces. The comparison of the performance between AFL and commercial cathode revealed a high peak power density for the AFL. When considering the maximum peak power density as a function of the anode thickness, the resulting volumetric power density for the AFL would yield a significantly higher power density than the commercial anode of the NextCell (62.2 mW cm^{-2}/µm AFL and 7.22 mW cm^{-2}/µm for the NextCell).

The next chapter investigated the addition of dopants into the Ni-YSZ AFL, for which the deposition pressure and post-annealing temperature remained at 0.7 Pa and at 1250 ºC.

9 Doping of state-of-the-art Ni-YSZ AFLs with vanadium and manganese

9.1 Introduction

Since this work aims to advance state-of-the-art AFLs in SOFC anodes by deploying magnetron sputtering as a manufacturing route, the effect of dopants within the previously created Ni-YSZ active functional layer (AFL) is of interest. The present literature review in section 2.3.3 has identified promising candidates, such as vanadium and manganese, to be investigated for their electrochemical performance under hydrogen atmospheres. While authors in [94] reported electrocatalytic activity for vanadium oxides of V_2O_3 and V_2O_5 in thin film SOFCs, studies in [72] presented an increased power density when adding MnO as a dopant into Ni-YSZ anodes (cf. section 2.3.3.2).

The following chapter is divided into two studies, as follows: (i) Firstly, vanadium was added during the deposition of the Ni-YSZ AFL and its influence on the microstructure and electrochemical performance of the Ni-YSZ catalyst was studied; (ii) Secondly, the first study was repeated, replacing vanadium with manganese during the reactive deposition of nickel and zirconium-yttrium, followed by electrochemical testing and materials characterisation.

9.2 Vanadium-doped Ni-YSZ films

9.2.1 Experimental

9.2.1.1 Deposition of vanadium-doped Ni(O)-YSZ

Three samples; 1V-Ni-YSZ, 3V-Ni-YSZ and 5V-Ni-YSZ; were prepared containing 1 mol.%, 3 mol.% and 5 mol% vanadium, respectively, which is displayed in Table 9.1. The V-doped Ni-YSZ films of 4-micron thickness were deposited onto substrates of YSZ with a diameter of 20 mm (from *fuelcellmaterials, USA* for electrochemical testing, 150 μm thick, and from the *University of Sheffield, UK* for material characterisation, ca. 800 μm thick) and silicon wafer (p-type (100) orientation, *PI-KEM, UK*). Identical parameters for the deposition of nickel and Zr-Y from the previous study at 0.7 Pa deposition pressure were applied (cf. section 8.4.1.1, 200 W, 75 kHz (70% duty) onto Ni, and 250 W, 75 kHz (70% duty) onto Zr-Y, at 0.05 Pa oxygen partial pressure, 12 cm target-substrate distance and a deposition angle of 60° for both targets). Due to restrictions of the deposition system (chamber dimensions and maximum applied power due to indirect water cooling), two targets of vanadium were used at 60º

to the normal of the substrate plane and a target-to-substrate-distance of 8 cm. In order to deposit films with the target dopant concentrations of 1 mol.%, 3 mol.% and 5 mol% vanadium, the applied power on the vanadium targets was varied using a set frequency of 100 kHz (55% duty), as shown in the table below.

Table 9.1: Sample IDs of specimens deposited with different vanadium concentrations of 1 mol.%, 3 mol.% and 5 mol.% within the Ni(O)-YSZ film.

Sample ID	Vanadium concentration/ mol.%	Applied power on targets
1V-Ni-YSZ	1	2x 50 W
3V-Ni-YSZ	3	2x 146 W
5V-Ni-YSZ	5	2x 200 W

9.2.1.2   *Electrochemical characterisation of vanadium-doped Ni(O)-YSZ films*

After deposition, the V-doped Ni(O)-YSZ AFLs were annealed in air for 1 h and then coated with a 20 µm-thick layer of LSM-YSZ (50:50 wt.%) ink (*fuelcellmaterials*, USA). The cathode layer was applied by doctor blading and dried on a heating plate at 100 ºC for 1 h. The dried LSM-YSZ-NiO/YSZ electrodes were then sintered in air at 1100 ºC for 1 h prior to electrochemical cell testing.

The electrochemical characterisation was performed under 100 sccm dry hydrogen (H_2 purity N5, 99.999%), and 100 sccm oxygen (O_2 purity N2.6, 99.6%) at an operating temperature of 850 ºC. This test was performed in-house by using the gas manifolds developed in this work. In order to evaluate the performance data of the doped Ni(O)-YSZ films using the in-house test setup, the best-performing undoped Ni(O)-YSZ AFL from the previous chapter (cf. section 8.4.3.3, the Ni(O)-YSZ film deposited at 0.7 Pa and annealed in air at 1250 ºC for 1 h) was retested.

9.2.1.3   *Material characterisation of vanadium-doped Ni(O)-YSZ films*

The influence of the vanadium concentration in the samples 1V-Ni-YSZ, 3V-Ni-YSZ and 5V-Ni-YSZ was analysed regarding their structural properties. Each sample which contained YSZ as the substrate was separated into three sections to undergo individual post-deposition heat treatment at 1250 ºC in air for 1 h, followed by a subsequent reduction in 10% H_2/N_2 atmospheres at 850 ºC for 10 h. The resulting sample IDs can be found in Table 9.2

The SEM images of the top surface and cross-section, as well as EDS and XRD analyses, were conducted after each individual state, *i.e.*, as-deposited, annealed and reduced. In addition to that, XPS analyses were carried out after deposition and TEM

analysis of the cross section of 1V-Ni-YSZ-A1250-R has been outsourced from the University of Manchester.

The EDS analysis was performed on as-deposited samples with YSZ and Si substrates to rule out penetration of the underlying YSZ substrate in the annealed and reduced samples.

Table 9.2: Sample IDs of specimens deposited with different dopant concentrations of 1 mol.%, 3 mol.% and 5 mol.% vanadium after annealing at 1250 °C and hydrogen reduction.

Sample ID	V(as-deposited)/ mol.%	Annealing / °C	H$_2$ reduction/ °C
1V-Ni-YSZ	1	1250	-
3V-Ni-YSZ	3	1250	-
5V-Ni-YSZ	5	1250	-
1V-Ni-YSZ-A1250	-	1250	-
3V-Ni-YSZ-A1250	-	1250	-
3V-Ni-YSZ-A1250	-	1250	-
1V-Ni-YSZ-A1250-R	-	1250	850
3V-Ni-YSZ-A1250-R	-	1250	850
3V-Ni-YSZ-A1250-R	-	1250	850

9.2.2 Electrochemical characterisation

Figure 9.1 reveals the polarisation curves (a) and power density curves (b) of the doped Ni(O)-YSZ films when adding 1 mol.%, 3 mol.% and 5 mol% vanadium to the best-performing undoped Ni-YSZ AFL from the previous study. For comparison, the performance data of the best-performing undoped Ni-YSZ AFL retested using the in-house test station was added to the figure.

All samples presented an OCV greater than 1 V with 1.05 V, 1.07 V and 1.08 V for 1 mol.%, 3 mol.% and 5 mol.% V-doped Ni(O)-YSZ, respectively. What can be clearly observed from the above figure is that the increase in vanadium concentration caused the peak power density to decline, as indicated by the lower performance of 44, 37 and 21 mW cm^{-2} for the respective samples, compared to the 75 mW cm^{-2} recorded for the undoped Ni-YSZ AFL.
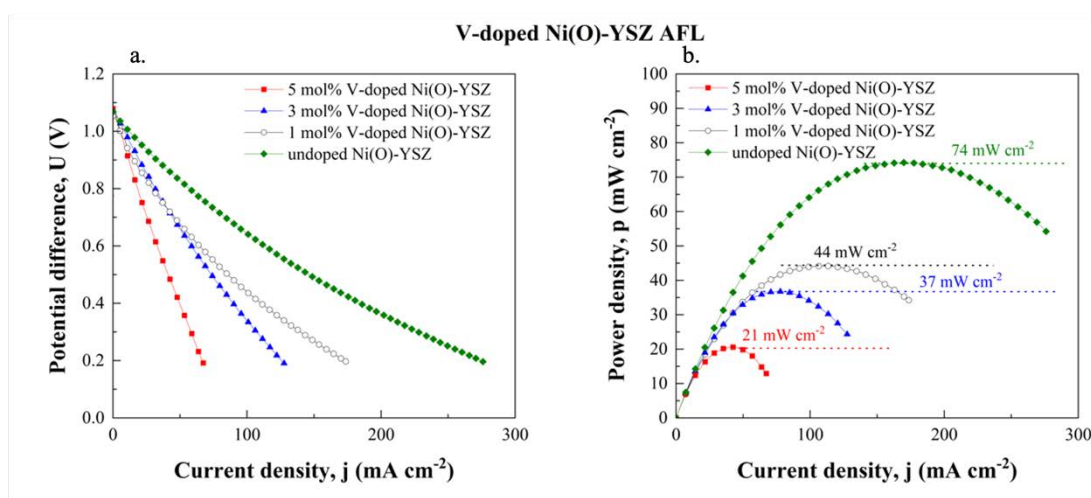
Figure 9.1: Electrochemical performance of vanadium-doped Ni-YSZ AFLs deposited with different dopant concentrations of 1 mol.%, 3 mol.% and 5 mol.%., tested at 850 °C in100 sccm dry hydrogen and 100 sccm oxygen for anode and cathode, respectively. Polarisation curves (a) and power density curves (b). *Testing was carried out in-house. Undoped sample was deposited at 0.7 Pa and annealed at 1250 ℃ in air for 1 h retested in-house for reference.*

9.2.3 Material characterisation

In the following sections, the results of the material characterisation are presented, in order to understand and explain the performance losses seen in the V-doped Ni-YSZ AFLs compared to the undoped Ni-YSZ AFLs, as illustrated in Figure 9.1.

9.2.3.1 Coatings microstructure

The SEM cross section and top surface micrographs of the samples doped with 1 mol.%, 3 mol.% and 5 mol.% vanadium are demonstrated in Figure 9.2.
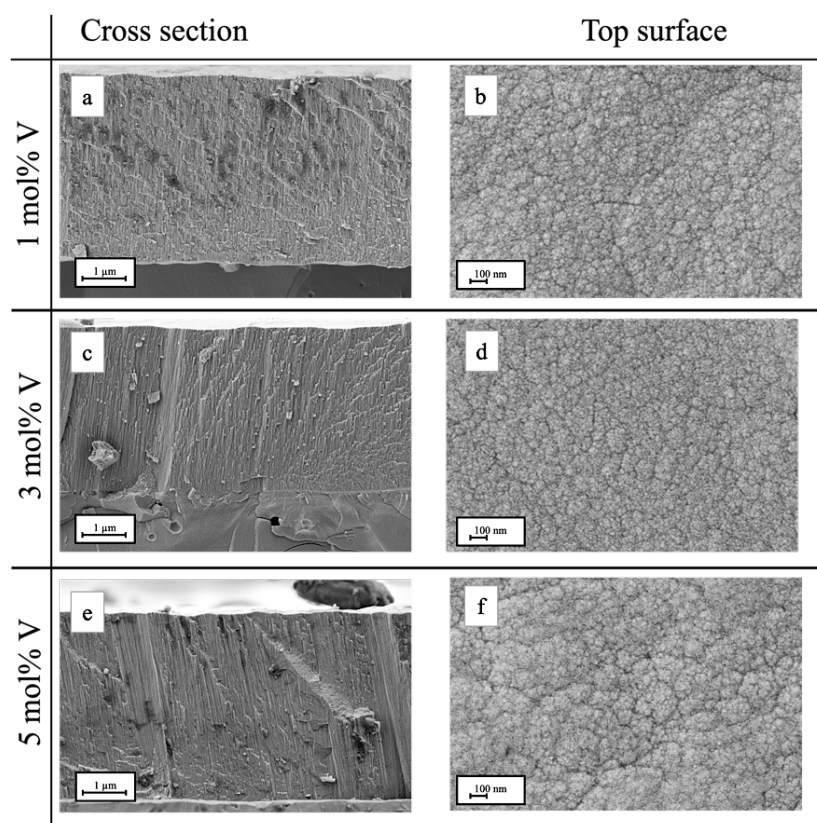
Figure 9.2: SEM images of fractured sections (a, c, e) and top surfaces (b, d, f) of as-deposited vanadium-doped Ni(O)-YSZ films at different dopant concentrations of 1 mol.% V (a, b), 3 mol.% V (c, d) and 5 mol.% V (e, f).

The cross-section images of the deposited samples (a), (c) and (e) present dense columnar films without significant differences observed when increasing the vanadium concentration in the film. The top surface micrographs indicate a potential increase in the grain size at 5 mol.% vanadium.

The changes in the microstructure in the three samples with the initial vanadium concentrations of 1 mol.%, 3 mol.% and 5 mol.% V were visible after the post-deposition annealing in air at 1250 °C, and are shown in Figure 9.3.
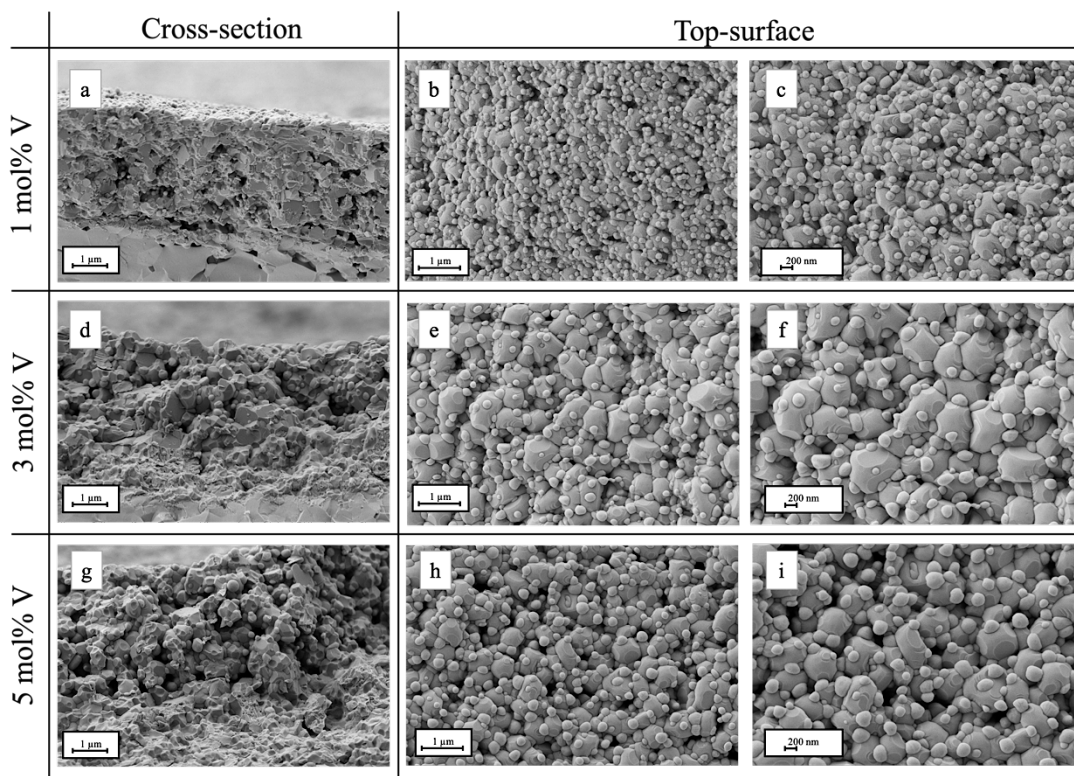
Figure 9.3: SEM images of fractured sections (a, d, g) and top surfaces at different magnifications (b, c, e, f, h, i) of vanadium-doped Ni(O)-YSZ films after the annealing in air at 1250 °C for 1 h deposited with different initial dopant concentrations of 1 mol.% V (a, b, c), 3 mol.% V (d, e, f) and 5 mol.% V (g, h, i).

The microstructures in the cross-sectional SEM images in (d) and (g) exhibit noticeably coarser features with smaller spherical particles attached. The decoration of these particles is even more pronounced in the top surface micrographs in all samples. As the initial concentration of vanadium increases, so does the size of the smaller spherical particles and the grain size of the surrounding matrix (cf. b-e-h and c-f-i). This phenomenon was not previously seen in the results of undoped Ni(O)-YSZ films after annealing (cf. Figure 8.20, TP7-A1250).

After a subsequent reduction in hydrogen, the microstructure of all three vanadium-doped samples transformed into a porous film with finer particle sizes, as shown in Figure 9.4.
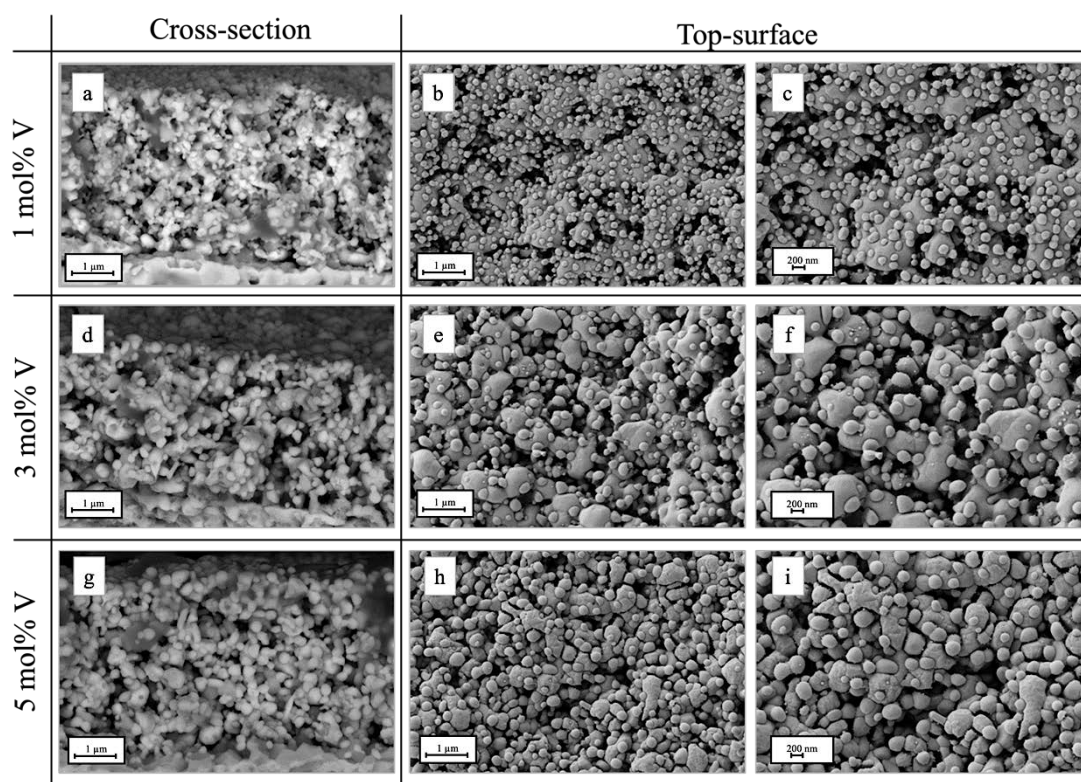
Figure 9.4: BSE images of fractured sections (a, d, g) and top surface images at different magnifications (b, c, e, f, h, i) of vanadium-doped Ni(O)-YSZ films after annealing in air at 1250 ºC for 1 h and subsequent reduction in 10% H_2/N_2 at 850 ºC for 10 h with different dopant concentrations of 1 mol.% V (a, b, c), 3 mol.% V (d, e, f) and 5 mol.% V (g, h, i).

No changes in the appearance of the spherical particles were observed between samples doped with different amount of V when comparing the BSE images in (c), (f), and (i) with each other. Following the annealing and hydrogen reduction, the particles were still disconnected from each other and attached to the coarser structures, as visible in the top surface images, suggesting that no further reaction between these spheres took place under a hydrogen atmosphere. Moreover, there is an apparent grain growth visible in the spheres with higher vanadium loadings, which causes the porosity to decrease slightly in (c), (f), and (i).

In order to perform phase identification on these disconnected spherical particles, elemental maps were generated using EDS analysis. Figure 9.5 illustrates the elemental map for 3 mol.% V-doped Ni(O)-YSZ films after hydrogen reduction.
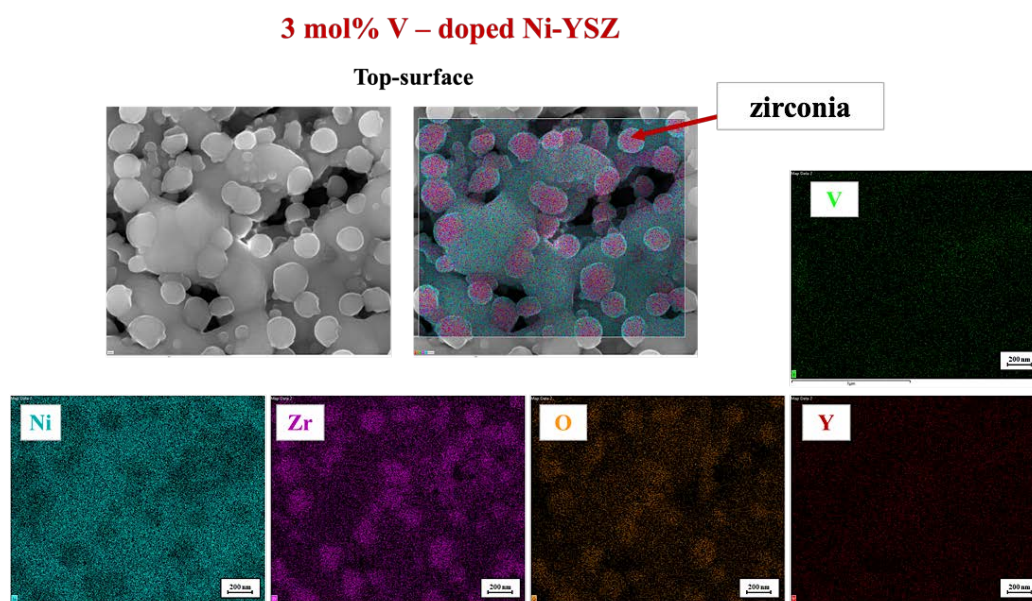
Figure 9.5: Elemental mapping collected from the top surface of 3V-Ni-YSZ-A1250-R using EDS. 3V-Ni-YSZ-A1250-R was initially doped with 3 mol.% V, subsequently annealed at 1250ºC in air for 1 h and reduced in hydrogen for 10 h.

The detached spherical particles can be identified as zirconia, as evidenced in elemental Zr and O maps in Fig. 9.5. The elemental maps did not give a clear indication of the presence of yttrium and vanadium. Therefore, no further information about the structure of zirconia can be provided at this stage, nor can any assumptions be made about the presence of vanadium within the coating structure.

Furthermore, the coarser structure to which the spheres are attached can be identified as nickel. The spheres do not form a network that could serve as a conduction pathway, as seen in the EDS maps of undoped Ni-YSZ AFLs (Chapter 8.4), which are shown in Appendix H for comparison.

9.2.3.2 *Film composition*

The composition data of the deposited V-doped Ni(O)-YSZ films, were acquired by EDS to investigate whether the concentration of vanadium differs after the subsequent process stages of annealing and hydrogen reduction, which can be found in Table 9.3.

The initial dopant concentrations for as-deposited 1V-Ni-YSZ, 3V-Ni-YSZ and 5V-Ni-YSZ are 1.2, 3.3 and 5.2 mol.% vanadium, respectively, confirming the targeted composition of vanadium in the Ni(O)-YSZ films of 1, 3 and 5 mol.% V. While the mol percentages for Ni and (Zr+Y) do not show significant deviations (max. < 1.5 mol.%), the amount of oxygen in the film decreased from 54 mol.% to 48 mol.%

with higher vanadium concentrations. This suggests that not enough oxygen, which was limited by the oxygen partial pressure, during the deposition was supplied at higher magnetron powers on the vanadium targets.

Table 9.3: Composition in mol.% of the deposited V-doped-Ni(O)-YSZ films with different vanadium concentrations of 1 mol. %, 3 mol.% and 5 mol.%, after deposition, annealing at 1250 ºC and reduction in hydrogen.

Sample ID	Ni	Zr	Y	V	O
1V-Ni-YSZ	38.5	5.7	0.8	1.2	53.9
3V-Ni-YSZ	40.0	6.0	0.8	3.1	50.1
5V-Ni-YSZ	39.2	6.9	0.7	5.2	48.0
1V-Ni-YSZ-A1250	42.3	6.0	0.9	0.7	50.4
3V-Ni-YSZ-A1250	38.4	5.7	0.3	0.6	54.9
5V-Ni-YSZ-A1250	34.2	7.0	0.7	1.1	57.0
1V-Ni-YSZ-A1250-R	68.0	10.3	0.9	1.2	19.6
3V-Ni-YSZ-A1250-R	71.2	8.8	0.6	1.3	18.1
5V-Ni-YSZ-A1250-R	55.9	11.8	1.1	1.8	29.4

After annealing at high temperatures, the dopant concentration dropped sharply to 0.7, 0.6 and 1.1 mol.% for 1V-Ni-YSZ-A1250, 3V-Ni-YSZ-A1250 and 5V-Ni-YSZ-A1250, respectively, leading to the assumption that the deposited vanadium was partially volatile during the sintering. The slight decline in nickel content and gain in oxygen can also be observed, which was also seen in the previous studies (cf. Figure 8.6, Ni-YSZ-NH-A1250) and thus, the cause of this change could be unrelated to the dopant.

The composition of the samples 1V-Ni-YSZ-A1250-R, and 3V-Ni-YSZ-A1250-R after hydrogen reduction is comparable, highlighting the presence of vanadium in the reduced state (1.2-1.3 mol.% V) unlike shown in the elemental map in Figure 9.5. Interestingly, sample 5V-Ni-YSZ-A1250-R contains additionally 10 mol.% more oxygen but 12-15 mol.% less nickel compared to the other samples. On the contrary, previous results reported an increase in nickel and a decrease in oxygen when reducing under hydrogen atmospheres (cf. Figure 8.6, Ni-YSZ-NH-A1250-R). Hence, the present observation could indicate the possible existence of a new phase formation that might retain more oxygen within the film.

9.2.3.3 XPS results

In order to understand any possible phase transformation at high temperatures that might have occurred in the deposited films due to the addition of vanadium in the Ni(O)-YSZ films, it is crucial to identify the oxidation state of vanadium at the time

of deposition. For that reason, XPS spectra were obtained from the as-deposited V-doped Ni(O)-YSZ films, which are demonstrated in Figure 9.6.
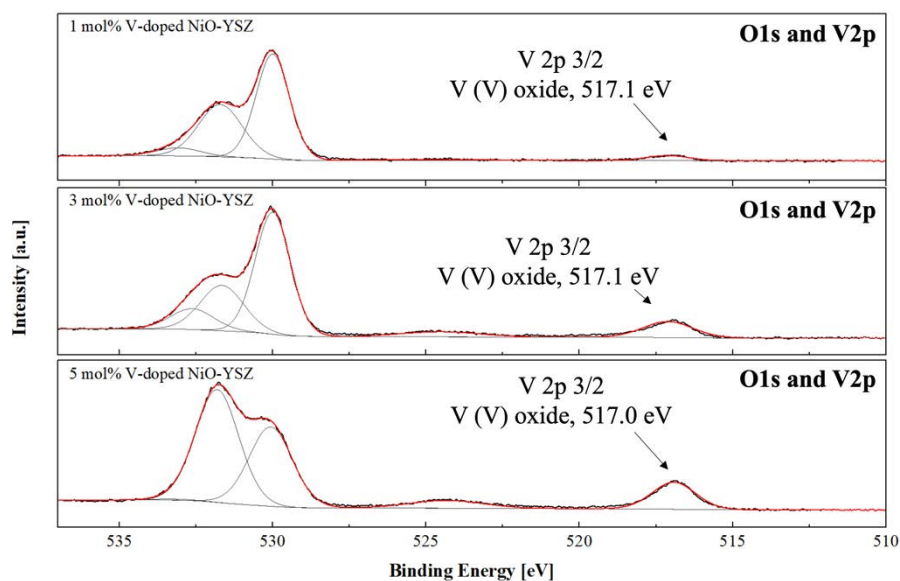
Figure 9.6: O 1s and V2p XPS spectra for as-deposited samples 1V-Ni-YSZ, 3V-Ni-YSZ and 5V-Ni-YSZ with 1 mol.%, 3 mol.% and 5 mol.% V, respectively, indicating the deposition of V_2O_5 as indicated by the peak positions for V(V) at 517.0 and 517.1 eV.

For the accurate peak fitting, the V2p and O 1s regions scans were simultaneously collected. Biesinger *et al.* reported binding energies in the V 2p3/2 region for V(V) at 517.16 ±0.01 eV and for V(IV) at 515.6 ±0.07 eV after the data were charge-corrected to the O 1s peak at 530.0 eV [174]. To compare the obtained XPS data for 1V-Ni-YSZ, 3V-Ni-YSZ and 5V-Ni-YSZ with the literature, the data in the above figure were also referenced to O 1s at 530 eV, yielding the binding energies for V being 517.1, 517.1 and 517.0 eV for the as-deposited samples with 1 mol%, 3 mol.% and 5 mol.% vanadium, respectively. The peak positions in all three samples matched that of V(V), revealing that the Ni(O)-YSZ films were most likely doped with V_2O_5 during the deposition.

9.2.3.4 XRD results
Figure 9.7 presents the XRD patterns of the sample 1V-Ni-YSZ, 3V-Ni-YSZ and 5V-Ni-YSZ after deposition, annealing in air at 1250 ºC and subsequent reduction in hydrogen/nitrogen atmospheres, respectively.

While only NiO and YSZ peaks are observed after the deposition, as seen previously in this work, the peak patterns after annealing at high temperatures revealed an additional phase present in all three samples, which can be identified by the COD ID 9011137 from the Crystallography Open Database in *HighScorePlus* as yttrium vanadate [175] (cf. light blue squares for $Y(VO_4)$ in Figure 9.7).
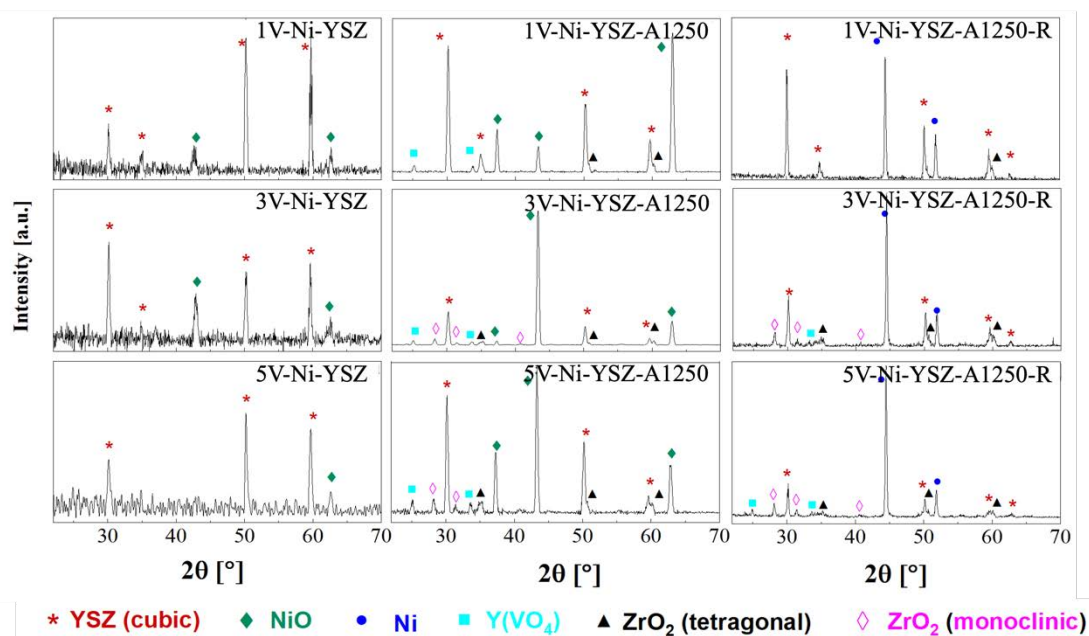
Figure 9.7: XRD patterns of V-doped Ni(O)-YSZ films using different dopant concentrations of 1 mol.% V (1V-Ni-YSZ), 3 mol.% V(3V-Ni-YSZ) and 5 mol.% V(5V-Ni-YSZ), after annealing at 1250 ºC in air for 1 h (1V-Ni-YSZ-A1250, 3V-Ni-YSZ-A1250 and 5V-Ni-YSZ-A1250) and after subsequent reduction at 850 ºC in 10% H_2/N_2 for 10 h (1V-Ni-YSZ-A1250-R, 3V-Ni-YSZ-A1250-R and 5V-Ni-YSZ-A1250R).

Furthermore, in addition to $Y(VO_4)$, the samples 3V-Ni-YSZ-A1250 and 5V-Ni-YSZ-A1250 show peak patterns of monoclinic and tetragonal zirconia that have been identified by the COD IDs 9016714 and 1521477, respectively [162], [176]. No presence of monoclinic zirconia was seen when doping with an initial V concentration of 1 mol.% in sample 1V-Ni-YSZ-A1250.

These findings suggest that the yttrium (Y^{3+}) used in the film to stabilise the cubic structure of zirconia (YSZ), reacted with vanadium (V^{5+}) present as V_2O_5 (cf. XPS analysis in Figure 9.6), forming yttrium vanadate $[Y^{3+}(V^{5+} (O^{-2})_4)]$.

After hydrogen reduction, nickel oxide was reduced to metallic nickel as seen in the previous chapter. The films deposited with 3 and 5 mol.% vanadium (3V-Ni-YSZ-A1250-R and 5V-Ni-YSZ-A1250-R) still contained $Y(VO_4)$ along with tetragonal and

monoclinic zirconia, indicating that yttrium vanadate is also stable after the exposure to hydrogen at elevated temperature.

Sample 1V-Ni-YSZ-A1250-R showed only peak patterns for nickel, YSZ and tetragonal zirconia, with yttrium vanadate and monoclinic zirconia absent.

When using the Rietveld refinement analysis in *HighScorePlus*, the amount of yttrium vanadate within the film can be estimated, as listed in Table 9.4.

Table 9.4: Phase quantification of $Y(VO_4)$ in the reduced films using Rietveld analysis in *Highscore Plus* after XRD analysis.

Sample	$Y(VO_4)$/ wt. %
1V-Ni-YSZ-A1250-R	-
3V-Ni-YSZ-A1250-R	6
5V-Ni-YSZ-A1250-R	9

According to Rietveld analysis, 3V-Ni-YSZ-A1250-R contains 6 % by weight of $Y(VO_4)$ and 5V-Ni-YSZ-A1250-R contains 9 % by weight in the reduced film when doping with the initial vanadium concentrations by weight of 4.2 % (3 mol.%) and 6.3 % (5 mol.%) during the deposition, respectively.

9.2.3.5   TEM results

Since sample 1V-Ni-YSZ-A1250-R showed no traces of yttrium vanadate in the XRD, TEM analysis was conducted to investigate its existence after hydrogen reduction when using initially low dopant ratios of vanadium during the deposition. The HAADF-TEM micrograph and resulting elemental maps of 1V-Ni-YSZ-A1250-R using STEM-EDS are demonstrated in Figure 9.8.
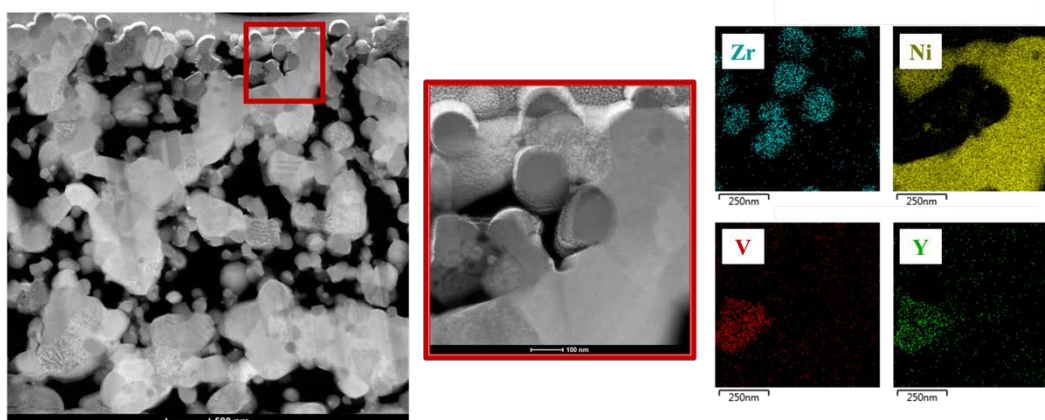
Figure 9.8: HAADF-TEM micrograph of 1 mol.% V-doped Ni-YSZ films after hydrogen reduction (1V-Ni-YSZ-A1250-R) showing elemental maps for zirconium, yttrium, vanadium and nickel obtained from STEM-EDS analysis.

The above elemental maps show that a particle of a size of about 250 nm contains both yttrium and vanadium. The overlap of yttrium and vanadium in the presented area indicates that $Y(VO_4)$ is still present at low concentrations, which might not have been detected in the XRD due to the overlapping strong signal of a metallic nickel peak.

In addition to that, Figure 9.9 demonstrates the HAADF-TEM micrographs of 5V-Ni-YSZ-A1250-R after hydrogen reduction. As expected, yttrium and vanadium also overlap at higher vanadium ratios, indicating the location of yttrium vanadate within the film structure. However, the particle size of yttrium and vanadium increased to about 700 nm.
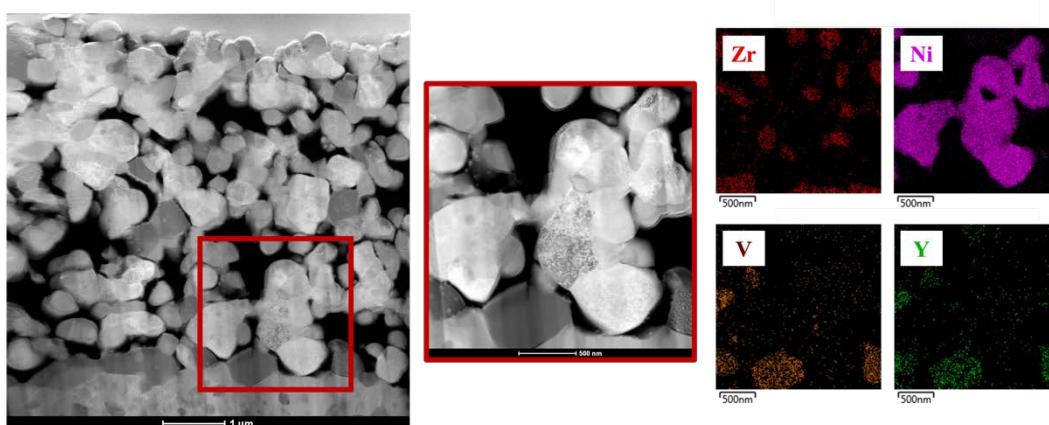
Figure 9.9: HAADF-TEM micrograph of 5 mol.% V-doped Ni-YSZ films after hydrogen reduction (5V-Ni-YSZ-A1250-R) showing elemental maps for zirconium, yttrium, vanadium and nickel obtained from STEM-EDS.

When comparing the micrographs in Figure 9.9 with Figure 9.8, it can be observed that the entire microstructure appears to have suffered from coarsening with higher vanadium loading (note the change in scale on the micrographs). Apart from the observed nickel coarsening, the size of zirconia particles also increased from ca. 150 nm to 250 nm. Nevertheless, the cross-sectional images showed that Zr particles remain disconnected, which most likely causes the weakening of the TPBs and reduced electrochemical performance of the AFLs due to the disarranged percolated conduction path of the reaction species.

9.2.4 Discussion

The electrochemical characterisation of the vanadium-doped samples presented decreased peak power densities with increasing dopant loading.

The microstructure exhibited significantly coarse features with smaller spherical particles attached which were identified as zirconia particles supported on a coarsened nickel structure with higher vanadium loadings (cf. TEM analysis Figure 9.8 and Figure 9.9). The composition data indicated the formation of a new secondary phase due to an increased amount of oxygen compared to samples with lower dopant concentrations. XRD analysis revealed that yttrium vanadate was formed during annealing, whose presence remained in the film after reduction in hydrogen (cf. XRD analysis in Figure 9.7). Since the XPS results identified the deposition of vanadium pentoxide (cf. XPS analysis in Figure 9.6), it was suggested that yttrium (Y^{3+}) added as a stabiliser of cubic YSZ, reacted with vanadium (V^{5+}) present as V_2O_5 in as-deposited film forming yttrium vanadate $[Y^{3+}(V^{5+}(O^{-2})_4)]$ after annealing in air at 1250°C. It should be noted that vanadium pentoxide suffers from a low melting point of 681 ºC [177], indicating instability at the high annealing temperatures used in this work. Hence, $Y(VO_4)$ appears to be a more stable form of V^{5+} at high temperatures than vanadium pentoxide.

The appearance of tetragonal and monoclinic zirconia supports the theory of a reaction of yttrium with vanadium during high-temperature annealing, which could have left lower concentrations of yttrium in the film available to stabilise the cubic structure of zirconia, resulting in the partial transformation of the YSZ phase into tetragonal and monoclinic zirconia.

When reviewing the literature regarding the formation of yttrium vanadate from yttria and vanadium pentoxide, a wealth of studies is presented on hot corrosion resistance of thermal barrier coatings (TBCs), as they comprise partially stabilised YSZ, which is sensitive to molten salt corrosion when using poor-quality fuels containing vanadium [178], [179], [180]. During corrosion experiments at high temperatures, yttria reacts with the corrosive medium, causing YSZ to undergo a phase transformation from tetragonal to monoclinic phase, leading to a significant volume expansion and mechanical failure of the TBC. Guo *et al.* performed hot corrosion tests of YSZ coatings that were covered with V_2O_5 (l) at 1000 ºC for 4 h. After testing they confirmed the presence of $Y(VO_4)$ by XRD analysis, indicating the leaching of the stabiliser (yttria) and YSZ phase transformation into the monoclinic phase. Based on these findings, they proposed the following reaction mechanism at 1000 ºC [180]:

$$V_2O_5 \text{ (l)} + ZrO_2(Y_2O_3) \text{ (s)} \rightarrow YVO_4(s) + m\text{-}ZrO_2 \text{ (s)} \qquad 9.1$$
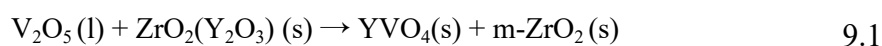
This reaction mechanism is in line with the results in the present work that used a temperature of 1250 ºC.

The decrease in electrochemical performance with higher dopant loadings could be explained as follows. Firstly, the microstructure showed significant coarsening with higher vanadium concentrations, which could result in a lower density of triple phase boundaries, indicated by rather exponential decline at lower current densities at concentrations of 1 and 3 mol. %. When using 5 mol.% V, the polarisation curve exhibits a more linear trajectory with a steeper decline. This could be associated with a higher ohmic resistance caused by an increased concentration of yttrium vanadate in the film, introducing more resistance.

Secondly, the attached spheres of zirconia on the nickel backbone seen in the top surface and cross section micrographs (cf. BSE in Figure 9.4 and TEM Figure 9.9) show no linked conduction path, which could have hindered the conduction of oxygen ions arriving from the electrolyte, which would lead to a performance decrease.

9.2.5   Conclusion

As presented in section 2.3.3.5, the literature presented catalytic activity for thin films of V_2O_3 and V_2O_5 at 410 ºC [94]. Hence, V_2O_3 was proposed as a promising candidate for doping the state-of-the-art SOFC anode. After depositing vanadium during the co-sputtering process of zirconium-yttrium and nickel, vanadium pentoxide was found to be present in the coating, which is known for its low melting point. When sintering at high temperatures, vanadium pentoxide showed a high affinity to react with yttria as the stabiliser for cubic YSZ, leading to the formation of yttrium vanadate (YVO_4) and monoclinic zirconia, which was also reported in the literature [180]. A subsequent reduction in hydrogen showed no further phase transformations of these two phases.

However, the electrochemical performance was observed to decrease as the initial vanadium loading was increased in the samples. Reasons for the performance decrease could be the reduced conductivity in the YSZ network due to the formation of monoclinic YSZ, presenting missing links between YSZ, and the increase in resistance due to the addition of YVO_4.

9.3   Manganese-doped Ni-YSZ films

In the following sections, vanadium was replaced by manganese during the co-deposition of nickel and zirconium, in order to create manganese-doped Ni-YSZ AFLs, which were then electrochemically tested and characterised.

9.3.1 Experimental

9.3.1.1 Deposition of manganese-doped Ni(O)-YSZ

To provide a comparable set of samples to the V-doped coatings, three samples 1Mn-Ni-YSZ, 3Mn-Ni-YSZ and 5Mn-Ni-YSZ were prepared containing 1 mol.%, 3 mol.% and 5 mol% manganese, respectively, which are displayed in Table 9.5. Unless otherwise stated, identical experiments for Mn-doped Ni(O)-YSZ films were carried out as in the previous section 9.2.1.1. In order to deposit films with the target dopant concentrations of 1 mol.%, 3 mol.% and 5 mol.% manganese, the applied power on the manganese target was varied using a set frequency of 100 kHz (55% duty), as shown in the table below.

Table 9.5: Sample IDs of specimens deposited with different manganese concentrations of 1 mol.%, 3 mol.% and 5 mol.% within the Ni(O)-YSZ film.

Sample ID	Manganese concentration/ mol.%	Applied power
1Mn-Ni-YSZ	1	50 W
3Mn-Ni-YSZ	3	100 W
5Mn-Ni-YSZ	5	175 W

9.3.1.2 Electrochemical characterisation of manganese-doped Ni(O)-YSZ films

Electrochemical testing was performed using the same methodology and type of experiment as described in the previous section for V-doped Ni(O)-YSZ films (cf. 9.2.1.2).

9.3.1.3 Material characterisation of manganese-doped Ni(O)-YSZ films

The effect of the manganese concentration in the samples 1Mn-Ni-YSZ, 3Mn-Ni-YSZ and 5Mn-Ni-YSZ on their microstructure was analysed. Each sample which contained YSZ as the substrate was separated into three sections to undergo individual post-deposition heat treatment at 1250 ºC in air for 1 h, followed by a subsequent reduction in 10% H_2/N_2 atmospheres at 850 ºC for 10 h. The resulting sample IDs can be found in Table 9.6

SEM of the top surfaces and cross-sections, EDS and XRD analyses were conducted after each individual state, *i.e.*, as-deposited, annealed and reduced.

The EDS analysis was performed on as-deposited samples with YSZ and Si substrates to rule out penetration of the underlying YSZ substrate in the annealed and reduced samples.

In addition to that, XPS analyses were carried out after the deposition and elemental maps were obtained from the top surface and the cross section of 5Mn-Ni-YSZ-A1250-R using SEM-EDS.

Table 9.6: Sample IDs of specimens deposited with different dopant concentrations of 1 mol.%, 3 mol.% and 5 mol.% manganese after annealing at 1250 °C and hydrogen reduction.

Sample ID	Mn (as-deposited)/ mol.%	Annealing/ ºC	H$_2$ reduction/ ºC
1Mn-Ni-YSZ	1	1250	-
3Mn-Ni-YSZ	3	1250	-
5Mn-Ni-YSZ	5	1250	-
1Mn-Ni-YSZ-A1250	-	1250	-
3Mn-Ni-YSZ-A1250	-	1250	-
3Mn-Ni-YSZ-A1250	-	1250	-
1Mn-Ni-YSZ-A1250-R	-	1250	850
3Mn-Ni-YSZ-A1250-R	-	1250	850
3Mn-Ni-YSZ-A1250-R	-	1250	850

9.3.2 Electrochemical characterisation

Figure 9.10 demonstrates the polarisation curves (a) and power density curves (b) of the doped Ni(O)-YSZ films after adding 1 mol.%, 3 mol.% and 5 mol.% manganese to the best-performing undoped Ni-YSZ AFL from Chapter 8. For comparison reasons, the performance data of the best-performing undoped Ni-YSZ AFL retested on the in-house test station was added to the figure.
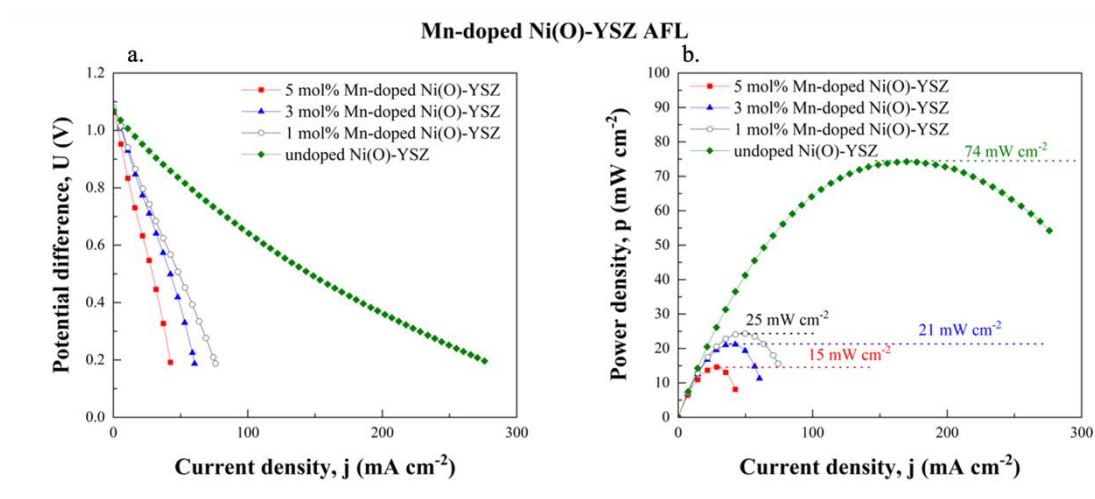
Figure 9.10: Electrochemical performance of manganese-doped Ni-YSZ AFLs deposited with different dopant concentrations of 1 mol.%, 3 mol.% and 5 mol.%, followed by annealing at 1250 ºC in air for 1 h prior to testing. Tested at 850 ºC in 100 sccm dry hydrogen and 100 sccm oxygen for anode and cathode, respectively. Polarisation

curves (a) and power density curves (b). *Testing was carried out in-house. The undoped sample was deposited at 0.7 Pa and annealed at 1250 ºC in air for 1 h retested in-house for reference.*

All samples presented an OCV greater than 1V, yielding 1.08 V, 1.08 V and 1.06 V for 1 mol.%, 3 mol.% and 5 mol.% Mn-doped Ni(O)-YSZ, respectively. However, significantly lower peak power densities of 25, 21 and 15 mW cm^{-2} were observed, compared to the 75 mW cm^{-2} recorded for the undoped Ni-YSZ AFL.

9.3.3 Material characterisation

To understand and explain the significant performance losses seen in Figure 9.10 in the Mn-doped Ni-YSZ AFLs compared to undoped Ni-YSZ AFLs and the V-doped AFLs, this section reports the findings of the material characterisation, which addresses changes introduced due to the addition of manganese.

9.3.3.1 Coatings microstructure

The SEM cross section and top surface micrographs of the samples doped with 1 mol.%, 3 mol.% and 5 mol.% manganese are presented in Figure 9.11.
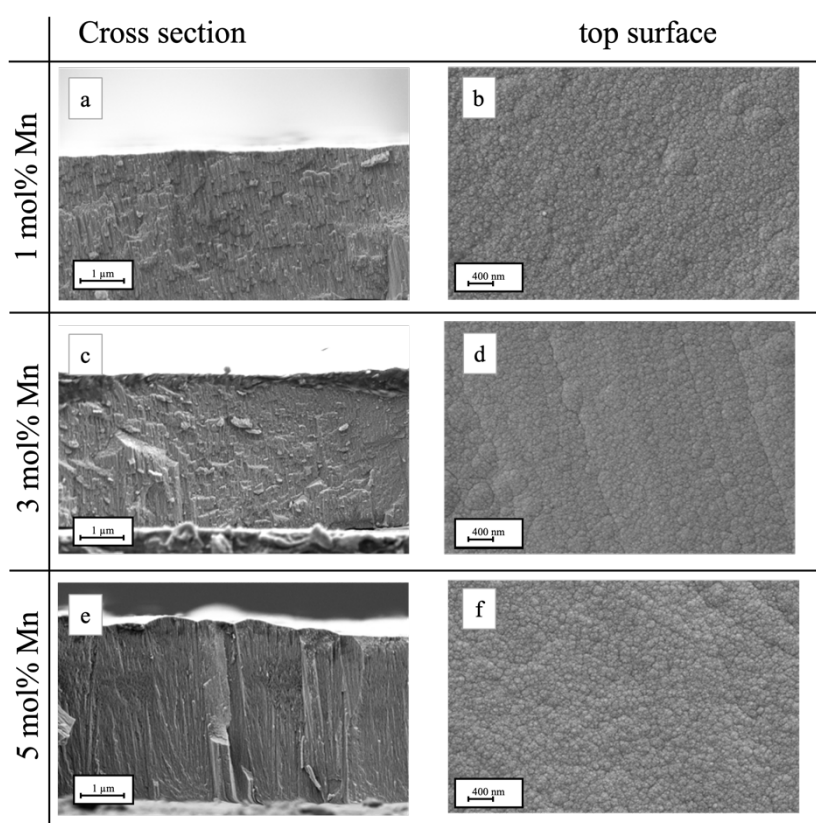
Figure 9.11: SEM images of fractured sections (a, c, e) and top surfaces (b, d, f) of as-deposited manganese-doped Ni(O)-YSZ films at different dopant concentrations of 1 mol.% Mn (a, b), 3 mol.% Mn (c, d) and 5 mol.% Mn (e, f).

The coatings presented dense columnar structures in (a), (c) and (e). More defined columns are observed in (e), which are not seen in the other two samples in (a) and (c). No changes in grain sizes were observed in the micrographs of the top surfaces in (b), (d) and (e).

After post-deposition annealing in air at 1250 ºC, the changes in microstructure in the three samples with the initial manganese concentrations of 1 mol.%, 3 mol.% and 5 mol.% Mn are shown in Figure 9.12
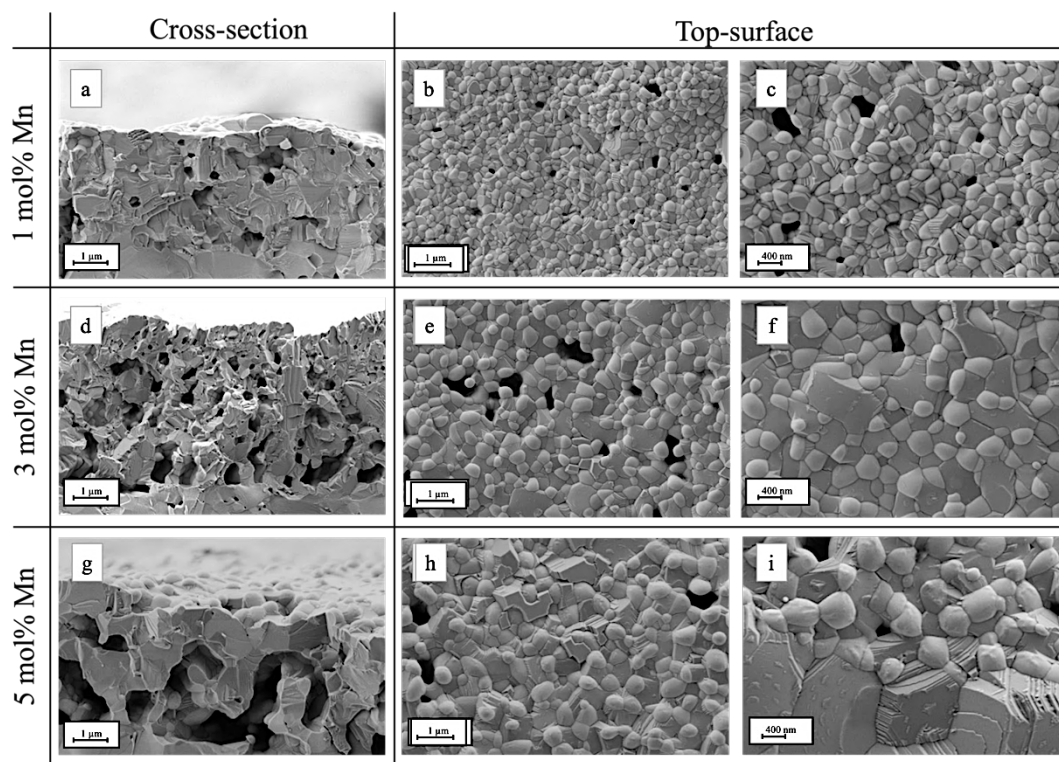
Figure 9.12: SEM images of fractured sections (a, d, g) and top surfaces (b, c, e, f, h, i) of manganese-doped Ni(O)-YSZ films after annealing in air at 1250 ºC for 1 h using different dopant concentrations of 1 mol.% Mn (a, b, c), 3 mol.% Mn (d, e, f) and 5 mol.% Mn (g, h, i).

The cross-section images in (a), (d) and (g) show extreme grain growth with increasing manganese ratios after sintering in air. When doping with 5 mol.% Mn, a severely coarse and bulky microstructure was observed with significantly enlarged pore channels (g). Grain growth of the spherical particles and coarsening of the surrounding structure can also be seen in the top surface images with higher Mn ratios in (c), (f) and (i).

After a subsequent reduction in hydrogen, the microstructure of all three manganese-doped samples transformed into a porous film, as shown in Figure 9.13. The cross-

sectional images in (a), (d) and (g) exhibit finer microstructures with smaller particle sizes compared to previous results. However, the top surface images in (f) and (i) reveal precipitations of two phases with a grain size between 0.7-2.2 µm in (f) and greater than 3 µm in (i). One phase has a dense, rounded structure, while the other features finely porous cubes (f). The sample containing initially 1 mol. % Mn, did not show any significant differences compared to 3 and 5 mol.% Mn.
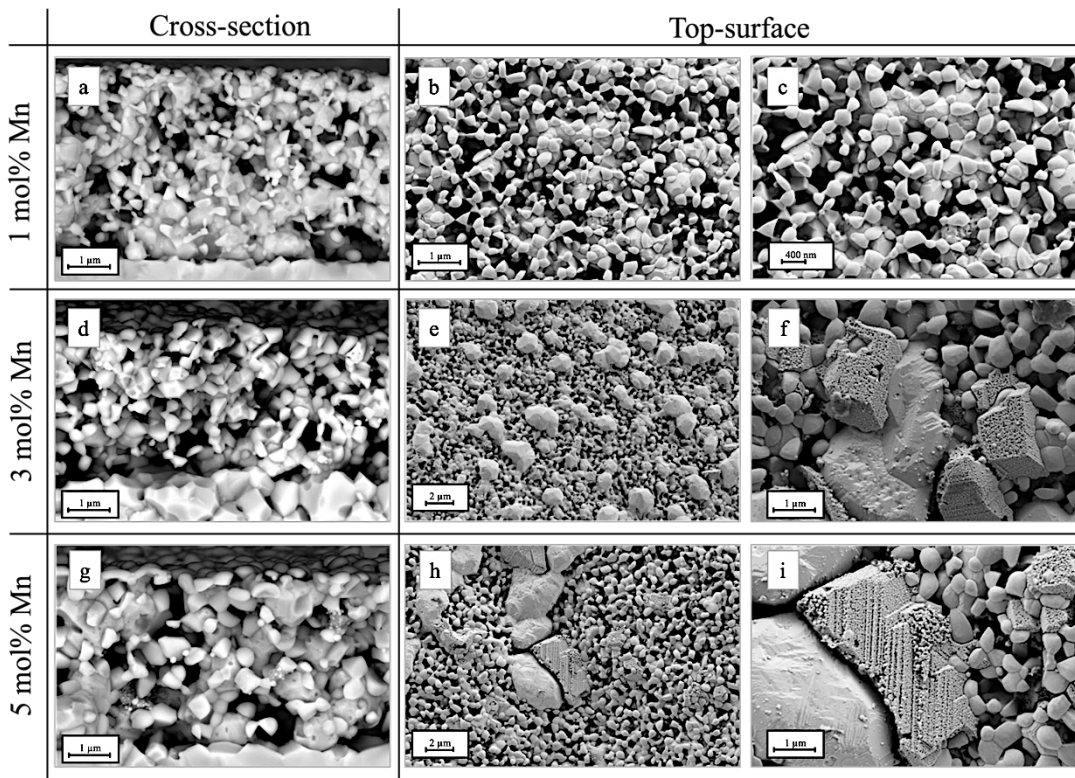
Figure 9.13: BSE images of fractured sections (a, d, g) and images of top surfaces (b, c, e, f, h, i) of manganese-doped Ni(O)-YSZ films after annealing in air at 1250 ºC for 1 h and subsequent reduction in 10% H_2/N_2 at 850 ºC for 10 h using different dopant concentrations of 1 mol.% Mn (a, b, c), 3 mol.% Mn (d, e, f) and 5 mol.% Mn (g, h, i).

In order to identify the two secondary phases obtained in the SEM top surface micrographs, elemental maps were generated using EDS analysis. Figure 9.14 illustrates the elemental maps for the top surface of 5 mol.% Mn-doped Ni(O)-YSZ films after the hydrogen reduction (5Mn-Ni-YSZ-A1250-R). While the rounded dense secondary phase can be identified as nickel, the fine porous cubes show manganese and oxygen overlapping, indicating the presence of a type of manganese oxide. Both secondary phases are embedded in a fine porous structure of YSZ.
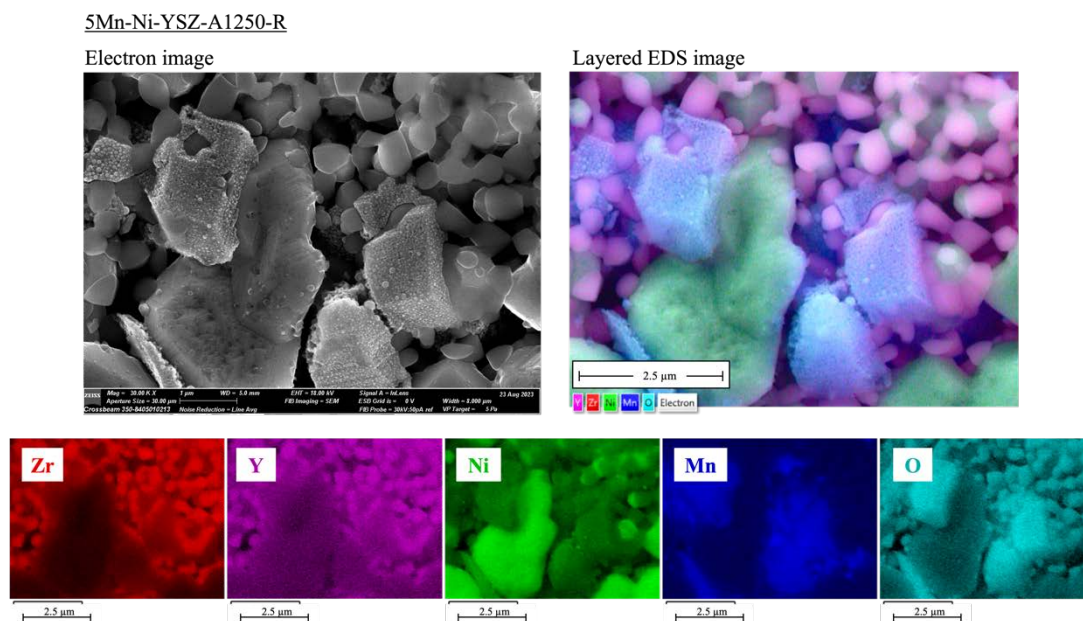
Figure 9.14: Elemental mapping of the top surface of 5Mn-Ni-YSZ-A1250-R using EDS. 5Mn-Ni-YSZ-A1250-R was initially doped with 5 mol.% Mn, subsequently annealed at 1250ºC in air for 1 h and reduced in hydrogen for 10 h.

Further elemental maps of the samples containing initially 1 and 3 mol.% Mn after hydrogen reduction can be found in Appendix I, showing the overlap of manganese and oxygen in present in the film.

Additionally, elemental maps of the cross section were performed to verify whether the secondary phase aggregates on the surface or remains within the coating, as presented in Figure 9.15 and Figure 9.16. The elemental maps show aggregations of manganese oxide within the cross sections for both samples. Considering the addition of initially 1 mol.% manganese during the deposition, the 1Mn-Ni-YSZ-A1250-R presents a substantial amount of the secondary phase. What can be also observed in the cross-sectional EDS maps is that nickel coarsens with higher manganese loading as the nickel grains appear larger in 5Mn-Ni-YSZ-A1250-R than in 1Mn-Ni-YSZ-A1250-R.
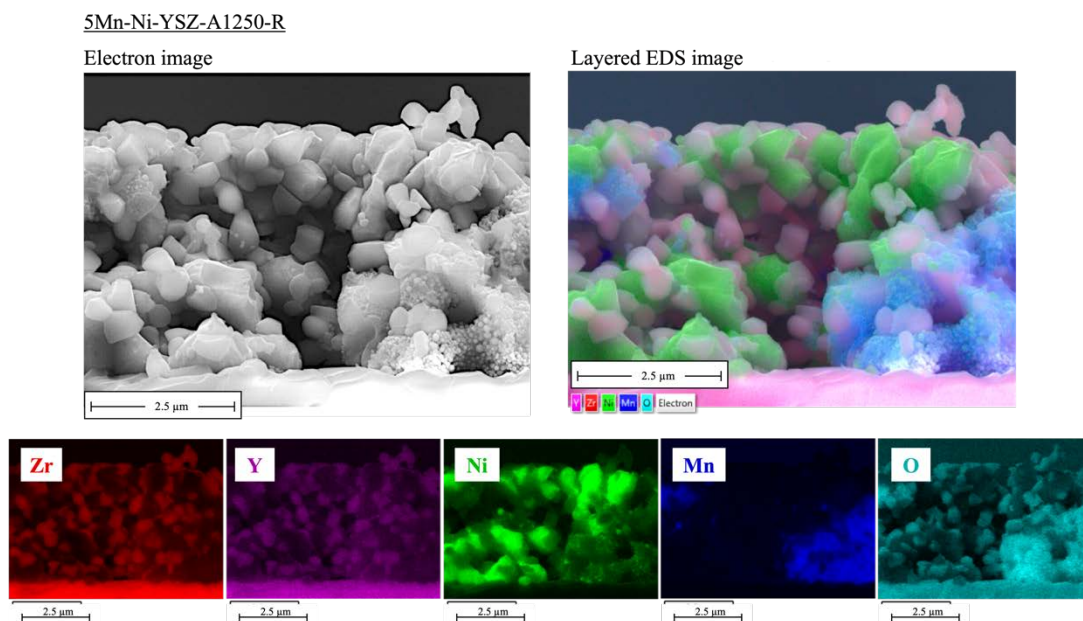
Figure 9.15: Elemental mapping of the cross section of 5Mn-Ni-YSZ-A1250-R obtained from EDS. 5Mn-Ni-YSZ-A1250-R was initially doped with 5 mol.% Mn, subsequently annealed at 1250°C in air for 1 h and reduced in hydrogen for 10 h.
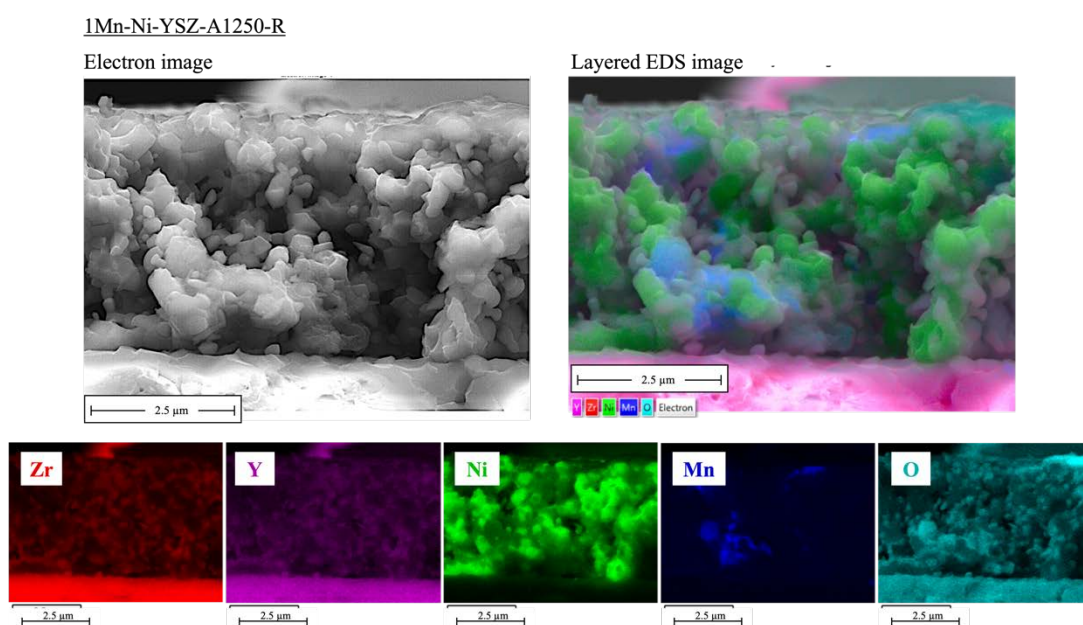
Figure 9.16: Elemental mapping of the cross section of 1Mn-Ni-YSZ-A1250-R obtained from EDS. 5Mn-Ni-YSZ-A1250-R was initially doped with 1 mol.% Mn, subsequently annealed at 1250°C in air for 1 h and reduced in hydrogen for 10 h.

9.3.3.2 Film composition

The composition data of the deposited Mn-doped Ni(O)-YSZ films can be found in Table 9.7, showing the difference in manganese ratios after the subsequent process stages of annealing and hydrogen reduction obtained from EDS analysis.

Table 9.7: Composition in mol.% of the deposited Mn-doped-Ni(O)-YSZ films with different manganese concentrations of 1 mol. %, 3 mol.% and 5 mol.%, after deposition, annealing at 1250 ºC and reduction in hydrogen.

Sample ID	Ni	Zr	Y	Mn	O
1Mn-Ni-YSZ	39.7	4.8	0.5	1.5	53.5
3Mn-Ni-YSZ	35.6	5.8	0.7	2.9	55.0
5Mn-Ni-YSZ	30.4	5.5	0.6	5.2	58.3
1Mn-Ni-YSZ-A1250	39.0	6.5	0.8	1.1	52.7
3Mn-Ni-YSZ-A1250	35.8	7.0	0.9	1.7	54.5
5Mn-Ni-YSZ-A1250	35.5	7.5	1.0	4.0	52.1
1Mn-Ni-YSZ-A1250-R	57.3	11.5	1.4	1.8	28.0
3Mn-Ni-YSZ-A1250-R	56.5	11.6	1.4	3.1	27.3
5Mn-Ni-YSZ-A1250-R	45.6	12.7	1.6	6.2	33.9

As the manganese content increased in the deposited films, the oxygen concentration increased from 53.5 to 58.3 mol.%, while the nickel content decreased from 39.7 to 30.4 mol.%.

After annealing the samples, a slight reduction in manganese ratios from 2.9 to 1.7 mol.% and 5.2 to 4.0 mol.% in the samples 3Mn-Ni-YSZ-A1250 and 5Mn-Ni-YSZ-A1250, respectively, was observed. Due to the decline in the manganese concentration in sample 3Mn-Ni-YSZ-A1250, its composition was comparable with that of 1Mn-Ni-YSZ-A1250. Sample 5Mn-Ni-YSZ-A1250 revealed differences in the oxygen and nickel concentrations when changing from as-deposited to annealed states. The oxygen content dropped from 58.3 to 52.1 mol.%, while the nickel ratio increased from 30.4 to 35.5 mol%.

After reduction in hydrogen, the dopant concentrations nearly returned to the targeted concentrations, yielding 1.8, 3.1 and 6.2 mol.% Mn for 1Mn-Ni-YSZ-A1250-R, 3Mn-Ni-YSZ-A1250-R and 5Mn-Ni-YSZ-A1250-R, respectively. Similar concentrations for the remaining elements in the samples 1Mn-Ni-YSZ-A1250-R and 3Mn-Ni-YSZ-A1250-R can be seen. However, 5Mn-Ni-YSZ-A1250-R shows a lower nickel content but a higher oxygen content in the reduced film. This suggests that the higher manganese ratio might have caused the retention of more oxygen, possibly due to the formation of manganese oxide. (cf. Figure 9.14-Figure 9.16: elemental maps).

9.3.3.3 XRD results

In order to understand any possible phase transformations during annealing and subsequent reduction in hydrogen that might have occurred due to the addition of manganese in the Ni(O)-YSZ films, secondary phases seen in the SEM micrographs (cf. Figure 9.13) needed to be identified. For that reason, XRD analysis was carried out on the samples 1Mn-Ni-YSZ, 3Mn-Ni-YSZ and 5Mn-Ni-YSZ after deposition, annealed in air at 1250 ºC and subsequently reduced in hydrogen/nitrogen atmospheres. The obtained XRD patterns for as-deposited, annealed and reduced states are displayed in Figure 9.17.
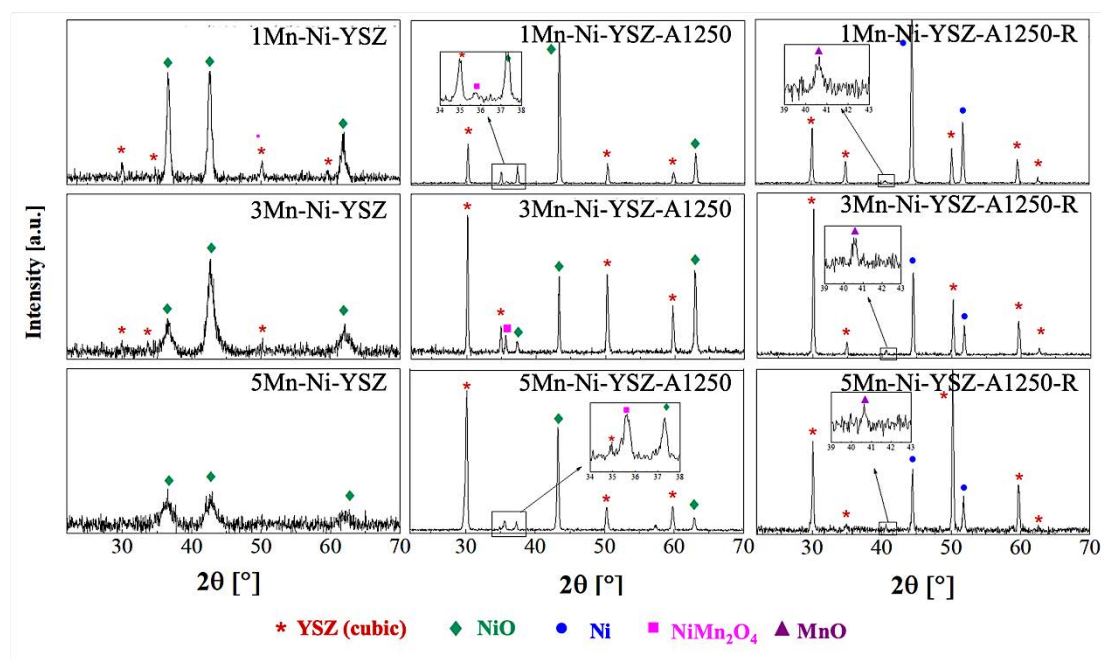
Figure 9.17: XRD patterns of Mn-doped Ni(O)-YSZ films after the deposition, annealing at 1250 ºC, and hydrogen reduction.

While only NiO and YSZ peaks were observed after deposition, as seen previously in this work, the peak patterns after annealing at high temperatures, reveal the presence of a new phase at a peak position of 37.3º in all three annealed samples, which was identified as nickel manganite ($NiMn_2O_4$) with the orientation (222) through the COD ID 1530384 in *HighScorePlus* [181]. This finding is consistent with the literature in [74]. Therein, Chung *et al.* reported the formation of a spinel-like secondary phase of $NiMn_2O_4$ after annealing MnO-doped Ni(O)-YSZ catalysts at high temperatures. They believed that this was caused by the solid-state reaction between NiO and MnO.

The reduction in hydrogen atmospheres of the samples caused nickel oxide to transform into catalytically active nickel, as seen in the previous chapter. Interestingly, no

nickel manganite was detected in the peak patterns after reduction, suggesting that the phase is not stable under reducing atmospheres. Instead, small peaks at 40.6º were observed in all samples which were identified as MnO using the COD ID 1514114 in *HighScorePlus* [182].

When using the Rietveld refinement analysis in *HighScorePlus*, the amount of MnO within the film can be estimated, as listed in Table 9.8.

Table 9.8: Phase quantification of MnO in the reduced films using Rietveld analysis in *Highscore Plus* after XRD analysis.

Sample	MnO/ wt. %
1Mn-Ni-YSZ-A1250-R	6
3Mn-Ni-YSZ-A1250-R	7
5Mn-Ni-YSZ-A1250-R	10

The Rietveld analysis yields 6, 7 and 10 % by weight of MnO for 1Mn-Ni-YSZ-A1250-R, 3Mn-Ni-YSZ-A1250-R and 5Mn-Ni-YSZ-A1250-R, respectively, when doping with the initial manganese concentrations by weight of 2.1 % (1 mol.%) 4.3 % (3 mol.%) and 8.0 % (5 mol.%) during the deposition.

9.3.3.4   XPS results

XPS analysis was carried out to investigate the oxidation state of manganese in the as-deposited samples, in order to understand the phase changes during the annealing and reduction. When acquiring the XPS spectra for the Mn 2p region, a chemical component appeared in the form of a shoulder at a binding energy of 637.6 eV, which does not match any characteristic peaks for manganese. The manufacturer of the instrument stated that the use of an Al source causes overlapping photoelectron lines between Mn $2p_{3/2}$ and Auger features of nickel, limiting the identification of the oxidation state [183], which was also reported in other studies [184]. The Mn 2p XPS spectra fitted with peaks for Mn $2p_{3/2}$ and Ni LMM can be found in Appendix J.

Although the manufacturer recommended switching to an Mg source to move the Auger lines by 233 eV to the relative photoelectron lines (Al: 1486.6 eV and Mg: 1253.3 eV) [183], the XPS instrument in this work was not equipped with an achromatic Al and Mg dual X-ray source. For that reason, Mn 3s region scans of the samples were collected to indicate the oxidation state of manganese in the sample. As coupling of non-ionised 3s electrons with 3d valence-band electrons causes a multiplet split in the 3s region, the difference in binding energies ΔE of the peak splitting can determine which oxide is present in the coating. By comparing the characteristic peak splitting

magnitudes of 6.0, 5.3 and 4.7 eV for MnO (Mn^{2+}), Mn_2O_3 (Mn^{3+}) and MnO_2 (Mn^{4+}), respectively, it is possible to distinguish the oxidation state of manganese [170], [185].

Figure 9.18 presents the Mn 3s region scans for the samples 1Mn-Ni-YSZ-A1250-R, 3Mn-Ni-YSZ-A1250-R and 5Mn-Ni-YSZ-A1250-R after reduction in hydrogen.
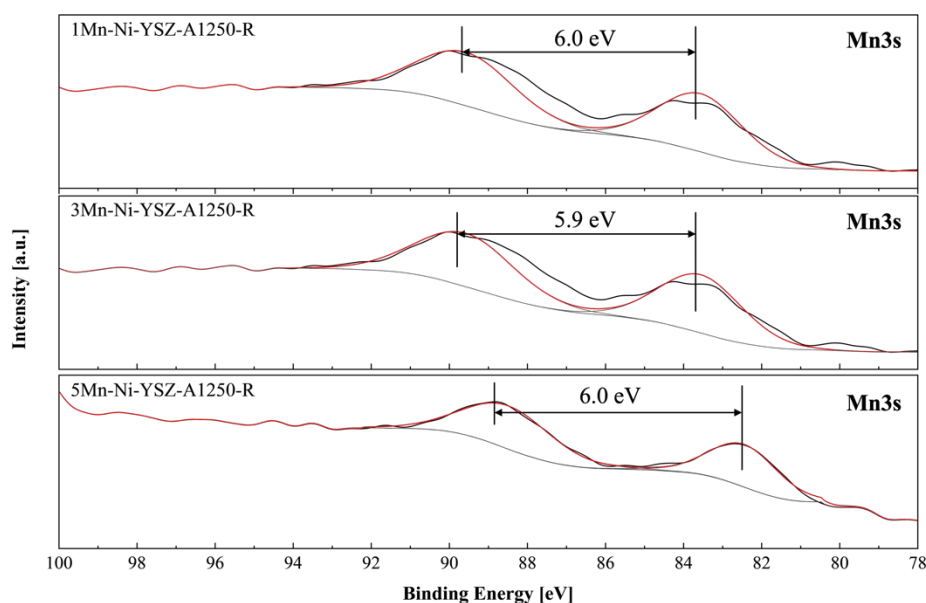
Figure 9.18: Mn 3s XPS spectra for reduced samples 1Mn-Ni-YSZ-A1250-R, 3Mn-Ni-YSZ-A1250-R and 5Mn-Ni-YSZ-A1250-R with initial dopant concentrations of 1 mol.%, 3 mol.% and 5 mol.% V, respectively, showing two multiplet split components to identify the oxidation state [185].

As the concentration of manganese in the film was low compared to a bulk material, the XPS spectra showed significant noise. For that reason, a Gaussian smoothing filter was first applied in *CasaXPS*. To determine the exact binding energies at the maximum peak intensity of the multiplet split, each multiplet was fitted with a single peak, rather than performing a deconvoluted peak analysis. The resulting binding energies and difference of the multiplet split are listed in the table below.

Table 9.9: Differences in binding energies of the multiplet split in eV of Mn 3s region to identify the oxidation state of manganese oxide after hydrogen reduction.

Sample	Mn^{2+} multiplet 1/ eV	Mn^{2+} multiplet 2/ eV	ΔE/ eV
1Mn-Ni-YSZ-A1250-R	83.4	89.3	6.0
3Mn-Ni-YSZ-A1250-R	83.6	89.5	5.9
5Mn-Ni-YSZ-A1250-R	82.4	88.5	6.0

The table presents peak splitting magnitudes of 6.0, 5.9 and 6.0 eV for 1Mn-Ni-YSZ-A1250-R, 3Mn-Ni-YSZ-A1250-R and 5Mn-Ni-YSZ-A1250-R, respectively, indicating the presence of manganese monoxide (MnO) in the film after hydrogen reduction. This finding corresponds well with the results of the XRD analysis, which showed a diffraction peak for MnO in all samples after the reduction.

In order to identify the oxidation state of manganese in as-deposited samples, Mn 3s XPS spectra of the samples 1Mn-Ni-YSZ, 3Mn-Ni-YSZ and 5Mn-Ni-YSZ were obtained, as demonstrated in Figure 9.19.
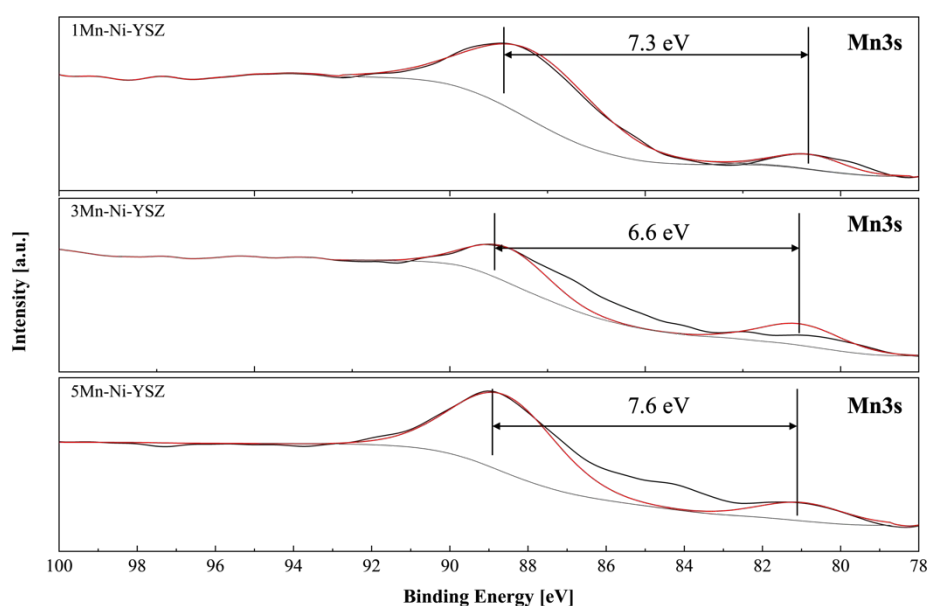
Figure 9.19: Mn 3s XPS spectra for as-deposited samples 1Mn-Ni-YSZ, 3Mn-Ni-YSZ and 5Mn-Ni-YSZ with 1 mol.%, 3 mol.% and 5 mol.% V, respectively, showing two multiplet split components [185].

Similar to the procedure described above (cf. Figure 9.18), the peak fitting magnitude for the as-deposited samples yielded 7.3, 6.6 and 7.6 eV, as shown in the table below.

Table 9.10: Differences in binding energies of the multiplet split in eV of Mn 3s region to identify the oxidation state of manganese oxide after the deposition and hydrogen reduction.

Sample	Mn^{2+} multiplet 1/ eV	Mn^{2+} multiplet 2/ eV	ΔE/ eV
1Mn-Ni-YSZ	80.5	87.9	7.3
3Mn-Ni-YSZ	81.1	87.7	6.6
5Mn-Ni-YSZ	81.0	88.6	7.6

The difference between the binding energies of the multiplet split is slightly higher than the reported value of 6.0 eV for MnO. As Mn_2O_3 (Mn^{3+}) and MnO_2 (Mn^{4+}) were

reported at an ΔE of 5.3 and 4.7 eV, respectively[170], [185], it is unlikely that the manganese was present in either of these forms. However, the XPS and XRD analyses do not provide detailed information on the oxidation state of manganese at the time of deposition. This is because the deposited manganese was amorphous after deposition, as shown in Figure 9.17.

9.3.4 Discussion

The electrochemical characterisation of the manganese-doped Ni(O)-YSZ films presented a drastic decline in performance, even more than that for the vanadium-doped samples, with increasing manganese loading in the coating (cf. Figure 9.10).

After annealing in air at 1250 ºC, significant morphological changes in the microstructure were observed with increasing manganese ratios, doubling the size of round clusters on the top surface (cf. Figure 9.12 (c) and (i)). The XRD analysis exhibited the presence of a secondary phase, identified as nickel manganite $NiMn_2O_4$ with a spinel-like structure (cf. Figure 9.17), where Ni^{2+} occupy tetrahedral holes and Mn^{3+} occupy octahedral holes. Following a reduction in hydrogen, the micrographs showed fine porous structures with the incorporation of two types of microcrystals with sizes larger than 3 μm in the case of 5 mol.% Mn-doped samples (cf. Figure 9.13). After EDS mapping, it was discovered that the microcrystals with round and dense shapes consisted of nickel, while the others with more cubic shapes and finer porosity showed overlapping manganese and oxygen elements (cf. Figure 9.14). The XRD and XPS analysis after hydrogen reduction (cf. XRD analysis in Figure 9.17 and Mn 3s XPS spectra in Figure 9.18) identified the second phase to be manganese monoxide MnO with Mn^{2+} oxidation state. These findings indicate that Mn^{3+} in $NiMn_2O_4$ was reduced to MnO (Mn^{2+}) during hydrogen reduction, as Mn^{2+} does not stabilise the octahedral phase as Mn^{3+} does. Due to instrumental limitations of the XPS data acquisition, no detailed information on the oxidation state of manganese in the Mn 2p region after each state could be given. However, Chung *et al.* also reported the formation of $NiMn_2O_4$ after sintering powders containing NiO, YSZ and MnO and observed the decomposition of the spinel structure into metallic nickel and manganese monoxide [74]. This agrees well with the findings of the present work, as the large microcrystals adjacent to each other in the SEM micrographs were found to be metallic nickel and MnO (cf. elemental maps in Figure 9.14 and XRD patterns after reduction in Figure 9.17).

The sharp decrease in electrocatalytic activity is most likely associated with the amount of MnO present in the film, as MnO is non-conductive. The literature reported a slight increase in electric conductivity up to 5.5 wt.% MnO in Ni-YSZ anodes but some authors have found a significant decline at 9.9 wt.% MnO [74]. For consistency with the V-doped coatings, the final MnO concentrations used in the present study were 6, 7 and 10 wt. % of MnO in the 1, 3 and 5 mol.% Mn-doped films. Unfortunately, the results suggest that the addition of such high ratios substantially decreased the degree of percolation. In addition to that, the observed larger metallic nickel aggregations in the reduced state could have contributed to a massively decreased percolation path and lower catalytical activity due to fewer triple-phase boundaries.

9.3.5 Conclusion

Manganese-doped Ni-YSZ AFLs were created by the co-deposition of nickel, zirconium-yttrium and manganese. After annealing in air at high temperatures, significant morphological changes were observed compared to undoped NiO-YSZ samples, caused by the formation of $NiMn_2O_4$. The subsequent reduction in hydrogen revealed the decomposition of this phase to nickel and manganese monoxide. However, the high concentrations of manganese used in this work led to large precipitations of nickel remaining after the reduction of $NiMn_2O_4$, and thus a decreased density of triple-phase boundaries. Besides, a sharp decline in electrical conductivity with manganese ratios higher than 5.5 wt.% was seen in the literature, suggesting that the MnO ratios in the present work were too high. Future studies should focus on dropping the Mn ratio at the time of deposition significantly.

IV.   Synopsis

10 Conclusion and Future Work

10.1 Conclusion

The aim of this work was to improve the electrocatalytic performance of solid oxide fuel cell (SOFC) anodes produced by magnetron sputtering through the careful design of the microstructure of the coating and the incorporation of promising dopant materials.

The first objective was fulfilled by understanding the effect of deposition parameters such as the deposition angle and deposition pressure on the structural properties of pure YSZ films. While using an oxygen partial pressure feedback control for reactive magnetron sputtering, stable process conditions were achieved. When pressure and angle were maximised, respectively, highly porous coatings of YSZ were successfully created using reactive pulsed DC magnetron sputtering.

The subsequent objective was to integrate nickel into the YSZ film to control the deposition of nanostructured state-of-the-art Ni-YSZ active functional layers (AFLs) for solid oxide fuel cells. In this comprehensive study, the influence of process parameters such as deposition temperature, oxygen partial and total pressures during sputtering and post-deposition annealing temperatures were investigated on the microstructure and electrochemical performance of the deposited Ni-YSZ films. Although it was found that the oxygen partial pressure does not significantly affect the microstructure of the film, high partial pressures should be avoided as target poisoning occurs earlier on the YSZ target than on Ni, leading to lower deposition rates and Ni:Zr+Y ratio imbalance. Moreover, this work uncovered that low deposition pressures and high substrate temperatures during deposition cause densification of the film, which resulted in lower electrochemical activity due to reduced reactive sites in the composite. Deposition at very high pressures also decreased the activity due to a higher porosity in the film. In contrast, high performance was achieved at medium deposition pressures and higher post-deposition annealing temperatures. The peak power density of the thin film was comparable to that of commercial cells, with a 14% sacrifice in power density but a 95% reduction in film thickness, indicating potential savings in material costs.

The principal goal for this work had been the doping of the best-performing nanostructured Ni-YSZ anode architecture by adding different ratios of non-precious elements,

i.e., vanadium and manganese. This work provides insight into why these materials have failed to perform as SOFC anodes. Adding vanadium to the co-sputtering process of nickel and zirconium yttrium resulted in deposited vanadium pentoxide which was found to react with yttria at high temperatures, leading to the formation of a secondary phase, yttrium vanadate (YVO$_4$), and the transformation of cubic YSZ into monoclinic zirconia (due to the leaching of yttrium as the stabiliser for cubic YSZ). The resulting loss in electrochemical activity with higher vanadium loading is therefore believed to be caused by missing links in the YSZ network because of the formation of monoclinic YSZ, and the increase in resistance due to the increased concentration of YVO$_4$. Manganese-doped Ni-YSZ suffered from significant morphological changes caused by the formation of the secondary phase, nickel manganite (NiMn$_2$O$_4$), which decomposed to nickel and manganese monoxide during the subsequent reduction in hydrogen. Using high dopant loadings of manganese resulted in large aggregations of nickel remaining after the reduction of nickel manganite, which lowered the content of nickel in the remaining films, leading to the decrease of reaction sites and drastic performance losses. Additionally, the decline in performance was also believed to be due to a significantly high concentration of non-conductive manganese monoxide which most likely decreased the electrical conductivity of the film.

Another part of this thesis included the development of a functional SOFC button cell test at the Manchester Fuel Cell Innovation Centre. A new set of gas manifolds for SOFC button cells has been developed and engineered. However, cell testing was only possible using pure oxygen due to the mass transport challenges when running on air streams on the cathode side.

Finally, this work demonstrates the relevance of magnetron sputtering for the deposition of advanced SOFC anodes and how it promotes potential cost reductions in SOFC systems. However, further work is necessary for the development of new materials in SOFCs for tomorrow's net-zero future.

10.2 Future work

10.2.1 Reducing the operation temperature

The Ni-YSZ cermet anodes are limited in lifetime because of microstructural degradation during long-term operation due to nickel grain coarsening. Hence, lowering the operation temperature of SOFCs is a major goal in present R&D. It can allow the application of lower-cost materials of the cell support and improve lifetime and thermal

cycling performance [37]. Recent studies have demonstrated superior ion conductivity for ceria based materials, such as gadolinium-doped ceria (GDC) that could operate at lower temperatures, compared to YSZ, which is eminently suitable as an electrolyte for low-temperature solid oxide fuel cells (LT-SOFC) [17]. When utilizing a GDC electrolyte, the same oxide is incorporated in the Ni-cermet anode. For that reason, a more comprehensive study regarding the optimal deposition pressure on the co-sputtering of nickel and cerium-gadolinium should be conducted to produce Ni-GDC active functional layers.

10.2.2 Vanadium-doped active functional layers

The obtained results of vanadium-doped Ni-YSZ films showed the formation of yttrium vanadate which was enabled by the excessive amount of oxygen during sintering in air. A short study should be conducted to anneal deposited V-doped Ni-YSZ films in nitrogen atmospheres to investigate which phase formation occurs at restricted oxygen presence. In addition to that, the dopant concentration should be significantly reduced.

As mentioned above, Ni-GDC anodes represent an alternative to allow lower operation temperatures. Doping of Ni-GDC with vanadium would prevent yttrium vanadate, as ceria uses gadolinia to stabilise its cubic form. Investigating the formation of any new secondary phases and the effect of vanadium oxides at lower temperatures represents an interesting approach to developing new materials.

10.2.3 Manganese-doped active functional layers

The high dopant concentration of manganese oxide used in this work resulted in significant morphology changes and loss in conductivity. For that reason, the initial dopant concentration should be significantly dropped in future studies. However, the literature deployed a dual-layer anode made of Ni-YSZ and Ni-MnO [72]. Future studies could create a gradient composition based on the dual layer of Ni-YSZ and Ni-MnO. When depositing a pure Ni-YSZ layer based on this work, adding MnO as the dopant with increasing concentration while decreasing the concentration of YSZ throughout the layer thickness using magnetron sputtering could represent the next step.

10.2.4 Alternative dopants for active functional layers

As the gap analysis in Chapter 4 presented other potential candidates such as tungsten, zinc, hafnium and tantalum that have not been researched to the author's knowledge, similar investigations could be conducted by substituting vanadium or manganese in

this study with the highlighted candidates and studying their effect on the microstructure and catalytic activity for SOFC anodes.

10.2.5 Modifying the SOFC button cell test stand

The developed gas manifolds for button cell testing suffered from mass transportation losses when running on air and not pure oxygen. The design was modified during a second design iteration, which increased the number of flow holes from three to eight on the cathode. Although a shift in the limiting current density for mass transportation towards higher current density was observed, it still did not provide sufficient transport of reactant between the inlet and outlet on the cathode, as presented in Appendix D. Future work needs to carry out another design iteration that addresses the challenges of mass transportation by increasing the reactant flow in the manifold.

V. Appendices

A. Operation with Hydrocarbon Fuels

A beneficial characteristic of SOFCs is the operation in a wide range of hydrocarbons through internal reforming processes. The reason for the application of hydrocarbon fuels is that they provide a good energy storage density compared to hydrogen, and the existing infrastructure of natural gas can be utilised as the gas supply for domestic applications.

When directly injected on the anode side, the oxidation of hydrocarbons is kinetically slow, therefore hydrocarbons are usually reformed internally with steam, resulting in smaller species, as shown in the following equations.

$$C_n H_m + n\, H_2O \rightarrow \ (\frac{m}{2} + n)\, H_2 + n\, CO \qquad\qquad\qquad A.1$$

$$C_n H_m + 2n\, H_2O \rightarrow \ (\frac{m}{2} + 2n)\, H_2 + CO_2 \qquad\qquad\qquad A.2$$
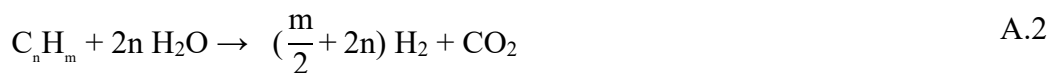
At high temperatures, hydrogen and carbon monoxide are then oxidised at the anode according to the following reactions:

$$CO + O^{2-} \rightarrow \ CO_2 + 2e^- \qquad\qquad\qquad A.3$$

$$H_2 + O^{2-} \rightarrow H_2O + 2e^- \qquad\qquad\qquad A.4$$

The oxidation of carbon monoxide is usually replaced by the faster water-gas shift reaction (WGSR) in equation A.5 where CO reacts with water from the inserted water steam or from the hydrogen oxidation reaction, forming more hydrogen and carbon dioxide.

$$CO + H_2O \rightarrow \ CO_2 + H_2 \qquad\qquad\qquad A.5$$
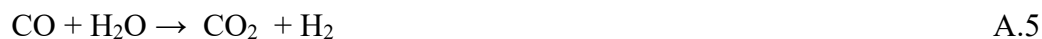
The internal reforming depends on the catalytic activity of the anode catalyst. Nickel provides a high activity for steam reforming of methane but suffers from a high catalytic activity for hydrocarbon cracking, resulting in the formation of carbon on the catalyst surface. This 'coke' formation arises from the Boudouard reaction and catalytic decomposition of methane (below 700 ºC), as presented in equation A.6 and A.7, respectively:

$$2\, CO \rightarrow \ C + CO_2 \qquad\qquad\qquad A.6$$

$$CH_4 \rightarrow C + 2\,H_2 \qquad\qquad A.7$$

Higher steam ratios are used to avoid these reactions and to erase the formation of carbon filaments, however, with the operation on higher hydrocarbons (C_nH_m for $n > 4$) the coke formation occurs faster than it could be removed from the surface [14], [22], [25].

B. Target impurities in zirconium-yttrium targets

Testbourne Ltd
Products for Industry, Research & Development

Certificate of Analysis

Part #:	Z2-9009-D12	LOT No	LOT014292	
Material:	Zirconium Yttrium	Our Ref No.:	SOR022800	
Formula:	Zr-Y 85-15 wt%	Prod Date:		
Size:	76.2mm dia. x 3.18mm Tk	Quantity:	2	
Purity:	99.5%	Customer:	Manchester Metropolitan University	
Density:	6.093g/cm³	Customer PO:	82155727	

Elements	Actual	Spec	Units	Elements	Actual	Spec	Units	Elements	Actual	Spec	Units
Li			ppm	Zn	<15		ppm	Pb	<10		ppm
B			ppm	Ga			ppm	Bi			ppm
F			ppm	Ge			ppm	Y	15(±0.5)		wt%
Na			ppm	As			ppm	Th			ppm
Mg	<20		ppm	Se			ppm	Er			ppm
Al	<150		ppm	Zr	Balance		wt%	Ru			ppm
Si	<50		ppm	Nb	<15		ppm	Re			ppm
P			ppm	Mo			ppm	Os			ppm
Cl			ppm	Pd			ppm	Cs			ppm
K			ppm	Ag			ppm	Cd			ppm
Ca			ppm	Sn			ppm	Tl			ppm
Ti			ppm	Sb			ppm	Be			ppm
V			ppm	Ba			ppm	In			ppm
Cr	<10		ppm	Hf	<1000		ppm				
Mn			ppm	Ta	<15		ppm	C			ppm
Fe	<500		ppm	W			ppm	S			ppm
Co	<10		ppm	Pt			ppm	O			ppm
Ni			ppm	Au			ppm	N			ppm
Cu	<60		ppm	Hg			ppm	H			ppm

Analytical Methods:
1. Metallic elements were analyzed using ICP-OES.
2. Gas elements were analyzed using LECO.

Unit C, The Loddon Centre
Wade Road, Basingstoke,
Hampshire, RG24 8FL, United Kingdom

05/01/2023	S Rushe	G. Stromdale
Date:	Completed By:	Approved:

MS= Quality, Environmental and Occupational Health and Safety Management System   NAGQF011

Figure B.1: Target impurities of zirconium-yttirum (85-15 wt%) provided by *Testbourne Ltd*.

C. Commissioning of Scribner 855 SOFC test station with 5x5 cm^2 gas manifolds

The newly purchased 855 SOFC test station was commissioned by performing electrochemical testing on a commercial SOFC NextCell (5x5 cm^2, supplied by fuelcellmaterials, USA). Cell assembly, conditioning and testing were conducted according to the methodology described in the sections 5.2.2.1, 5.2.3.1 and 5.2.4.1, respectively.

Polarisation curves and electrochemical impedance spectra were obtained at different operational parameters, such as temperature, flow directions between anode and cathode, cell compression and flow rates, to study their effect on the fuel cell performance.

The polarisation and performance curves of the NextCell at 850 °C using the described parameters in section 5.2.4.1, is shown in Figure C.1, in order to present characteristic data obtained from the polarisation curve.
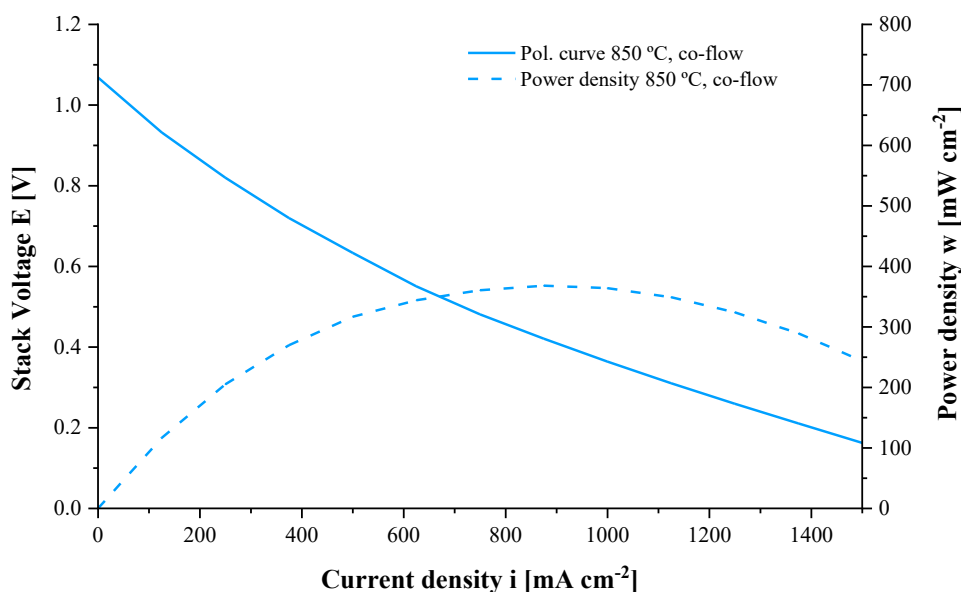
Figure C.1: Performance of the NextCell at 850 °C in co-flow for fuel and oxidant directions.

The commercial 5x5 cm^2 SOFC shows an OCV of 1.07 V at 850 °C and a peak power density of 368 mW/cm^2 at 0.476 V.

The current-interrupt method was used to determine the voltage drop iR representing the pure ohmic losses in the cell. It yields an ohmic resistance of 0.420 Ω cm^2 (active surface area of the electrolyte is 16 cm^2) between 0.7 and 0.9 V, which is characteristic for electrolytes with thicknesses of 150 μm.

Hereafter, influences on the polarisation curve in terms of different temperatures, flow rates and flow arrangements are discussed.

C.1 Effects on the polarisation curve

Firstly, the influence of the compression of the cell assembly on the results has been analysed. The polarisation curve was recorded at a compression load of 12 and 20 lbs, respectively, representing 3 and 5 PSI (20.7 and 34.5 kPa) for a cell area of 25 cm^2, as illustrated in Figure C.2.
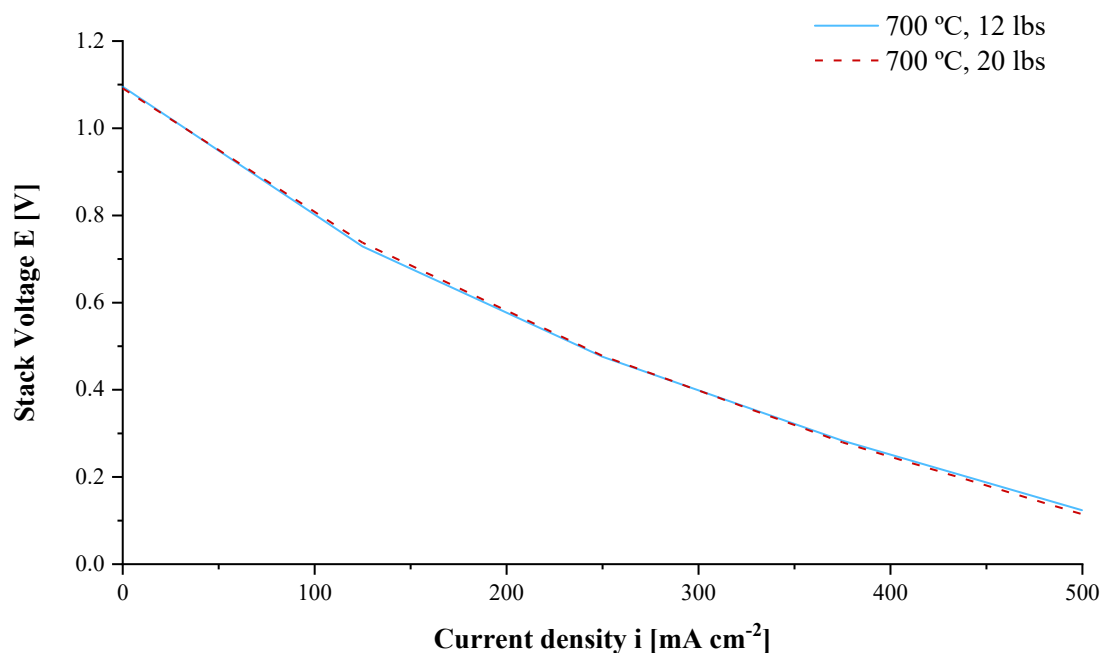
Figure C.2: Polarisation curves at 700 ºC with varying compression of the cell assembly.

Both polarisation curves show an OCV of 1.09 V. The impact of compression between 3 and 5 PSI SI (20.7 and 34.5 kPa) onto the cell assembly did not affect its performance. A higher compression forms a better contact between either the Ni or Ag mesh and the manifolds, while decreasing the contact resistance. However, further compression could lead to damage to the cell. For that reason, the system was set to the manufacturer's guideline at 5 PSI (34.5 kPa) in subsequent performance tests.

Secondly, the impact of the gas delivery system on the cell performance was measured. The arrangement of the gas inlets was changed from co-flow to counter-flow by swapping the air inlet and outlet fittings. Figure C.3 presents the recorded polarisation curves in both configurations.
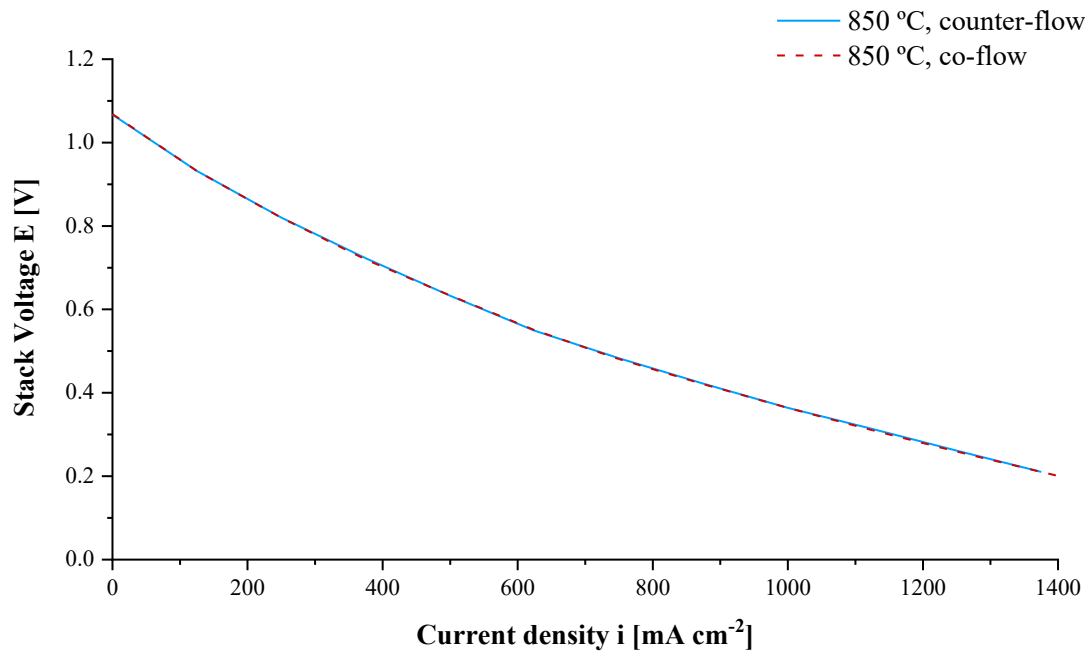
Figure C.3 Polarisation curves at 850 ºC in co-flow and counter-flow configurations.

From this data, it can be observed that the cell performance did not depend on the flow arrangement. The manufacturer stated that the test fixture has a better performance in a cross-flow configuration. However, a co-flow arrangement was chosen due to restrictions in the laboratory.

Figure C.4 shows a comparison of the cell performance of the Nextcell at 700 and 850 ºC. The internal ohmic losses are 1.01 Ω cm^2 and 0.42 Ω cm^2 at 700 and 850 ºC between 0.7 and 0.9 V, respectively. What can be clearly seen is the rapid decrease in the cell voltage at 700 ºC, resulting in higher ohmic losses due to lower activation of ionic conductivity of the used scandia-stabilised zirconia electrolyte in the NextCell at lower temperatures.
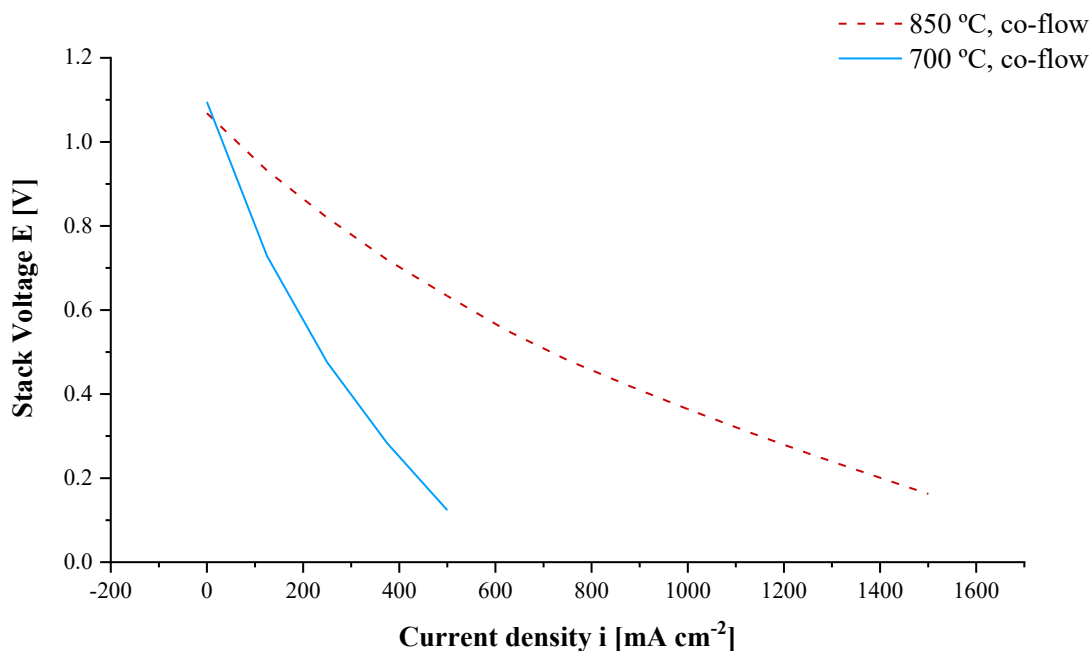
Figure C.4 Polarisation curves of NextCell at 700 and 850 ºC.

Finally, the performance was studied at various flow rates of 300, 600 and 900 sccm for both, hydrogen and air. The I-V curves and resulting power densities are displayed in the following figure.
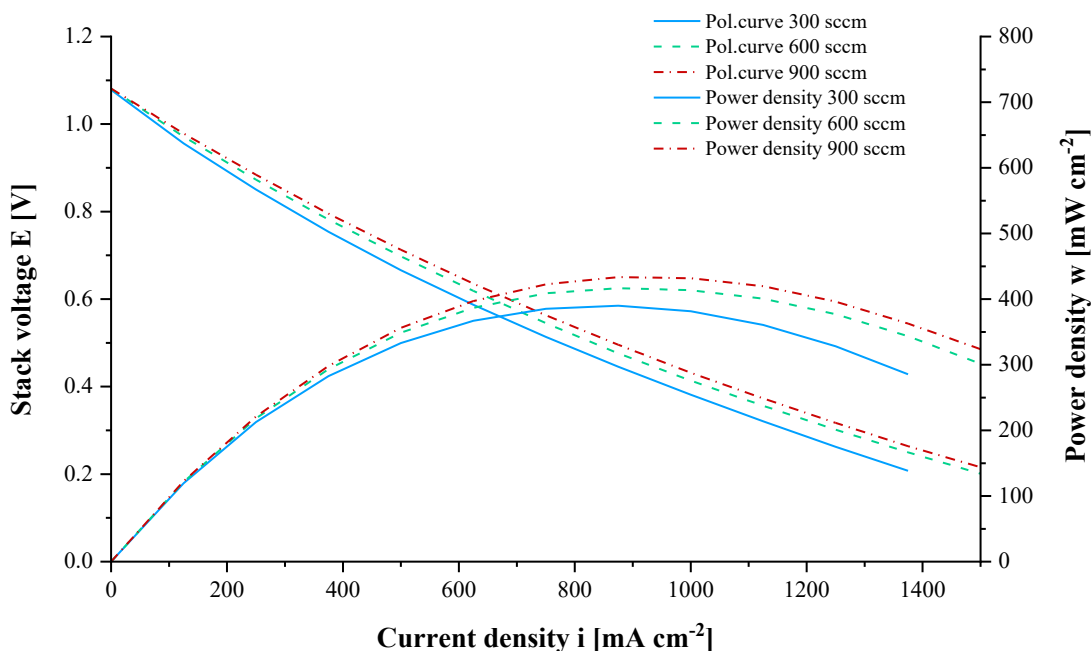
Figure C.5 Polarisation curves and power density curves at 850 ºC and various flow rates.

A clear trend of improved performance with higher flow rates can be noted. The measured OCV increased from 1.07 to 1.08 V. Significantly higher flowrates lead to an

increase in the partial pressure of the reactants, resulting in a slight voltage increase based on the Nernst equation [11].

The following table presents the resulting peak power densities and internal ohmic losses R_Ω from the iR drop with increasing flow rates. In addition to that, the total resistance of the cell ASR_{total} between 0.7 and 0.9 V was calculated from the slope of the I-V curve (cell area 25 cm^2). Since ohmic losses are not affected by the flow rates, the results indicate lower mass transfer losses (concentration polarisation) at higher flow rates.

Table C.1: Maximum power densities and area-specific resistance ASR at varying flow rates at 850 ºC.

Hydrogen flowrate [sccm]	Oxygen flowrate [sccm]	Peak power density [W cm^{-2}]	ASR_{total} [Ω cm^2]	R_Ω [Ω cm^2]
300	300	0.390	1.205	0.412
600	600	0.416	1.184	0.414
900	900	0.434	1.072	0.412

When considering the optimal operation conditions to achieve the best performance in terms of fuel utilisation of the inserted reactants, the fuel rates have to be adjusted, depending on the current drawn from the cell. The Fuelcell software from Scribner Associates provides the application of stoichiometric flow rates, while keeping minimum reactant flows in the background. After setting the utilisation for hydrogen and oxygen (air) in the software, the requested amount of gas will be delivered depending on the current drawn during the experiment. For instance, at 50% hydrogen utilisation (stoichiometry $S = 2$) and a minimum flowrate of 100 sccm in the background, the system will increase the flow rate at currents above 7 A to provide the demanded amount of fuel. Stoichiometry values for hydrogen and oxygen are usually around 2 and 2.5, respectively, [28].

C.2 Effects on the impedance

The impedance sweeps were performed at a superposed AC current of 0.5 A and a DC current of 2 A between 10000 Hz and 0.1 Hz under the conditions similar to those of the polarisation curves.

Figure C.6 presents the impedance spectra at different compressions of the cell assembly at 700 ºC. The spectra reveal two impedance arcs, showing two-time constants for the polarisation resistance of the electrochemical processes.

The ohmic resistance R_Ω is represented by the first intercept on the x-axis at high frequencies and the total resistance of the cell (ASR_{total}) correlates with the second intercept at low frequencies.

The impedance spectra at a higher compression of the cell assembly show a shift towards lower values of R_Ω, while maintaining the same shape. This is an indication that only resistive components (probably related to interfacial contacts among the several components constituting the cell) are affected. Ohmic losses at 12 lbs and 20 lbs yield 0.062 Ω and 0.056 Ω, respectively, leading to a difference of 0.006 Ω (0.16 Ω cm^2) at a temperature of 700 ºC, which represents the decrease in contact resistance of the cell assembly with increasing compression.

The impedance spectrum at 700 ºC and 20 lbs yield ohmic losses of 0.912 Ω cm^2 compared to 1.012 Ω cm^2 measured by the iR drop method. The impedance measurements lead to a more precise differentiation between the ohmic and polarisation resistance compared to the polarisation curve or the current-interrupt method.
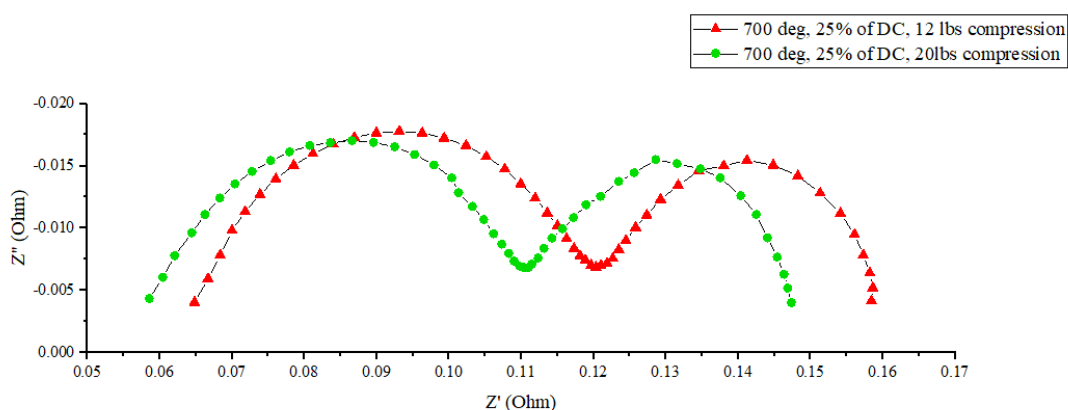
Figure C.6: Impedance spectra at 700 ºC with varying compression of 3 and 5 PSI.

Furthermore, the influence of increasing flow rates on the impedance spectra is illustrated in Figure C.7 at a higher temperature of 850 ºC. The ohmic losses at a higher temperature decreased substantially to 0.395 Ω cm^2 (0.025 Ω) due to the greater ionic conductivity.

Leonide *et al.* presented an equivalent circuit model, where processes at the anode/electrolyte interface occur at higher frequencies and at the cathode/electrolyte at lower frequencies [186]. Thus, the impedance arc at high frequencies is most likely to be attributed to the anode polarisation and the other one to the cathode polarisation. The anode polarisation shows no significant changes with higher flow rates, whereas

the cathode polarisation decreases significantly, implying reduced concentration losses due to a greater amount of reactant available in the electrode.
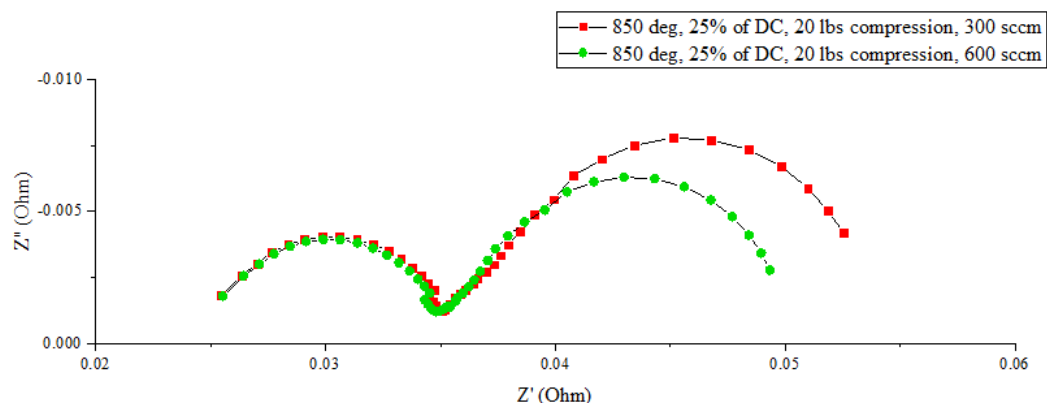
Figure C.7: Impedance spectra with varying flow rates of 300 and 600 sccm for both reactants at 850 ºC, 0.5 A, 5 PSI compression.

Equivalent circuit model

In the following, the principle of equivalent circuit modelling is presented by applying the simplest equivalent circuit model (ECM) on the impedance spectrum from the above chart at 850 ºC, 600 sccm H_2 and 600 sccm air. This ECM comprises two parallel circuits of resistor and constant phase element for capacitive behaviour, representing the cathode and anode, and an ohmic resistance of the electrolyte, as shown in Figure C.8.

Since the impedance spectrum shows a suppressed impedance arc rather than a complete semicircle, the behaviour of the double-layer capacitance does not correspond to a pure capacitor with a 90° phase angle. For that reason, a constant phase element, so-called CPE, was used instead. The phase angle is displayed by the parameter CPE-P and ranges from 0 to 1. The value 1 is indicative of a pure capacitor.

From the data in Figure C.8, the double layer capacitance of the interface between anode/electrolyte (CPE2A) and cathode/electrolyte (CPE1C) accounts for 65.9 mF and 23.27 F, respectively at a phase angle of 85°. The ohmic resistance at a temperature of 850 ºC is around 25 mΩ, which is shown in the previous data. Furthermore, the polarisation resistance of a cathode and an anode is determined by the intercept of the impedance arcs on the x-axis. The equivalent circuit modelling yields 10.3 mΩ (0.17 Ω cm^2) for the charge transfer resistance of the hydrogen oxidation reaction and 15.4 mΩ (0.25 Ω cm^2) for the oxygen reduction reaction.

Element	Freedom		Value	Error	Error%
Rs	[+]	Free(+)	0.024964	0.00019266	0.77175
R2A	[+]	Free(±)	0.010319	0.0002506	2.4285
CPE2A-T	[+]	Free(+)	0.065945	0.0096876	14.69
CPE2A-P	[+]	Free(+)	0.84501	0.02004	2.3716
R1C	[+]	Free(+)	0.015435	0.00026955	1.7464
CPE1C-T	[+]	Free(+)	23.27	0.63578	2.7322
CPE1C-P	[+]	Free(+)	0.85047	0.015344	1.8042
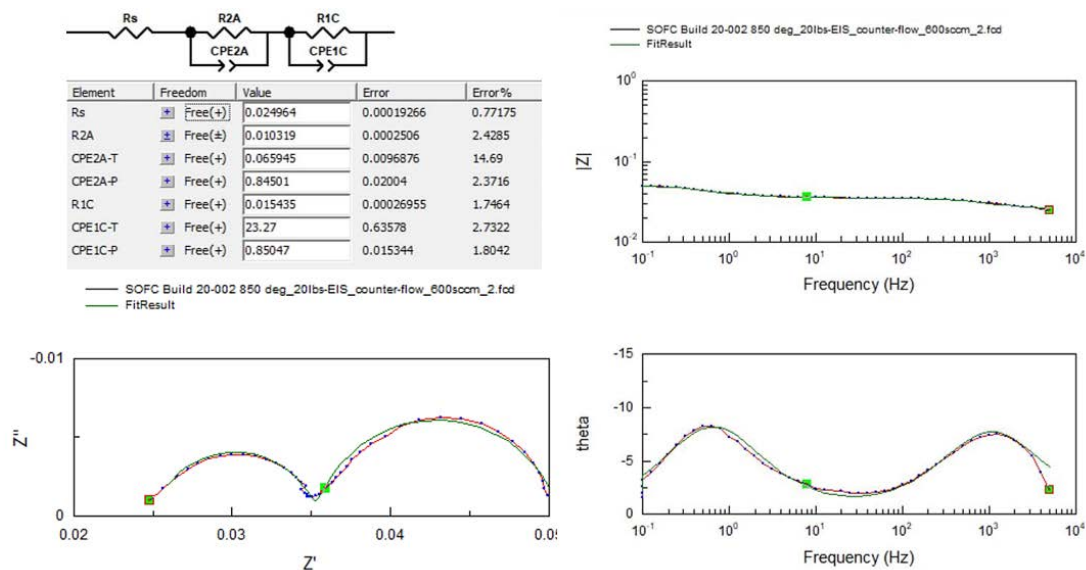
Figure C.8: Equivalent circuit model (top) of EIS at 850 ºC, 0.5 A and 600 sccm H_2 and 600 sccm O_2, fit into Nyquist plot (bottom left) and bode plot (top and bottom right).

The Nyquist plots in Figure C.7 indicates a linear slope at the transition from the high frequency arc to the lower frequency arc. This behaviour might be caused by gas diffusion processes in the anode substrate [186]. Although, adding additional electric circuit elements, such as finite length Warburg elements to characterise and distinguish associated processes, like diffusion, leads to a more appropriate fit of the impedance data, it also makes the results more difficult to understand and interpret.

When comparing the results of the polarisation curves and impedance spectroscopy, it stands out that the impedance spectra characterises ohmic losses and polarisation losses more precisely and gives detailed information of the processes in addition to the I-V curve.

D. Technical drawings of the gas manifolds developed in this work
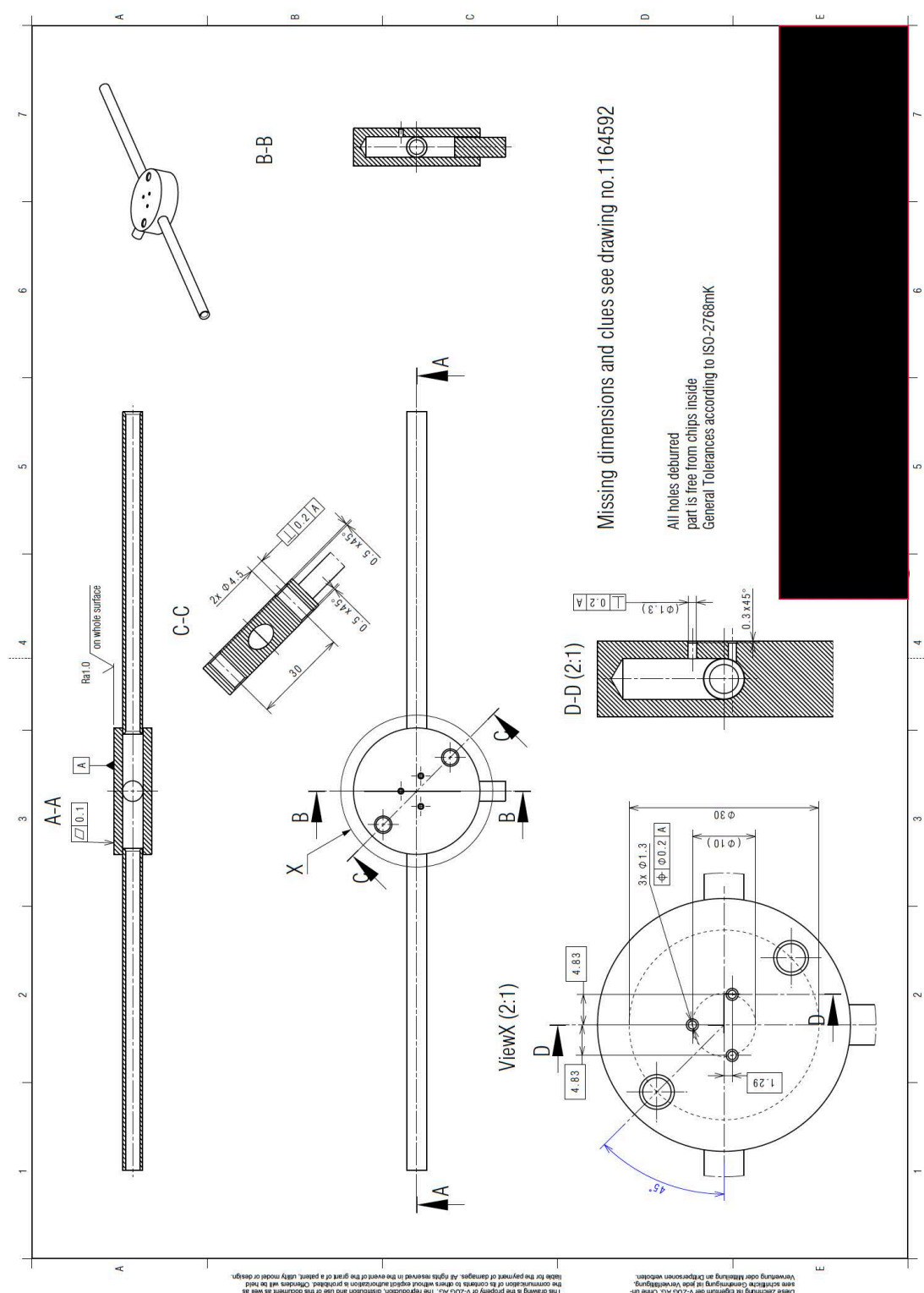
Figure D.1: Gas manifold for SOFC button cell testing, developed within this work.
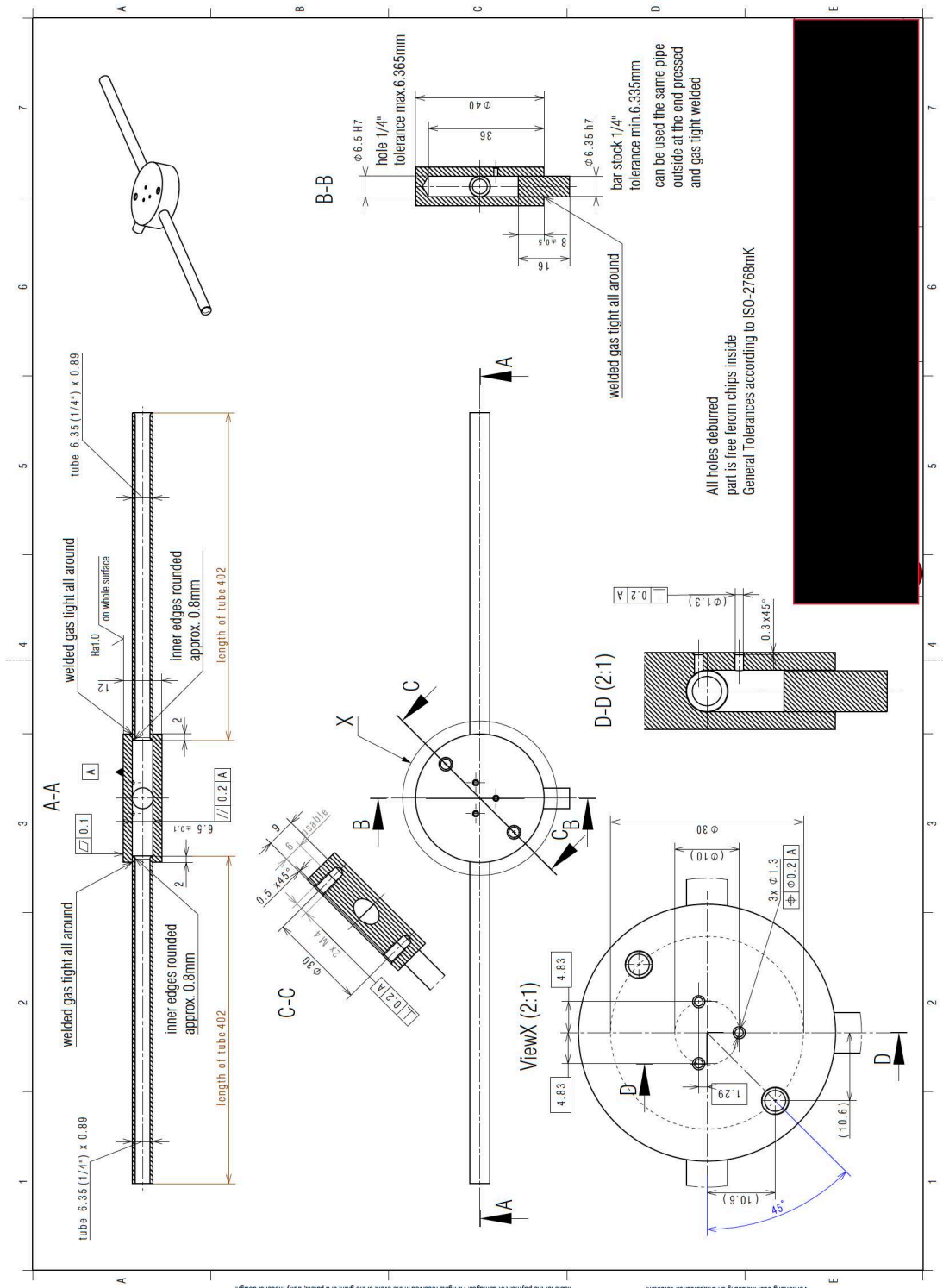
Figure D.2: Gas manifold for SOFC button cell testing, developed within this work, showing concept with detailed dimensions.

E. Commissioning of Scribner 855 SOFC test station with in-house made gas manifolds

Commercial SOFC button cells (NextCell, fuelcellmaterials, USA) have been used to commission gas manifolds developed in this work. Unless other conditions were stated, the cell assembly, conditioning and testing was carried out according to the sections 5.2.2.2, 5.2.3.2 and 5.2.4.2, respectively. The presented design in Figure 5.10, herein referred to Design 1, comprised three gas ports for anode and cathode manifolds.

Figure E.1 exhibits the electrochemical performance at different cathode flows of 100 sccm oxygen (green rectangles), 200 sccm air (red triangles) and 400 sccm air (blue circles), while the hydrogen flow remained at 100 sccm.
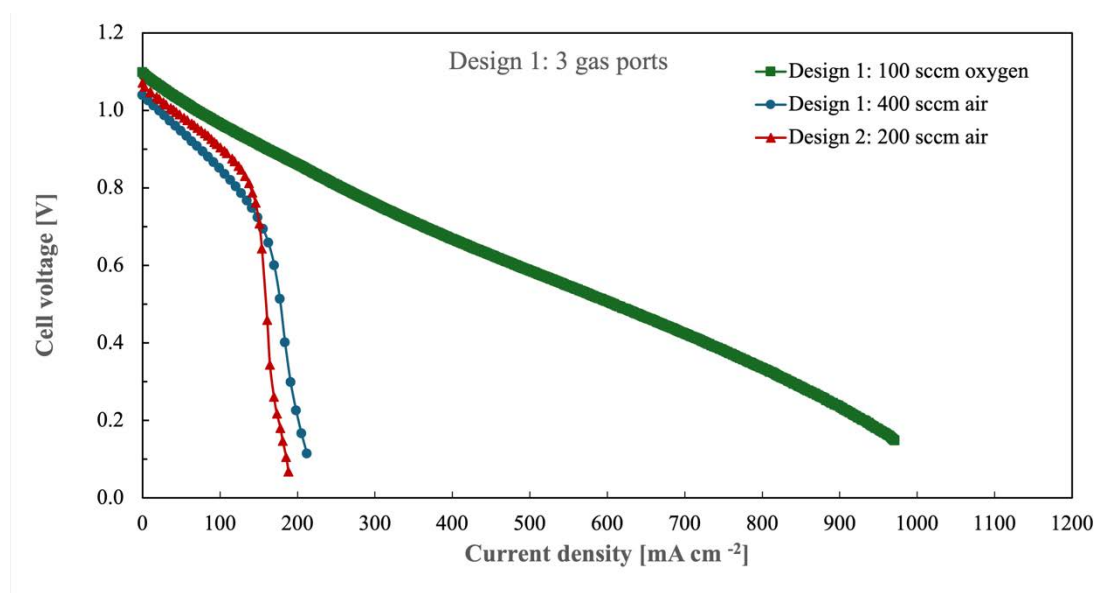
Figure E.1: Electrochemical performance of SOFC NextCell using in-house developed gas manifolds with three gas ports (Design 1) at varied cathode flows of 100 sccm oxygen, 200 sccm air and 400 sccm air. Hydrogen flow rate was kept at 100 sccm.

When running on 200 sccm air, severe mass transport limitations were observed due to the sharp decline in the polarisation curve. The flow rate was increased to 400 sccm air in the expectation of an improvement in transport losses, however, the polarisation curve showed a further decline in the activation region and a slightly lower OCV, indicating possible damage to the electrolyte due to the higher gas pressure. For comparison, the cathode flow was switched from air to oxygen. Operation on a pure reactant flow on the cathode showed no significant concentration losses, suggesting that Design 1 suffers from limitations in transport of air out of the cathode manifold.

For that reason, Design 1 was modified by increasing the number of gas ports in the gas manifold from three to eight, herein referred to Design 2, as shown in the figure below.
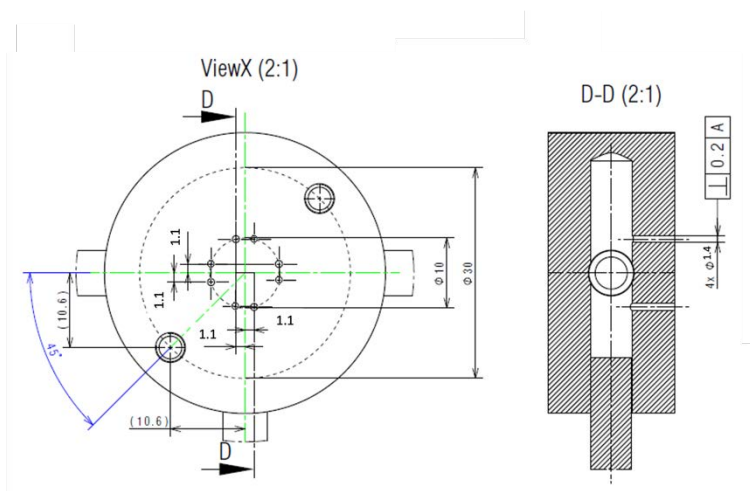
Figure E.2: CAD design of gas manifolds with eight gas ports for SOFC button cells (Design 2).

The resulting polarisation curves using Design 2 gas manifolds are demonstrated in Figure E.3. It can be seen that the new design slightly improved the mass transport at cathode flows of 200 and 400 sccm air compared to the results of Design 1. No severe mass transport limitations are observed when operating on pure oxygen, as seen previously. However, the new design shows an increase in limiting current density from 971 to 1118 A cm^{-2}.

As mentioned in section 10.2.5, further work is required to improve the transport within the air inlet and outlet of the gas ports when running on air. Due to time constraints in this work, the electrochemical testing in-house was carried out on oxygen using Design 2.
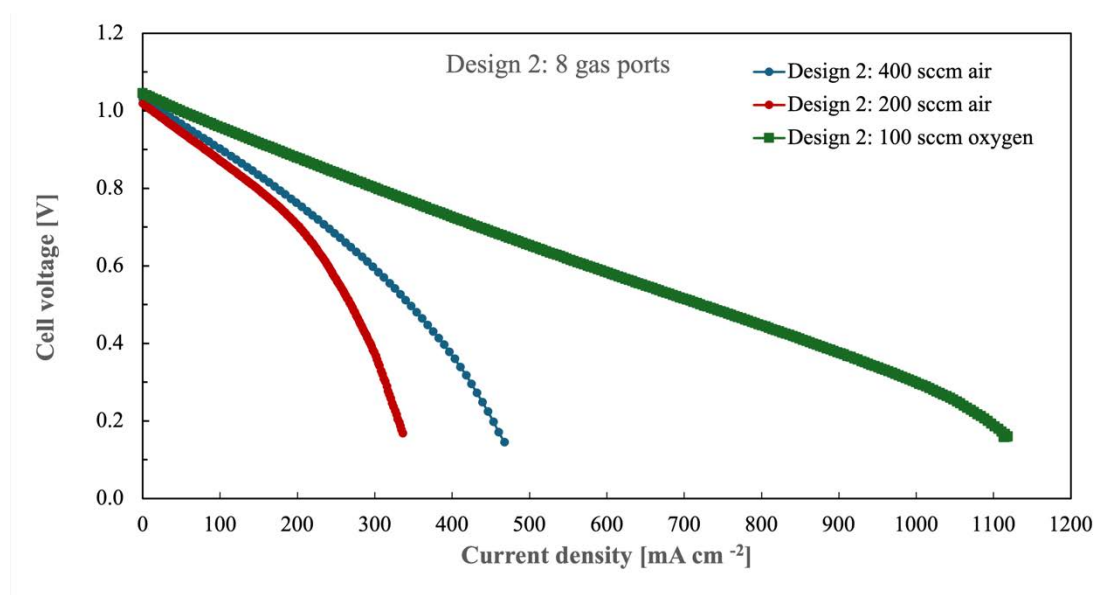
Figure E.3: Electrochemical performance of SOFC NextCell using in-house developed gas manifolds with three gas ports (Design 1) at varied cathode flows of 100 sccm oxygen, 200 sccm air and 400 sccm air. Hydrogen flow rate was kept at 100 sccm.

F. Effect of the cathode layer thickness on the SOFC performance

In order to electrochemically test the Ni-YSZ AFLs which were deposited onto YSZ substrates, a cathode layer needed to be deposited to the back side of the YSZ pellet. In this work, the cathode comprises a mixture of 50:50 wt.% LSM-YSZ and was doctor-bladed on the back of the YSZ substrate after the deposition and annealing at 1250 ºC of three identical Ni-YSZ AFLs. The thickness of the cathode was varied at 20, 40 and 60 μm, as shown in the following SEM images.
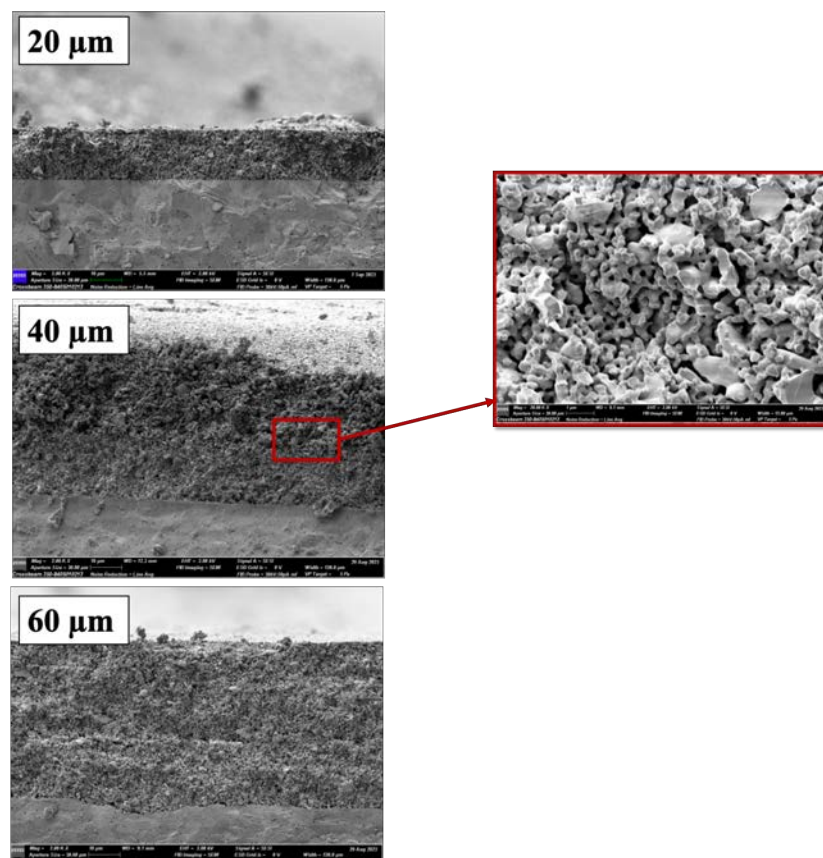
Figure F.1: Electrochemical performance of SOFC button cells deposited with 20, 40 and 60 μm thick LSM-YSZ cathode layers.

The resulting electrochemical performance is shown in Figure F.2.
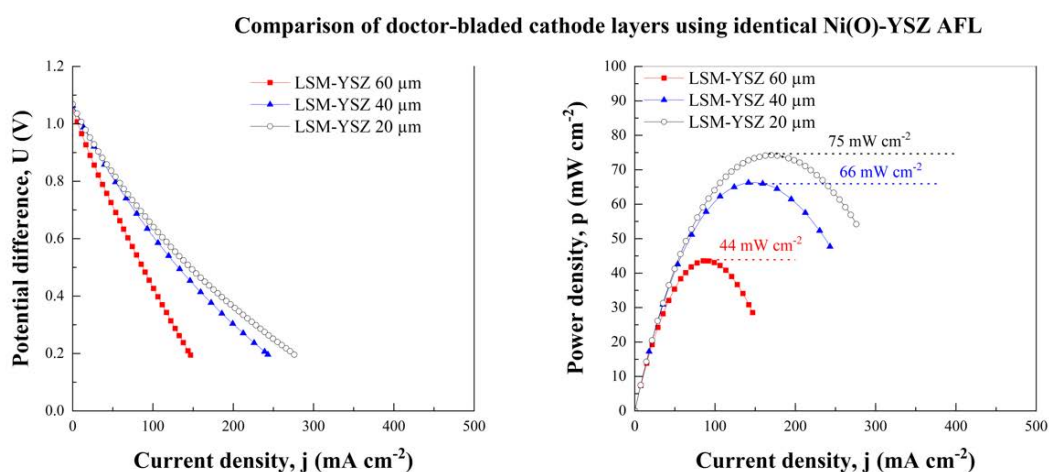
Figure F.2: Electrochemical performance of SOFC button cells deposited with 20, 40 and 60 μm thick LSM-YSZ cathode layers.

The peak power densities are 44, 66 and 77 mW cm^{-2} for 20, 40 and 60 μm, respectively. The thicker the cathode layer, the more resistance was introduced into the cell.

For that reason, the electrochemical tests in this work were carried out using a target cathode layer thickness of 20 µm.

G.   XRD results for Ni(O)-YSZ films using post-deposition annealing temperature of 1250 ºC when depositing without the heater and with substrate heater applied at 400 ºC

The comparison of the XRD data annealed at 1200 ºC and 1250 ºC is illustrated in Figure G.1. After reduction in hydrogen, the samples deposited without substrate heater (Ni-YSZ-NH-A1200-R and Ni-YSZ-NH-A1250-R), as well as samples deposited with applied heater at 400 ºC (Ni-YSZ-H-A1200-R and Ni-YSZ-H-A1250-R) presented no major differences in the peak patterns. However, when calculating the crystallite size, slight differences were observed (cf. Table 8.10).
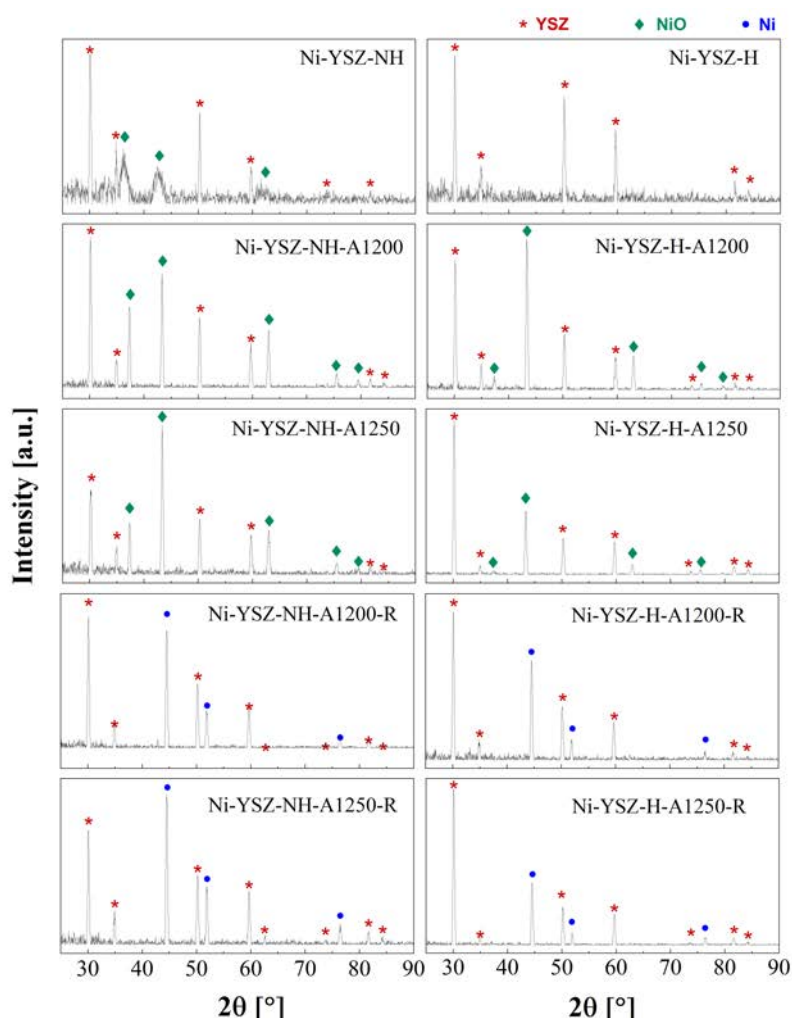
Figure G.1: XRD patterns of the as-deposited Ni(O)-YSZ films without using a heater (Ni-YSZ-NH) and with a substrate heater (Ni-YSZ-H), after annealing at 1200 ºC and 1250 ºC in air for 1 h (Ni-YSZ-NH-A1200, Ni-YSZ-H-A1200, Ni-YSZ-NH-A1250 and Ni-YSZ-H-A1250) and after subsequent reduction at 850 ºC in 10% H_2/N_2 for

10 h (Ni-YSZ-NH-A1200-R and Ni-YSZ-H-A1200-R, Ni-YSZ-NH-A1250-R and Ni-YSZ-H-A1250-R).

H. Elemental mapping of undoped Ni-YSZ AFL after reduction

Elemental maps were acquired to present the nanostructured Ni-YSZ AFL deposited at 0.7 Pa and annealed at 1250 ºC and compare it to the morphology of vanadium and manganese-doped Ni-YSZ AFLs. The elemental map of the undoped Ni-YSZ AFL is presented in the figure below, showing a significantly finer nanostructure.
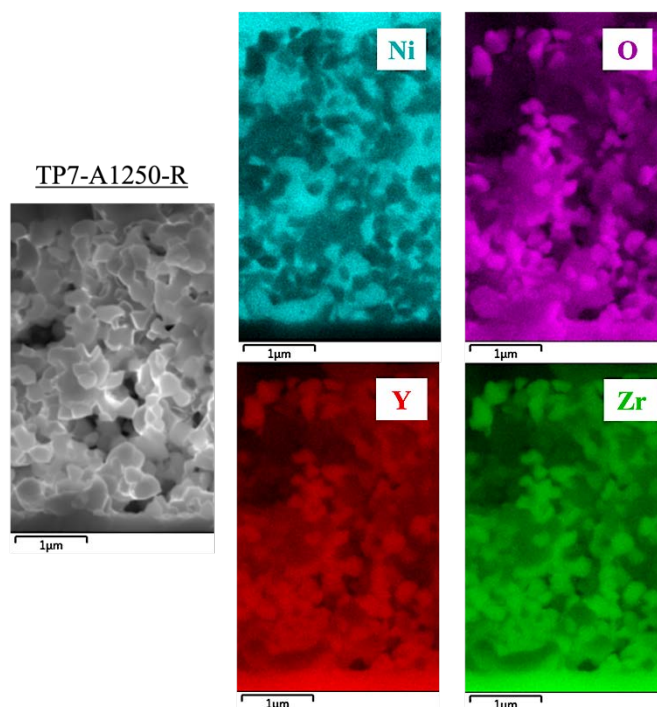
Figure H.1: Elemental mapping collected from the top surface of 7TP-A1250-R using EDS. 7TP-A1250-R was deposited at 0.7 Pa and subsequently annealed at 1250ºC in air for 1 h and reduced in hydrogen for 10 h.

I. Elemental maps for the samples containing initially 1 and 3 mol.% Mn after hydrogen reduction

Additional elemental maps for samples 1Mn-Ni-YSZ-A1250-R and 3Mn- Ni-YSZ-A1250-R are presented in Figure I.1 and Figure I.2, respectively. The figures confirm the presence of manganese oxide at low concentrations after hydrogen reduction.
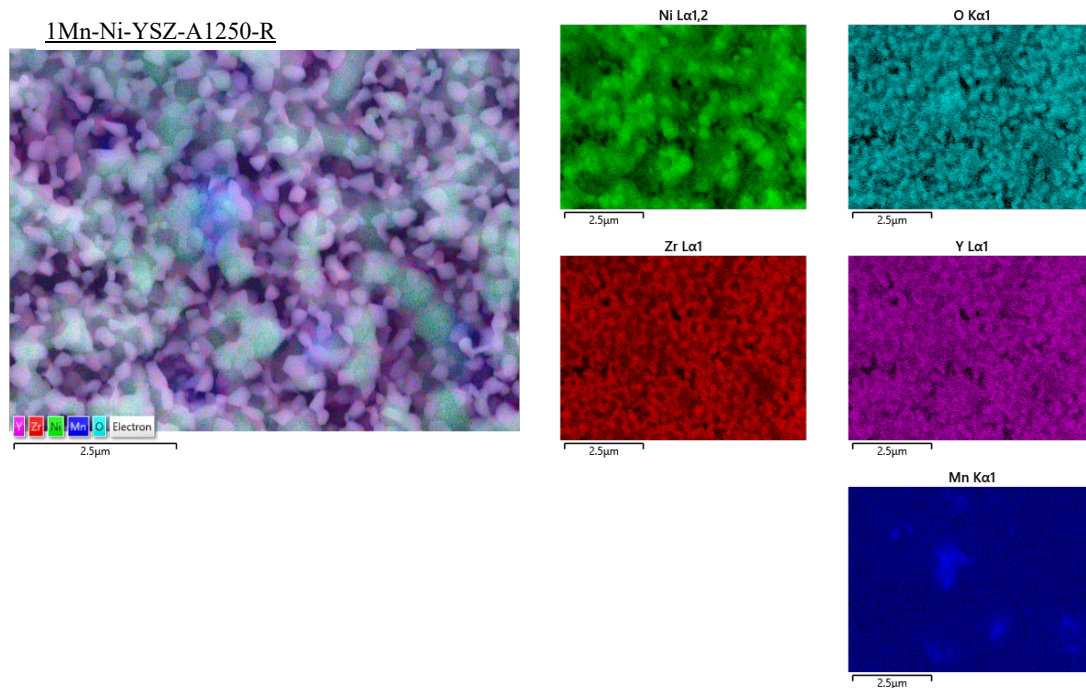
Figure I.1: Elemental mapping of the top surface of 1Mn-Ni-YSZ-A1250-R using EDS. 5Mn-Ni-YSZ-A1250-R was initially doped with 1 mol.% Mn, subsequently annealed at 1250ºC in air for 1 h and reduced in hydrogen for 10 h.
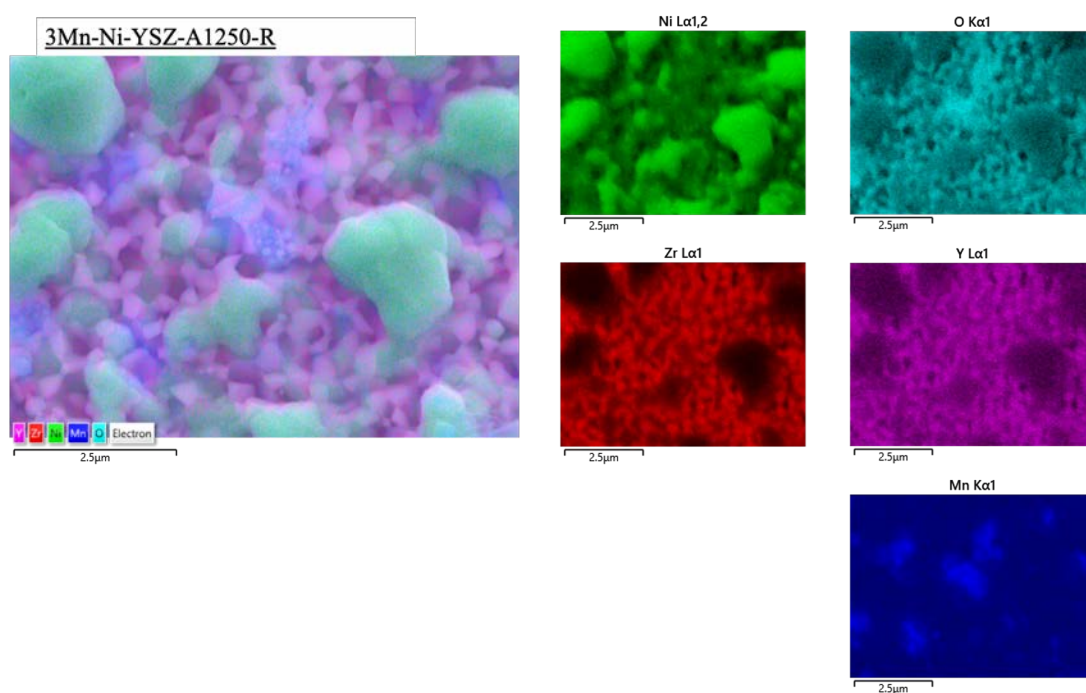
Figure I.2: Elemental mapping of the top surface of 3Mn-Ni-YSZ-A1250-R using EDS. 5Mn-Ni-YSZ-A1250-R was initially doped with 3 mol.% Mn, subsequently annealed at 1250ºC in air for 1 h and reduced in hydrogen for 10 h.

J. Mn 2p XPS spectrum

As mentioned before, the XPS instrument used in this work was equipped with an Al source which caused overlapping photoelectron lines between Mn $2p_{3/2}$ and Auger features of nickel, making it difficult to identify its oxidation state [183]. The Mn 2p XPS spectra fitted with peaks for Mn $2p_{3/2}$ and Ni LMM, as seen in other studies [184], is shown in the figure below.
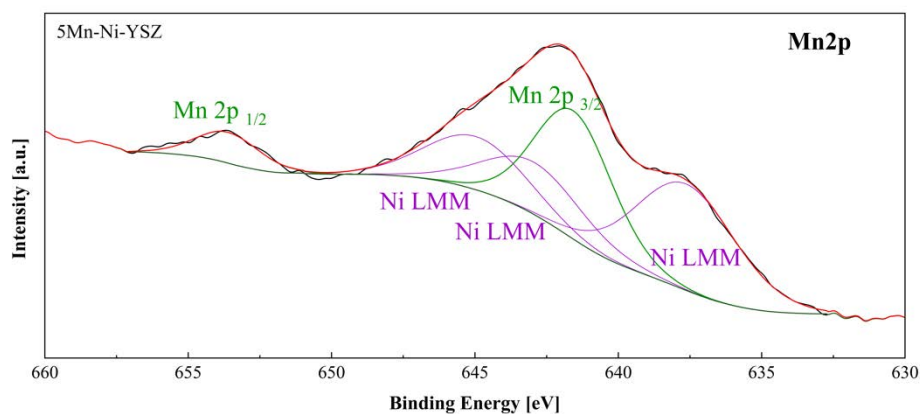
Figure J.1: Mn 2p XPS spectrum for as-deposited sample 5Mn-Ni-YSZ with 5 mol.% Mn, showing overlapping Mn $2p_{3/2}$ with Ni LMM, when using Al as XPS source [183], [184].

References

[1] United Nations Framework Convention on Climate Change, "The Paris Agreement | UNFCCC." Accessed: Mar. 27, 2024. [Online]. Available: https://unfccc.int/process-and-meetings/the-paris-agreement

[2] ESO, "Britain's Electricity Explained: 2022 Review." Accessed: Mar. 27, 2024. [Online]. Available: https://www.nationalgrideso.com/news/britains-electricity-explained-2022-review

[3] UK Government, "Renewable and low carbon energy." Accessed: Mar. 28, 2024. [Online]. Available: https://www.gov.uk/guidance/renewable-and-low-carbon-energy#particular-planning-considerations-for-hydropower-active-solar-technology-solar-farms-and-wind-turbines

[4] IRENA, "Hydrogen: A renewable energy perspective," Abu Dhabi, 2019.

[5] Energy Systems Catapult, "Heat decarbonisation guide." Accessed: Mar. 28, 2024. [Online]. Available: https://es.catapult.org.uk/guide/decarbonisation-heat/#

[6] E. & I. S. Department for Business, "Clean Growth - Transforming Heating - Overview of Current Evidence," 2018.

[7] ITM Power, "HyDeploy: UK Gas Grid Injection of Hydrogen in Full Operation." Accessed: Apr. 09, 2020. [Online]. Available: https://www.itm-power.com/news/hydeploy-uk-gas-grid-injection-of-hydrogen-in-full-operation

[8] J. P. Hodges, W. Geary, S. Graham, P. Hooker, and R. Goff, "Injecting Hydrogen into the Gas Network- A Literature Search," Jan. 2015, Accessed: Mar. 28, 2024. [Online]. Available: https://www.h2knowledgecentre.com/content/policypaper1193

[9] I. Staffell *et al.*, "The role of hydrogen and fuel cells in the global energy system," *Energy Environ. Sci*, vol. 12, p. 463, 2019, doi: 10.1039/c8ee01157e.

[10] R. Howard *et al.*, "Too Hot to Handle? How to decarbonise domestic heating," 2016, Accessed: Mar. 28, 2024. [Online]. Available: www.policy-exchange.org.uk

[11] A. L. Dicks and D. A. J. Rand, *Fuel Cell Systems Explained*, Third. Hoboken: John Wiley & Sons, Inc, 2018. doi: 10.1002/9781118706992.

[12] H. Tschöke, P. Gutzmer, and T. Pfund, *Elektrifizierung des Antriebsstrangs Grundlagen - vom Mikro-Hybrid zum vollelektrischen Antrieb*. Springer Berlin Heidelberg, 2015. doi: 10.1007/978-3-662-60356-7.

[13] P. E. Dodds *et al.*, "Hydrogen and fuel cell technologies for heating: A review," *Int J Hydrogen Energy*, vol. 40, no. 5, pp. 2065–2083, Feb. 2015, doi: 10.1016/J.IJHYDENE.2014.11.059.

[14] M. M. Mench, *Fuel Cell Engines*. 2008. doi: 10.1002/9780470209769.

[15] R. Leah *et al.*, "Ceres Power Steel Cell Technology: Rapid Progress Towards a Truly Commercially Viable SOFC," *The Electrochemical Society*, vol. 68, no. 1, pp. 95–107, 2015.

[16] Green Car Congress, "Ceres Power unveils 5 kW SteelCell SOFC stack, V5 SteelCell technology," BioAge Group. Accessed: May 21, 2020. [Online]. Available: https://www.greencarcongress.com/2018/04/201805406.html

[17] Z. Shao and M. O. Tadé, *Intermediate- Temperature Solid Oxide Fuel Cells Materials and Applications*. Berlin, Heidelberg: Springer Nature, 2016. doi: 10.1007/978-3-662-52936-2.

[18] S. Swann, "Magnetron sputtering," *Physics in Technology*, vol. 19, no. 2, p. 67, Mar. 1988, doi: 10.1088/0305-4624/19/2/304.

[19] Z. Zakaria, Z. Awang Mat, S. H. Abu Hassan, and Y. Boon Kar, "A review of solid oxide fuel cell component fabrication methods toward lowering temperature," *Int J Energy Res*, vol. 44, no. 2, pp. 594–611, Feb. 2020, doi: 10.1002/er.4907.

[20] U.S. Department of Energy, "Cost Study for Manufacturing of Solid Oxide Fuel Cell Power Systems," Alexandria, VA, 2013.

[21] S. J. Cooper and N. P. Brandon, *Solid Oxide Fuel Cell Lifetime and Reliability*. Academic Press, 2017.

[22] K. Kendall and M. Kendall, *High-Temperature Solid Oxide Fuel Cells for the 21st Century - Fundamentals, Design and Applications*, 2nd ed. Oxford: Academic Press is an imprint of Elsevier, 2016.

[23] S. C. Singhal and K. Kendall, *High-temperature Solid Oxide Fuel Cells: Fundamentals, Design and Applications*. New York: Elsevier Advanced Technology, 2003. doi: 10.1016/B978-185617387-2/50018-0.

[24] R. O'Hayre, S.-W. Cha, W. G. Colella, and F. B. Prinz, *Fuel Cell Fundamentals*, 3rd ed. New Jersey: John Wiley & Sons Inc, 2016.

[25] H. Zhu and R. J. Kee, "Modeling Electrochemical Impedance Spectra in SOFC Button Cells with Internal Methane Reforming," *J Electrochem Soc*, vol. 153, no. 9, p. A1765, 2006, doi: 10.1149/1.2220065.

[26] B. C. H. Steele and A. Heinzel, "Materials for fuel-cell technologies," in *Materials for Sustainable Energy: A Collection of Peer-Reviewed Research and Review Articles from Nature Publishing Group*, World Scientific Publishing Co., 2010, pp. 224–231. doi: 10.1142/9789814317665_0031.

[27] Q. A. Huang, R. Hui, B. Wang, and J. Zhang, "A review of AC impedance modeling and validation in SOFC diagnosis," *Electrochim Acta*, vol. 52, no. 28, pp. 8144–8164, 2007, doi: 10.1016/j.electacta.2007.05.071.

[28] Scribner Associates Inc., "Fuel Cell Test Software - Operating Manual," 2020, *Scribner Associates Inc., Southern Pines*: 4.2.

[29] M. E. Orazem and B. Tribollet, *Electrochemical Impedance Spectroscopy*. Hoboken: John Wiley & Sons, Inc, 2008.

[30] J. E. B. Randles, "Kinetics of Rapid Electrode Reactions," *Discuss Faraday Soc*, vol. 1, no. 11, pp. 11–19, 1947, doi: 10.1039/df9470100011.

[31] B. J. M. Sarruf, J. E. Hong, R. Steinberger-Wilckens, and P. E. V. de Miranda, "Influence of novel anode design on the performance and coke resistance towards methane directly-fed solid oxide fuel cells," *Ceram Int*, vol. 46, no. 4, pp. 5368–5379, 2020, doi: 10.1016/j.ceramint.2019.10.292.

[32] T. Ramos, J. Hjelm, and M. Mogensen, "Towards Quantification of Relations Between Electrode Polarisation and Microstructure," *J Electrochem Soc*, vol. 158, no. 7, p. B814, 2011, doi: 10.1149/1.3587113.

[33] K. Momma and F. Izumi, "VESTA 3 for three-dimensional visualization of crystal, volumetric and morphology data," *J Appl Crystallogr*, vol. 44, pp. 1272–1276, Oct. 2011, doi: 10.1107/S0021889811038970.

[34]   A. Tarancón, "Strategies for lowering solid oxide fuel cells operating tempera-
       ture," *Energies (Basel)*, vol. 2, no. 4, pp. 1130–1150, 2009, doi:
       10.3390/en20401130.

[35]   A. Selçuk, G. Merere, and A. Atkinson, "The influence of electrodes on the
       strength of planar zirconia solid oxide fuel cells," *J Mater Sci*, vol. 36, no. 5,
       pp. 1173–1182, Mar. 2001, doi: 10.1023/A:1004833909780.

[36]   C. K. Lin, T. T. Chen, Y. P. Chyou, and L. K. Chiang, "Thermal stress analy-
       sis of a planar SOFC stack," *J Power Sources*, 2007, doi: 10.1016/j.jpow-
       sour.2006.10.089.

[37]   Z. Gao, L. V. Mogni, E. C. Miller, J. G. Railsback, and S. A. Barnett, "A per-
       spective on low-temperature solid oxide fuel cells," *Energy Environ Sci*, vol.
       9, no. 5, pp. 1602–1644, 2016, doi: 10.1039/c5ee03858h.

[38]   B. C. H. Steele, "Materials for IT-SOFC stacks - 35 years R&D: The inevita-
       bility of gradualness?," *Solid State Ion*, vol. 134, pp. 3–20, 2000, doi:
       10.1016/S0167-2738(00)00709-8.

[39]   T. Ishihara, J. Yan, M. Shinagawa, and H. Matsumoto, "Ni-Fe bimetallic an-
       ode as an active anode for intermediate temperature SOFC using LaGaO 3
       based electrolyte film," *Electrochim Acta*, vol. 52, pp. 1645–1650, 2006, doi:
       10.1016/j.electacta.2006.03.103.

[40]   Y. W. Ju, H. Eto, T. Inagaki, S. Ida, and T. Ishihara, "Preparation of Ni–Fe bi-
       metallic porous anode support for solid oxide fuel cells using LaGaO3 based
       electrolyte film with high power density," *J Power Sources*, vol. 195, no. 19,
       pp. 6294–6300, Oct. 2010, doi: 10.1016/J.JPOWSOUR.2010.04.068.

[41]   B. Shri Prakash, R. Pavitra, S. Senthil Kumar, and S. T. Aruna, "Electrolyte
       bi-layering strategy to improve the performance of an intermediate tempera-
       ture solid oxide fuel cell: A review," *J Power Sources*, vol. 381, no. Septem-
       ber 2017, pp. 136–155, 2018, doi: 10.1016/j.jpowsour.2018.02.003.

[42]   T. H. Kwon, T. Lee, and H. I. Yoo, "Partial electronic conductivity and elec-
       trolytic domain of bilayer electrolyte Zr0.84Y0.16O1.92/Ce 0.9Gd0.1O1.95,"
       Solid State Ion, vol. 195, no. 1, pp. 25–35, 2011, doi:
       10.1016/j.ssi.2011.05.002.

[43] H.-W. Choi and S.-H. Yang, "Fabrication of YSZ/GDC Bilayer Electrolyte Thin Film for Solid Oxide Fuel Cells," *Transactions on Electrical and Electronic Materials*, vol. 15, no. 4, pp. 189–192, 2014, doi: 10.4313/TEEM.2014.15.4.189.

[44] A. A. Solovyev, A. V. Shipilova, I. V. Ionov, A. N. Kovalchuk, S. V. Rabotkin, and V. O. Oskirko, "Magnetron-Sputtered YSZ and CGO Electrolytes for SOFC," *J Electron Mater*, vol. 45, no. 8, pp. 3921–3928, 2016, doi: 10.1007/s11664-016-4462-0.

[45] T. Park *et al.*, "Effect of the thickness of sputtered gadolinia-doped ceria as a cathodic interlayer in solid oxide fuel cells," in *Thin Solid Films*, Elsevier, Jun. 2015, pp. 120–124. doi: 10.1016/j.tsf.2015.03.010.

[46] Y. B. Kim, J. H. Shim, T. M. Gür, and F. B. Prinz, "Epitaxial and Polycrystalline Gadolinia-Doped Ceria Cathode Interlayers for Low Temperature Solid Oxide Fuel Cells," *J Electrochem Soc*, vol. 158, no. 11, p. B1453, Oct. 2011, doi: 10.1149/2.001112jes.

[47] B. C. H. Steele, "Materials for high-temperature fuel cells," *Philosophical Transactions of the Royal Society A: Mathematical, Physical and Engineering Sciences*, vol. 354, no. 1712, pp. 1695–1710, Jul. 1996, doi: 10.1098/rsta.1996.0074.

[48] J. H. Lee, H. Moon, H. W. Lee, J. Kim, J. D. Kim, and K. H. Yoon, "Quantitative analysis of microstructure and its related electrical property of SOFC anode, Ni-YSZ cermet," *Solid State Ion*, vol. 148, p. pp.12-26, 2002, doi: 10.1016/S0167-2738(02)00050-4.

[49] I. Horiuti and M. Polanyi, "Exchange Reactions of Hydrogen on Metallic Catalysts," *Transactions of Faraday Society*, vol. 30, pp. 1164–1172, 1934.

[50] S. P. Daley, A. L. Utz, T. R. Trautman, S. T. Ceyer, and S. T. Faraday, "Ethylene Hydrogenation on Ni(111) by Bulk Hydrogen," *J Am Chem Soc*, vol. 116, no. 13, pp. 6001–2002, 1994, Accessed: Oct. 13, 2023. [Online]. Available: https://pubs.acs.org/sharingguidelines

[51] J. Rossmeisl and W. G. Bessler, "Trends in catalytic activity for SOFC anode materials," *Solid State Ion*, vol. 178, pp. 1694–1700, 2008, doi: 10.1016/j.ssi.2007.10.016.

[52] W. G. Bessler, J. Warnatz, and D. G. Goodwin, "The influence of equilibrium potential on the hydrogen oxidation kinetics of SOFC anodes," *Solid State Ion*, vol. 177, pp. 3371–3383, 2007, doi: 10.1016/j.ssi.2006.10.020.

[53] S. Trasatti, "Work Function, Electronegativity, and Electrochemical Behaviour of Metals III. Electrolytic Hydrogen Evolution in Acid Solutions," *J Electroanal Chem Interfacial Electrochem*, vol. 39, no. 1, pp. 163–184, 1972.

[54] T. Setoguchi, K. Okamoto, K. Eguchi, and H. Arai, "Effects of Anode Material and Fuel on Anodic Reaction of Solid Oxide Fuel Cells," *J Electrochem Soc*, vol. 139, pp. 2875–2880, Oct. 1992, doi: 10.1149/1.2068998/XML.

[55] A. Atkinson *et al.*, "Advanced anodes for high-temperature fuel cells," *Nat Mater*, vol. 3, no. 1, pp. 17–27, 2004, doi: 10.1038/nmat1040.

[56] B. Shri Prakash, S. Senthil Kumar, and S. T. Aruna, "Properties and development of Ni/YSZ as an anode material in solid oxide fuel cell: A review," *Renewable and Sustainable Energy Reviews*, vol. 36, pp. 149–179, 2014, doi: 10.1016/j.rser.2014.04.043.

[57] A. Buekenhoudt, A. Kovalevsky, J. Luyten, and F. Snijkers, "Basic Aspects in Inorganic Membrane Preparation," in *Comprehensive Membrane Science and Engineering*, vol. 1, Elsevier Inc., 2010, pp. 217–252. doi: 10.1016/B978-0-08-093250-7.00011-6.

[58] K. Rhazaoui, N. P. Brandon, C. S. Adjiman, and Q. Cai, "Solid Oxide Fuel Cell microstructure and performance modeling," Imperial College London, 2013.

[59] A. M. Abdalla *et al.*, "Nanomaterials for solid oxide fuel cells: A review," *Renewable and Sustainable Energy Reviews*, vol. 82, no. September 2017, pp. 353–368, 2018, doi: 10.1016/j.rser.2017.09.046.

[60] A. Atkinson *et al.*, "Advanced anodes for high-temperature fuel cells," *Nat Mater*, vol. 3, no. 1, pp. 17–27, 2004, doi: 10.1038/nmat1040.

[61] D. W. Dees, T. D. Claar, and D. C. Fee, "Conductivity of Porous Ni / ZrO2-Y2O3 Cermets," *Electrochemical Storage*, vol. 134, no. 9, pp. 2141–2146, 1987.

[62]   T. Kawashima and M. Hishinuma, "Analysis of Electrical Conduction Paths in Ni/YSZ Particlate Composites Using Perlocation Theory," *Mater Trans*, vol. 37, no. 7, pp. 1397–1403, 1996.

[63]   E. Ramírez-Cabrera, A. Atkinson, and D. Chadwick, "Influence of point defects on the resistance of ceria to carbon deposition in hydrocarbon catalysis," *Solid State Ion*, vol. 136–137, pp. 825–831, 2000, doi: 10.1016/S0167-2738(00)00507-5.

[64]   C. R. He and W. G. Wang, "Alumina Doped Ni/YSZ Anode Materials for Solid Oxide Fuel Cells," 2009, doi: 10.1002/fuce.200800152.

[65]   H. Nahor, Y. Kauffmann, and W. D. Kaplan, "The Cr-Doped Ni-YSZ(111) interface: Segregation, oxidation and the Ni equilibrium crystal shape," 2018, doi: 10.1016/j.actamat.2018.12.023.

[66]   A. Holt and P. Kofstad, "Electrical conductivity and defect structure of Cr2O3. I. High temperatures (>~1000°C)," *Solid State Ion*, vol. 69, no. 2, pp. 127–136, Jul. 1994, doi: 10.1016/0167-2738(94)90401-4.

[67]   S. B. Simonsen, T. T. Muhl, K. T. S. Thydén, C. Chatzichristodoulou, J. Nielsen, and B. R. Sudireddy, "Effect of Fe on high performing nanostructured Ni/Gd-doped ceria electrocatalysts," *Solid State Ion*, vol. 340, p. 115019, 2019, doi: 10.1016/j.ssi.2019.115019.

[68]   P. Tiwari and S. Basu, "Performance studies of electrolyte-supported solid oxide fuel cell with Ni-YSZ and Ni-TiO2-YSZ as anodes," *Journal of Solid State Electrochemistry*, vol. 18, no. 3, pp. 805–812, Mar. 2014, doi: 10.1007/s10008-013-2326-6.

[69]   P. K. Tiwari and S. Basu, "CeO2and Nb2O5modified Ni-YSZ anode for solid oxide fuel cell," *Ionics (Kiel)*, vol. 23, no. 10, pp. 2571–2577, 2017, doi: 10.1007/s11581-016-1945-1.

[70]   X. Yao *et al.*, "Coking-resistant NbOx-Ni-Ce0.8Sm0.2O1.9 anode material for methanol-fueled solid oxide fuel cells," *Int J Hydrogen Energy*, vol. 43, no. 28, pp. 12748–12755, 2018, doi: 10.1016/j.ijhydene.2018.03.186.

[71]   Z. Jiang, N. A. Arifin, P. Mardle, and R. Steinberger-Wilckens, "Electrochemical performance and carbon resistance comparison between tin, copper and

silver-doped nickel/yttria-stabilized zirconia anodes SOFCs operated with bio-gas," *J Electrochem Soc*, vol. 166, no. 6, pp. F393–F398, 2019, doi: 10.1149/2.1011906jes.

[72]   X. Hou, K. Zhao, O. A. Marina, M. Grant Norton, and S. Ha, "NiMo-ceria-zir-conia-based anode for solid oxide fuel cells operating on gasoline surrogate," *Appl Catal B*, vol. 242, no. September 2018, pp. 31–39, 2019, doi: 10.1016/j.apcatb.2018.09.095.

[73]   B. Hua, M. Li, B. Chi, and L. Jian, "Enhanced electrochemical performance and carbon deposition resistance of Ni-YSZ anode of solid oxide fuel cells by in situ formed Ni-MnO layer for CH4 on-cell reforming," *J Mater Chem A Mater*, vol. 2, pp. 1150–1158, 2014, doi: 10.1039/c3ta12766d.

[74]   Y. S. Chung, H. Kim, H. C. Yoon, J. S. Chung, and N. M. Sammes, "Effects of Manganese Oxide Addition on Coking Behavior of Ni/YSZ Anodes for SOFCs," *Fuel Cells*, vol. 15, no. 2, pp. 416–426, Apr. 2015, doi: 10.1002/FUCE.201400166.

[75]   W. An, D. Gatewood, B. Dunlap, and C. H. Turner, "Catalytic activity of bi-metallic nickel alloys for solid-oxide fuel cell anode reactions from density-functional theory," *J Power Sources*, vol. 196, pp. 4724–4728, 2011, doi: 10.1016/j.jpowsour.2011.01.007.

[76]   A. Sin *et al.*, "Performance and life-time behaviour of NiCu-CGO anodes for the direct electro-oxidation of methane in IT-SOFCs," *J Power Sources*, vol. 164, no. 1, pp. 300–305, Jan. 2007, doi: 10.1016/j.jpowsour.2006.10.078.

[77]   M. Miyake, M. Iwami, M. Takeuchi, S. Nishimoto, and Y. Kameshima, "Elec-trochemical performance of Ni0.8Cu0.2/Ce0.8Gd0.2O1.9 cermet anodes with functionally graded structures for intermediate-temperature solid oxide fuel cell fueled with syngas," *J Power Sources*, vol. 390, no. April, pp. 181–185, 2018, doi: 10.1016/j.jpowsour.2018.04.051.

[78]   L. M. Toscani, M. G. Zimicz, J. R. Casanova, and S. A. Larrondo, "Ni-Cu/Ce0.9Zr0.1O2 bimetallic cermets for electrochemical and catalytic appli-cations," *Int J Hydrogen Energy*, pp. 8759–8766, 2014, doi: 10.1016/j.ijhydene.2013.12.035.

[79] J. S. O'Brien and J. B. Giorgi, "Solid oxide fuel cell with NiCo-YSZ cermet anode for oxidation of CO/H 2 fuel mixtures," *J Power Sources*, vol. 200, pp. 14–20, Feb. 2012, doi: 10.1016/j.jpowsour.2011.10.080.

[80] C. M. Grgicak, M. M. Pakulska, J. S. O'Brien, and J. B. Giorgi, "Synergistic effects of Ni1-xCox-YSZ and Ni1-xCux-YSZ alloyed cermet SOFC anodes for oxidation of hydrogen and methane fuels containing H2S," *J Power Sources*, vol. 183, no. 1, pp. 26–33, Aug. 2008, doi: 10.1016/j.jpowsour.2008.05.002.

[81] R. Da Paz Fiuza, M. Aurélio Da Silva, and J. S. Boaventura, "Development of Fe-Ni/YSZ-GDC electrocatalysts for application as SOFC anodes: XRD and TPR characterization and evaluation in the ethanol steam reforming reaction," *Int J Hydrogen Energy*, vol. 35, pp. 11216–11228, 2010, doi: 10.1016/j.ijhydene.2010.07.026.

[82] K. Li *et al.*, "High performance NieFe alloy supported SOFCs fabricated by low cost tape casting-screen printing-cofiring process," 2014, doi: 10.1016/j.ijhydene.2014.09.146.

[83] C. J. Fu, S. H. Chan, X. M. Ge, Q. L. Liu, and G. Pasciak, "A promising Ni-Fe bimetallic anode for intermediate-temperature SOFC based on Gd-doped ceria electrolyte," *Int J Hydrogen Energy*, vol. 36, pp. 13727–13734, 2011, doi: 10.1016/j.ijhydene.2011.07.119.

[84] X. Wang *et al.*, "Porous Ni-Fe alloys as anode support for intermediate temperature solid oxide fuel cells: I. Fabrication, redox and thermal behaviors," *J Power Sources*, vol. 277, pp. 474–479, 2014, doi: 10.1016/j.jpowsour.2014.10.165.

[85] J. Choi *et al.*, "A Highly Efficient Bifunctional Electrode Fashioned with In Situ Exsolved NiFe Alloys for Reversible Solid Oxide Cells," *ACS Sustain Chem Eng*, vol. 10, no. 23, pp. 7595–7602, Jun. 2022, doi: 10.1021/ACSSUSCHEMENG.2C01360/SUPPL_FILE/SC2C01360_SI_001.PDF.

[86] H. C. Tsai, S. I. Morozov, T. H. Yu, B. V. Merinov, and W. A. Goddard, "First-Principles Modeling of Ni4M (M = Co, Fe, and Mn) Alloys as Solid Oxide Fuel Cell Anode Catalyst for Methane Reforming," *Journal of Physical Chemistry C*, vol. 120, no. 1, pp. 207–214, Jan. 2016, doi: 10.1021/ACS.JPCC.5B06847/SUPPL_FILE/JP5B06847_SI_001.PDF.

[87] F. Yu *et al.*, "All-solid-state direct carbon fuel cells with thin yttrium-stabilized-zirconia electrolyte supported on nickel and iron bimetal-based anodes," *Int J Hydrogen Energy*, vol. 41, no. 21, pp. 9048–9058, Jun. 2016, doi: 10.1016/J.IJHYDENE.2016.04.063.

[88] M. Wang, N. Li, Z. Wang, C. Chen, and Z. Zhan, "Electrochemical performance and redox stability of solid oxide fuel cells supported on dual-layered anodes of Ni-YSZ cermet and Ni-Fe alloy," *Int J Hydrogen Energy*, vol. 47, pp. 5453–5461, 2022, doi: 10.1016/j.ijhydene.2021.11.129.

[89] C. Fu, S. Hwa Chan, Q. Liu, X. Ge, and G. Pasciak, "Fabrication and evaluation of Ni-GDC composite anode prepared by aqueous-based tape casting method for low-temperature solid oxide fuel cell," *Int J Hydrogen Energy*, vol. 35, pp. 301–307, 2010, doi: 10.1016/j.ijhydene.2009.09.101.

[90] R. J. Gorte, H. Kim, and J. M. Vohs, "Novel SOFC anodes for the direct electrochemical oxidation of hydrocarbon," *J Power Sources*, vol. 106, no. 1–2, pp. 10–15, Apr. 2002, doi: 10.1016/S0378-7753(01)01021-7.

[91] X. F. Ye, S. R. Wang, Q. Hu, J. Y. Chen, T. L. Wen, and Z. Y. Wen, "Improvement of Cu-CeO2 anodes for SOFCs running on ethanol fuels," *Solid State Ion*, vol. 180, no. 2–3, pp. 276–281, Mar. 2009, doi: 10.1016/j.ssi.2008.11.010.

[92] R. J. Gorte, S. Park, J. M. Vohs, and C. Wang, "Anodes for Direct Oxidation of Dry Hydrocarbons in a Solid-Oxide Fuel Cell," *Advanced Materials*, vol. 12, no. 19, pp. 1465–1469, Oct. 2000, doi: 10.1002/1521-4095(200010)12:19<1465::AID-ADMA1465>3.0.CO;2-9.

[93] O. Costa-Nunes, R. J. Gorte, and J. M. Vohs, "Comparison of the performance of Cu-CeO 2-YSZ and Ni-YSZ composite SOFC anodes with H 2 , CO, and syngas," *J Power Sources*, vol. 141, pp. 241–249, 2005, doi: 10.1016/j.jpowsour.2004.09.022.

[94] Q. Van Overmeere and S. Ramanathan, "Thin film fuel cells with vanadium oxide anodes: Strain and stoichiometry effects," *Electrochim Acta*, vol. 150, pp. 83–88, 2014, doi: 10.1016/j.electacta.2014.10.152.

[95] P. I. Cowin, C. T. G. Petit, R. Lan, J. T. S. Irvine, and S. Tao, "Recent progress in the development of anode materials for solid oxide fuel cells," May 01, 2011, *John Wiley & Sons, Ltd*. doi: 10.1002/aenm.201100108.

[96] H. Tu, H. Lv, Q. Yu, K. Hu, and X. Zhu, "Ce0.8 M0.2 O2-δ (M=Mn, Fe, Ni, Cu) as SOFC anodes for electrochemical oxidation of hydrogen and methane," in *Journal of Fuel Cell Science and Technology*, American Society of Mechanical Engineers Digital Collection, Aug. 2008. doi: 10.1115/1.2927764.

[97] V. Vasechko, "Thermo-Mechanical Investigations of Reoxidation-Stable Material Concepts for Solid Oxide Fuel Cells," RWTH Aachen University, 2014.

[98] T. L. Cable and S. W. Sofie, "A symmetrical, planar SOFC design for NASA's high specific power density requirements," *J Power Sources*, vol. 174, no. 1, pp. 221–227, Nov. 2007, doi: 10.1016/J.JPOWSOUR.2007.08.110.

[99] M. Haydn, K. Ortner, T. Franco, N. H. Menzler, A. Venskutonis, and L. S. Sigl, "Development of metal supported solid oxide fuel cells based on powder metallurgical manufacturing route," *Energy Materials: Materials Science and Engineering for Energy Systems*, vol. 8, no. 4, pp. 382–387, 2013, doi: 10.1179/1743290113Y.0000000075.

[100] F. C. Krebs, "Fabrication and processing of polymer solar cells: A review of printing and coating techniques," Apr. 01, 2009, *Elsevier*. doi: 10.1016/j.solmat.2008.10.004.

[101] G. . Ertl, H. . Knözinger, and J. . Weitkamp, "Preparation of solid catalysts," p. 622, 1999, Accessed: Nov. 20, 2024. [Online]. Available: https://www.wiley.com/en-gb/Preparation+of+Solid+Catalysts-p-9783527620685

[102] Z. Liu, B. Liu, D. Ding, M. Liu, F. Chen, and C. Xia, "Fabrication and modification of solid oxide fuel cell anodes via wet impregnation/infiltration technique," *J Power Sources*, vol. 237, pp. 243–259, Sep. 2013, doi: 10.1016/J.JPOWSOUR.2013.03.025.

[103] S. P. Jiang, "A review of wet impregnation—An alternative method for the fabrication of high performance and nano-structured electrodes of solid oxide fuel cells," *Materials Science and Engineering: A*, vol. 418, no. 1–2, pp. 199–210, Feb. 2006, doi: 10.1016/J.MSEA.2005.11.052.

[104] F. S. Torknik, A. Maghsoudipour, M. Keyanpour-Rad, G. M. Choi, S. H. Oh, and G. Y. Shin, "Microstructural refinement of Ni/Ce0.8Gd0.2O2−δ anodes for low-temperature solid oxide fuel cell by wet infiltration loading of PdCl2,"

Ceram Int, vol. 40, no. 8, pp. 12299–12312, Sep. 2014, doi: 10.1016/J.CERA-MINT.2014.04.075.

[105] F. S. Torknik, G. M. Choi, A. Maghsoudipour, and M. Kianpour Rad, "Nanostructuring Platinum Nanoparticles on Ni/Ce0.8Gd0.2O2-δ Anode for Low Temperature Solid Oxide Fuel Cell via Single-step Infiltration: A Case Study," *Advanced Ceramics Progress*, vol. 4, no. 1, pp. 45–51, Feb. 2018, doi: 10.30501/ACP.2018.90833.

[106] H. Frey and H. R. Khan, *Handbook of Thin-Film Technology*. Springer-Verlag Berlin Heidelberg, 2015. doi: 10.1007/978-3-642-05430-3.

[107] M. Grao, "Development of photocatalytic functional coatings via magnetron sputtering deposition and their integration into a laboratory-scale water treatment reactor," Manchester Metropolitan University, Manchester, 2022.

[108] M. Leskelä and M. Ritala, "Atomic layer deposition (ALD): from precursors to thin film structures," *Thin Solid Films*, vol. 409, no. 1, pp. 138–146, Apr. 2002, doi: 10.1016/S0040-6090(02)00117-7.

[109] J. H. Shim, C. C. Chao, H. Huango, and F. B. Prinz, "Atomic layer deposition of yttria-stabilized zirconia for solid oxide fuel cells," *Chemistry of Materials*, vol. 19, no. 15, pp. 3850–3854, Jul. 2007, doi: 10.1021/CM070913T/AS-SET/IMAGES/MEDIUM/CM070913TN00001.GIF.

[110] M. Ohring, *The Materials Science of Thin Films*. London: Academic Press, 1992.

[111] Z. Liu, "Laser Applied Coatings," *Shreir's Corrosion*, pp. 2622–2635, Jan. 2010, doi: 10.1016/B978-044452787-5.00141-4.

[112] A. Anders, "Discharge physics of high power impulse magnetron sputtering," *Surf Coat Technol*, vol. 205, no. supplement 2, pp. S1–S9, Jul. 2011, doi: 10.1016/J.SURFCOAT.2011.03.081.

[113] J. T. Gudmundsson and D. Lundin, "Introduction to magnetron sputtering," in *High Power Impulse Magnetron Sputtering : Fundamentals, Technologies, Challenges and Applications*, 1st ed., D. Lundin, T. Minea, and J. T. Gudmundsson, Eds., Amsterdam: Elsevier, 2020, ch. 1, pp. 1–48. doi: 10.1016/B978-0-12-812454-3.00006-1.

[114] W. Kiyotaka, K. Isaku, and K. Hidetoshi, *Handbook of Sputter Deposition Technology: Fundamentals and Applications for Functional Thin Films*, First Edit. Elsevier, 2012. doi: 10.1016/B978-1-4377-3483-6.00001-2.

[115] P. J. Kelly and R. D. Arnell, "Magnetron sputtering: A review of recent developments and applications," *Vacuum*, vol. 56, no. 3, pp. 159–172, Mar. 2000, doi: 10.1016/S0042-207X(99)00189-X.

[116] J. J. Moore, I.-W. Park, J. Lin, B. Mishra, and K. H. Kim, "Nanostructured, Multifunctional Tribological Coatings," in *Nanocomposite Thin Films and Coatings: Processing, Properties and Performance*, S. Zhang and N. Ali, Eds., London: Imperial College Press, 2007, ch. 6, pp. 329–380.

[117] P. J. Kelly and R. D. Arnell, "Magnetron sputtering: A review of recent developments and applications," *Vacuum*, vol. 56, no. 3, pp. 159–172, Mar. 2000, doi: 10.1016/S0042-207X(99)00189-X.

[118] R. D. Arnell and P. J. Kelly, "Recent advances in magnetron sputtering," *Surf Coat Technol*, vol. 112, no. 1–3, pp. 170–176, 1999, doi: 10.1016/S0257-8972(98)00749-X.

[119] P. J. Kelly and J. W. Bradley, "Pulsed magnetron sputtering - process overview and applications," *Journal of Optoelectronics and Advanced Materials*, vol. 11, no. 9, pp. 1101–1107, 2009.

[120] D. Depla, S. Heirwegh, S. Mahieu, J. Haemers, and R. De Gryse, "Understanding the discharge voltage behavior during reactive sputtering of oxides," *J Appl Phys*, vol. 101, no. 1, 2007, doi: 10.1063/1.2404583.

[121] L. Banko, Y. Lysogorskiy, D. Grochla, D. Naujoks, R. Drautz, and A. Ludwig, "Predicting structure zone diagrams for thin film synthesis by generative machine learning," *Commun Mater*, vol. 1, no. 15, Mar. 2020, doi: 10.1038/s43246-020-0017-2.

[122] B. A. Movchan and A. V Demchishin, "Structure and properties of thick condensates of nickel, titanium, tungsten, aluminium oxides, and zirconium dioxide in vacuum," *Fiz. Metal. Metalloved.*, vol. 28, pp. 653–660, Jan. 1969, doi: 10.1149/1.2096222.

[123] J. A. Thornton, "Influence of apparatus geometry and deposition conditions on the structure and topography of thick sputtered coatings," *Journal of Vacuum*

Science and Technology, vol. 11, pp. 666–670, Jul. 1974, doi: 10.1116/1.1312732.

[124] P. J. Kelly and R. D. Arnell, "Development of a novel structure zone model relating to the closed-field unbalanced magnetron sputtering system," *Journal of Vacuum Science & Technology A: Vacuum, Surfaces, and Films*, vol. 16, no. 5, pp. 2858–2869, Sep. 1998, doi: 10.1116/1.581432.

[125] I. Petrov, L. Hultman, J. -E. Sundgren, and J. E. Greene, "Polycrystalline TiN films deposited by reactive bias magnetron sputtering: Effects of ion bombardment on resputtering rates, film composition, and microstructure," *Journal of Vacuum Science & Technology A*, vol. 10, no. 2, pp. 265–272, Mar. 1992, doi: 10.1116/1.578074.

[126] R. Messier, A. P. Giri, and R. A. Roy, "Revised structure zone model for thin film physical structure," *Journal of Vacuum Science & Technology A*, vol. 2, no. 2, pp. 500–503, Apr. 1984, doi: 10.1116/1.572604.

[127] K. Kendall and M. Kendall, *High-Temperature Solid Oxide Fuel Cells for the 21st Century - Fundamentals, Design and Applications*, 2nd ed. Oxford: Academic Press is an imprint of Elsevier, 2016.

[128] J. T. Gudmundsson and D. Lundin, "Introduction to magnetron sputtering," in *High Power Impulse Magnetron Sputtering : Fundamentals, Technologies, Challenges and Applications*, 1st ed., D. Lundin, T. Minea, and J. T. Gudmundsson, Eds., Amsterdam: Elsevier, 2020, ch. 1, pp. 1–48. doi: 10.1016/B978-0-12-812454-3.00006-1.

[129] S. J. Cooper and N. P. Brandon, *Solid Oxide Fuel Cell Lifetime and Reliability*. Academic Press, 2017.

[130] I. V. Ionov *et al.*, "Reactive co-sputter deposition of nanostructured cermet anodes for solid oxide fuel cells," *Jpn J Appl Phys*, vol. 57, no. 1, pp. 30–34, 2018, doi: 10.7567/JJAP.57.01AF07.

[131] F. J. Garcia-Garcia, A. M. Beltran, F. Yubero, A. R. Gonzalez-Elipe, and R. M. Lambert, "High performance novel gadolinium doped ceria / yttria stabilized zirconia / nickel layered and hybrid thin film anodes for application in solid oxide fuel cells," *J Power Sources*, vol. 363, pp. 251–259, 2017, doi: 10.1016/j.jpowsour.2017.07.085.

[132] Federal Institute for Geosciences and Natural Resources (BGR), "Preismonitor Dezember 2022," 2022. Accessed: Oct. 23, 2023. [Online]. Available: https://www.bgr.bund.de/DE/Themen/Min_rohstoffe/Produkte/Preis-liste/pm_22_12.pdf?__blob=publicationFile&v=5

[133] Z. Xu, J. Luo, and K. T. Chuang, "V2O3 Anode Catalyst for Solid Oxide Fuel Cell using H2S-containing Hydrogen," *ECS Trans*, vol. 11, no. 20, pp. 1–17, Oct. 2008, doi: 10.1149/1.2912042/XML.

[134] Scribner Associates Inc., "Model 855 Installation Procedure," Southern Pines, 2019.

[135] Fuelcellmaterials, "Test Fixture Operation Manual," Ohio, 2020.

[136] I. Jang and G. H. Kelsall, "Fabrication of 3D NiO-YSZ structures for enhanced performance of solid oxide fuel cells and electrolysers," *Electrochem commun*, vol. 137, Apr. 2022, doi: 10.1016/J.ELECOM.2022.107260.

[137] C. R. Brundle, C. A. Evans Jr, and W. Shaun, *Encyclopedia of Materials Characterization: Surfaces, Interfaces, Thin Films*. Stoneham, Greenwich: Butterworch-Heinemann, Manning Publications Co, 1992.

[138] A. Nanakoudis, "SEM Signal - Electron Imaging - Advancing Materials." Accessed: Jan. 20, 2023. [Online]. Available: https://www.thermofisher.com/blog/materials/sem-signal-types-electrons-and-the-information-they-provide/

[139] M. Suga *et al.*, "Recent progress in scanning electron microscopy for the characterization of fine structural details of nano materials," *Progress in Solid State Chemistry*, vol. 42, no. 1–2, pp. 1–21, May 2014, doi: 10.1016/J.PROGSOLIDSTCHEM.2014.02.001.

[140] G. N. Dolenko, O. K. Poleshchuk, and J. N. Latosińska, "X-ray emission spectroscopy, methods," in *Encyclopedia of Spectroscopy and Spectrometry*, 3rd ed., J. Lindon, G. E. Tranter, and D. Koppenaal, Eds., London: Elsevier, 2016, pp. 691–694. doi: 10.1016/B978-0-12-803224-4.00313-7.

[141] L. Spieß, G. Teichert, R. Schwarzer, H. Behnken, and C. Genzel, *Moderne Röntgenbeugung: Röntgendiffraktometrie für Materialwissenschaftler, Physiker und Chemiker*, 2nd ed. Wiesbaden: Vieweg+Teubner, 2009. doi: 10.1017/CBO9781107415324.004.

[142] E. Rezugina, A. L. Thomann, H. Hidalgo, P. Brault, V. Dolique, and Y. Tessier, "Ni-YSZ films deposited by reactive magnetron sputtering for SOFC applications," *Surf Coat Technol*, 2010, doi: 10.1016/j.surfcoat.2010.01.006.

[143] National Institute of Standards and Technology (NIST), "X-ray Photoelectron Spectroscopy (XPS) Database." Accessed: Jan. 20, 2023. [Online]. Available: https://srdata.nist.gov/xps/main_search_menu.aspx

[144] Thermo Fisher Scientific Inc., "Table of Elements." Accessed: Jan. 20, 2023. [Online]. Available: https://www.thermofisher.com/uk/en/home/materials-science/learning-center/periodic-table.html

[145] C. B. Vicent, "Fundamental XPS Data from Pure Elements , Pure Oxides , and Chemical Compounds," *Handbook of Monochromatic XPS Spectra - Elements and Native Oxides*, p. 2, 2000.

[146] J. F. Moulder, W. F. Stickle, P. E. Sobol, and K. D. Bomben, "Handbook of X-ray Photoelectron Spectroscopy Edited by," pp. 1–261, 1993.

[147] M. C. Biesinger, B. P. Payne, L. W. M. Lau, A. Gerson, and R. S. C. Smart, "X-ray photoelectron spectroscopic chemical state Quantification of mixed nickel metal, oxide and hydroxide systems," *Surface and Interface Analysis*, vol. 41, no. 4, pp. 324–332, 2009, doi: 10.1002/sia.3026.

[148] R. E. Loehman, "Characterization of Ceramics," in *Materials Characterization Series*, vol. 15, no. 1, L. E. Fitzpatrick, Ed., New York: Momentum Press, 2010, pp. 54–55. doi: 10.1016/0261-3069(94)90065-5.

[149] F. J. Garcia-Garcia, F. Yubero, J. P. Espinós, A. R. González-Elipe, and R. M. Lambert, "Synthesis, characterization and performance of robust poison-resistant ultrathin film yttria stabilized zirconia - Nickel anodes for application in solid electrolyte fuel cells," *J Power Sources*, vol. 324, pp. 679–686, 2016, doi: 10.1016/j.jpowsour.2016.05.124.

[150] R. M. Langford and A. K. Petford-Long, "Preparation of transmission electron microscopy cross-section specimens using focused ion beam milling," *Journal of Vacuum Science & Technology A*, vol. 19, no. 5, pp. 2186–2193, Sep. 2001, doi: 10.1116/1.1378072.

[151] P. Pavliček and E. Mikeska, "White-light interferometer without mechanical scanning," *Opt Lasers Eng*, vol. 124, p. 7, Jan. 2020, doi: 10.1016/j.optlaseng.2019.105800.

[152] B. Maniscalco, P. M. Kaminski, and J. M. Walls, "Thin film thickness measurements using Scanning White Light Interferometry," *Thin Solid Films*, vol. 550, pp. 10–16, Jan. 2014, doi: 10.1016/j.tsf.2013.10.005.

[153] A. A. Solovyev, S. V. Rabotkin, A. V. Shipilova, and I. V. Ionov, "Magnetron sputtering of gadolinium-doped ceria electrolyte for intermediate temperature solid oxide fuel cells," *Int J Electrochem Sci*, vol. 14, no. 1, pp. 575–584, 2019, doi: 10.20964/2019.01.03.

[154] S. Venkataraj, O. Kappertz, H. Weis, R. Drese, R. Jayavel, and M. Wuttig, "Structural and optical properties of thin zirconium oxide films prepared by reactive direct current magnetron sputtering," *J Appl Phys*, vol. 92, no. 7, pp. 3599–3607, 2002, doi: 10.1063/1.1503858.

[155] J. Joos, "Microstructural Characterisation, Modelling and Simulation of Solid Oxide Fuel Cell Cathodes," Karlsruher Institut für Technologie, 2015.

[156] P. J. Kelly, J. O'Brien, and R. D. Arnell, "The production of porous and chemically reactive coatings by magnetron sputtering," *Vacuum*, vol. 74, no. 1, pp. 1–10, May 2004, doi: 10.1016/j.vacuum.2003.11.002.

[157] A. Anders, "A structure zone diagram including plasma-based deposition and ion etching," *Thin Solid Films*, vol. 518, no. 15, pp. 4087–4090, 2010, doi: 10.1016/j.tsf.2009.10.145.

[158] K. Koski, J. Hölsä, and P. Juliet, "Properties of zirconium oxide thin films deposited by pulsed reactive magnetron sputtering," *Surf Coat Technol*, vol. 120–121, pp. 303–312, 1999, doi: 10.1016/S0257-8972(99)00501-0.

[159] P. K. Song, Y. Shigesato, I. Yasui, C. W. Ow-Yang, and D. C. Paine, "Study on crystallinity of tin-doped indium oxide films deposited by DC magnetron sputtering," *Japanese Journal of Applied Physics, Part 1: Regular Papers and Short Notes and Review Papers*, vol. 37, no. 4 SUPPL. A, pp. 1870–1876, Apr. 1998, doi: 10.1143/JJAP.37.1870/XML.

[160] M. M. Hawkeye and M. J. Brett, "Glancing angle deposition: Fabrication, properties, and applications of micro- and nanostructured thin films," *Journal*

of Vacuum Science & Technology A: Vacuum, Surfaces, and Films, vol. 25, no. 5, pp. 1317–1335, Sep. 2007, doi: 10.1116/1.2764082.

[161] N. Smith, "The Structure of Thin Films of Metallic Oxides and Hydrates," *J Am Chem Soc*, vol. 58, no. 1, pp. 173–179, 1936, doi: 10.1021/ja01292a050.

[162] D. G. Lamas and N. E. Walsöe De Reca, "X-ray diffraction study of compositionally homogeneous, nanocrystalline yttria-doped zirconia powders," *J Mater Sci*, vol. 35, no. 22, pp. 5563–5567, 2000, doi: 10.1023/A:1004896727413.

[163] S. Graulis *et al.*, "Crystallography Open Database - An open-access collection of crystal structures," *J Appl Crystallogr*, vol. 42, no. 4, pp. 726–729, 2009, doi: 10.1107/S0021889809016690.

[164] G. Beamson and D. Briggs, "High Resolution XPS of Organic Polymers: The Scienta ESCA300 Database," *J Chem Educ*, vol. 70, no. 1, p. A25, Jan. 1992, doi: 10.1021/ED070PA25.5.

[165] F. J. Garcia-Garcia *et al.*, "Porous, robust highly conducting Ni-YSZ thin film anodes prepared by magnetron sputtering at oblique angles for application as anodes and buffer layers in solid oxide fuel cells," *Int J Hydrogen Energy*, vol. 40, no. 23, pp. 7382–7387, 2015, doi: 10.1016/j.ijhydene.2015.04.001.

[166] A. A. Solovyev, N. S. Sochugov, I. V. Ionov, A. V. Shipilova, and A. N. Kovalychuk, "Magnetron Formation of Ni/YSZ Anodes of Solid Oxide Fuel Cells," *Russian Journal of Electrochemistry*, vol. 50, no. 7, pp. 647–655, 2014, doi: 10.1134/S1023193514070155.

[167] I.-K. Suh, H. Ohta, and Y. Waseda, "High-temperature thermal expansion of six metallic elements measured by dilatation method and X-ray diffraction," *J Mater Sci*, vol. 23, no. 2, pp. 757–760, 1988, doi: 10.1007/BF01174717.

[168] J. H. Park *et al.*, "Impact of nanostructured anode on low-temperature performance of thin-film-based anode-supported solid oxide fuel cells," *J Power Sources*, vol. 315, pp. 324–330, May 2016, doi: 10.1016/J.JPOWSOUR.2016.03.055.

[169] Y. Lim, H. Lee, S. Hong, and Y. B. Kim, "Co-sputtered nanocomposite nickel cermet anode for high-performance low-temperature solid oxide fuel cells," *J Power Sources*, vol. 412, no. November 2018, pp. 160–169, 2019, doi: 10.1016/j.jpowsour.2018.11.025.

[170] M. C. Biesinger, B. P. Payne, A. P. Grosvenor, L. W. M. Lau, A. R. Gerson, and R. S. C. Smart, "Resolving surface chemical states in XPS analysis of first row transition metals, oxides and hydroxides: Cr, Mn, Fe, Co and Ni," *Appl Surf Sci*, vol. 257, no. 7, pp. 2717–2730, 2011, doi: 10.1016/j.apsusc.2010.10.051.

[171] H. S. Noh, J. W. Son, H. Lee, H. Il Ji, J. H. Lee, and H. W. Lee, "Suppression of Ni agglomeration in PLD fabricated Ni-YSZ composite for surface modification of SOFC anode," *J Eur Ceram Soc*, vol. 30, no. 16, pp. 3415–3423, 2010, doi: 10.1016/j.jeurceramsoc.2010.07.035.

[172] U. P. Muecke, S. Graf, U. Rhyner, and L. J. Gauckler, "Microstructure and electrical conductivity of nanocrystalline nickel-and nickel oxide/gadolinia-doped ceria thin films," 2007, doi: 10.1016/j.actamat.2007.09.023.

[173] X. Lu *et al.*, "Correlation between triple phase boundary and the microstructure of Solid Oxide Fuel Cell anodes: The role of composition, porosity and Ni densification," *J Power Sources*, vol. 365, pp. 210–219, Oct. 2017, doi: 10.1016/J.JPOWSOUR.2017.08.095.

[174] M. C. Biesinger, L. W. M. Lau, A. R. Gerson, and R. S. C. Smart, "Resolving surface chemical states in XPS analysis of first row transition metals, oxides and hydroxides: Sc, Ti, V, Cu and Zn," *Appl Surf Sci*, vol. 257, no. 3, pp. 887–898, 2010, doi: 10.1016/j.apsusc.2010.07.086.

[175] G. Lohmüller, G. Schmidt, B. Deppisch, V. Gramlich, and C. Scheringer, "Die Kristallstrukturen von Yttrium-Vanadat, Lutetium-Phosphat und Lutetium-Arsenat," *Acta Crystallographica Section B*, vol. 29, no. 1, pp. 141–142, Jan. 1973, doi: 10.1107/S0567740873002098.

[176] C. J. Howard, R. J. Hill, and B. E. Reichert, "Structures of ZrO2 polymorphs at room temperature by high-resolution neutron powder diffraction," *Acta Crystallographica Section B*, vol. 44, no. 2, pp. 116–120, Apr. 1988, doi: 10.1107/S0108768187010279.

[177] Haynes William M, *CRC Handbook of Chemistry and Physics*. CRC Press, 2016. doi: 10.1201/9781315380476.

[178] Y. Li, Y. She, and K. Liao, "Hot-Corrosion Behavior of Gd2O3–Yb2O3 Co-Doped YSZ Thermal Barrier Coatings in the Presence of V2O5 Molten Salt,"

Coatings 2023, Vol. 13, Page 886, vol. 13, no. 5, p. 886, May 2023, doi: 10.3390/COATINGS13050886.

[179] T. Chen *et al.*, "Hot corrosion behavior of Y3Al5O12/LaPO4 materials exposed to molten V2O5," *Ceram Int*, vol. 48, no. 10, pp. 14856–14864, May 2022, doi: 10.1016/J.CERAMINT.2022.02.022.

[180] L. Guo, H. Xin, Z. Zhang, X. Zhang, and F. Ye, "Microstructure modification of Y2O3 stabilized ZrO2 thermal barrier coatings by laser glazing and the effects on the hot corrosion resistance," *Journal of Advanced Ceramics*, vol. 9, no. 2, pp. 232–242, Apr. 2020, doi: 10.1007/S40145-020-0363-Z/METRICS.

[181] A. Meenakshisundaram, N. Gunasekaran, and V. Srinivasan, "Distribution of Metal Ions in Transition Metal Manganites AMn2O4 (A: Co, Ni, Cu, or Zn)," *physica status solidi (a)*, vol. 69, no. 1, pp. K15–K19, Jan. 1982, doi: 10.1002/PSSA.2210690149.

[182] C. A. Barrett and E. B. Evans, "Solid Solubility and Lattice Parameter of NiO-MnO," *Journal of the American Ceramic Society*, vol. 47, no. 10, pp. 533–533, Oct. 1964, doi: 10.1111/J.1151-2916.1964.TB13806.X.

[183] Kratos Analytytical Ltd., "Analysis of Ni/Co/Mn alloy using an automated monochromated Ag Lα X-ray source." Accessed: Mar. 22, 2024. [Online]. Available: https://www.kratos.com/sites/default/files/application-downloads/MO405%281%29%20Analysis%20of%20NiCoMn%20alloy%20with%20Ag%20La%20x-rays.pdf

[184] R. Azmi, M. Masoumi, H. Ehrenberg, V. Trouillet, and M. Bruns, "Surface analytical characterization of LiNi0.8-yMnyCo0.2O2 (0 ≤ y ≤ 0.4) compounds for lithium-ion battery electrodes," in *Surface and Interface Analysis*, John Wiley and Sons Ltd, Nov. 2018, pp. 1132–1137. doi: 10.1002/sia.6415.

[185] "Manganese | Periodic Table | Thermo Fisher Scientific - UK." Accessed: Mar. 22, 2024. [Online]. Available: https://www.thermofisher.com/uk/en/home/materials-science/learning-center/periodic-table/transition-metal/manganese.html

[186] A. Leonide, Y. Apel, and E. Ivers-Tiffee, "SOFC Modeling and Parameter Identification by Means of Impedance Spectroscopy," Karlsruhe Institute of Technology (KIT), 2010. doi: 10.1149/1.3247567.